Università degli Studi di Trieste

XXXIV ciclo del dottorato di ricerca in

Fisica

EOS: a new Atmospheric Radiative Transfer procedure for Habitable Worlds based on HELIOS

Settore scientifico-disciplinare: Astronomia e Astrofisica

Dottorando:

Paolo Matteo Simonetti

Coordinatore:

Prof. Francesco Longo

Supervisore di tesi:

Prof. Giovanni Vladilo

Anno accademico 2020-2021

Contents

Abstract

The next generation of ground- and space-based astronomical facilities will be able to retrieve exoplanetary atmospheric spectra in increasing quantity and of increasing quality. Radiative transfer (RT) models of these atmospheres are essential both for interpreting observational data and for linking these data to the planetary physical state with the aid of dedicated climate models.

Here I present EOS, a new RT model tailored for terrestrial-type planets. This model is based on HELIOS and HELIOS-K, which are novel and publicly available codes developed by the University of Bern as a part of the Exoclime Simulation Platform (ESP) repository. These codes make full use of the computing power of Graphics Processing Units and are integrated with a variety of molecular and atomic line repositories such as HITRAN, HITEMP, ExoMol and Kurucz. Until now, HELIOS and HELIOS-K have been mostly applied to study Jupiter-like planets. My work consisted in adapting these codes for the studying of rocky planet atmospheres, which are the most interesting for future searches of atmospheric bisognatures.

The immediate goal is to provide a state-of-the-art RT for the Earth-like planets Surface Temperature Model (ESTM), an energy balance climate model with upgraded treatment of the vertical and horizontal energy transport developed in Trieste. The long term purpose is to provide the astrophysical community with an interdisciplinary tool able to provide a link between climate model results and observational data.

In the First Chapter I make a brief introduction on the known properties of the exoplanet population and the many existing limitations to its study.

In the Second Chapter I focus on the topic of climate and atmospheric modeling and I outline the main climate feedback processes, specifically concerning their role in defining the Circumstellar Habitable Zone (CHZ).

In the Third Chapter I detail the structure of the EOS procedure. After introducing the equations of radiative transfer for clear sky conditions and the approximations adopted by HELIOS, I describe the molecular cross section parameters adopted in this study, especially those concerning the treatment of continuum absorption features of CO2 and H2O.

In the Fourth Chapter I show the testing and intercomparison work done on EOS. Concerning the former, I studied how the procedure responded to variatios of both model parameters and physical inputs. Concerning the latter, I observed how EOS predictions compared to those of other published RT codes.

In the Fifth Chapter I describe the work done to update the ESTM model by enhancing the prescriptions for the treatment of the main properties of clouds and ice. This activity allowed me to indirectly test EOS predictions against observational data of Earth.

In the Sixth Chapter I present my statistical analysis of planetary habitability in binary star systems (published in 2020 in ApJ). This parallel analysis yielded a set of cases that I then investingated using the coupled EOS-ESTM model.

In the Seventh Chapter I present three applications of EOS and ESTM: a preliminary study of the habitability of two circumsecondary planets in a binary system, motivated by the statistical results presented in the previous Chapter; the study of the effects on the Archean Earth climate of different atmospheric chemical makeups; and how the EOS-generated synthetic emission/reflectance spectra can help the data analysis of future space missions.

Finally, in the Conclusions I wrap up the content of this work and present some future perspectives.

Chapter 1

Exoplanets: an introduction

The goal of my PhD was to provide an up-to-date and flexible radiative transfer module to be used in the Earth-like planet Surface Temperature Model (ESTM, Vladilo et al., 2015), which is an energy balance climate model featuring an advanced treatment of the meridional and vertical transport. This goal has been achieved by adapting an already existent RT code, called HELIOS (Malik et al., 2017, 2019a,b), to the peculiarities of terrestrial-type planetary atmospheres.

The broader objective of this work is to provide to the community a fast tool for the characterization of exoplanet surfaces and atmospheres from the limited amount of information that can be retrieved by ground- and space-based astronomical facilities.

Planetary atmospheres are complex, interconnected systems. Radiative transfer is just one piece of the multifaceted topic of atmospheric modelization, yet it cannot be considered apart from the other prominent aspects of this subject. As such, a little bit of introduction is necessary in order to put the reader in the condition to appreciate the content of this thesis.

In this Chapter, I will introduce the object of study, namely the exoplanets. In particular, I will briefly describe the history of detections and the main physical and statistical features of the known exoplanet population.

1.1 History of discoveries

As per the International Astronomical Union (IAU) an extrasolar planet or exoplanet is a celestial object that satisfy a list of three criteria[1]. First of all, it must orbit a star other than the Sun, a stellar remnant or a brown dwarf. Second, it must have an estimated mass comprised between an upper limit of < 13 Jupiter masses (or $M_{\jmath}$) and a lower limit equal to that used for the planets in the Solar System. Third, it must have a mass ratio with the most massive body in its system below $2/49$, which is the limit for the existence of stable L4 and L5 Lagrangian points.

The existence of these objects were supposed, on a philosophical basis, since the XVI century. As a corollary of the recently developed heliocentric Copernican cosmology, in his *De l'Infinito, Universo e Mondi* (1584) Giordano Bruno supported the idea that the stars are similar to the Sun and that around these stars, planets as our own must be present. A century later, that idea was considered again in the appendix of the second edition of the

[1]The text of the working definition as approved by the F2 Commission at IAU can be found at https://www.iau.org/science/scientific_bodies/commissions/F2/info/documents/

Principia Mathematica Phiosophiae Naturalis (1713) by Isaac Newton.

Early detection claims based on scientific data began in the XIX century, when supposed astrometrical anomalies of certain stars were occasionally interpreted as caused by gravitational perturbations of dark companions, generally referred to as planets. The binary star 70 Ophiuchi was identified two times as the host of a third, unseen, planetary body (Jacob, 1855; See, 1896), but in both cases the discovery was eventually disproven. During the XX century, an increasing number of tentative detections were made, notably around 61 Cygni (Strand, 1957), Lalande 21185 (Lippincott, 1960) and Barnard's Star (van de Kamp, 1963, 1969). None of these resisted subsequent reanalysis: as an example, the anomalies identified by Lippincott and van de Kamp were ascribed to small changes in the position of the lenses of the telescope at which the photographic plates were taken (Hershey, 1973). In 1988, the first non-rejected discovery of a planetary mass object around Errai (gamma Cephei A) was made using the radial velocity technique by Campbell et al. (1988), even if the definitive confirmation arrived more than a decade later (Cochran et al., 2002). From 2015, this exoplanet is officially known as Tadmor[2]. In 1992, the first confirmed Earth-mass exoplanets (Poltergeist and Phobetor) were found around Lich (PSR B1257+12), by analyzing the pulsar timing (Wolszczan & Frail, 1992) and finally, in 1995, the first Jupiter-mass planet (Dimidium) was discovered around the Main Sequence Sun-like star Helvetios (51 Pegasi, Mayor & Queloz, 1995). The importance of this last accomplishment was recognized by the assignation of the Nobel Prize in Physics to the two authors in 2019.

In the years following, a number of other relevant stepping stones in this field have been achieved. Among them can be cited for their relevance the detection of the first long-period exoplanet (Thapao Thong or 47 UMa b, Butler & Marcy, 1996), the first confirmation of a multiplanetary system (around Titawin or υ And A, Butler et al., 1999), the first detection via gravitational microlensing (OGLE 2003-BLG-235, Bond et al., 2004) and the first directly imaged exoplanet (2M1207 b, Chauvin et al., 2004). HD 209458 b has been the subject of a number of records on its own, being the first exoplanet to be detected also by transit photometry (Charbonneau et al., 2000; Henry et al., 2000), the first to have its atmosphere detected (Charbonneau et al., 2002) and studied (Richardson et al., 2007; Tinetti et al., 2007), the first to have its upper atmospheric winds detected (Snellen et al., 2010) and magnetic field inferred from the surrounding plasma environment (Kislyakova et al., 2014). Between 2007 and 2013, the French (CNES) and European (ESA) space agencies jointly operated the CoRoT (Convection, Rotation et Transits planétaires) spacecraft, which was the first space-based mission designed for searching short-period transiting planets down to two Earth radii[3], and thus very likely rocky in composition. The mission delivered 34 confirmed bodies and over 600 candidates. In 2009, NASA launched the Kepler Space Telescope, marking the dawn of a golden age in exoplanetary astronomy. During its 9 year operational life, the mission detected 2662 transiting exoplanets, populating especially the intermediate region of exoplanets' sizes (from Earth-size to Neptune-size) and contributing decisively to the current understanding in this field. Among them, there are also 11 of the 12 exoplanets with circumbinary orbits around Main Sequence stars currently known (see Table 6.6). In 2013, the Kepler mission also found the first Earth-sized exoplanet in the circumstellar habitable zone (CHZ) of his star (Kepler-186 f, Quintana et al., 2014), an event that was especially relevant for astrobiology. CHZ is

[2]in this thesis, when possible, exoplanets and their host stars will be referred with their proper names as assigned by the IAU, alongside the nomenclature derived from the binary star name scheme. See https://www.iau.org/public/themes/naming_exoplanets

[3]see www.esa.int/Science_Exploration/Space_Science/COROT_overview

the ring around the parent star in which the equilibrium temperature of a planet allow for the existence of liquid water on its surface. The equilibrium temperature is given by the balance between the incoming radiation from the parent star and the outgoing thermal radiation of the planet. These concepts will be detailed in the next sections. Of special interest was also the discovery of another potentially habitable world around the nearest star, namely Proxima Centauri (Anglada-Escudé et al., 2016). This have sparked several speculative designs for mid-to-far future in-situ missions, given the uniquely accessible position of this exoplanet with respect to Earth (Lubin, 2016). Another relevant discovery in astrobiological terms was that of the TRAPPIST-1 system (Gillon et al., 2017), in which three of the seven small rocky planets orbit in the CHZ. Moreover, their configuration allow for a good characterization of their planetary and orbital parameters. Finally, in 2020, the first free-floating (i.e. unbound from any star) Earth-mass exoplanet has been detected via microlensing (OGLE-2016-BLG-1928, Mróz et al., 2020).

As of July 2021, 4777 confirmed planets have been detected in 3534 planetary systems[4]. Currently, there are several ongoing space- and ground-based missions to continue the search for, and the characterization of, exoplanets. In 2018, NASA put in orbit the Transiting Exoplanet Survey Satellite (TESS[5]), to continue the work begun by the Kepler spacecraft, which had to be deactivated at the end of the same year. It is currently in its extended mission. In 2019 ESA launched the Characterizing Exoplanets Satellite (CHEOPS[6]) with the goal of estimating the radii of known transiting exoplanets. There are also more than 40 ground-based ongoing detection and characterization programs, the most successful of which in terms of detections are the Wide Angle Search for Planets (WASP, Pollacco et al., 2006), the High Accuracy Radial Velocity Planet Searcher (HARPS, Mayor et al., 2003) and the Hungarian Automated Telescopes network (HAT, Bakos et al., 2002).

The future of exoplanetary science rests in a plethora of proposed projects. Among the space based facilities under development can be cited the Planetary Transits and Oscillations of stars (PLATO[7]) and the Atmospheric Remote-sensing Infrared Exoplanet Large-survey (Ariel[8]) spacecrafts, both under development at ESA and expected to be launched in the late 2020s. The former will continue the search for new, rocky extrasolar planets while the latter will characterize the chemical and thermal atmospheric structures of known transiting exoplanets. On the other hand, while it is not its main scientific goal, the joint NASA-ESA-CSA James Webb Space Telescope (JWST) is also expected to deliver high quality near-infrared (NIR) emission and transmission spectra from Jupiter- and Neptune-sized exoplanets (Greene et al., 2016). Concerning the ground based instruments, of particular interest are the Extremely Large Telescope (E-ELT) under construction at the European Southern Observatory (ESO), the Thirty Meter Telescope (TMT) under construction at Mauna Kea and the Large Magellan Telescope (LMT) under construction at the Las Campanas Observatory. All these instruments will be able to support a new generation of projects aimed at characterizing known exoplanets, especially concerning their atmospheres.

[4]as indicated in the Extrasolar Planets Encyclopedia by the Observatory of Paris (Schneider et al., 2011). Note that the Exoplanet Catalog by NASA considers “confirmed" a planet that has been detected by two or more different methods, which reduces the number of objects to 4424 in 3280 star systems. The number of unconfirmed objects is currently 7472.

[5]https://tess.mit.edu/

[6]https://www.esa.int/Science_Exploration/Space_Science/Cheops/Cheops_overview2

[7]https://platomission.com/category/science/science-objectives/

[8]https://arielmission.space/

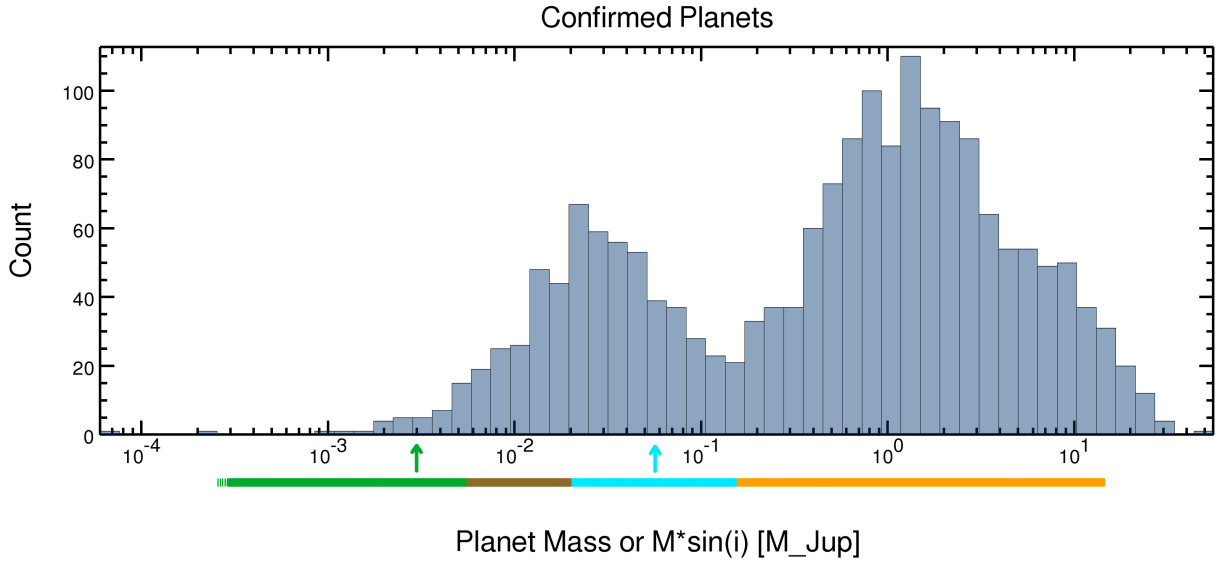

Figure 1.1: The distribution in mass of exoplanets for which this quantity has been determined either as a measurement or as a lower limit. The colored lines identify the four commonly used mass categories in which they are classified: Earths (green), Super-Earths (brown), Neptunes (light blue) and Jupiters (orange). The green and light blue arrows mark the mass of Earth and Neptune, respectively. It should be noted that objects with masses above 13 $M_{\mathcal{Y}}$ (right end of the orange line) are generally considered brown dwarfs rather than planets. Credit: NASA Exoplanet Archive.

1.2 Exoplanet classification

First of all, it must be remembered that only a relatively small amount of data can be retrieved for individual extrasolar planets. Apart from a very small subset of objects whose atmospheres has been spectroscopically probed, our knowledge is usually limited to a combination of mass (or minimum mass), radius, orbital semi-major axis and eccentricity. Moreover, several physical and technological limitations reduce the probability or completely prevent the detection in parts of the exoplanetary parameter space. Hardly accessible regions of this space are, for example, those occupied by low-mass and long-period planets, while face-on small-radius exoplanets will remain completely undetectable even with the next generation of instruments. Technical and physical limitations of different detection methods will be presented in Section 1.3.

1.2.1 Mass classification

Exoplanets are generally classified by their mass (see Fig. 1.1) and their equilibrium temperature. Concerning the mass, exoplanets are classified as "Earths" if their mass in between 0.5 and 2 $M_{\oplus}$, as "Super-Earths" if their mass is between 2 and 8 $M_{\oplus}$, as "Neptunes" if their mass is between 8 and 50 $M_{\oplus}$ and as "Jupiters" if their mass is above 50 $M_{\oplus}$. Jupiters can also be referred to as "gas giant planets". This is not an official nomenclature and therefore different authors may use slightly different mass brackets. There exist also further subdivisions and several overlappings: for example, exoplanets whose mean density (calculated from radius and mass) is strongly below that of silicate rock are called "Mini-Neptunes" even if their mass

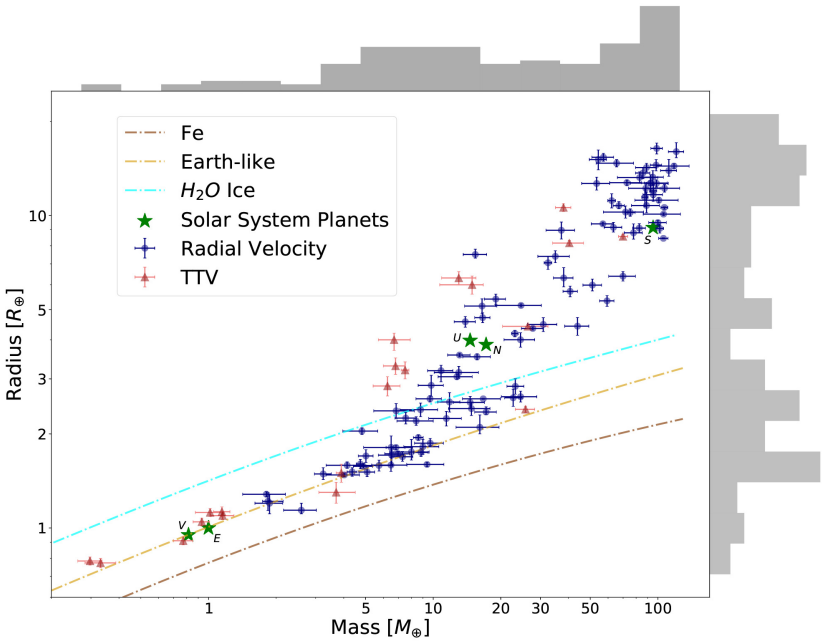

Figure 1.2: The radius versus mass plot for sub-Jovian exoplanets. The cyan, yellow and brown curves represent the ideal mass-radius relation for a planet made of (i) ice, (ii) rocks with the same composition as Earth and (iii) iron, respectively. Blue and red dots stand for exoplanets discovered by radial velocity and transit time variations methods, respectively. On the upper and right borders are reported the cumulative distributions. Credit: Otegi et al. (2020).

would put them in the Super-Earths category. Another used sub-class is that of "Saturns" for planets within the 30-100 $M_\oplus$ (0.1-0.3 M_Jup) bracket. Finally, planets less massive than Earth are associated with their closer analog in the Solar System. These mass brackets seems to be justified by both known and unknown physical processes regarding planetary formation.

At the lower end of the mass spectrum we found the rocky planets, which are expected to be composed mainly by silicate rocks. Differentiation during formation leads to the formation of an iron core and the availability of iron in the protoplanetary disk determines its dimension. This is a very common feature, since it happened even in large asteroids in the Solar System like Vesta, which has a mass of $\sim 4\times10^{-5}$ $M_\oplus$ (Russell et al., 2012). Radioactive decay heating in the core and mantle provides energy for a variety of geological processes such as interior outgassing and the formation of new crust via volcanic eruptions, which are expected to be stronger and long-lasting on more massive bodies. According to some authors (Valencia et al., 2007), Super-Earths should be able to sustain plate tectonics even in the absence of liquid water (which on Earth has the fundamental role of lubricant), but it is not a settled question (O'Neill & Lenardic, 2007). Above the solid surface, rocky planets can gravitationally hold a gaseous atmosphere and, if the pressure and temperature conditions are right, also a liquid layer. If the planet is geologically active, the atmosphere is coupled with the interiors, whose chemical and physical state must be assessed in order to study its evolution (Kasting et al., 1993a; Trail et al., 2011; Wordsworth et al., 2018). Differently from more massive planets, the gas and liquid (or "volatile") part of rocky planets are expected to be very small with respect to the total mass of the body. As an example, Earth's surface water inventory and atmosphere

account, respectively, for 0.02% and 0.0001% of the planet mass[9]). Given that the ability to retain a large atmosphere depends on the escape velocity, Super-Earths are expected to be able to support larger atmospheres, even though this assertion cannot be proved with the current generation of astronomical instruments.

Having only a modest volatile envelope may be a requirement for the origin and evolution of life. First of all, life as we know it requires relatively narrow range of pressure and temperature conditions to thrive and this requirement may not hold true in large fluid envelopes of Neptune- and Jupiter-like planets. In fact, the vigorous convection that dominates the energy transmission throughout most of their thick atmospheres rapidly reshuffle gas between cool, low pressure layers and hot, high temperature ones. The range of variation increases with the total mass of the fluid envelope, therefore the physical limits of life may impose an upper limit on atmospheric thickness. Moreover, the presence of a mineral substrate (i.e. clay) might have played a fundamental role in the origin of life, by concentrating prebiotic molecules and catalyzing the formation of amminoacids, nucleotides and ATP[10] (Lahav et al., 1978; Cleaves et al., 2012). As such, rocky exoplanets are especially important from an astrobiological point of view and are the focus of most of the modeling effort in relation to the topic of planetary habitability.

Transitioning from a Super-Earth to a Neptune the typical composition of a planet changes drastically: the fraction of low density volatile substances (like water, ammonia, carbon dioxide and methane) on the total mass increases markedly, producing a kink in the mass-radius relation that can be clearly seen in Fig. 1.2. As such, planets below the 8 $M_\oplus$ threshold are mostly composed by a mix of silicates and iron, while those above that threshold has deep and dense fluid envelopes surrounding a solid core. This transition is also marked by a valley in the radii distribution, centered around 2 $R_\oplus$ and especially visible at mid-to-short orbital periods (20-80 d), known as Sub-Neptunian Desert or Fulton Gap (Fulton et al., 2017; Van Eylen et al., 2018). This gap seems to be related to the inability of Super-Earth-mass cores to accrue and retain such an envelope of volatiles, especially if subjected to large stellar fluxes, while larger cores can. A competing explanation, proposed by Ginzburg et al. (2018), is that the mass loss for this class of planets is not driven by the star, but rather by the energy flux of the cooling rocky core.

Increasing the mass of the planet also increase the fraction of lighter elements (specifically, H and He) with respect to metals[11] (e.g. C, N and O) in the planetary composition. At a certain point, the planet becomes dominated by the former and can be categorized as a Jupiter. Also in this case the transition from one class to another is marked by a valley, visible both in the mass and in the radius distribution. This gap is called the Sub-Jovian or Hot Neptune Desert and manifests itself as a scarcity of very short period ($\lesssim$ 6 days) planets in a triangular-shaped region in the mass-period plane, at around 30-80 $M_\oplus$ (Szabó & Kiss, 2011; Mazeh et al., 2016). Multiple physical explanations have been proposed for it: different formation mechanisms (West et al., 2019), stellar induced photoevaporation (Kurokawa & Nakamoto, 2014) or tidal disruption during migration and the subsequent orbital circularization (Owen & Lai, 2018). In particular, photoevaporation has been proposed to explain the low-mass border of the desert, while the tidal disruption is a more adequate to understand the high-mass border of the desert. This scarcity could also be caused by a combination of a physical mechanism and an observational bias: differences in planetary

[9] See www.usgs.gov

[10] Adenosine Tri-Phosphate

[11] In astrophysics, elements different from H and He are traditionally called metals.

migration would prevent Neptune-size planets to access close orbits around their parent stars and therefore remain undetected or under-detected due to observational difficulties.

Finally, the upper limit for Jovian-type planets (at around ∼4200 $M_\oplus$ or ∼13 M_{Jup}) relates to the conditions at which deuterium-proton thermonuclear reaction becomes possible in the body's core[12], effectively transitioning in the realm of self-luminous objects. Once again, this is not an entirely settled definition. The deuterium burning limit depends on the helium mass fraction, the deuterium abundance and the metallicity of the object. Moreover, the fraction of deuterium burned over a 10^{10} yr period is a continuous function of the body's mass. When all these variables are accounted for, the upper planetary mass limit can range from ∼11 M_{Jup} for high metallicity (three times that of Sun) and low burned fraction (10%) to ∼16 M_{Jup} for zero metallicity and high (90%) burned fraction (Spiegel et al., 2011). This has stimulated others to search for an alternative mass cutoff. Among them we can cite (i) the mass at which the planetary interiors are supported mainly by the degeneracy pressure of free electrons rather than Coulomb repulsion (at around 5 M_{Jup}) and (ii) the mass distribution minimum of the sub-stellar companions of G- and K-type stars at around 20-40 M_{Jup} (Sahlmann et al., 2011; Schneider et al., 2011). The former limit spurs from the consideration that there exist a variety of other non-planetary bodies where free electron degeneracy pressure is dominant, including high-mass brown dwarfs and compact stellar remnants like white dwarfs. The latter limit would distinguish planets from non-planets on the basis of the formation mechanism, identified by a change in the shape of the mass distribution of these bodies. However, derivations of this distribution from stellar clusters observations seem to not support the existence of such a divide (Peña Ramírez et al., 2012).

1.2.2 Temperature classification

The equilibrium temperature of a planet is defined by the equilibrium between the incoming stellar radiation $\tilde{\mathcal{I}}$ absorbed and the outgoing thermal radiation $\tilde{\mathcal{O}}$ emitted to space. For a circularly orbiting planet, the first quantity can be expressed as:

$$\tilde{\mathcal{I}} = L_\star(1-\alpha)f_{\text{geom}} = 4\pi R_\star^2 \sigma_{\text{SB}} T_\star^4 (1-\alpha)\left(\frac{R_p^2}{4a_p^2}\right) \tag{1.1}$$

where $L_\star$ is the star bolometric luminosity, α is the fraction of light reflected by the planet (called Bond albedo) and f_{geom} is the fraction of the stellar luminosity intercepted by the planet. The latter term depends on the intercepting area πR_p^2 and the planetary semi-major axis a_p. $R_\star$ and R_p are the stellar and planet radii, respectively, σ_{SB} is the Stefan-Boltzmann constant and $T_\star$ is the effective temperature of the star. The second quantity, $\tilde{\mathcal{O}}$, is equal to $4\pi R_p^2 \sigma_{\text{SB}} T_p^4$. Equating $\tilde{\mathcal{I}}$ and $\tilde{\mathcal{O}}$ it is possible to derive:

$$T_p = \left(\frac{R_\star^2 T_\star^4 (1-\alpha)}{4a_p^2}\right)^{1/4} \tag{1.2}$$

For exoplanets, the variables needed to calculate T_p are uncertain (such as stellar and orbital parameters) or unknown (like the albedo). As such, the equilibrium temperature

[12] At around 1 M_{Jup}, the high-pressure metallic hydrogen layer that forms between the solid core and the fluid envelope start to dissolve the former (Wilson & Militzer, 2012; Wahl et al., 2013). This process is thought to be more efficient if the metallic hydrogen layer is deeper, i.e. if the planet's mass is larger. Therefore, at some M_{Jup}, at the planet's center there is not a rocky core anymore, but rather an extremely high pressure mix of hydrogen and heavier elements.

bears error of several percentage points: for example, the sole uncertainty on the incoming flux received by TOI-700d is ∼12% (see Table 1 of Suissa et al., 2020). Moreover, T_p is equal to the surface temperature only for airless or nearly airless bodies, since the presence of an atmosphere can substantially reduce the ability of the surface to cool by radiating energy to space. The calculation of this effect constitutes an important part of the present work, thus it will be discussed in detail in the next Chapters. Nevertheless, it constitutes an important information to assess the possible evolution of the body and its current state.

On the basis of their estimated T_p, exoplanets are classified as "Hot" if it is above 1000 K, "Warm" if it is between 1000 and 300 K, "Cool" if it is between 300 and 150 K and "Icy" if below 150 K. "Temperate" is used specifically to describe planets with an Earth-like T_p (i.e. between 250 K and 300 K). Also in this case, the nomenclature is not official but widespread. These classes follow approximately the temperatures of the planets of the Solar System and allow researchers to draw a comparison between them and exoplanets.

Hot exoplanets receive a stellar flux that is far (even orders of magnitude) higher than the highest flux received by any Solar System planet, allowing for exotic conditions like vaporized rock (silicate) atmospheres and surface magma oceans on rocky objects (Léger et al., 2011), and consistent expansion and escape of the upper planetary layers on gas giant planets (Mandushev et al., 2007).

Warm exoplanets receive fluxes that are comparable with that of the innermost Solar System planet, Mercury, therefore Earth- and Super-Earth-type exoplanets in this class are expected to be similar to Mercury and Venus, with solid surfaces and possible CO_2 atmospheres. On the other hand, warm gaseous planets are not present in our system and their features are much more speculative. While warm Jupiters are expected to be stable against hydrogen photoevaporation and thus their composition should be similar to that of other planets of similar mass, warm Neptunes can be stripped of their hydrogen component, leaving behind helium-dominated atmospheres (Hu et al., 2015).

Cool exoplanets receive a stellar flux similar to that received by the Earth or Mars. These objects are especially interesting in astrobiology because they orbit inside the CHZ of their star and can, at least theoretically, bear liquid water on their surfaces (if rocky) or on their large moons' surfaces (if gaseous). The real surface temperature of these bodies depend strongly on the radiative properties of their atmospheres and can significantly differ from the equilibrium temperature. As an example, Venus receive 1.9 times the flux of Earth and, thanks to its high albedo, has $T_p \simeq 230$ K. However, its average surface temperature exceeds 730 K. For this reason, accurate atmospheric models coupled with climate models and a solid knowledge of the atmosphere-surface interaction are needed to assess the true conditions on these worlds, especially in conjunction to habitability studies.

Finally, icy Neptune- and Jupiter-type exoplanets are expected to be similar to the outer planets of our Solar System from which these classes draw their names, while icy Earths and Super-Earths should be similar to the bodies of the Kuiper belt or the moons of the planets of the outer Solar System, i.e. composed by a mix of rocks and ices. They can or cannot have atmospheres, depending on their mass and equilibrium temperature. For very low T_p, much of the chemical species that can reasonably compose an atmosphere would be condensed in liquid or solid form on the surface.

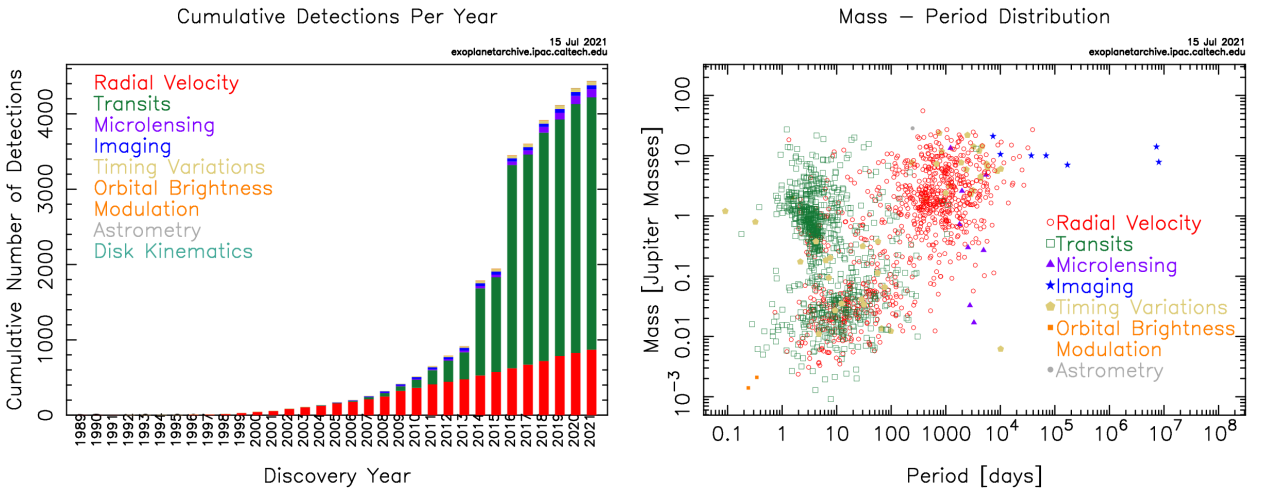

Figure 1.3: Left panel: the cumulative exoplanet detections per year. Right panel: the mass-period distribution of discovered exoplanets. Detection methods are identified by different colors, reported in both panel legend. Credit: NASA Exoplanet Archive.

1.3 Detection methods

As anticipated in the previous sections, there exist a variety of different detection methods for exoplanets. Unfortunately, each method is subject to a number of observational biases and yields only part of the information that researchers need to characterize the observed body. Understanding these limitations is important to clarify the role of modeling in this field of knowledge. Below I will briefly present the main techniques employed to detect exoplanets, together with their main strengths and limitations under the current generation of astronomical instruments.

1.3.1 Astrometry

Historically, the first claims of unseen bodies around other stars have been supported by supposed periodic anomalies in the proper motion of stars, even though none of these early claims have resisted the following scrutiny. The motion of a star around the common barycenter of the system due to the gravitational pull of an undetected exoplanet would cause the star itself to follow an helical path on the celestial sphere (Fig. 1.4, left panel) which, if it is sufficiently marked, can be detected from Earth.

The entity in terms of angular displacement of this anomalous wiggle depends on three quantities: the mass ratio between the planet (p) and the star ($\star$), the planetary semi-major axis (a_p) and the distance of the system from the Earth ($d_\star$) and can be calculated as:

$$\alpha = \left(\frac{M_p}{M_\star}\right)\left(\frac{a_p}{1\ \mathrm{AU}}\right)\left(\frac{1\ \mathrm{pc}}{d_\star}\right)\mathrm{arcsec} \tag{1.3}$$

The distance of the star from the observer can be derived via parallax, while in principle the degeneracy between M_p and a_p can be solved by measuring the orbital period of the planet. Being able to trace the entire orbital trajectory allows for a full determination of other orbital parameters, most notably the eccentricity and the inclination with respect of the line of sight.

Inserting the value for a Jupiter analog (i.e. a planet exactly like Jupiter, both in mass and in its orbital parameters) around a Sun-like star at 10 pc of distance, the amplitude of

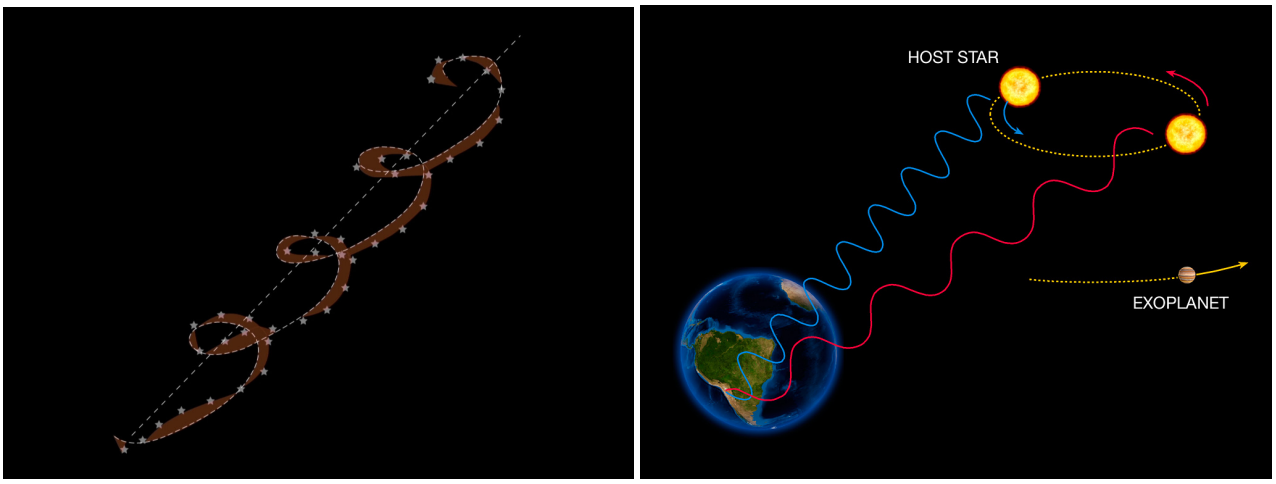

Figure 1.4: Illustrations of the astrometrical (left) and radial velocity (right) detection methods for exoplanets. Left panel: the apparent motion in the sky of a star under the gravitational pull of an unseen object (credit: ESA). Right panel: the Doppler shift in the star light due to its motion around the common barycenter of the planet-star system (credit: ESO).

the perturbation would be ∼500 μas during a time baseline of ∼6 years (half of the orbital period of the planet), while for an Earth analog it would be ∼0.3 μas. For comparison, the Gaia astrometric satellite is able to evaluate the position of stars up to magnitude 15 with a precision of 24 μas as reported by the Gaia mission overview[13]. From these numbers it is clear that astrometric detections, at least with current technology, is restricted to Jupiter-type exoplanets with large orbits around relatively close, and low-mass (M- and K-type), stars. It also requires observational campaigns that are many years (or even decades) long. Due to these limitations, up to this date, very few exoplanets have been detected with this method. The Extrasolar Planets Encyclopedia (EPE from now on, Schneider et al., 2011) lists only 3 objects with a measured mass below 13 M_{Jup} as being discovered in this way: HD 176051 b (Muterspaugh et al., 2010), 2MASS J0249-0557 AB c (Dupuy et al., 2018) and TVLM 513-46546 b (Curiel et al., 2020).

1.3.2 Radial velocimetry

Instead of detecting the actual motion of a star around the common barycenter of the system as in the astrometry methodology, it is possible to try to detect the Doppler shift in the spectral lines of a star due to its line-of-sight velocity variation. In fact, if the orbital plane of the unseen object is seen edge-on, its gravitational pull results in a periodic approach and departure of the star with respect of its mean motion (Fig. 1.4, right panel). If this wobbling motion is sufficiently strong, it can be detected by taking high resolution spectra of the star. This is commonly called radial velocity method.

The amplitude of the line-of-sight velocity due to the planet is equal to:

$$K_{\text{RV}} = \frac{2\pi a_p M_p \sin(i)}{(M_p + M_\star)P\sqrt{1-e^2}} \tag{1.4}$$

where i is the inclination of the orbital plane of the planet with respect to the observer, P is the orbital period and e is the eccentricity (Haswell, 2010). Substituting the third Kepler

[13] see www.esa.int/Science_Exploration/Space_Science/Gaia_overview.

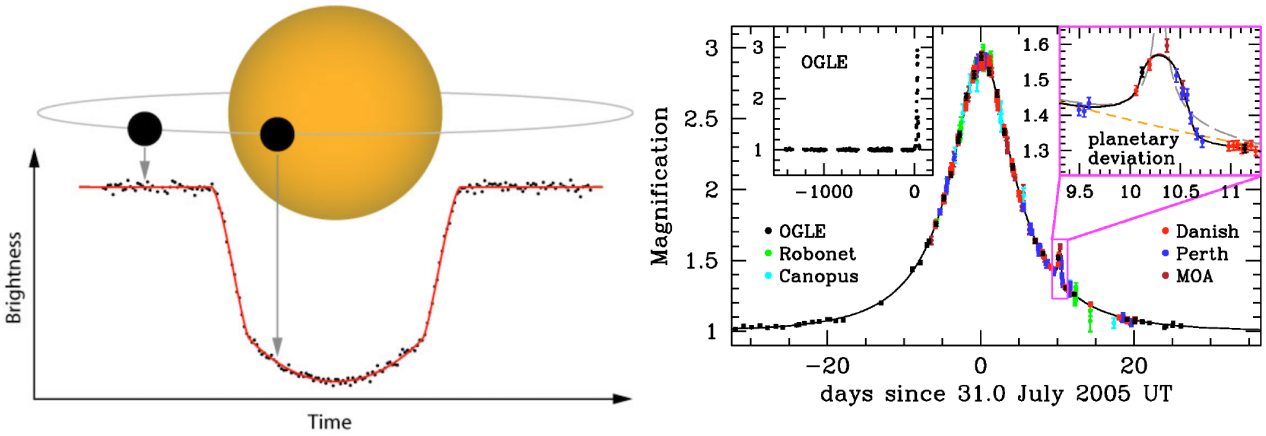

Figure 1.5: Illustrations of the transit photometry (left) and gravitational microlensing (right) detection methods for exoplanets. Left panel: the dimming of a star caused by the passage of a planet in front of its disk (credit: NASA TESS Mission). Right panel: the light curve of a bulge star produced by the lensing effect of a planetary system passing in front of it (fig. 1 of Beaulieu et al., 2006).

law for the period yields:

$$K_{\mathrm{RV}} = \sqrt{\frac{G}{a_p(M_p + M_\star)(1-e^2)}} M_p \sin(i) \tag{1.5}$$

where G is the universal gravitational constant. This equation makes clear that the signal is stronger for massive planets in close, face-on orbits around their parent stars. This introduces an observational bias that is clearly visible in the mass-period plot of known exoplanets (Fig. 1.3, right panel): there are no radial velocity detection in the lower right corner of the plot, which corresponds to low mass, long period planets. The current generation of instruments, like the Echelle Spectrograph for Rocky Exoplanets and Stable Spectroscopic Observations (ESPRESSO), has a sensibility of $\sim$0.1 m s^{-1}, which is equal to the signal produced by an Earth analog orbiting around a Sun-like star[14]. This value is also similar to the value at which the jitter motion of the gas due to stellar activity becomes the dominant source of uncertainty (Makarov et al., 2009). On the other hand, a Jupiter analog produces a signal of around 10 m s^{-1} and hot Jupiters can produce signals of several hundreds m s^{-1}. Until now, 870 exoplanets have been detected so far via radial velocimetry, including the first successful detection of an exoplanet around a Main Sequence star (Mayor & Queloz, 1995).

The form of the velocity curve allow for the determination of the planetary orbital parameters, apart from the inclination i. This introduces a degeneracy between M_p and i. As such, only the lower limit of the planetary mass, usually indicated as $M \sin(i)$, is retrievable.

1.3.3 Transit photometry

If a planet transits in front of the star disk with respect to the observer, it will produce a temporary, periodic reduction of the apparent luminosity of that star (see Fig. 1.5, left panel). If the eclipsing body is large enough, the luminosity variation will be detectable. The

[14] see www.eso.org/sci/facilities/paranal/instruments/espresso/science.html.

geometrical condition required for a transit in case of a circular planetary orbit is:

$$a_p \cos(i) < R_p + R_\star \tag{1.6}$$

where R_p and $R_\star$ are the planetary and stellar radii, respectively. This condition is fairly restrictive, in the sense that only a small percentage of exoplanets can be observed transiting in front of their parent stars. Charbonneau et al. (2007) estimated that the probability of a transit, in the hypothesis of randomly distributed orbital planes, is equal to $0.0045\,(1\,\mathrm{AU}/a_p)\,(R_\star/R_\odot)$. Another problem is that the transit has a limited duration with respect of the total orbital period, which can be calculated as:

$$t_{\mathrm{tran}} \simeq 13 \left(\frac{M_\star}{M_\odot}\right)^{-1/2} \left(\frac{a_p}{1\,\mathrm{AU}}\right)^{1/2} \left(\frac{R_\star}{R_\odot}\right) \quad \text{hours} \tag{1.7}$$

Considering that the orbital period of Earth is ∼8766 hours, the transit amounts to 0.15% of that time. In order to make up for the lost detections, a large number of stars must be studied at once in wide field surveys, continuously and for long periods of time (multiple times the orbital period of the targeted class of exoplanets). As such, space based instruments are especially suited for this type of observations.

The intensity of the signal is given by the dip in the measured flux F incoming from the star, which is equal to:

$$\frac{\Delta F}{F} = \frac{R_p^2}{R_\star^2} \tag{1.8}$$

for mid-transit, fully superimposed exoplanets. This allow to estimate the planetary radius, once the stellar radius has been estimated by spectral class and evolutionary models. The entity of the signal is in the order of 1% and of 0.01% for Jupiter and Earth analogs around a Sun-like star, respectively. The latter value is well within the operational range of the current astronomical facilities. The recently concluded Kepler mission was designed to detect luminosity variations down to 0.002%, a value at which the stellar intrinsic variability becomes a relevant source of noise (Gilliland et al., 2011).

Other information that can be retrieved are the orbital period from the observation of multiple transits and the exact inclination from the shape of the dip. The duration of the transit contributes to the determination of the mass and radius of the star, and of the semi-major axis of the planet. A transit exoplanet offers also the possibility of retrieving the absorption spectrum of its atmosphere which, for Earth and Super-Earth class exoplanets, is one of the very few ways to estimate the physical conditions on their surfaces. Being interconnected with the topic of this thesis, this aspect will be discussed in detail in another section.

There are several observation biases linked to this technique. First of all, the probability of a transit becomes vanishingly small for a semi-major axis above 5 AU. Moreover, for larger distances the temporal baseline of observations becomes unwieldy. This explains why most of transit photometry detections concentrate in the left part of the mass-period plot (Fig. 1.3, right panel). Second, larger bodies around small stars produce a stronger signal. Finally, the problem of false positives produced by stellar activity requires follow ups for transit photometry detections, generally in the form of a confirmation via another method such as radial velocimetry, which favours massive Neptune- and Jupiter-like exoplanets over lighter Earth-like ones. This leaves the lower part of the mass-period plot scarcely populated.

1.3.4 Gravitational microlensing

When a star system crosses in front of another star in background due to relative proper motion, the former acts as a gravitational lens, producing a characteristic increase in the luminosity of the latter. If the geometry of the crossing is right, the exoplanets act themselves as lenses, producing additional transient peaks (see Fig. 1.5, right panel).

The theoretical basis for this method comes from Einstein's General Relativity. In particular, gravity is predicted to bend light rays that otherwise would not be connected to the observer, producing a ring of light with an angular radius of:

$$\theta_E = \sqrt{\frac{4GM_\star d_{\star-\star}}{c^2 d_{\star-\oplus}(d_{\star-\oplus} + d_{\star-\star})}} \tag{1.9}$$

where $d_{\star-\star}$ is the distance between the background star and the crossing star and $d_{\star-\oplus}$ is the distance between the crossing star and the Earth. The lensing effect is maximum when $d_{\star-\oplus} \sim 0.5\, d_{\star-\star}$. This request, plus the necessity to have a crowded star field to maximize the probability of this type of transit, makes the Galactic Bulge an optimal region of the sky to observe for gravitational microlensing events. As for the transit photometry method, also in this case a continuous observation is required. The intensity, both of the main signal and the secondary peaks, depend on the square root of the lensing body mass and therefore exoplanets with large masses, and especially large planet-star mass ratios, are favored, although even Earth-mass objects are detectable. Moreover, the exoplanet signal is strongest if the planet-star line-of-sight distance is equal to the Einstein radius $\theta_E d_{\star-\star}$, and as such bodies with intermediate semi-major axes of some AU are favored. This is clear from the mass-period plot (Fig. 1.3, left panel): microlensing detections concentrate at mid-to-high orbital periods.

This method has several advantages: (i) multiple exoplanets can be discovered in a single event, (ii) low, Earth mass exoplanets and exoplanets with large (multiple AU) semi-major axes can be detected and (iii) is effective for the detection of distant (several kiloparsecs) planetary systems, where other methods can be employed only up to few hundreds of parsecs. Moreover, gravitational microlensing can be used to detect free floating exoplanets, which are planetary mass bodies gravitationally unbound from any star. On the other hand, there are two main disadvantages, namely the fact that these are unpredictable and non-repeatable events and the fact that the lensing star is not observable, which means that the system cannot be well characterized. Regarding the exoplanets, this method allows us to determine the planet-star mass ratio and their instantaneous distances.

So far, 157 exoplanets have been detected via microlensing. 27 of these bodies are free floating exoplanets, although mass uncertainties can put some of them above the brown dwarf limit.

1.3.5 Pulsar and transit timing variations

Exoplanets can be detected also via their altering influence of periodic signatures coming from the planetary system. Rather than a single technique, this constitutes a class of methods that have been applied to variety of different astronomical objects.

These methods can be subdivided in two categories. In the first one, the signal of a planet is searched in the pulsating nature of the central star. In this case, the gravitational pull of the unseen exoplanet can change the time of arrival of the signal if the central body is a pulsar, like in the case of Lich (Wolszczan & Frail, 1992), or can vary the pulsation period

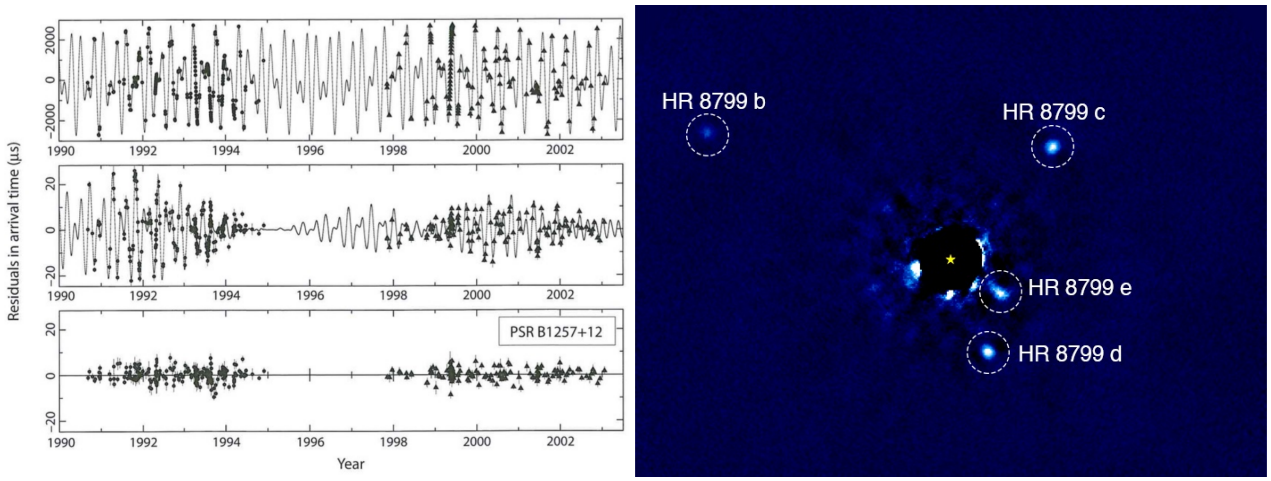

Figure 1.6: Examples of pulsar timing (left) and direct imaging (right) detection methods for exoplanets. Left panel: the time of arrival residuals in the radio signal from Lich (top), the residuals after the inclusion of the effect of three exoplanets (mid) and the residuals after the inclusion of planet-planet second-order perturbations (bottom). Credit: Konacki & Wolszczan (2003). Right panel: the near infrared image of the HR 8799 planetary system (Marois et al., 2008) taken at the Keck Observatory (credit: Jason Wang).

of a pulsating variable star, like in the case of V391 Peg (Silvotti et al., 2007). An example of this can be seen in Fig. 1.6, left panel. In the second category of timing methods, the signal of the planet is searched in the periodicity of transits, either if the light source is an eclipsing binary or in the case there is already a known transiting planet in the system. These are exemplified by the detection of two exoplanets in the DA/M5 (white dwarf/red dwarf) NN Ser binary system (Beuermann et al., 2010) and the discovery of a second non-transiting exoplanet in the Kepler-19 system (Ballard et al., 2011), respectively.

The performance of the timing variation methods depend on the intrinsic stability of the pulsating signal. Wolszczan (1999) gives the following equation for the signal amplitude produced by a circular, edge-on orbiting body around a pulsar:

$$K_\tau \simeq 1.2 \left(\frac{M_p}{M_\oplus}\right)\left(\frac{P_p}{1\mathrm{yr}}\right) \quad \mathrm{ms} \tag{1.10}$$

from which it can be seen that small, sub-terrestrial mass planets can be easily detected. This is due to the extreme regularity of the pulsars. Also transit timing variations applied to transiting exoplanets allow for the detection of relatively small mass bodies like Super-Earths. On the other hand, binary star minima perturbations require Jupiter-like masses to produce a detectable signal.

Exoplanets detected via timing variation methods can have their physical features characterized with a varying degree of precision. Usually, only the lower mass limit is known due to the lack of data about inclination with respect to the line of sight. Another datum that can be derived is the orbital period of the unseen body, and in certain cases also the eccentricity.

Until now, ~30 exoplanets have been discovered with these methods combined, most of them in “exotic" systems, where either the central star is actually a post-Main Sequence remnant or the binary system has undergone a common envelope phase. These discoveries were unexpected due to the destabilizing nature of the post-Main Sequence phase on a planetary system and give unique insight on planetary formation processes if, as it has been hypoth-

esized, these exoplanets have formed from the leftover matter after the death of the parent body. On the other hand, they are not as interesting from an astrobiological point of view, given the very small probability that life, at least as we know it, can survive such a cataclysmic event.

1.3.6 Direct imaging

While the methods discussed above allow for the indirect detection of an exoplanet, via its influence on the visible parent body that they are orbiting, direct imaging detection corresponds to the actual capture of radiation emitted or reflected by the exoplanet. In other words, it corresponds to take a picture of the celestial body in analysis. An example of this type of technique is reported in Fig. 1.6, right panel.

The EPE lists 53 exoplanets as having been detected via direct imaging. The number of directly imaged exoplanets is kept low by two serious observational challenges. The first one is related to the high star-planet luminosity contrast. Stars are $\sim 10^9 - 10^{10}$ times more luminous in the visible, and $\sim 10^5 - 10^7$ more luminous in the mid-infrared, than a planet. This means that very sensitive detectors, together with coronagraphs to mask the incoming star light, must be used. The second one is related to the small angular separation between the light sources, which requires the use of large aperture telescopes in order to resolve them. Combining the equation for the first Airy disk minimum and the definition of parsec, it is possible to obtain the minimum diameter D of a telescope:

$$D \simeq 0.31 \left(\frac{\lambda}{1\,\mu\text{m}}\right)\left(\frac{d_\star}{1\,\text{pc}}\right)\left(\frac{1\,\text{AU}}{a_p}\right) \quad \text{m} \tag{1.11}$$

where λ is the wavelength at which the observation is done, $d_\star$ is the distance of the star system from Earth and a_p is the planet-star separation. Moreover, these two problems are related to each other: due to the point spread function of the stellar light, the maximum contrast allowed for a detection increases with the angular separation. This relation is more stringent for ground based instruments, for which the turbulence of the Earth atmosphere contributes to diffusing the incoming radiation, an effect called seeing. The seeing is measured by the full width at half maximum (FWHM) of the light distribution produced by this effect, and the best achievable seeing from surface is ~ 0.4 arcsec. For comparison, an Earth analog at 10 pc of distance would have an angular separation from its parent star of 0.1 arcsec. Techniques such as adaptive optics and speckle imaging can improve the angular resolution of surface telescopes by 5-10 times, bringing the effect of the seeing down to 0.04-0.06 arcsec. The instruments mounted on next generation facilities such as the Multi-AO Imaging Camera for Deep Observations (MICADO) at the E-ELT are expected to further reduce this effect down to 0.004 arcsec[15].

The limitations related to direct imaging techniques impose a limit on the type of exoplanets observable by the current generation of instruments. Jupiter-size exoplanets with large (tens of AU) which have been recently formed, and thus have high intrinsic emission in the infrared due to accretion heat, are clearly favored. A high $M_p/M_\star$ ratio also helps reducing the overall contrast.

On the other hand, direct imaging offer a wide range of information on the targeted exoplanet. Orbital parameters can be inferred by few, discontinuous snapshots of the system.

[15] https://elt.eso.org/instrument/MICADO

The emission spectrum of the exoplanet can be used to derive properties such as its effective temperature and, for particularly bright sources, the chemical composition.

1.4 Exoplanet statistics

The number of currently known exoplanets is sufficiently large as to allow for a statistical analysis of their properties. This kind of study is fundamental in many ways. First of all, it gives us a better understanding of the planetary formation processes, no more confined to a single case study, i.e. our Solar System. Second, it allows us to estimate the frequency of certain classes of planets, like cool Earth-mass ones, which is relevant for astrobiology and the search for life outside our planet. Third, their architecture shed light on the dynamical evolution of planetary systems.

Different properties of exoplanet population can be related with each other and with the properties of the environment in which those planets exists, e.g. the properties of their parent star. Here we will present a brief overview of these properties, as described in reviews of the subject such as Zhu & Dong (2021).

1.4.1 Properties of the host stars

The nature of the host star (or multiple star system) has several different impacts on the occurrence rate of exoplanets, F_p. First of all, about 30% of A-, F-, G-, K- and M-type single stars host exoplanets down to Earth-like masses and radii. The average planetary multiplicity n_p of these systems is $\sim$3, producing a global planet-to-star ratio of $\sim$1.

The first distortion effect regards the presence of a second star in the system: in binary star systems, the frequency of circumstellar planet is suppressed depending on the binary semi-major axis. For separations $\gtrsim$100 AU the suppression effect is negligible and the ratio between the actual and the theoretical fractions of binary star hosting circumstellar planets around the primary (i.e. the most massive star in the couple) is above 85%. This suppression increases linearly when the binary separation is reduced, and for binary semi-major axes $\lesssim$10 AU the planet-hosting binaries reduces to less than 15% (Moe & Kratter, 2019). This can be easily explained invoking the perturbations in the circumstellar protoplanetary disk induced by the companion. Kraus et al. (2016) concluded that $\sim$43% of binaries with FGK primaries could not host planets due to the inability to form them. The planetary formation suppression in binary stars is relevant on the global statistics of exoplanets, since $\sim$50% of FGK field stars are binaries (Duchêne & Kraus, 2013; Tokovinin, 2014). A much more detailed analysis of this distortion effect is presented in Section 6.1.

A second distortion effect is produced by the metallicity of the host star. Stellar metallicity in astrophysics refers to the fraction of the star mass locked in elements heavier than helium, which for the Sun is $\sim$1.3% (Asplund et al., 2009). It is usually tracked by the iron content of the star and expressed by the quantity:

$$[\mathrm{Fe/H}] = \log(N_{Fe}/N_H)_\star - \log(N_{Fe}/N_H)_\odot \tag{1.12}$$

where N_{Fe} and N_H are, respectively, the number fractions of Fe and H in the stellar photosphere, usually referred to as abundances. The first logarithm is calculated on the abundances of the target star as derived from spectroscopic observations and line modeling, while the second logarithm is calculated on the abundances of the Sun, as derived by meteorite sampling,

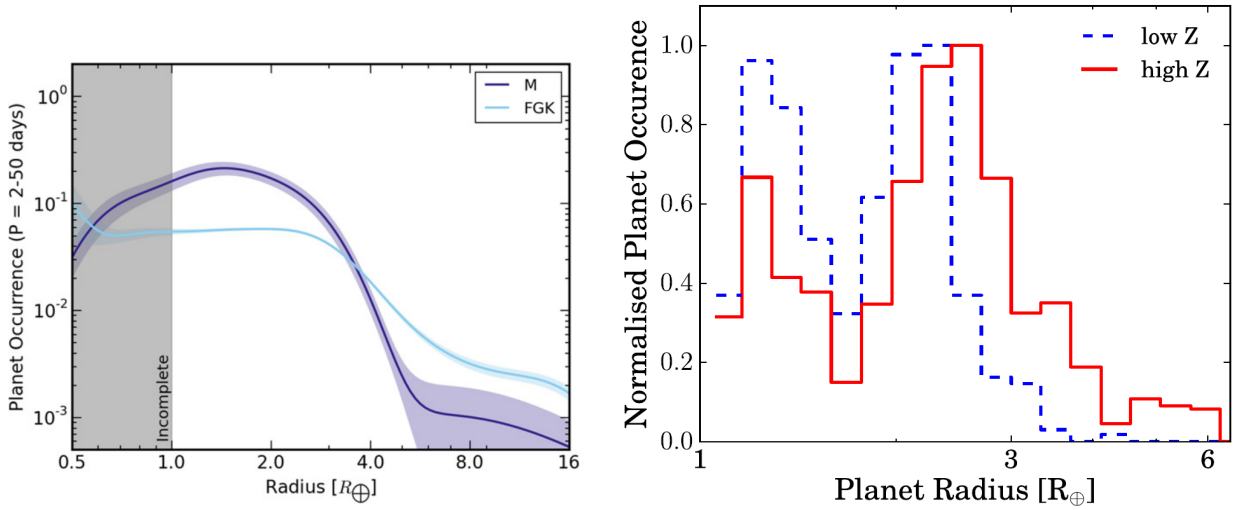

(a) (b)

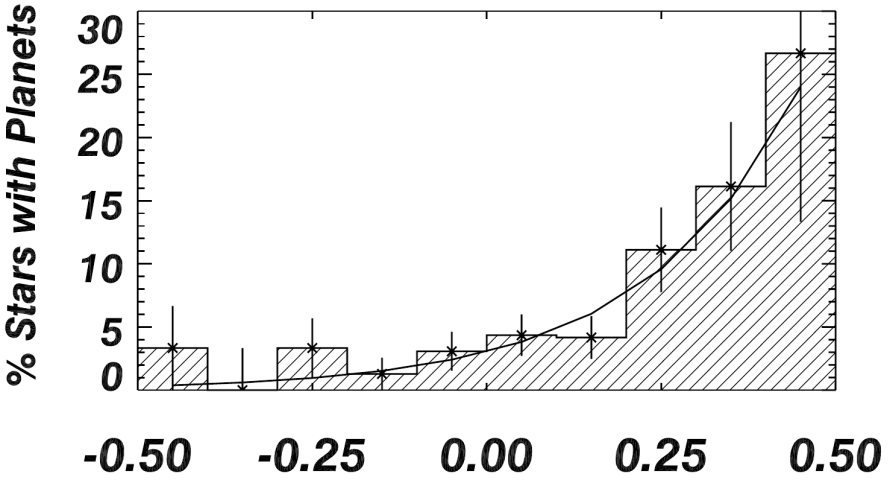

(c)

Figure 1.7: The influence of stellar parameters on the exoplanet population. Panel (a) shows the occurrence rate of planets with different radii for lower (M-type) and higher (FGK-type) mass stars (Mulders et al., 2015). Panel (b) shows the normalized occurrence rate of planets with different radii for low and high metallicity stars (Owen & Murray-Clay, 2018). Panel (c) shows the percentage of stars with at least one Jupiter-like planet as a function of stellar metallicity (Fischer & Valenti, 2005).

on the hypothesis that their composition reflect that of the primordial Solar Nebula. The metallicity of a star thus indicates the amount of elements with high melting and vaporization temperatures (also called "refractory") that was present in the gas cloud from which that star was born and as such, it also indicates how much material was available to form planets. Thus it is expected that higher metallicity favors planetary formation, and observations partially confirm this expectation: the presence of a Jupiter-like planet correlates strongly with the metallicity of the parent star. (Fischer & Valenti, 2005) modeled the probability F_J of hosting a gas giant planet in the $-0.5 < [\mathrm{Fe/H}] < +0.5$ range with the following formula:

$$F_J \propto 10^{\gamma[\mathrm{Fe/H}]} \tag{1.13}$$

finding a $\gamma = 2$ from the fit (see Fig. 1.7, panel c). On the other hand, this correlation seems to be weaker or non-existent for hot/warm Neptunes and Super-Earths (Buchhave et al., 2012; Zhu, 2019) and reversed for cool Super-Earths and Earths. The two latter types seem to be marginally more common around low-metallicity stars (Owen & Murray-Clay, 2018), a fact that is usually explained as the result of the disruptive effects of the presence of Hot Jupiters in the system. In particular, gas giant planets form on shorter timescales than rocky planets and can then interact with the still present protoplanetary disk. These interactions lead to a loss of orbital angular momentum, thus inducing the planet to migrate from the outer parts of the protoplanetary disk, where they coalesced, to its inner parts. The inspiralling gas giant disperses the remaining part of the disk, thus preventing the formation of smaller Super-Earths and Earth-like planets. Another feature related to the metallicity is the average radius of Neptunes and Jupiters, which is larger for metal-rich stars (Owen & Murray-Clay, 2018). This is shown in Fig. 1.7, panel (b). The correlation probably arises due to the fact that higher metallicity protoplanetary disks can form larger solid cores which in turn are able to accrete larger gas envelopes.

A third distortion effect is produced by the mass of the central star. The mass of the central is correlated with the mass of the protoplanetary disk, even though there is a one order of magnitude scatter in the data (Ansdell et al., 2016). Larger protoplanetary disks can theoretically produce more planets and/or more massive planets. Johnson et al. (2010) found a strong linear relationship between the probability of hosting gas giant planets F_J with $a_p < 2.5$ AU and the host star mass, going from 3% for M dwarfs, to 8.5% for FGK stars and reaching 14% for A-type stars. Mulders et al. (2015) confirmed this trend, as shown in Fig. 1.7, panel (a). However, a following analysis on a similar sample by Clanton & Gaudi (2016) calculated an occurrence rate for M-type hosts much more similar to that for G-type hosts than expected. On the other hand, both occurrence rate and the multiplicity of Earths and Super-Earths in the Kepler sample seems to be anti-correlated with the star mass (Yang et al., 2020). Regarding the former, it reduces from ∼75% for M- and K-type stars to less than ∼35% for F- and A-type stars. Regarding the latter, it reduces from ∼2.8 to less than 1.8. Mulders et al. (2015) also found that, in low-mass star systems, a larger fraction of metals is locked into planets.

1.4.2 Properties of the exoplanets

As said in previous sections, data about individual exoplanets are scarce. Among the various properties of the bulk population of exoplanets, three are simpler to derive and thus have been the subject of detailed study: the mass distribution, the period distribution and the eccentricity distribution.

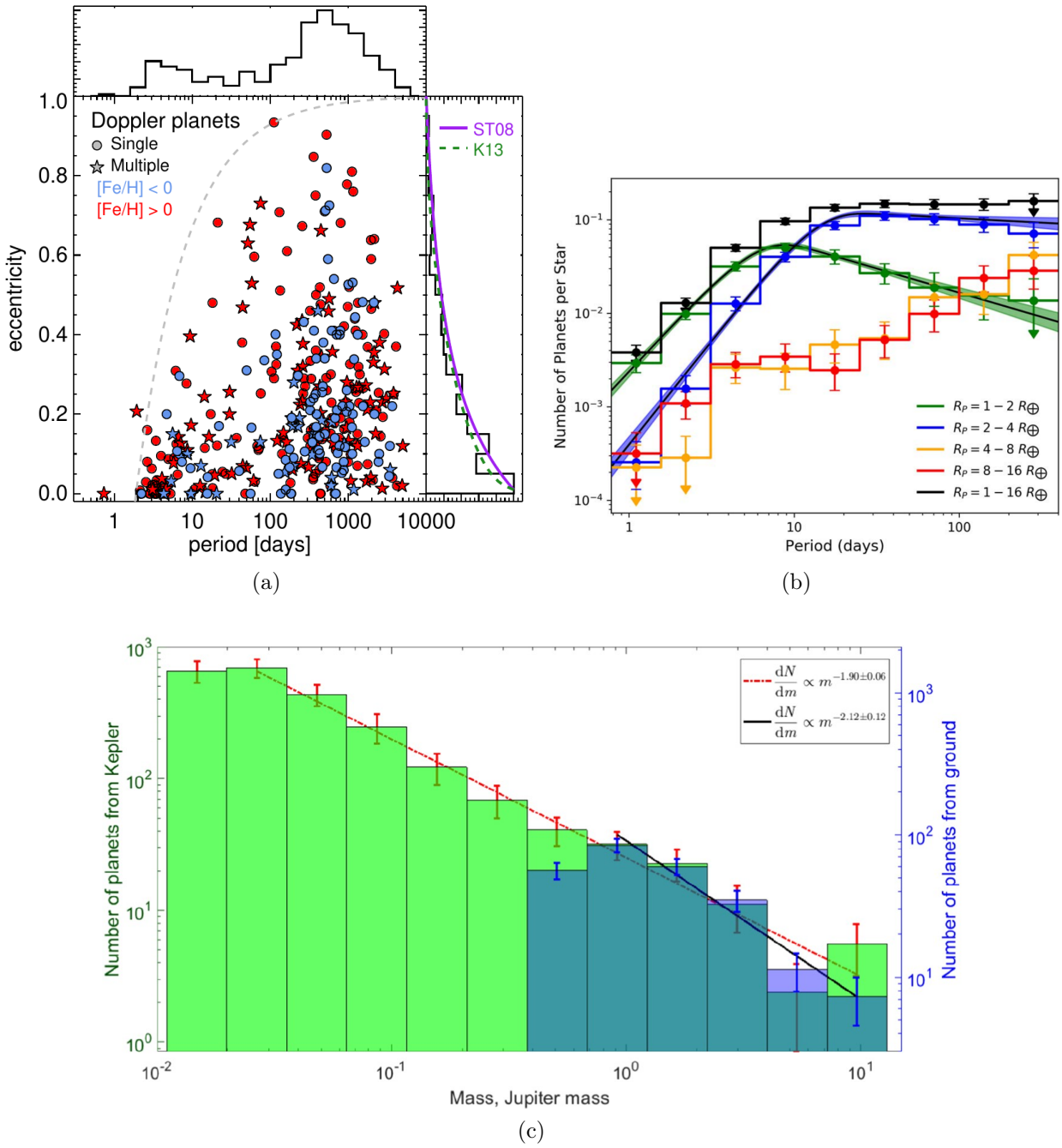

(a) (b) (c)

Figure 1.8: The distribution of exoplanet eccentricity (panel a, Winn & Fabrycky, 2015), orbital period (panel b, Kunimoto & Matthews, 2020) and mass (panel c, Ananyeva et al., 2020). Panel (a) shows the eccentricity distribution of exoplanets discovered via radial velocimetry, for different metallicity ranges and in single or multiple star systems (see the legend). The fits for the marginal distribution depicted on the right part of the plot are taken from Shen & Turner (2008) and from Kipping (2013). Panel (b) shows the period distribution evaluated for different size intervals. Of particular interest are the green curve, which refer to Earth-size and Super-Earth-size planets, and the red curve for Jupiter-size planets. Panel (c) shows the de-biased mass distribution of the Kepler sample in green and the combination of ground-based and CoRoT surveys sample in blue.

The mass distribution suffers mainly from two problems: the first one is the lack of precise determination of the masses of a conspicuous fraction of the total population, for which only the $m_p \sin i$ is known. The second one is the incompleteness of the sample, especially at low mass values. Despite these issues, several studies have modeled the mass function of exoplanets in the Super-Earth, Neptune and Jupiter mass intervals as a single-slope power law:

$$\frac{dN}{dm_p} \propto m_p^{-\beta} \tag{1.14}$$

where N is the de-biased occurrence rate and m_p is the mass of the body. Analyzing the population of objects for which only $m_p \sin i$ is known yielded exponents in the $1 < \beta < 1.5$ range (Marcy et al., 2005; Butler et al., 2006; Cumming et al., 2008). More recent re-evaluations (Ananyeva et al., 2020), based on transiting exoplanets (for which the true mass can be derived) and corrected to take care of the observational biases, yielded a slightly higher value, in the $1.5 < \beta < 2$ range together with a statistically significant plateau in the 0.3-2 M_ν interval (see Fig. 1.8, panel c). This is closer to the exponent calculated from planetary population synthesis models ($\beta \sim 2$, Mordasini, 2018). While the general trend can be described by a simple power law, it must be considered that there exists statistically significant gaps which coincide with the classification intervals, as discussed in Section 1.2.1. Anyway, a conclusion that can be drawn from the study of the mass distribution is that small, Earth-like planets should be much more common than larger Neptune and Jupiter-like ones, a fact which is very relevant for astrobiology.

The period distribution behaves differently for low-size and high-size exoplanets. Kunimoto & Matthews (2020) found that, in the 1-400 d range and for Earth-size exoplanets, the distribution can be described as a two-slope power-law dependent on $\log P_p$ (i.e. the planetary orbital period), with a steep increase (with an exponent ~2) up to a critical period of ~6 d followed by a mild decrease (with an exponent ~0.5) for larger periods. On the other hand, Neptune- and Jupiter-size exoplanets show an ever-increasing distribution, with no sign of the pile-up at 3 d identified by previous authors like Udry et al. (2003) and Wright et al. (2009) (see Fig. 1.8, panel b). Another possible feature specifically of Jupiter-like bodies is the so-called period valley (Wittenmyer et al., 2010), which is a reduction of the detection rate in the 10-100 d range. The shape of the period distribution suggest the possible existence of a large population of yet undetected (and difficult to detect) cold, large exoplanets. It also underlines the fact that the Solar System, which has small, rocky planets orbiting closer to the star and large, gaseous planets orbiting at larger distances, might not be a special case among the planetary systems of our Galaxy.

Regarding the eccentricity distribution, the exoplanet population exhibits a decreasing distribution peaked in 0. However, for exoplanets with $P_p \gtrsim 6$ d the median eccentricity is 0.29, which is far larger than that of planets in the Solar System, and the entire [0-1[eccentricity range is covered. This high dispersion is present both in exoplanets orbiting single stars and exoplanets in binary star systems and is usually modeled using a Rayleigh distribution:

$$\frac{dN}{de} = \frac{e}{\sigma^2} \exp\left(-\frac{e^2}{2\sigma^2}\right) \tag{1.15}$$

which is theoretically expected as the outcome of planet-planet interactions in closely spaced multiplanet systems (Jurić & Tremaine, 2008). Van Eylen & Albrecht (2015) proposed $\sigma = 0.05$ for systems with multiple transiting planets, while Xie et al. (2016) found a higher value (0.3) when analyzing systems with single transiting planets. Both studies were conducted

on the Kepler sample and concluded that there is a correlation between eccentricity and multiplicity: systems with more planets show a lower average eccentricity. He et al. (2020) confirmed this result, modeling this relation as a single slope power law:

$$\tilde{e} \propto n^{-1.74} \tag{1.16}$$

where n is the number of planet and $\tilde{e}$ is the median eccentricity of that system's planets. Shen & Turner (2008), studying in particular radial velocity-detected planets, proposed a different relation that fits better the low-eccentricity part of the distribution than the Rayleigh distribution:

$$\frac{dN}{de} \propto \frac{1}{(1+e)^a} - \frac{e}{2^a} \tag{1.17}$$

with $a = 4$, while Kipping (2013) proposed instead a two-parameter Beta distribution. These are shown in Fig. 1.8, panel a (taken from Winn & Fabrycky, 2015). On the same sample, Limbach & Turner (2015) found again a correlation between median eccentricity and multiplicity, modeled as $\tilde{e} \propto n^{-1.2}$. Finally, eccentricity has two more known correlations: one with the inclination of the planetary orbital plane with respect to the stellar spin axis in the form of a strong linear correlation between the two (Tremaine & Dong, 2012; Xie et al., 2016), and another with stellar metallicity in the form of higher maximum and larger spread in eccentricity for [Fe/H] > 0 subsample with respect to the [Fe/H] $\leqslant 0$ one (Dawson & Murray-Clay, 2013).

1.5 Exoplanet composition

The very first step in our understanding of planetary atmospheres is the identification of the main chemical compounds that we may expect to find. This is an important task since there are 92 known long-lived chemical elements, which can combine to form an extremely large number of polyatomic molecules. A comprehensive study of this variety would be impossible. Fortunately, there are some general criteria that we can apply in order to narrow down the scope of our research to a much smaller set of chemical compounds that are more likely to dominate the composition of Earth-like planet atmospheres.

(i) **Availability**

The first of these criteria is linked to the availability of different chemical species. Availability can be further distinguished in a universal component, linked to cosmic abundances, and a local component, linked to planetary fractionation. Elements other than H, He and Li are entirely produced by nuclear fusion processes in stars (see e.g. Matteucci, 2012). Without entering too much into detail, we can retrace the steps by which these elements are formed and made available to planetary formation as following. Stars are born from collapsing clouds of gas. A fraction of the H and He initially present in these clouds are converted into heavier elements during the star life cycle via nuclear fusion in stellar cores, releasing energy in the process. In the final phases of this cycle, part of the mass of the star is expelled back into space, thus enriching the Interstellar Medium (ISM) with newly formed metals. The next generation of stars then forms from gas that has been polluted by the previous ones. The types of nuclear reactions that can happen in a given star depend on its mass, its initial composition and the possible presence of companions (i.e., if the star is in a binary system) which interfere with the

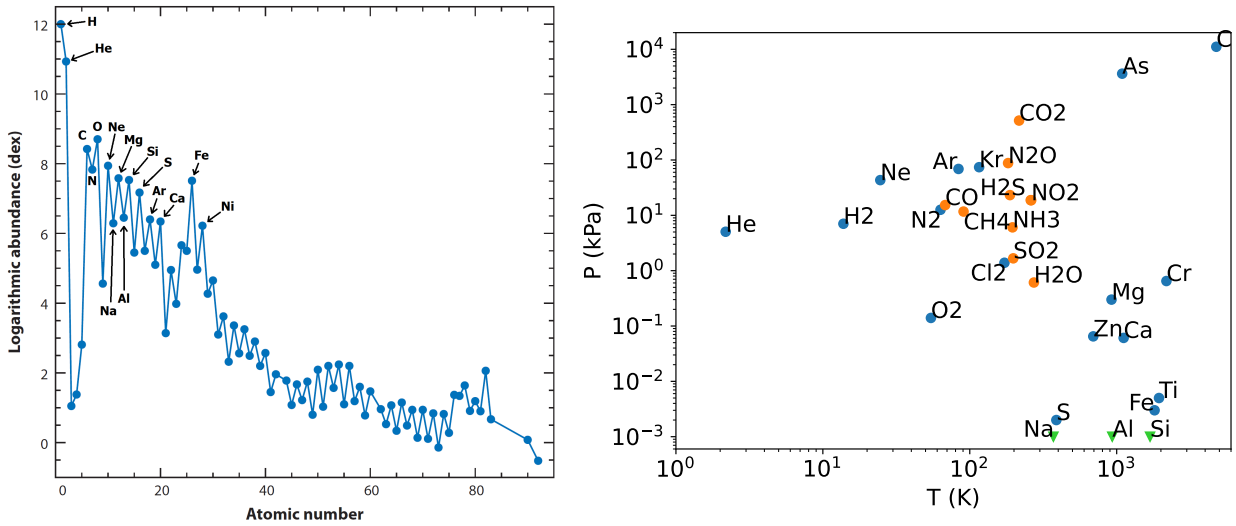

Figure 1.9: Left panel: the chemical abundance pattern in the Solar System, as reconstructed by spectroscopic data from the Sun atmosphere and direct measurements from meteorites (Asplund et al., 2009). Abundances are logarithmic and expressed relative to that of H, which has been fixed at 12 dex. Right panel: the triple points for some cosmically abundant elements and molecules. Green triangles refer to elements with triple point pressures lower than 1 Pa. Blue cicles refer to pure elements and diatomic molecules. Orange circles refer to multispecies molecules. C is considered in graphite form. The triple point of HCN is very similar to that of NO_2, thus its label is not reported in the plot. Data has been taken from NIST.

stellar evolutionary process. As such, several successive generations of stars produce a distinct chemical abundance pattern in the ISM: some metals become far more abundant than others (see Fig. 1.9, left panel). Since planets form from the leftovers of the star-forming gas cloud, they too are influenced by this pattern. The composition of the solid part of a planet is thus dominated by magnesium, silicon and iron variably combined with oxygen. Other elements found in large quantities are sodium, aluminum, sulphur, chlorine, calcium and nickel. By virtue of their different densities, oxides and iron compounds undergo differentiation during planetary formation, producing a distinct iron core enveloped in a mantle dominated by silicate minerals. Less abundant elements become instead concentrated in one of these two layers by means of their chemical affinity with either iron or silicates, rather than mass. Siderophile (iron-loving) species sink towards the center of the planet, while lithophile (rock-loving or, more specifically, silicate-loving) and chalcophile (sulfur-loving) species remain buoyant. The chemical makeup and the differentiation is expected to be general to all rocky planets. While there are differences in the proportions between different elements, both in situ analyses (for Earth and Mars Halliday et al., 2001; Yoshizaki & McDonough, 2021) and models (for Mercury and Venus Morgan & Anders, 1980; Aitta, 2012; Shah et al., 2022) support the universality of these considerations. There are, however, other abundant elements that have not been considered yet in this discussion: hydrogen, carbon, nitrogen and the three lightest noble gases (helium, neon and argon). Elements of the former group are relevant for both the solid and the fluid part of a planet, while those of latter group are mostly found in the fluid part (atmosphere and oceans). These are the so called at-

mophile species, which is the last of the four categories in the geochemical classification of elements (Goldschmidt, 1937). The physical difference between atmophile elements and the others is clear by observing Fig. 1.9, right panel: they all have higher triple point pressures and/or lower triple point temperatures, meaning that they tend to stay in the gaseous phase. This last point is connected with the concept of volatility, that we now discuss.

(ii) **Volatility**

The presence of H, C and N in the atmosphere of cool, Earth-like planets is related with the second criterion, which concerns the volatility of chemical species. The volatility issue, just like the availability, can be separated in two components, that is the ability to a given species be stay in gaseous state on one hand and the ability to escape from (or to avoid to be captured in) the solid planet via biological and geological processes on the other. The first can be tackled by considering the triple point pressure p_3 and temperature T_3 as a proxy for the position of the condensation curve on the pressure-temperature plane. A combination of high p_3 and low T_3 values imply higher vapor pressures over a wider temperature range, thus making it easy for a given species to accumulate in the atmosphere in larger quantities without condensing to the surface. In fact, the oxides of H, C and N have very low T_3 values compared to those of the other elements abundant elements cited so far. For comparison, it can be considered that T_3 for H_2O, CO_2 and N_2O are equal to 273.2, 216.6 and 182.3 K, respectively, while for MgO and SiO_2 are equal to 1986 and 3125 K. The triple points of pure hydrogen and nitrogen are even lower (13.4 and 63.2 K, respectively). Thus, we can expect that molecules composed by some combination of these elements (plus oxygen) make up the bulk of planetary atmospheres. In principle, also hydrogen sulfide and sulfur dioxide should be common, since they have low triple points (191 and 201 K). However, the chemical pathways in the surface-atmosphere interaction disfavor the accumulation of large quantities of these molecules in the atmosphere. Similarly, the physical and chemical conditions of the Earth-like mantles disfavor the release of ammonia (NH_3) with respect to molecular nitrogen (Johnson & Goldblatt, 2015), making it irrelevant as an atmospheric component. Another gas that is not expected to be present is molecular oxygen because of its high reactivity and in fact, without the vigorous biogenic flux, O_2 pressure on Earth would collapse to that of a minor component in $\sim 10^3$-10^4 years (Masson-Delmotte et al., 2021). Surface reactivity is also important for CO_2, especially in presence of an hydrological cycle. CO_2 dissolves in liquid water as carbonic acid that can then react with metallic ions freed from silicate minerals, to form less soluble carbonates. These carbonates deposit on the bottom of oceans, thus sequestering CO_2 from the atmosphere. Plate tectonics can then recycle CO_2 by cooking it off the carbonates during metamorphism. The geophysical processes than can release (or capture) chemical species in gaseous form, under the typical conditions expected for a rocky exoplanet, is thus the second factor to be considered when talking about volatility. Biochemical pathways, in particular for habitable (and potentially inhabited) planets, can contribute strongly to the picture, as the case of Earth shows. Apart for O_2, biological activity is also responsible for the presence of nitrogen oxides (especially N_2O), produced via denitrification processes at ground level. Without it, their concentration would probably fall 100-fold, since lightning production in an anoxic atmosphere is very inefficient (Navarro-González et al., 2001; Homann et al., 2018).

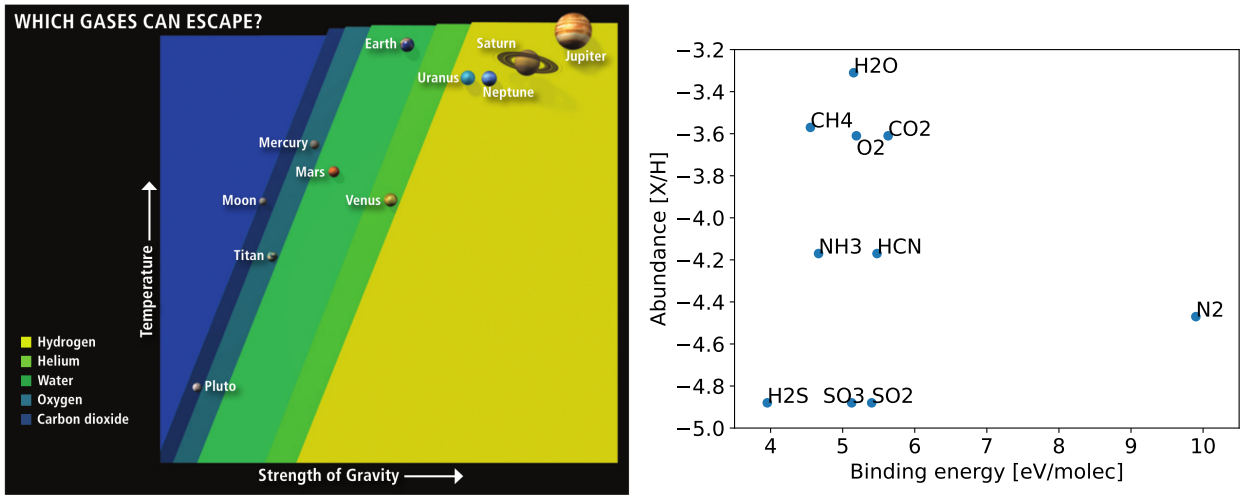

Figure 1.10: Left panel: a quantitative representation of the ability of different planets of the Solar System to retain the most common atmospheric chemical species. Note that "temperature" refers to the exospheric temperature, rather than the surface temperature. Credit: Catling & Zahnle (2009). Right panel: binding energies of different molecules versus their logarithmic relative abundances with respect to that of H, calculated from the abundances of the least common chemical species in each molecule. Binding energies reported here refer to the removal of one atom, and not the entire destruction of the molecule. Data taken from Hollister & Sinanoglu (1966) and Blanksby & Ellison (2003).

(iii) **Survivability against atmospheric escape**

The third criterion is related to the ability of a planet with a given surface gravity to retain, over geological timescales, different chemical compounds in its atmosphere: in other words, the survivability of a given chemical species against atmospheric escape. This is related with our fourth criterion, which concerns the stability of different molecules against photochemical reactions with other species and the light from the parent star. Both these criteria depend partly on the state of the interplanetary and interstellar environment in which the planet is immersed, namely the local space weather conditions. Using the atmospheric escape criterion we can rule out the presence of long-lasting H_2 and He-dominated atmospheres on planets with similar mass and temperature to that of Earth (see Fig. 1.10, left panel), due atmospheric escape processes (even though this might not be the case for cooler planets with higher escape velocities). Ne also is expected to escape in large quantities, dragged by hydrogen during hydrodynamic escape[16]. This is demonstrated by their isotopic ratios measured in the Earth atmosphere with respect of that of the Sun (see e.g. Chapter 5 of Catling & Kasting, 2017).

(iv) **Survivability against photochemical reactions**

Lastly, as a fourth criterion, it is improbable to find atmospheres dominated by chemical species that are sensitive to photo-dissociation by UV radiation such as methane and water vapor (see Fig. 1.10, right panel). In fact, while they do contribute to the overall radiative budget of a planet, their concentration is generally limited by photochemical reactions in the atmosphere. In the event of a large, impulsive input of these species,

[16]High UV fluxes in lightweight (i.e. H-dominated) atmospheres can cause the thermodynamic expansion of the upper part of the atmosphere, which can thus escape in bulk.

as in theory happens to water during a runaway greenhouse (see Section 2.4.1), the H_2O-dominated atmosphere produced has a short ($\ll$1 Gyr) survival time (Wordsworth & Pierrehumbert, 2013). Instability against UV radiation plays a role in relation to the concentration of sulfur compounds too, in particular H_2S. SO_2 and SO_3 are again prone to photodissociation and either sedimentation of S_8[17] aerosol or rain-out of H_2SO_4 at surface (Catling & Zahnle, 2020). Modeled concentration of the former is $\sim$1 ppb for an Archean Earth-like planet (see e.g. Claire et al., 2014). On the other hand, if a sufficiently large amount of sulfur compounds accumulate in the atmosphere (via e.g. volcanism) a layer of S_8 haze can form in the upper atmosphere and shield the planet from UV radiation, stabilizing H_2S and SO_2 concentrations (Kasting et al., 1989). Chemical equilibrium also plays a role, since gases react with each other. For example, while CO constituents are abundant and CO has the highest bond energy of any neutral molecule (11.16 eV), its presence is disfavored in oxidizing atmospheres, where it rapidly converts in CO_2. The same happens in atmospheres where H_2O is present due to the fact that the water-gas shift reaction $CO + H_2O \rightleftharpoons CO_2 + H_2$ has its equilibrium moved to the right in the temperature interval that we want to investigate.

By putting together these considerations, we can conclude that (i) long-lasting atmospheres of temperate, Earth-like planets are most probably dominated by either CO_2 or N_2 and that (ii) only a relatively small number of chemical species formed by H, C, N, O and S can be present in small but non-negligible fractions (1 ppm to few percent points). This allows us to cautiously generalize the overall chemical makeup of the atmospheres found on rocky planets and moons of the Solar System (Venus, Earth, Mars and Titan) also to exoplanets. As such, in the present worlk we have mainly investigated either Earth-like atmospheres dominated by N_2 or Venus- and Mars-like atmospheres dominated by CO_2. However, the procedure that we have developed for RT calculations and that I will present in the next Chapters can be applied to atmospheres with compositions that are wildly different than those. Some of the more exotic cases briefly presented in this Section can potentially be the starting point for future analyses.

[17]The most common allotrope of pure sulfur, that takes the form of a ring of 8 sulfur atoms.

Chapter 2

Climate models

Planetary climate simulations are fundamental tools in the search for Earth-like habitable worlds outside the Solar System because, with a proper parameterization of physical quantities, they allow us to estimate the physical conditions in the deeper atmospheric layers and on planetary surfaces from the limited amount of data which are typically available. Climate models can also be used to study the past (and foresee the future) conditions of Solar System planets, including the Earth.

During the years, many different climate models have been published. In general, they can be categorized either as intermediate/high complexity General Circulation Models (GCMs) or as low complexity Energy Balance Models (EBMs). GCMs perform 3-D hydrodynamical calculations of the atmosphere, taking into account the surface geography and tracking a large number of interactions between different components of the climate system like cloud formation, oceanic currents and biologically driven surface-atmosphere interactions (Lin & Rood, 1996; Hourdin et al., 2006). They allow for state-of-the-art predictions, both large scale and local, but require a large number of input parameters that are usually not known for exoplanets and are very computationally intensive. On the other hand, EBMs make use of simplified relations based on general conservation principles to calculate quantities averaged inside latitudinal bands, as represented in Fig. 2.1, left panel (North & Coakley, 1979; Caldeira & Kasting, 1992; Vladilo et al., 2013). Despite lacking the accuracy of GCMs and being subject to a set of constraints (for example, on the planetary spin period), they are nonetheless capable of capturing some relevant climate feedbacks, like the ice-albedo feedback. EBMs require a relatively small number of input parameters and far less computational resources, which in turn allow for their use in the rapid exploration of the broad parameters space that characterize exoplanets (Silva et al., 2017; Murante et al., 2020). While the results obtained during my PhD can be applied to both GCMs and EBMs, they have been used to update a specific EBM, namely the Earth-like planet Surface Temperature Model (ESTM, Vladilo et al., 2015). ESTM is a detailed EBM with enhanced prescriptions for the horizontal and vertical transport of energy, which will be detailed in Section 2.3. The right panel of Fig. 2.1 shows an example of the predictions that can be made with it. As such, in the following subsections we will detail specifically this type of climate simulations. As an important note, the features of the model presented in this Chapter refer to the first version of ESTM (ESTM1). The improvements to the code that have been done during the PhD with my contribution are instead described in Chapter 5 and published in Biasiotti et al. (2022). This new version of ESTM will be referred to as ESTM2.

This Chapter is organized as follows. In the first section I describe the main driver of

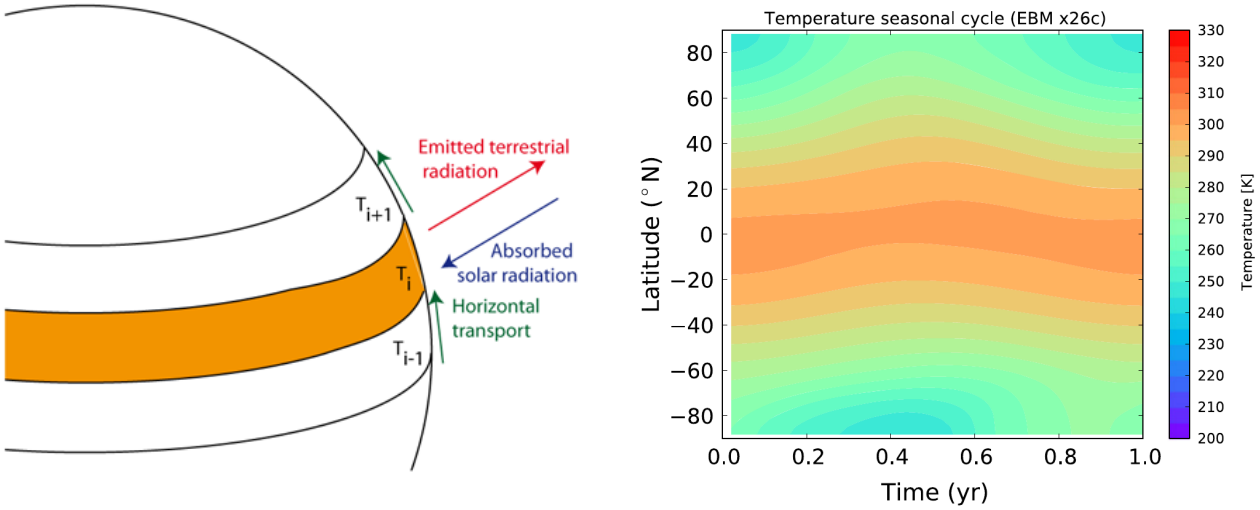

Figure 2.1: Left panel: diagram of a generic climate Energy Balance Model with latitudinal band averaging. Credit: Université Catholique de Louvain. Right panel: the predicted yearly evolution of temperature for Earth in the ESTM1 climate model. Credit: Vladilo et al. (2015).

the planetary climate, namely the planetary energy budget, both in general and as treated in the first published version of ESTM (referenced here as ESTM1). The newer, upgraded version of this code (ESTM2) will instead be described in Chapter 5. In the second section I present several published formulations used to calculate the vertical thermal profile of the lower atmosphere, which is integral in causing the so-called Greenhouse Effect. As part of the PhD work, I wrote and tested the scripts that implement these formulations in the EOS procedure described in the next Chapter. In the third section I describe how the horizontal (i.e. meridional) energy transport is modeled in ESTM. Finally, in the fourth section I briefly review the climate feedbacks mechanisms and their relevance in determining the planetary habitability.

2.1 The planetary energy budget

The planetary energy budget plays the biggest role in determining the general physical state of a rocky planet (see e.g. Pierrehumbert, 2010) and depends on three quantities: the Incoming Shortwave Radiation (ISR or $\mathcal{I}$, also called Insolation or Instellation), the Outgoing Longwave Radiation (OLR or $\mathcal{O}$) and the Bond albedo, which from now on will be referred to as the top-of-atmosphere (TOA) albedo, $\alpha_{\rm TOA}$. ISR and OLR are fluxes, expressed in Wm^{-2}, and as such are slightly different from the quantities used in Eq. 1.1 and 1.2, which are powers expressed in W instead. ISR and OLR are slightly misleading terms, given that the first one includes also the power emitted by the star as infrared radiation, and the second one may include a non-negligible fraction of optical radiation if the considered planet is very hot ($\gtrsim$ 1200 K). These three quantities are related as following:

$$\mathcal{O} = \mathcal{I}(1 - \alpha_{\rm TOA}) \tag{2.1}$$

and we will now analyze more in detail each of them.

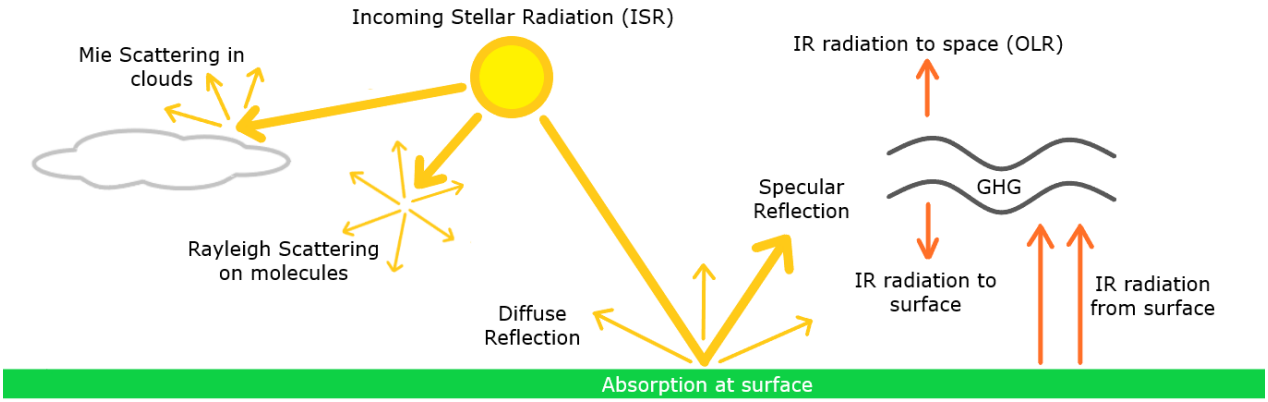

Figure 2.2: A simplified diagram of the main radiative transfer processes that must be tracked to calculate the OLR and TOA albedo of a planet.

2.1.1 The incoming radiation

The ISR depends on the orbital parameters of the planet and the bolometric luminosity of the star. In turn, the luminosity depends on the physical size and the effective temperature of the star. For Main Sequence (MS) stars, which are stars in their stable, hydrogen-fusing phase that comprise ∼90% of the their total lifetime, both the effective temperature and the stellar radius are functions of the star mass $M_\star$, with a marginal dependence also on its metallicity $Z_\star$ and age $t_\star$. As such, is not necessary to evaluate luminosity case-by-case, but rather it can be derived from combining observable quantities and stellar evolutionary models. Concerning the orbital parameters, the time-dependent ISR depends only on the instantaneous distance between the star and the planet, while its averaged value over one orbit $\bar{\mathcal{I}}$ can be calculated from the semi-major axis and the eccentricity as follows (Williams & Kasting, 1997):

$$\bar{\mathcal{I}} = \frac{L_\star(M_\star, Z_\star, t_\star)}{4\pi a_p^2 \sqrt{1-e^2}} \tag{2.2}$$

Given that the climate system exhibits a certain level of inertia[1], $\bar{\mathcal{I}}$ can be appropriate for a first-order evaluation of the long-term surface conditions.

In general, the instantaneous amount of flux impinging at each point on the planetary surface depends on the instantaneous stellar zenith angle z, which in turn depends on the hour angle $h_\star$, the latitude ϕ, the planetary spin axis tilt with respect to the orbital plane ϵ and the orbital phase (identified, for example, by the true anomaly ν). In latitudinal EBMs, $\mathcal{I}$ must necessarily be evaluated as a daily average in each latitudinal band, which still depends on ϕ, ϵ and ν. This can be done by calculating the mean diurnal value of the variable $\mu_\star = \cos(z)$ which, if the planetary rotation period $P_{\rm rot}$ is much smaller than the orbital period $P_{\rm orb}$, is equal to:

$$\bar{\mu_\star} = \frac{\int_{-H}^{+H} \mu_\star \, dh_\star}{\int_{-H}^{+H} dh_\star} = \sin\phi \sin\delta_\star + \cos\phi \cos\delta_\star \frac{\sin H}{H} \tag{2.3}$$

[1]Thermal inertia can be evaluated considering the ratio between the thermal capacity of the the oceanic mixed layer and the ISR, which for the Earth is ∼ 4.7 yr (North & Coakley, 1979). The variation in heat content sufficient to radically change the planet climate is actually much smaller, but amounts nonetheless to a few months.

where H is the half-day length and $\delta_\star$ is the parent star declination. By definition, the star is above the horizon when $h_\star \in [-H, +H]$ and $H = \arccos(-\tan\phi \tan\delta_\star)$. In order to calculate the parent star declination $\delta_\star$, it is possible to introduce the planetocentric orbital longitude of the star $\lambda_\star$, defined as the angle between the star and the line of nodes as seen from the planet. The former is defined by the intersection between the orbital and the equatorial planes of the planet. If $t = 0$ is set as the instant in which the planet crosses the ascending node, then $\delta_\star$ is equal to:

$$\delta_\star = \arcsin(\sin\epsilon \sin\lambda_\star) \tag{2.4}$$

In turn, $\lambda_\star$ as a function of t can be calculated by considering its relation with the true anomaly ν:

$$\lambda_\star(t) = \nu(t) + \omega \tag{2.5}$$

where ω is the argument of the pericenter. The angle ν can be calculated from its relation with the eccentric anomaly E:

$$\tan(\nu/2) = \left(\frac{1+e}{1-e}\right)^{1/2} \tan(E/2) \tag{2.6}$$

which is related to the mean anomaly M by the Kepler's equation:

$$E - e\sin E = M \tag{2.7}$$

Finally, $M = 2\pi t/P_{\rm orb} + M_0$, where M_0 is determined by the initial conditions. The orbital period is then sampled on a given number of points to produce seasonal maps of the surface temperature.

Concerning specifically ESTM (both the first and the second version), the orbital period is sampled in 48 points and the climate simulation typically needs ∼30 orbits to attain a stationary solution in the form of a periodic oscillation of the latitudinal temperature profile. Using this procedure is thus possible to follow the seasonal evolution of surface conditions, which is fundamental to determine di continuous habitability of a given zone of the planet, especially for highly tilted or highly eccentric planets. More details on this procedure can be found in Vladilo et al. (2013). The value of $\bar{\mu_\star}$ as a function of the latitude and the time of the year is needed also for the calculation of horizontal heat transport that will be presented in Section 2.3.

2.1.2 The planetary albedo

The $\alpha_{\rm TOA}$ depends on the radiative transfer (RT) properties of the atmosphere, the features of the surface and the stellar spectral energy distribution (SED). It can be studied as the composition of an atmospheric albedo $\alpha_{\rm atm}$ and a surface albedo $\alpha_{\rm srf}$, both of them dependent on several other factors.

Atmospheric albedo

The atmospheric albedo $\alpha_{\rm atm}$ is produced by the elastic interaction of light with gas molecules and suspended particles, a process which is called scattering. Depending on the ratio between the incident radiation wavelength λ and the diameter of the particle, there are three different types of scattering process. If this ratio is $\lesssim 0.1$ it can be modeled as Rayleigh scattering, if it is ~ 1 it can be modeled as Mie scattering and if it is $\gtrsim 10$ it can be modeled as classical

geometric scattering. For a planetary atmosphere, Rayleigh scattering is good to model the diffusion of light due to gas molecules, while Mie and geometric scattering are good to model the diffusion of light caused by clouds or dust grains. As such, it is possible to write the atmospheric albedo as a product by two distinct factors: the clear-sky atmospheric albedo α_{Ray} that is always present, and the cloud albedo α_{clo}, that depends on the cloud coverage fraction.

The α_{Ray} term is strictly linked to the cross-section for Rayleigh scattering σ_{Ray}, which in turn depends on the molecular electric polarizability and, inversely, on the fourth power of the incoming radiation wavelength λ. It can also be expressed in terms of molecular diameter d and the refractive index of the gas n as:

$$\sigma_{\mathrm{Ray}} = \frac{2\pi^5}{3}\frac{d^6}{\lambda^4}\left(\frac{n^2-1}{n^2+2}\right)^2 \tag{2.8}$$

Therefore, Rayleigh scattering acts far more efficiently on short-wavelength (ultraviolet and visible) than on infrared radiation. This fact clarifies the link between α_{TOA} and the star SED: if the star has a lower surface temperature and thus a larger part of its energy comes in form of near infrared radiation, the fraction of light subject to Rayleigh scattering will be lower. In other words, any atmosphere under a redder parent star has a lower α_{TOA}. Mie scattering cross-section has instead a more complex dependence on λ and is calculated as an infinite sum of spherical Bessel functions. It depends on the multipole expansion of the electric and magnetic polarizability of the material, which produces a peak-structured spectrum which is dependent on the chemical composition of the scatterer. There is not, however, a strong monotonic dependence like in the Rayleigh scattering case, thus averaging over a population of differently-sized Mie scatterers produces a behaviour that is largely wavelength-independent. For this reason, clouds and hazes are usually equally effective at reflecting short- and long-wave incoming radiation up to mid infrared, where molecular absorption bands are generally located. Finally, in the geometric scattering limit for large particles, the cross-section is again only marginally dependent on λ via the refractive index.

Another important factor in scattering calculations is the direction into which the photon is scattered. In general, this is described by the scattering phase function $p(\lambda, \phi, \theta)$, where ϕ and θ are the polar and azimuthal angles with respect to the direction of the incoming radiation. For spherically simmetric scatterers (an assumption made both in the Rayleigh and in the Mie theory), p does not depend on θ. Since usually a photon undergoes multiple scatterings in a planetary atmosphere, p can be averaged over the polar angle ϕ. The resulting quantity is called asymmetry parameter:

$$g_0(\lambda) = \int_0^{\pi} p(\lambda, \phi)\cos\phi\sin\phi d\phi \tag{2.9}$$

which describes the forward-backward asymmetry in the scattered radiation. By definition, g_0 values can range between -1 and +1. At -1, radiation is completely scattered backwards, while at +1 it is completely scattered forwards. For Rayleigh scattering, $g_0 = 0$. Mie and geometric scattering have instead a positive and generally large asymmetry parameter, and in the case of Mie scattering, a pronounced dependence on λ.

Since the fraction of light scattered increases with the optical path, the atmospheric albedo increases both with the surface pressure and the incident radiation angle z, also called zenith distance. Moreover, given that both the structure and the composition of planetary atmospheres change with surface temperature, α_{atm} is also a function of it.

λ interval $[\mu m]$	$0.2-0.5$	$0.5-0.7$	$0.7-0.85$	$0.85-4.0$
surface		α_{srf}		
coniferous forest	0.03-0.04	0.04-0.06	0.20-0.30	0.20-0.30
tropical forest	0.03-0.05	0.04-0.10	0.15-0.20	0.20-0.22
deciduous forest	0.03-0.07	0.04-0.13	0.19-0.30	0.28-0.30
grassland	0.05-0.08	0.10-0.17	0.25-0.30	0.30-0.35
basalt	0.06-0.08	0.09-0.14	0.11-0.16	0.09-0.11
desert sand	0.15-0.28	0.25-0.40	0.35-0.50	0.40-0.50
fresh ice	0.70-0.75	0.60-0.70	0.45-0.55	0.40-0.50
fresh snow	0.76-0.85	0.76-0.85	0.30-0.40	0.30-0.40

Table 2.1: The albedo values for four spectral bands (from near UV to near IR) for some widespread surface types on the Earth. Data has been taken from (Briegleb & Ramanathan, 1982; Briegleb et al., 1986). Data for basalt has been taken from Kokaly et al. (2017)[2].

Cloud albedo

Cloud albedo α_{clo} presents a singular challenge, given that it behaves partially as a sort of surface albedo, hiding the underlain terrain and a fraction of the atmospheric column. A first approximation, used also in ESTM1, is to consider α_{clo} as applied to the planetary surface. This neglects both the fact that the atmospheric layer below the cloud coverage does not participate in the α_{Ray} calculation and any possible contribution to the total albedo given by the actual surface. However, this choice is justified by the tendency of the thickest clouds to form at low altitudes (2000-3000 m), at least in the current Earth atmosphere, thus leaving the majority of the atmospheric mass above them, and by being dominant in the albedo contribution with respect to most surface types. Moreover, clouds have generally a 3-D structure that induces a dependence on the zenith angle. In ESTM1 this z dependence is modeled as suggested by Williams & Kasting (1997):

$$\alpha_{\text{clo}} = \max\left[\alpha_{\text{clo},0}\,,\ \alpha + \beta z\right] \tag{2.10}$$

with $\alpha = -0.11$ and $\beta = 7.98 \times 10^{-3}\ (^o)^{-1}$, tuned to fit Earth experimental data of cloud albedo as function of zenith distance. A minimum cloud albedo $\alpha_{\text{clo},0} = 0.19$ is adopted for low z values. Experimental data have been taken from Cess (1976). The cloud coverage fraction f_{clo} also must be considered. In general, it depends on the properties of the underlying surface. The main factors that influence their formation are the surface evaporation, the formation or presence of nucleation particles and the atmospheric circulation pattern. The circulation is influenced by orography, which creates zones where air is forced to change altitude, thus triggering condensation in moist air. Most of this features are difficult to capture in a zonally averaged EBM. As such, in ESTM1 the cloud coverage is determined by the underlain terrain and fixed to 60% over land and frozen surfaces and 70% over oceans. These values have been calculated by Sanromá & Pallé (2012) and, despite its simplicity, this scheme is nonetheless able to product an excellent agreement with the real Earth data (Stubenrauch et al., 2013). Given that the coverage of ice changes with temperature and that the cloud cover over ice is different that the cloud cover over ocean, the model is able to capture indirectly the dependence of f_{clo} on T_s.

Surface albedo

The surface albedo α_{srf} is caused by the reflective properties of the planetary surface. Solid surfaces can be approximated as exhibiting Lambertian reflection, which is the idealized isotropic diffusion of light produced by coarsed surfaces. It represents the opposite of specular reflection produced by mirrors. Thus, under this idealization, their albedo do not depend on the z angle. Another typical approximation is to consider the α_{srf} as wavelength-independent, which is reasonable for most substances in the visible and near-infrared, especially once it has been convolved for the stellar spectrum (see Table 2.1). Even with these simplifications, though, a good estimate the α_{srf} produced by various materials is not simple, mainly due to the fact that the surface can be chemically or mechanically altered. As such, the derived values are more physically sound when applied to large surfaces and thus act as averages. In ESTM1, three types of surface are considered: land, water ocean and water ice. No other condensables (such as CO_2) are considered. For each latitudinal zone the fractions of land and ocean can be initialized, thus allowing to test different, simplified longitude-averaged geographies. The ice fraction too can be initialized, but is then dynamically adjusted as a function of T_s, progressively substituting land and ocean at low temperatures. Land albedo α_{lnd} is set to 0.18, tuned to reproduce the observed latitudinal albedo profile of Earth. As such, this value is representative specifically of Earth, and it is an average between those of the vegetation and of desert sands. However, it is also near to that of weathered basalt (0.14) that can be expected for lifeless planets with an atmosphere and an hydrological cycle. Ocean albedo α_{ocn} is generally very low but it exhibits a very strong dependence on z at high angles. As such, the Lambertian approximation must be dropped to properly calculate T_s in the polar regions. A possible formulation of this dependence, adopted also in ESTM1 and 2, has been proposed by Briegleb et al. (1986):

$$\alpha_{\text{ocn}}(z) = \frac{0.026}{1.1\mu^{1.7} + 0.065} + 0.15(\mu - 0.1)(\mu - 0.5)(\mu - 1.0) \tag{2.11}$$

where the numerical coefficients have been calibrated using experimental data from Enomoto (2007). Ice albedo α_{ice} can be again taken as independent from z and in ESTM1 is fixed to 0.70 to match Earth observations. Again, this value is an average between that of fresh snow, which is very high (0.85) and that of blue marine ice and old, dirty glaciers, which is consistently lower (0.55). Also, for water ice is especially important to consider the SED of the incoming radiation, since it has very strong absorption bands in the infrared that can consistently lower the albedo (see e.g. Shields et al., 2014). Given both its importance in the stability of the climate system (see Section 2.4.2) and its strong dependence on T_s, the dynamical formation of ice cannot be neglected. Following Williams & Kasting (1997), the fraction of both land and ocean surface occupied by ice f_{i} can be calculated as:

$$f_{\text{i}} = \max\left[0\,,\, 1 - \exp\left(\frac{T - 273.15}{10}\right)\right] \tag{2.12}$$

with T equal to the average surface temperature in that band expressed in K. While this is good to represent the deposition of snow, it cannot represent the formation of thick, permanent glaciers, since f_{i} goes to zero as soon as $T > 273.15$ K. To mimic this phenomenon, f_{i} is considered constant throughout the orbit if the latitudinal zone is below the freezing point for more than half of the orbital period. In that case, f_{i} is evaluated using the annual average temperature for that zone, rather than the instantaneous one.

[2] https://crustal.usgs.gov/speclab/QueryAll07a.php

gas	lifetime [yr]	CO_2e over...		
		20 yr	100 yr	500 yr
H_2	6	4	33	11
CH_4	12	84	28	7.6
N_2O	109	264	265	130
CFC-11	52	6900	4660	2093

Table 2.2: The CO_2-equivalent calculated for four GHGs over a time span of 20, 100 and 500 yr, as reported in Warwick et al. (2022, for H_2) and in Shukla et al. (2019, for the others). The forcing of secondary GHGs produced by their destruction or recombination is neglected. CFC-11 is the industrial name of CCl_3F or trichlorofluoromethane.

2.1.3 The outgoing radiation

The OLR depends on the surface temperature, the thermal vertical structure of the atmosphere and the RT properties of the gases in the atmosphere. First of all, for an airless body the OLR is simply a function of the surface temperature T_s. Since it generally behaves as a blackbody, it follows the Stefan-Boltzmann law:

$$\mathcal{O}_{\max} = \sigma_{\mathrm{SB}} T_s^4 \tag{2.13}$$

The OLR calculated in this way is also the maximum allowed for a planet with a given T_s and no heat fluxes from the interior. If an atmosphere is present, a fraction of the infrared radiation emitted by the surface is absorbed by the gas molecules and cannot reach the space. As such, the infrared photosphere of the planet moves away from the surface and up to a given altitude h, which depends on the chemical species present and the vertical density profile of the atmosphere. Given that atmospheres are not isothermal, T_s must change in the process. For non-optically thin atmospheres, the lowest atmospheric layer has always a negative dT/dh (a quantity called altimetric lapse rate), which means that T_s is always higher than the temperature of the infrared photosphere. The infrared photosphere must emit an amount of radiation which is in equilibrium with the absorbed incoming radiation, thus must have a temperature equal to the planetary equilibrium temperature T_p calculated using Eq. 1.2. This process is the well-known greenhouse effect and causes T_s to diverge from the planetary equilibrium temperature T_p. Infrared photospheres that are higher above the ground (due to, for example, an higher concentration of efficient infrared absorbers) induce higher T_s. The difference between T_s and T_p is small if the planetary atmosphere is thin (i.e if the surface pressure is low and/or the columnar mass is small) or if the concentration of infrared-active chemical species is negligible, but in extreme cases can amount to several hundreds of Kelvin, as in the case of Venus. Given their role in the greenhouse effect, gases with strong absorption bands in the infrared region are called greenhouse gases or GHG.

In a OLR vs T_s plot, the greenhouse effect can be seen as the difference between the $\mathcal{O}_{\max}$ calculated using Eq. 2.13 and the true OLR shed by that specific atmosphere to space. This difference is called radiative forcing or $\mathcal{F}$. For a given T_s, a first-order approximation of the greenhouse effect in terms of radiative forcing induced by a concentration variation of CO_2 in an otherwise IR-transparent atmosphere can be expressed by the so-called Arrhenius rule, which reads:

$$\mathcal{F}_{\mathrm{CO2}} = \tilde{\mathcal{F}}_{\mathrm{CO2}} \ln\left(\frac{X_{\mathrm{CO2}}}{X_{\mathrm{CO2,0}}}\right) \tag{2.14}$$

where $\tilde{\mathcal{F}}_{CO2}$ is an empirical factor and X_{CO2} and $X_{CO2,0}$ are CO_2 final and initial concentrations (in volumetric parts per million, ppmv), respectively. It is valid for low, Earth-like concentrations. A widely used value for $\tilde{\mathcal{F}}_{CO2}$ is 5.35 Wm^{-2} (Myhre et al., 1998). The forcing caused by other GHGs (again, in trace amounts) can be roughly estimated using the concept of CO_2-equivalent (CO_2e), which is the increase in concentration of CO_2 that produces the same forcing as an increase in concentration of a given GHG. As such, it is possible to convert the concentrations of all the GHGs present in a given atmosphere in CO_2e and calculate the forcing induced by their variations as variations of CO_2e. There are, however, three caveats in using the CO_2e concept. The first one is the fact that different GHGs can have their absorption bands partially superimposed, thus reducing their radiative forcing potential when they are mixed together. The second one concerns the way in which the CO_2e is calculated. In fact, CO_2e is evaluated as the energy retained in the climate system over a given time span Δt by a single impulse of GHG at $t = 0$. Therefore, CO_2e is a metric that factors in the lifetime of that GHG in the Earth atmosphere. This phenomenon is visible in the evolution of the CO_2e over different timeframes in Table 2.2. Finally, when a GHG is destroyed (by oxidation or photolysis) it can transform in another GHG, thus inducing a secondary forcing. As an example, CH_4 oxidizes in CO_2 in the Earth atmosphere. Calculations that make use of the CO_2e concept generally adopt the value computed over 100 yr (third column), even though a more suitable choice would be the one closer to the average lifetime of the chemical species under consideration.

A more precise assessment of the forcing produced by Earth-like concentrations of CO_2, CH_4 and N_2O in a dry Earth-like atmosphere can be done using the relations by Etminan et al. (2016):

$$\mathcal{F}_{CO2} = (-2.4\times10^{-7}(X_{CO2}-X_{CO2,0})^2+7.2\times10^{-4}(X_{CO2}-X_{CO2,0})-2.1\times10^{-4}\bar{X}_{N2O}+5.36)\times \ln(X_{CO2}/X_{CO2,0}) \quad (2.15)$$

$$\mathcal{F}_{CH4} = (-1.3\times10^{-6}\bar{X}_{CH4} - 8.2\times10^{-6}\bar{X}_{N2O} + 0.043)(\sqrt{X_{CH4}} - \sqrt{X_{CH4,0}})$$

$$\mathcal{F}_{N2O} = (-8.0\times10^{-6}\bar{X}_{CO2} + 4.2\times10^{-6}\bar{X}_{N2O} - 4.9\times10^{-6}\bar{X}_{CH4} + 0.117)(\sqrt{X_{N2O}} - \sqrt{X_{N2O,0}})$$

where X_{CH4} and X_{N2O} are, respectively, the final concentrations of CH_4 and N_2O (in volumetric parts per billion or ppbv), $X_{CH4,0}$ and $X_{N2O,0}$ refer to their initial concentrations and $\bar{X}_{CH4}$ and $\bar{X}_{N2O}$ refer to the average between the initial and the final condition. As it is possible to see, these relations solve the issues related to the use of the CO_2e, given that they (i) give the instantaneous forcing instead of the total energy retained over a fixed amount of time and (ii) consider the superposition of the absorption bands of these three gases. These relations are valid for $X_{CO2} \in [180; 2000]$ ppm, $X_{CH4} \in [340; 3500]$ ppb and $X_{N2O} \in [200; 525]$ ppb.

Formulations discussed above are valid and useful for an Earth-twin, but what happens in the case of a radically different atmosphere, such as one composed by ∼bars of CO_2? While some fits of the OLR as a function of CO_2 concentrations up to 10 bars do exist (see e.g. Williams & Kasting, 1997), most of these more exotic cases are treated via ad-hoc radiative transfer calculations. The results are then stored in lookup tables and interpolated when needed in climate simulations. Computing the OLR as a function of T_s and the chemical-physical features of the atmosphere, especially when these conditions are very different from the current Earth ones, is central to my PhD work and will be described in much more detail in Chapter 3. The robustness, sensitivity and validity of our radiative transfer code under both Earth-like and exotic conditions will be explored in Chapters 4 and 5.

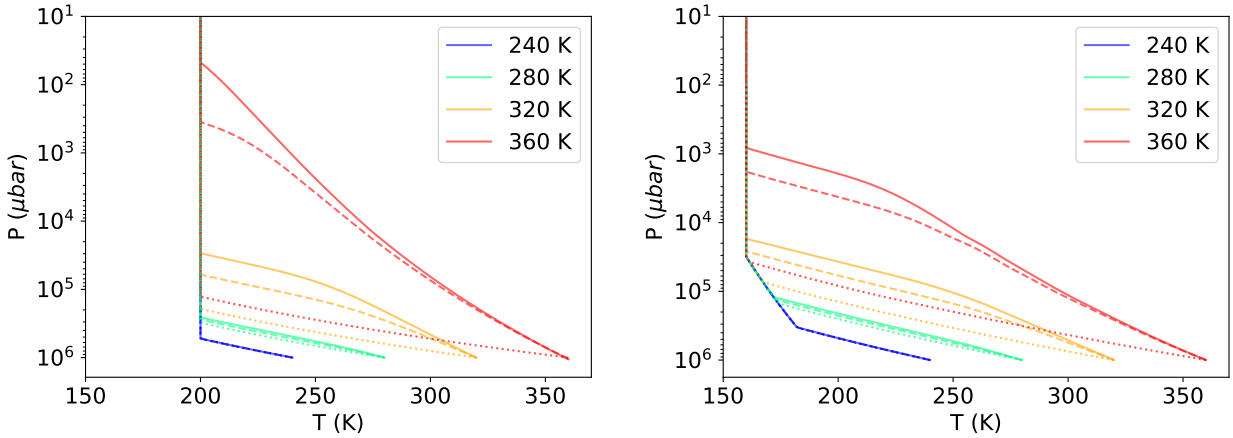

Figure 2.3: Vertical P-T profiles adopted for the two sets of atmospheres considered in this work. Left: profiles for an Earth-like atmosphere with a 200 K tropopause. Right: profiles for a CO_2-dominated atmosphere with a 160 K tropopause. Dotted, dashed and solid lines refer to dry, 60% moist and 100% moist (in relative humidity) adiabatic lapse rates, respectively. Different colors refer to different surface temperatures as indicated in the legend. To allow for an easier comparison between lapse rates, the P_s is set equal to 1 bar regardless of the RH, while in the tests we actually accounted for the increase of the surface pressure due to enhanced evaporation.

As a closing remark, also clouds must be considered in the assessment of the OLR. Apart from their influence on the TOA albedo, clouds are also efficient at absorbing the infrared radiation. However, given that clouds can form at different altitudes, do not have the same thickness, do not have the same temperature and, on different planets, can form from the condensation of gases other than H_2O, their influence is difficult to assess. As such, in simpler RT models they are either neglected in favor of the so-called clear-sky calculations or considered in terms on average forcing on the climate system. For water vapor clouds in an Earth-like atmosphere, it is reasonable to adopt the mean cloud forcing calculated from observations of the modern Earth, which is equal to 26.4 Wm^{-2} (Stephens et al., 2012). In ESTM1, this average value is re-scaled to the cloud coverage in each latitudinal zone, which in turn depends on the land, ocean and ice fractions in that same zone (as described in Section 2.1.2).

2.2 The vertical structure of the atmosphere

2.2.1 The density profile

The first thing to consider in the study of the atmosphere is its vertical pressure profile. The relation between pressure and height can be calculated starting from the hydrostatic relation:

$$dP = -\rho\, g(z)\, dz \tag{2.16}$$

where ρ is the density of an atmospheric parcel, $g(z)$ is the gravitational acceleration at a given height and z is the vertical coordinate, and then using the perfect gas law to replace ρ with P. If the layer under consideration is isothermal, and g is taken constant, Eq. 2.16 can

be integrated as follows:

$$\int_{P_0}^{P} \frac{dP}{P} = -\frac{\mu g}{R_{\text{gas}} T} \int_{h_0}^{h} dz \tag{2.17}$$

where P_0 is the pressure at h_0, to obtain:

$$P = P_0 \exp\left(-\frac{\mu g (h - h_0)}{R_{\text{gas}}\, T}\right) = P_0 \exp\left(-\frac{h - h_0}{\tilde{h}}\right) \tag{2.18}$$

where μ is the molar mass of the gas mixture, R_{gas} is the ideal gas constant and $\tilde{h}$ is the scale height of the atmosphere. This is called barometric relation. In general, atmospheres are well mixed and chemically homogeneous. The only exceptions are chemical species close to their condensation (such as water vapor in the Earth atmosphere or methane in the Titan atmosphere) and chemical species with significant sources and sinks (like ozone in the Earth atmosphere, which has very short lifespan and is generated in a specific atmospheric layer).

2.2.2 The dry adiabat

The barometric relation derived in the previous section can be applied in an isothermal atmosphere, but given that the lower parts of an atmosphere are generally optically thick in the infrared, they show a positive dT/dP gradient (the barometric lapse rate or, simply, the lapse rate). In other words, the atmosphere temperature reduces progressively when moving upward, to less dense layers. In general, the lapse rate depends on how much opaque is the atmosphere to the infrared radiation: optically thicker atmospheres can sustain larger gradients. However, once a certain limiting lapse rate is reached, convective motions start, preventing it to further increase. The pressure-temperature (PT) relation that describes such a convecting atmosphere is given by an adiabatic transformation, also called dry adiabat:

$$T(P) = T(P_0)\left(\frac{P}{P_0}\right)^{\frac{\gamma-1}{\gamma}} \tag{2.19}$$

where $\gamma = c_p/c_v = 1 + 2/f$ is the adiabatic index and c_p and c_v are, respectively, the isobaric and isochoric heat constants. The internal energy of a gas is stored as kinetic energy of the constituent particles and this energy must be equally subdivided among all their degrees of freedom (DOFs). As such, the adiabatic index is also related directly to the number of DOFs of the involved molecules f, which is equal to 3, 5 and 6 for monoatomic, biatomic and polyatomic ideal gases, respectively[3]. Some real triatomic gases (such as carbon dioxide) have an empirical value for γ which is compatible with $f = 7$ (Pierrehumbert, 2010). This equation is also valid for a mixture of gases, once the proper empirical γ is considered. Therefore, because of the large scale convection and except for localized turbolences, the PT profile of the lower part of an atmosphere will be determined by a dry adiabat.

Due to the hydrostatic relation, at larger heights the atmosphere becomes optically thin enough to be able to efficiently cool by radiating to space. In that condition, the convection stops and the atmosphere becomes nearly isothermal. The region in which the temperature gradient is determined by convection is called troposphere, while the overlain isothermal layer

[3]For ideal biatomic gases there are 3 translational and 2 rotational DOFs. For ideal polyatomic gases without a cylindrical symmetry there are 3 rotational DOFs. Internal (i.e. vibrational) DOFs are usually accessible only at higher (> 500 K) temperatures, at least for simpler polyatomic molecules (Halliday et al., 2009).

is called stratosphere. At even higher heights, the low thermal conductivity due to the very low density prevents the downward redistribution of the heat which is absorbed in the ultraviolet and ionizing part of the spectrum. As such, above the stratosphere there forms another layer with a negative lapse rate (that produces higher temperatures at lower pressures), called thermosphere. The upper bound of the thermosphere is the exobase, above which the mean free path of a gas particle is larger than the atmospheric scale height $\tilde{h}$. The exobase defines the beginning of the exosphere, which is the collisionless part of the atmosphere that in the end blend into the interplanetary medium. While these last two layers can reach temperatures of thousands of Kelvins, they are not relevant in determining the planetary energy budget and thus they are not considered in RT models for climate simulations.

2.2.3 The moist pseudoadiabat

All gases, under the right physical circumstances, can change phase, condensing as a liquid or depositing as a solid. During such transitions, the gas cedes a certain amount of heat, called latent heat. In a pressure-temperature plot, the locus of (T, P) points at which the phase transition occurs is called condensation curve. The pressure at which, for a certain temperature, condensation or deposition occurs is called saturation pressure P_{sat}. The saturation pressure can be calculated using the Clausius-Clapeyron equation, that is derived from thermodynamical considerations on the work done during the condensation process and therefore can be applied to all substances:

$$\frac{dP_{\text{sat}}}{dT} = \frac{1}{T(\rho_v^{-1} - \rho_c^{-1})} \tag{2.20}$$

where ρ_v and ρ_c are the densities of the vapor and condensed phases, respectively. Supposing that (i) the perfect gas law holds, (ii) the latent heat L is constant in temperature and (iii) that $\rho_c \gg \rho_v$, the Clausius-Clapeyron equation can be integrated to obtain the following approximation:

$$P_{\text{sat}}(T) = P_{\text{sat}}(T_0) \exp\left(\frac{-L\mu}{R}\left(\frac{1}{T} - \frac{1}{T_0}\right)\right) \tag{2.21}$$

from which it becomes evident the exponential dependence of the saturation pressure on temperature. This relation is valid up to a certain critical temperature T_c, above which the substance cannot condense anymore, regardless of the pressure. Different chemical species have different T_c. For any given parcel of gas with pressure P and temperature $T < T_c$, it is possible to define the ratio between P and $P_{\text{sat}}(T)$, which is called saturation ratio or relative humidity (RH), especially when referred to water vapor. This quantity is useful to determine how far the gas parcel is from the condensation condition.

For simplicity, an atmosphere composed by a single chemical species can be considered. A parcel of that atmosphere, during its convective ascent, can encounter the saturation curve of its constituent gas. When this happens, the gas starts to condense, ceding its latent heat to the parcel. As such, the PT profile of the atmosphere changes from that described by a dry adiabat to that described by the Clausius-Clapeyron equation. Inverting Eq. 2.21, it is possible to express temperature as a function of pressure:

$$T(P) = \frac{T(P_0)}{1 - \frac{RT(P_0)}{L} \ln\left(P/P_{\text{sat}}(T_0)\right)} \tag{2.22}$$

This new PT profile is called single-component moist adiabat[4] and it is in general less steeper than the dry adiabat one. The single-component moist adiabat can also be used as a good approximation of a multi-component atmosphere, provided that the condensing component is dominant ($\gtrsim 95\%$ of the total) as per volume fraction.

2.2.4 Earth-like tropospheres

Atmospheres are generally made up of a mixture of gases, each with its own condensation curve. It is possible that only one component is below T_c and with a sufficiently high RH as to condense somewhere in the atmospheric column. The modern Earth atmosphere is a good example of this situation. By volume and considering a typical relative water vapor humidity of 60%, a parcel of air at 15^o C contains 77.30% of N_2, 20.73% of O_2, 1.00% of H_2O, 0.92% of Ar, 0.0415% (or 415 ppm) of CO_2 and 0.00018% (or 1.8 ppm) of CH_4, plus other comparable traces of Ne, He and Kr[5]. Of these species, H_2O, CO_2 and CH_4 are below their T_c but only H_2O has a partial pressure sufficiently high as to actually condense during convection. A case like this can be modeled considering the atmosphere as formed by only two components: one non-condensable (the dry air mixture), and another condensable (the water vapor). Condensation can occur only when the RH of the condensable reaches 100%. Therefore, until that condition is reached, the atmosphere follows a dry adiabat. As soon as dew begin to form in the parcel, the PT profile changes. To calculate it, the heat budget in the parcel must be considered:

$$(m_n + m_v)\delta Q = m_a c_{p,n} dT - \frac{m_n}{\rho_n} dP_n + m_v c_{p,v} dT - \frac{m_v}{\rho_v} dP_v + L dm_v \tag{2.23}$$

where the subscripts "n" and "v" indicate, respectively, the quantities referred to the non-condensable and condensable (vapor) component, m are the masses of each component and c_p are the specific isobaric heat constants. Using the ideal gas law to substitute ρ for P, differentiating Eq. 2.21 to evaluate P_v (which is equal to the saturation pressure, being RH=100%) and setting $\delta Q = 0$ leads to the following equation:

$$\frac{d\log T}{d\log P_n} = \frac{R}{\mu_n c_{p,n}} \frac{1 + \frac{L\mu_n r_v(T)}{RT}}{1 + \left(\frac{c_{p,v}}{c_{p,n}} + \frac{L}{c_{p,n}T}\left(\frac{L\mu_v}{RT} - 1\right)\right) r_v(T)} \tag{2.24}$$

where r_v is the mass density ratio between condensable and non-condensable components, which depends on T and can be calculated separately using again the Clausius-Clapeyron approximation 2.21. A step-by-step derivation of this equation can be found in Section 2.7 of Pierrehumbert (2010). Integrating Eq. 2.24 allows to construct the PT profile of the atmosphere, which is called two-component moist adiabat. The lapse rate of this profile depends on $c_{p,n}$, $c_{p,v}$ and L, but in general it is in-between a dry and a single-component moist adiabat. The results for different T_s can be seen in Fig. 2.3, left-hand panel, as solid lines.

[4] In order to avoid the complications related to a multiphase atmosphere, the condensed part can be supposed to be instantly removed by precipitation. This makes the process irreversible and thus this relation should be called *pseudo*adiabat.

[5] Values calculated from the dry air mixture reported in the *CRC Handbook of Chemistry and Physics* (Haynes, 2017), re-scaled for the CO_2 concentration reported at December 2020 and for the water vapor content as described in the text.

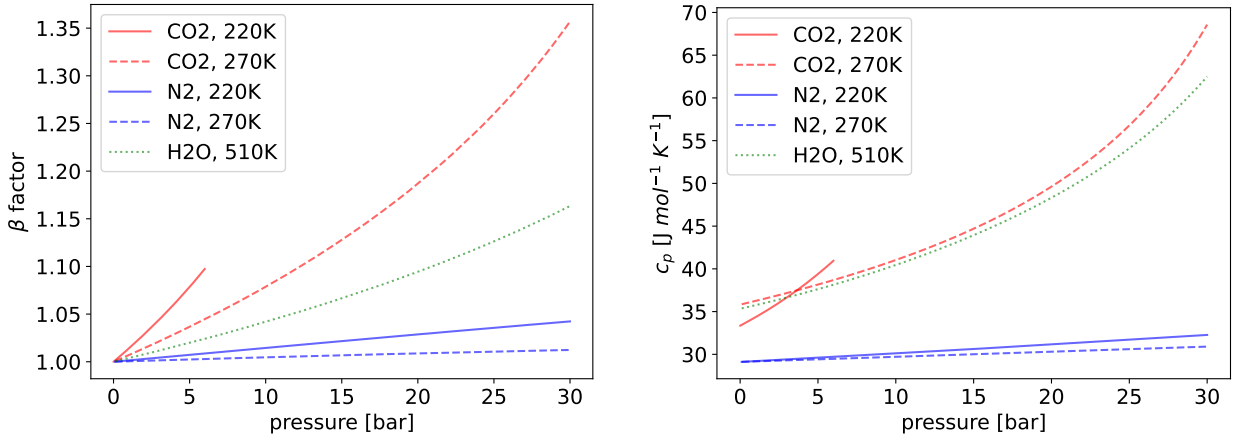

Figure 2.4: The non-ideal behaviour of CO_2 and H_2O as tracked by β and c_p, compared to the nearly ideal behaviour of N_2. Left panel: the pressure dependence of the β factor of CO_2 and N_2 at 220 K and at 270 K, and of H_2O at 510 K. 30 bar is very near to the saturation pressure of CO_2 at 270 K (32.03 bar) and of H_2O at 510 K (31.66 bar). The saturation pressure of CO_2 at 220 K is instead 5.99 bar. Right panel: the pressure dependence of c_p of the same gases under the same conditions. Data have been taken from the NIST.

Alongside the standard moist adiabat derived from thermodynamics, for my PhD work we also considered a slightly modified version where the H_2O partial pressure in the r_v term has been scaled with a RH lower than 100%. In theory, this should not be possible: if air is not saturated, water cannot condense and the atmosphere should show a dry adiabatic lapse rate. However, the real average lapse rate on Earth is neither moist nor dry, but somewhat in-between. This is caused by a large number of factors, the most relevant of which is the general inhomogeneity of the real terrestrial atmosphere (Pierrehumbert et al., 2007). Given that (i) our intent here is to construct a new RT model for an EBM that cannot capture such small scale variations, (ii) the non-radiative vertical energy flux in an Earth-like atmosphere is non-negligible and (iii) H_2O condensation plays an important role in this flux, we modified the moist adiabat profile by re-scaling the partial pressure of water vapor according to the relative humidity. As one can see in Fig. 2.3 (dashed lines in the left panel), this change has the effect of steepening the pressure-temperature (P-T) relation in the troposphere, giving it a shape that is in-between those of the theoretical moist (solid lines) and dry adiabatic models (dotted lines). The strongest effect of this change is felt at high T_s (> 320 K).

2.2.5 CO_2-dominated tropospheres

The two-component moist adiabat described above has been derived under the hypothesis that the atmospheric gas mixture behaves ideally, or in other words that: (i) the ideal gas law holds and (ii) that $c_{p,v}$, $c_{p,n}$ and L are constant in temperature and pressure. This is a good approximation for the modern Earth atmosphere but it is not so for denser or chemically different ones. A measure of the non-ideal behaviour of a gas is given by the compressibility factor Z or by its inverse β:

$$Z = \frac{1}{\beta} = \frac{PV}{nRT} \tag{2.25}$$

which for an ideal gas is equal to 1. The β factor is then dependent on the temperature and the pressure (or equivalently, the density). Some gases, like CO_2, exhibit a non-negligible deviation from the ideal behaviour, especially when approaching the saturation pressure for a given temperature (Fig. 2.4, left panel). The non-ideality manifests itself also in other characteristics of the gas, such as the specific heat c_p (Fig. 2.4, right panel) and the latent heat L, both of which cannot be hold constant in T and P. These deviations must be considered during the calculations of the T-p atmospheric profiles. The lapse rate equation for a non-ideal atmosphere can be derived by general considerations on the entropy of the ascending parcel and leaving the thermodynamic derivatives unsolved. Such an equation can then be solved numerically inserting the empirical values for the input variables. A particularly interesting case is that of CO_2-dominated atmospheres, such as that of early Mars, which is relevant also because it is related to the definition of the outer edge of the CHZ, as it will be detailed in Section 2.4.3. In my PhD work, we have adopted the lapse rate derived in the Appendix A of Kasting (1991, Eq. A18), which holds for a two-component atmosphere constituted by a large fraction of a non-ideal noncondensable (CO_2) and a small fraction of an ideal saturated condensable (H_2O) and reads:

$$\frac{dP}{dT} = \frac{c_{p,n} + r_v\left(c_c + \frac{dL}{dT} + \frac{L}{T}\left(\frac{\mu_v L}{RT} + \frac{T}{V}\left(\frac{\partial V}{\partial T}\right)_P\right)\right)}{\frac{T}{\mu_n}\left(\frac{\partial V}{\partial T}\right)_P - \frac{r_v L}{V}\left(\frac{\partial V}{\partial P}\right)_T} \tag{2.26}$$

where c_c is the specific heat of the condensed phase of the condensable, V is the molar volume and the subscripts "P" and "T" indicate that the relevant partial derivatives have been taken at constant pressure and temperature, respectively. The only approximation made is considering $P \simeq P_n$, thus neglecting the pressure contribution of the minor component. This is reasonable for CO_2 pressures at or above $\sim$ 1 bar and temperatures below 310 K, given that $P_{\rm sat}(310\text{K}) = 0.062$ bar for H_2O. Eq. 2.26 can describe also the dry lapse rate produced by a non-ideal atmosphere, if r_v is set to zero. In that case, Eq. 2.26 reduces to:

$$\frac{dP}{dT} = \frac{c_{p,n}\mu_n}{T\left(\frac{\partial V}{\partial T}\right)_P} \tag{2.27}$$

which is the Eq. (A19) in the Appendix of Kasting (1991).

For particularly dense CO_2-dominated tropospheres, also the main component can condense above a certain height. In this case, the troposphere is divided in two parts: a lower one where only H_2O condenses, that follows Eq. 2.26, and an upper one where both CO_2 and H_2O condense. Since the condensation curves of CO_2 and H_2O are distant to each other (i.e., for any given T, the condensation pressure of H_2O is more than four orders of magnitude less than that of CO_2) we can suppose that the upper troposphere is devoid of water and thus follows Eq. 2.22 (the single-component moist adiabat). The usage of a single-component moist adiabat for the upper troposphere is possible because, when CO_2 start condensing, the partial pressure of H_2O is very low. This situation is shown in Fig. 2.3, left panel. Thermodynamic quantities relevant to this calculation have been taken from the reference tables produced by the National Institute of Standards and Technology (NIST) and based on the work of Span & Wagner (1996).

The results of the numerical integration of Eq. 2.26 for $P_s = 1.0$ bar and different T_s are reported in Fig. 2.5 as dashed lines. The solid lines represent instead the results of integrating Eq. 2.24 using the appropriate thermochemical data for the same set of atmospheres. It should be noted that, given the approximation done in K91 to derive the lapse rate, the P-T profiles

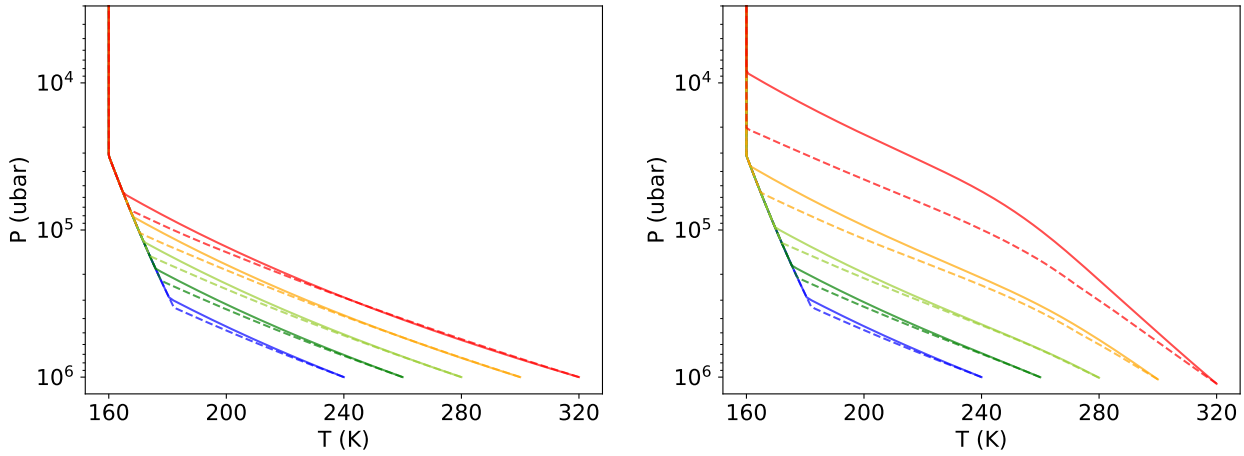

Figure 2.5: Comparison between atmospheric P-T profiles calculated considering (dashed lines) or not (solid lines) the non-ideal behaviour of CO_2. Different colors codify different surface temperatures: blue for 240 K, green for 260 K, yellow for 280 K, orange for 300 K and red for 320 K. In the panel on the left the H_2O RH has been set to zero, while in the panel on the right the RH has been set to 100%.

for hotter atmospheres are less accurate, given that the saturation water vapor pressure becomes non-negligible.

2.2.6 CO_2-N_2 tropospheres

The two-component moist adiabat described in Section 2.2.4 allow for the proportion between the partial pressures of the condensable and the non-condensable to be set freely, but has been derived under the assumption that they both behave ideally. On the other hand, the two-component moist adiabat described in Section 2.2.5 considers the non-ideal behaviour of the main species in the mix, but it has been derived under the assumption that the condensable partial pressure is negligible with respect to the total pressure of the mix. The assumptions made in both cases break down when a cold and dense CO_2-N_2 atmosphere is considered, given that a non-ideal, non-negligible CO_2 can condense above a certain height. A similar problem can also be encountered for very high temperature (> 500 K) H_2O-N_2 atmospheres (associated to a Runaway Greenhouse condition, see Section 2.4.1). In these cases another, more general expression is needed and as such we have adopted the Eq. 5 of Kasting et al. (1993b):

$$\frac{d\ln P}{d\ln T} = \frac{d\ln P_{\rm sat}}{d\ln T} - \left(\frac{1}{1 + r_v\mu_n/\beta_v\mu_v}\right)\frac{d\ln r_v}{d\ln T} \tag{2.28}$$

where β_v is the inverse of the compressibility factor of the condensable component, which accounts for its non-ideal behaviour. Another advantage of this equation is the possibility to use an empirical relation or tabulated values for the saturation pressure $P_{\rm sat}$. For CO_2, we used the same relation reported in the Appendix A of Kasting (1991), which reports the empirical fit of Ambrose (1956) for $P_{\rm sat}$ over solid CO_2 and of Vukalovich & Altunin (1968)

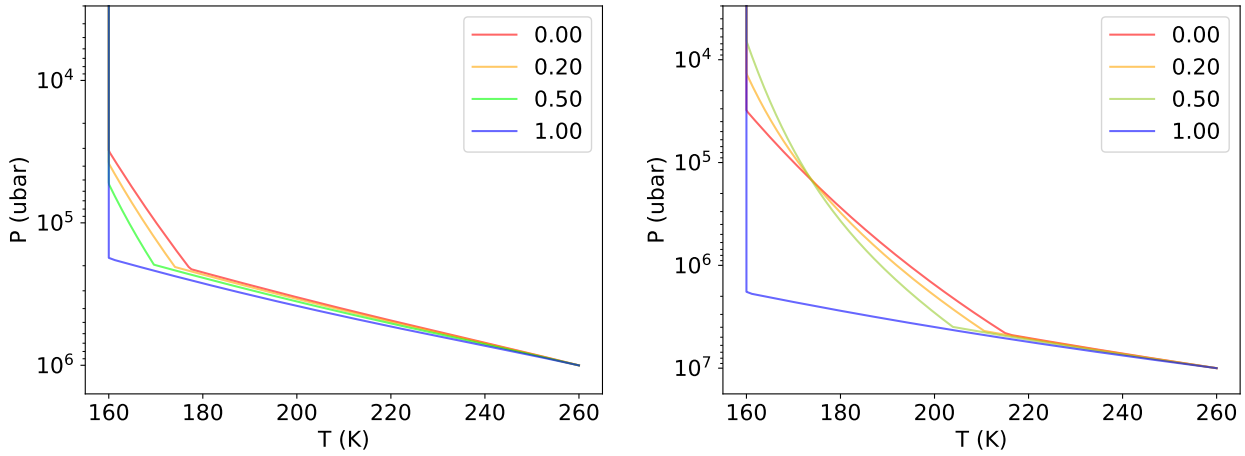

Figure 2.6: Comparison between atmospheric P-T profiles calculated considering four different N_2 mixing fractions in a CO_2-N_2-H_2O atmosphere with RH=100%, from 0 (red lines, CO_2-only) to 1 (blue lines, N_2-only). The models on the left have a P_s of 1 bar, while the models on the right have a P_s of 10 bars. The T_s is fixed for all cases to 260 K.

for $P_{\rm sat}$ over liquid CO_2:

$$\begin{cases} \log_{10} P_{\rm sat} = 6.760956 - \frac{1284.07}{T-4.718} + 1.256 \times 10^{-4}(T - 143.15) & \text{if } T < 216.56 \text{ K} \\ \log_{10} P_{\rm sat} = 3.128082 - \frac{867.2124}{T} + 18.65612 \times 10^{-3} T + & \\ -72.4882 \times 10^{-6} T^2 + 93 \times 10^{-9} T^3 & \text{if } T \geqslant 216.56 \text{ K} \end{cases} \tag{2.29}$$

where the third term in the first relation has been added by Kasting such as to make it continuous at the triple point temperature with the second relation. This produces a small ($< 2\%$) difference with respect to the original formulation.

The results of the numerical integration of Eq. 2.28 is shown in Fig. 2.6 for four N_2 mixing fractions and two P_s values (1 bar on the left panel, 10 bars on the right panel). All models have the same T_s, equal to 260 K. As it is possible to see, changing the proportion between CO_2 and N_2 primarily affects the upper troposphere where CO_2 condenses, since now the profile of this region does not follow anymore the condensation curve of CO_2, while leaving nearly unaffected the lower troposphere. The difference between different models is more marked when the upper troposphere is more extended, which happens when T_s is low ($\lesssim$ 260 K) and P_s is high ($\gtrsim$ 1 bar), while for higher temperatures and lower pressures the CO_2-condensing region can effectively disappear. On the other hand, the effect on the lower troposphere is mainly caused by the relatively small differences in the isobaric specific heat between CO_2 and N_2.

2.2.7 The stratosphere

As said before, the stratosphere is the optically thin part of the atmosphere, and as such it can be considered isothermal. Its temperature (also called skin temperature, $T_{\rm skin}$) can be evaluated considering the radiative equilibrium of this layer, which despite being optically thin has a nonzero opacity. First of all, this layer is heated (as the rest of the atmosphere) by the radiation incoming from below. Given that it has a low opacity, this radiation can be considered equal to the OLR. It then re-radiates from both its top (to space) and its bottom

(to the lower atmosphere) with $T_{\rm skin}$. The radiative balance is then equal to:

$$2\epsilon_{\rm IR}\sigma_{\rm SB}T_{\rm skin}^4 = \epsilon_{\rm IR}\mathcal{O} \tag{2.30}$$

where ϵ is the infrared emissivity/absorbivity of the layer. Hence:

$$T_{\rm skin} = \left(\frac{\mathcal{O}}{2\sigma_{\rm SB}}\right)^{1/4} \simeq 0.84\,T_p \tag{2.31}$$

where T_p is the planetary equilibrium temperature. Given that this line of reasoning can be applied to every sublayer in which the stratosphere can be subdivided, this also explains why it is isothermal.

This derivation is valid for an atmosphere composed by a grey gas, i.e. a gas that absorbs equally at all frequencies in the infrared. Real gases, however, absorb and emit in specific electromagnetic infrared bands. In real atmospheres, the portion of the OLR spectrum that can be efficiently absorbed by the gases in the stratosphere is depleted due to the absorption by the same gases in the troposphere. On the other hand the stratosphere emission is unchanged, thus moving the equilibrium to lower temperatures. This is a well-known feature of non-grey models (see e.g. Pierrehumbert, 2010). In calculations of ozone-free Earth-like atmospheres, Leconte et al. (2013) obtained a stratospheric temperature equal to $\sim$ 140 K and confirmed that the stratospheric temperature reduces when the opacity of the troposphere increases, as happens when T_s increase due to the increased fraction of H_2O in the atmosphere. In theory there is no lower limit for the stratospheric temperature and its exact value depends on the specific optical properties of both the stratosphere and the troposphere. However, the production of ozone in oxygen-rich atmospheres and its ability to absorb efficiently ultraviolet stellar radiation heats up the stratosphere and partially counteract the enhanced cooling. This explain why the real Earth stratosphere has an average temperature of 200 K (Seidel et al., 2001; Kuell et al., 2005), which is much closer to the ideal $T_{\rm skin} \simeq 0.84 \times 255\,{\rm K} = 214\,{\rm K}$. The former value is also adopted in many works in literature, and as such for this work we stuck with it.

Parameterized values for $T_{\rm skin}$ as a function of several atmospheric quantities and T_s have also been derived. As an example, we reported the Williams & Kasting (1997) formulation, obtained by fitting $\sim$300 runs of their radiative-convective model for a N_2-dominated atmosphere with a 100% H_2O RH and different amounts of CO_2:

$$\begin{aligned} T_{\rm skin} = -188.1 - 1.995\mathcal{X} + 3.810\mathcal{X}^2 + 2.328T_s - 3.329\times10^{-3}T_s^2 + \\ +3.733\times10^{-4}\mathcal{X}T_s - 2.856\times10^{-2}\mathcal{X}^2T_s + 2.214\times10^{-5}\mathcal{X}T_s^2 + \\ +4.605\times10^{-5}\mathcal{X}^2T_s^2 \end{aligned} \tag{2.32}$$

where $\mathcal{X} = \ln(p_{\rm CO2}/3.3\times10^{-4})$. This relation has been reported to be valid for $p_{\rm CO2} \in [10^{-5}; 10^{1}]$ bars and $T_s \in [190; 380]$ K.

For CO_2-dominated atmospheres, we adopted instead a value equal to 160 K (as done by Halevy et al., 2009). This value is close to the range of values (150-170 K) derived by Kasting (1991) by running a radiative-convective equilibrium calculation of a specific case (that with a $P_s = 0.35$ bar), choosing the cold-trap temperature and then scaling that result for the other tested cases using the skin temperature relation derived above. Given the increased scattering in thicker atmospheres and the relation existing between $\mathcal{O}$ and $\alpha_{\rm TOA}$, the skin temperature decreases when surface pressure increases. However, the latter work shows that

the skin temperature variations as a function of the surface pressure are (i) small ($\sim$ 10 K increasing P_s from 0.35 to 5 bar) and (ii) have little influence on the surface temperature. Therefore, we decided to fix it to a specific value, as done in the Earth model.

2.3 The horizontal energy transport

In most EBMs surface temperature is treated as a function of two variables: time t and longitude ϕ. The set of points at a given ϕ share the same physical features, which are the average physical features of the planet at that latitude. The temperature is actually a mean over one rotation period, which acts as the unit of time for the model. The surface temperature $T = T(t, \phi)$ can be evaluated considering the time evolution of the energy density per planetary unit area $\mathcal{E}$ contained in an infinitesimal latitudinal band. The fluxes moving energy in and out the strip are the radiative terms plus the meridional horizontal transport $\mathcal{H}$ divided by the area of the strip A:

$$\frac{\partial \mathcal{E}}{\partial t} = \text{flux in} - \text{flux out} = \mathcal{I}(1 - \alpha_{\text{TOA}}) - \mathcal{O} + \frac{d\mathcal{H}}{dA} \tag{2.33}$$

The area element of the band is equal to the length of the circle at latitude ϕ times its width, or $2\pi R_p \cos(\phi) \times R_p \, d\phi$ and, in general, the horizontal transport can be expressed as a down-gradient diffusion process. As such, it can be written as:

$$\mathcal{H} = -2\pi R_p^2 \cos(\phi) D \frac{\partial T}{\partial \phi} \tag{2.34}$$

where D is a coefficient analogous to the thermal conductivity. Moreover, the energy surface density can be re-written as the product of the thermal capacity C and the surface temperature. Substituting $\mathcal{E}$, dA and $\mathcal{H}$ and rearranging the terms in Eq. 2.33 yields:

$$C\frac{\partial T}{\partial t} - \frac{1}{2\pi R_p^2 \cos(\phi)} \frac{\partial}{\partial \phi}\left(-2\pi R_p^2 D \cos(\phi) \frac{\partial T}{\partial \phi}\right) = \mathcal{I}(1 - \alpha_{\text{TOA}}) - \mathcal{O} \tag{2.35}$$

Finally, cancelling out the constant terms and and letting $x = \sin(\phi)$ leads to:

$$C\frac{\partial T}{\partial t} - \frac{\partial}{\partial x}\left(D(1 - x^2)\frac{\partial T}{\partial x}\right) = \mathcal{I}(1 - \alpha_{\text{TOA}}) - \mathcal{O} \tag{2.36}$$

In general, all the coefficients in this equation depends on both the time t and the position x, either directly or indirectly through their dependence on T.

The horizontal transport is governed by the second term of Eq. 2.36. The ability of EBMs (and of ESTM1 and 2 in particular) to precisely capture the details of general circulation depends on the correct parameterization of the $D(1 - x^2)\partial T/\partial x$ term. Given that oceanic circulation is (i) less important in the horizontal transport, accounting for less than 10% of the meridionally redistributed heat on Earth and (ii) presents a different set of challenges in modeling it (for example, due to the fact that continents act as hard barriers to the flow), it is generally neglected in EBMs. From now on, we will focus on the specific modelization of the horizontal transport term in ESTM1.

The energy budget of an air parcel can be expressed in terms of moist static energy per unit mass:

$$m = c_p T + L r_v + g z \tag{2.37}$$

where the first, second and third terms measure respectively the sensible heat, the latent heat and the potential energy of the parcel. Integrating the fluid momentum and continuity equations longitudinally and vertically yields the average zonal flux:

$$D = \frac{P}{R^2 g}\left(\frac{\partial T}{\partial y}\right)^{-1} \overline{vm} \tag{2.38}$$

where v is the average meridional wind speed and $y = \phi R$ is the meridional arc length. This relation is valid if condensation takes away only a minimal part of the atmospheric mass, as in the case of the current Earth atmosphere in which the only condensable is a trace gas: water vapor. A less constraining requirement is that the atmosphere must be shallow, i.e. variations of the gravitational acceleration along the considered column g must be negligible. As already mentioned, the physical quantities are averaged over one rotation period which means that this treatment traces the seasonal evolution of the planet.

Inside the tropical region, the horizontal transport of energy takes the form of large convective cells that originate in the hottest region of the planet, namely the Intertropical Convergence Zone or ITCZ. For a planet with a rotation axis perpendicular to the ecliptic the ITCZ coincides with the geographical equator, while for the Earth it shifts seasonally towards the most irradiated (by diurnal average) latitude. The hot (and possibly moist) air ascend at the ITCZ, then split and move poleward. On a rotating planet, the poleward movement of air is influenced by the Coriolis effect: due to conservation of angular momentum, the angle between the air velocity vector and a latitude circle reduces. At a certain limiting latitude, the air parcels are effectively moving eastward in the northern hemisphere and westward in the southern hemisphere. This closes the cycle, since the air cannot move latitudinally anymore. Once it is sufficiently cooled, it sinks and returns to the equator. The two large convective cells (one to the north and the other to the south of the equator) produced by this motion are called Hadley cells. Outside the tropical region the turbulence tends to increase and therefore diffusion becomes dominant in the latitudinal transport of heat. Due to these differences, $\mathcal{H}$ must be calculated differently inside and outside the tropical region. Below we present the derivation of the horizontal transport in the tropical and extratropical regions as derived in Vladilo et al. (2015) and adopted in the ESTM1.

2.3.1 Transport in the extratropical region

Transport in the mid and high latitudes is dominated by turbulent eddies. In order to evaluate it, a common approach is to consider the variables involved as the sum of a the average plus a perturbative term: $m = \bar{m} + m'$. Expressed in this way, it is possible to demonstrate that $\overline{vm} = \bar{v}\bar{m} + \overline{v'm'}$. If the transport is dominated by eddies, then $\bar{v}\bar{m} \ll \overline{v'm'}$. Substituting the moist static energy evaluated at the surface ($z = 0$) yields $c_p\overline{v'T'} + L\overline{v'r'_v}$. At this point, the two eddy terms can be calculated in terms of root mean square (rms, identified by the $\langle\,\rangle$ brackets) of the variables times a correlation coefficients k, giving $c_p k_S \langle v'\rangle\langle T'\rangle + L k_L \langle v'\rangle\langle r'\rangle$.

Now, two sets of quantities must be evaluated: the rms value of the perturbative terms and the correlation coefficients. Concerning the first set, eddy diffusivity theories allows for writing them as the product of the quantity spatial gradient and the mixing length $l_{\rm mix}$. For temperature, this is simply:

$$\langle T'\rangle = -l_{\rm mix}\frac{\partial T}{\partial y} \tag{2.39}$$

For the water vapor mass mixing ratio a change of variables is needed, given that it is only indirectly dependent on y. Explicitating it yields:

$$\langle r' \rangle = -l_{\text{mix}} \frac{\partial r_v}{\partial T} \frac{\partial T}{\partial y} = -l_{\text{mix}} \frac{q_v}{P_{\text{dry}}} \frac{\mu}{\mu_{\text{dry}}} \frac{dP_{\text{sat}}}{dT} \frac{dT}{dy} \tag{2.40}$$

where μ and μ_{dry} are the molar masses of moist and dry air, respectively, and q is the relative humidity. For the meridional velocity there exists a large number of analytical formulations. Vladilo et al. (2015) adopted the formalism of Barry et al. (2002), which modeled the mid to high latitude transport of energy as a heat engine operating between an hot region with temperature T_h and a cold region with temperature T_c. The kinetic power per unit mass E generated by this engine can be calculated as the product between the heat per unit time and unit mass absorbed by the atmosphere Q times the maximum ideal thermodynamic efficiency $(T_h - T_c)/T_c = \delta T/T_c$ times an efficiency factor η:

$$E = \eta \frac{\delta T}{T_c} Q \tag{2.41}$$

If there are not other sources or sinks of power per unit mass, dimensional analysis yields an eddy velocity term equal to:

$$\langle v' \rangle = (l_{\text{mix}} E)^{1/3} \tag{2.42}$$

The adoption of this formalism for the eddy velocity is supported by comparisons with 3D GCMs, as shown in Barry et al. (2002).

Regarding l_{mix}, a widely adopted choice is the Rhines scale (Rhines, 1979):

$$l_{\text{mix}} = \left(\frac{2\langle v' \rangle}{\beta} \right)^{1/2} \tag{2.43}$$

where $\beta = \partial f/\partial y$ and $f = 2\Omega \sin(\phi)$, or the Coriolis parameter. The $\langle v' \rangle$ must be evaluated at the latitude corresponding to the maximum kinetic energy of the flow (ϕ_m). In this modelization, the characteristic mixing length of the atmosphere is determined by the inverse of the Rhines wavenumber k_{Rhines}, which in turn marks the transition from a wave-dominated ($k < k_{\text{Rhines}}$) to a turbulent flow ($k > k_{\text{Rhines}}$). Rhines demonstrated theoretically that at this wavenumber there is a pile-up of the inverse energy cascade, i.e. the transfer of energy from thermal turbulence to small eddies and finally, to larger ones. This result has been shown to be in good agreement with moist static energy transport experiments in 3D GCM models (Frierson et al., 2007) and thus adequate for the horizontal transport treatment.

Concerning the second set of quantities, i.e. the correlation coefficients, they must be derived empirically from observations of the Earth. Then, numerical experiments performed with GCMs (Barry et al., 2002; Frierson et al., 2007) show that they can be treated as latitude-independent model constants.

Substituting Eqs. 2.39 to 2.43 in Eq. 2.38, together with the considerations on the efficiency of eddies elucidated at the beginning of the subsection, yields:

$$D = \frac{k_S c_p \eta^{3/5} P}{(\cos \phi_m)^{4/5} R^{6/5} \Omega^{4/5} g} \left(\frac{\delta T}{T_h} Q \right)^{3/5} \left(1 + \frac{k_L L}{k_S c_p} \frac{\mu}{\mu_{\text{dry}}} \frac{q_v}{P_{\text{dry}}} \frac{dP_{\text{sat}}}{dT} \right) \tag{2.44}$$

This equation can then be solved considering a set of conditions. First of all, $Q = \mathcal{I}(1 - \alpha_{\text{TOA}})/(P/g)$ where the numerator is the incoming flux received by the planet averaged over

one rotation and the denominator is the atmospheric columnar mass. Second, the operational temperatures of the atmospheric thermodynamic engine T_c and T_h are chosen as to be equal to the annual means evaluated at 28^o and 68^o of each hemisphere, which are the limits of the mid-latitude region on the Earth. GCM experiments (Barry et al., 2002) showed that changing these values yields negligible differences in the final results. Third, k_S, k_L, η and ϕ_m are taken as constants based on suitable corresponding values for Earth.

2.3.2 Transport in the tropical region

Transport at low latitudes is dominated by the Hadley cell circulation. The Hadley cell is extremely efficient in smoothing the temperature gradients inside this region and thus cannot be ignored. On the other hand, the formalism of eq. 2.36 forces to model it as a diffusion even though it is not a diffusive process and its pattern is influenced by the specificities of the planetary general circulation. An example of the latter is the seasonal shift of the ITCZ. In order to model the effects produced by this type of circulation without changing the core equation of the EBM, the enhanced horizontal transport in the tropical region is modeled by multiplying the D term by a scaling factor ξ. Given that the structure of the Hadley cells depends, in first approximation, on the seasonal variation of the average zenith distance of the star, the scaling factor is a function of the ϕ and time of the year. In practice, this term is modeled as:

$$\xi(\phi, t) = c_0 + c_1 \cdot \mu(\phi, t) \tag{2.45}$$

of $\mu(\phi, t)$ calculated on the basis of the orbital position and the axial tilt of the planet. The coefficients c_0 and c_1 are calculated from the normalization condition, which states that the mean annual global value of ξ must be equal to 1, and from the $\xi_{\max}/\xi_{\min}$ ratio, where $\xi_{\max/\min}$ are the absolute maximum and minimum of ξ in the (ϕ, t) space. This is actually a free parameter that can be tweaked as to obtain a latitudinal T_s profile similar to the real one. In their EBM, North et al. (1983) used a value equal to 3, while for ESTM1 a value equal to 2.2 has been chosen. In general there is not a solid theoretical support for the ξ term and as such, for other planets than Earth the safest assumption is to take a ξ value equal to 1.

2.3.3 Thermal capacity of zonal bands

In order to properly model the seasonal temperature profile of an Earth-like planet, the thermal capacity of the planet cannot be neglected. In ESTM1 and 2, the thermal capacity per unit area of each latitudinal zone is calculated by considering the weighted average of the thermal capacities of the three types of surface considered (land, ocean and ice) plus the thermal capacity of the atmospheric column. The fraction of the rocky crust and the ocean that contribute to the thermal capacity of the planet depends on the considered timescale. Since ESTM1 has been developed to study the seasonal temperature profile under constant conditions, rather than follow the secular or geological evolution of the planet, this fraction is quite small. For lands, the first 0.5-m slab of rock is considered contributing to C_{lnd}, which is equal to $\sim$1 MJ m^{-2} K^{-1}. For oceans, contributions come from the wind-mixed layer that extends down to $\sim$50 m of depth. This gives a C_{ocn} value equal to $\sim$210 MJ m^{-2} K^{-1}. Ices are treated in two different ways depending if they are stable (i.e. notundergoing a phase transition) or not. Below 263 K, $C_{\text{i}} = C_{\text{lnd}}$, while between 263 and 273 K $C_{\text{i}} = C_{\text{lnd}} + C_{\text{ocn}}/5$. Finally, C_{atm} is evaluated by considering the equivalent ocean depth of the Earth atmosphere

(2.4 m, Pierrehumbert, 2010) and rescaling the corresponding thermal capacity (10 MJ m^{-2} K^{-1}) for the surface pressure and the specific heat c_p.

2.4 Climate feedbacks

A fundamental feature of the climate system is the presence of several feedback mechanisms that arise from the interaction of its different components. These feedback cycles can be triggered by several factors, such as a release of GHGs from the planetary interior via volcanism, a meteorite impact or the brightening of the parent star due to its natural evolution. These factors can be all treated as radiative forcings, since they are associated with variations to either the ISR, the OLR or the TOA albedo, which in turn produce a change in the surface temperature. The transformations induced in other parts of the climate system by this surface temperature change either amplify or damp the change itself. In the first case, we are describing a positive, or self-reinforcing, feedback. The second case describes a negative feedback. Considering that the surface temperature is fundamental in determining the climate state of a planet, positive feedbacks can be intended as destabilizing and negative feedbacks as stabilizing for the climate system. Following Cess et al. (1990), the strength of climate feedbacks can be evaluated via the linear radiative feedback parameter λ_f, that links a change of the net radiative flux $\mathcal{N} = \mathcal{I}(1 - \alpha_{\text{TOA}}) - \mathcal{O}$ to the related change in the surface temperature:

$$\lambda_f = \frac{d\mathcal{N}}{dT_s} \tag{2.46}$$

where it should be remembered that both $\mathcal{O}$ and α_{TOA} depend on T_s. The first and most important of these feedbacks is the so-called blackbody or Planck feedback, which is the direct dependence (hence the use of the partial derivative) of $\mathcal{N}$ on T_s via the Stefan-Boltzmann law, for a fixed atmospheric emissivity:

$$\lambda_f^0 = \frac{\partial \mathcal{N}}{\partial T_s} = -\frac{\partial \mathcal{O}}{\partial T_s} = -4\epsilon\sigma_{SB}T^3 \tag{2.47}$$

In other words, this parameter captures the interdependence between $\mathcal{O}$ and T_s when all the other variables of the climate system remain constant. From this relation, it can be calculated that for the modern Earth atmosphere and temperature $\lambda_f^0 = -3.4$ $\text{Wm}^{-2}\text{K}^{-1}$, while for an airless body ($\epsilon = 1$) with the same average temperature is -5.4 $\text{Wm}^{-2}\text{K}^{-1}$.

At variance with the Planck feedback, all the other climate feedbacks are only indirectly dependent from T_s. In general, a change in T_s produces a change in the X_i variable of the climate system (for example, the ice coverage fraction), that in turn produces a change in $\mathcal{N}$. In first approximation, in the vicinity of a given T_s the contributions from each climate feedback can be treated separately, which is equal to hypothesize that different components of the climate systems interact via T_s only. With this assumption it is possible to write the total feedback parameter as:

$$\lambda_f = \frac{d\mathcal{N}}{dT_s} = \frac{\partial \mathcal{N}}{\partial T_s} + \sum_{i=0}^{n} \frac{\partial \mathcal{N}}{\partial X_i}\frac{\partial X_i}{\partial T_s} = \lambda_f^0 + \sum_{\text{i}=0}^{n} \lambda_f^{\text{i}} \tag{2.48}$$

Therefore, if a planet is subject to a small radiative forcing $\Delta\mathcal{R}$, the induced variation in the surface temperature can be calculated considering that:

$$\Delta\mathcal{N} + \Delta\mathcal{R} = 0 \quad \Rightarrow \quad \frac{d\mathcal{N}}{dT_s}\Delta T_s = -\Delta\mathcal{R} \quad \Rightarrow \quad \Delta T_s = -\frac{\Delta\mathcal{R}}{\lambda_f} \tag{2.49}$$

Given that the Planck feedback has a negative sign, any feedback associated with a positive λ_f^{i} value amplifies the T_s variation with respect to the purely Planckian one. Thus, using this sign convention, positive (negative) feedbacks are associated with positive (negative) λ_f^{i}.

As it is possible to see, if the sum of all the i climate feedbacks approaches the value of λ_f^0, the temperature variation can become arbitrarily large for a given value of $\Delta\mathcal{R}$. When this happens, T_s decouples from the net radiative flux and the climate becomes unstable. This situation is referred to as a runaway state. Runaway states produce radical changes in the surface conditions of a planet and, as such, are fundamentally linked to another important concept, which is that of the CHZ. A planet with a reservoir of water in the CHZ can in principle sustain a liquid ocean on its surface, thus complying with one of the requirements of life (at least, as we know it). The outer and inner limits of the CHZ are defined on the basis of some very strong positive feedbacks that inevitably transition the planet either to a glaciated Snowball state, in which all the water is locked up in ice, or in a Runaway Greenhouse state, in which all the surface liquid water evaporates and is then exposed to photodissociation caused by the ultraviolet radiation in the upper atmosphere. The two feedbacks that define the edges of the CHZ are, respectively, the ice albedo feedback (coupled with the existence of a maximum possible greenhouse attainable with any given gas) and the water vapor feedback and they will be discussed in more detail in two following subsections.

Another important aspect that should be considered is the timescale onto which a given feedback acts. The simple model presented above cannot take this into consideration, applying instead all the effects at the same time. However, time-related considerations are important, given that a fast positive feedback can overcome a stronger negative one, disrupting the climate system before the other can kick in. The timescale problem, together with the multiplicity of climate feedbacks and the fact that there exists lingering uncertainties in their physics makes difficult to accurately estimate their impact. This has also direct consequences on extensively studied problems such as forecasting the effects of the anthropogenic greenhouse emissions.

Finally, life itself provides several feedback mechanisms to the planetary climate system, which are even less understood than abiotic feedback cycles. Early qualitative investigations on the influence of life over the environment begun in the XIX century (see e.g. Spencer, 1844). During the XX century an increasing amount of observational and experimental data confirmed the fundamental role of biological activity in determining the planetary climate, via geochemical (Sillen, 1966) and geophysical (Charney et al., 1975) interactions. Lovelock & Margulis (1974a,b) pushed the idea forward, proposing that the aggregated influence of life tends to make the planet even more suited for life itself. In particular, they postulated that life acts as a strong negative feedback which induces thermal homeostasis on the planet, which is known as the "Gaia hypothesis". In support of this, Watson & Lovelock (1983) developed the so-called Daisyworld model, in which a hypothetical planet is colonized by two species of daisies, respectively with a higher and a lower albedo than the barren surface. In the model their growth rate is linked to the temperature via a parabolic relation, characterized by a minimum and a maximum viable temperature and an optimal value in between. Thanks to their color, darker and lighter daisies can maintain different internal temperatures for the same insolation. As such, darker daisies are favored when the insolation (and hence the surface temperature) is low, whereas lighter daisies are favored when the insolation is high. The interesting result of the model is the ability of these two daisies populations to influence the overall surface temperature of the planet, spontaneously pushing it to the best value for the daisies growth, thus optimizing the biosphere duration, total mass and spatial

extension. The Daisyworld model has been criticized from several different points of view as too simplistic to produce results valid for a real Earth-like biosphere, thus voiding the Gaia hypothesis. Kirchner (2002) offers a brief review of the main counterarguments, highlighting the fact that (i) known biological feedbacks are mostly positive and (ii) natural selection seems not to favor traits that are good for the entire biosphere over those that are not good. From this analysis, the results of the original Daisyworld model seems to be driven by the specific choices that the modelers made rather than being general. More recent simulations of the biosphere-climate interactions try to address these issues by increasing the complexity and incorporating the results of observational studies. While the validity of the Gaia hypothesis is still largely debated, it has been demonstrated that considering a larger variety of species (Harding, 1999), increasing the number of trophic layers[6] and introducing simplified Darwinian evolution schemes (Lenton & Lovelock, 2001) tend to reinforce the homeostatic properties of the simulated system.

2.4.1 Water vapor feedback and the inner edge of the CHZ

Water vapor is a very effective GHG due to its numerous absorption bands, their wavelength position with respect the peak emission of cool Earth-like planets (around 10 μm) and the tendency to form dimers which in turn produce an extra opacity called continuum. These features will be explored in detail in the next Chapter. If water is present on the surface of a planet, it will also be present in its atmosphere as a vapor in equilibrium with the solid or liquid reservoir. As described in Section 2.2.3, the partial pressure of that vapor is an exponential function of temperature and as such, an increase in T_s will increase the amount of water in the atmosphere and thus the greenhouse effect, which in turn will amplify the temperature increase. The T_s increase then induces a new increase of the water vapor content of the column, potentially starting a chain reaction. This feedback loop produces a state called Runaway Greenhouse (RG), that exhausts itself only when the surface reservoir is completely evaporated into the atmosphere. If a sufficiently large quantity of H_2O is present, the planetary troposphere can become completely opaque to the infrared radiation, thus preventing the surface to shed its thermal energy to space. In practice, this means that there exist a maximum OLR value called Komabayashi-Ingersoll limit[7] (Komabayashi, 1967; Ingersoll, 1969). If the absorbed radiation exceeds the K-I limit, the planetary surface cannot reach a thermal equilibrium via the emission of infrared radiation and this causes T_s to potentially rise to over 1200 K (see Fig. 2.7, left panel). A new, very high temperature equilibrium can be reached when the surface begins to radiate in the visible, where an H_2O atmosphere is nearly transparent. The amount of stellar radiation capable of activating this feedback loop defines the inner edge of the CHZ, since no planet can have a stable hydrosphere in that case.

Calculating the inner edge of the CHZ is not an easy task. There are two large groups of factors that make this challenging: opacity-related uncertainties and cloud-related uncertainties. The former group is related to the opacity of water vapor specifically. Using different absorption line repositories and continuum opacity models gives different results on the lim-

[6]The steps in the food web, in order to simulate grazing by herbivores and predation by carnivores.

[7]Another maximum OLR value, derived under slightly different assumptions, is the Simpson-Nakajima limit (Simpson, 1927; Nakajima et al., 1992). It takes into account the lapse rate of the troposphere, thus it is more correct from a theoretical point of view. Anyway, both the Komabayashi-Ingersoll and the Simpson-Nakajima limits convey the same concept.

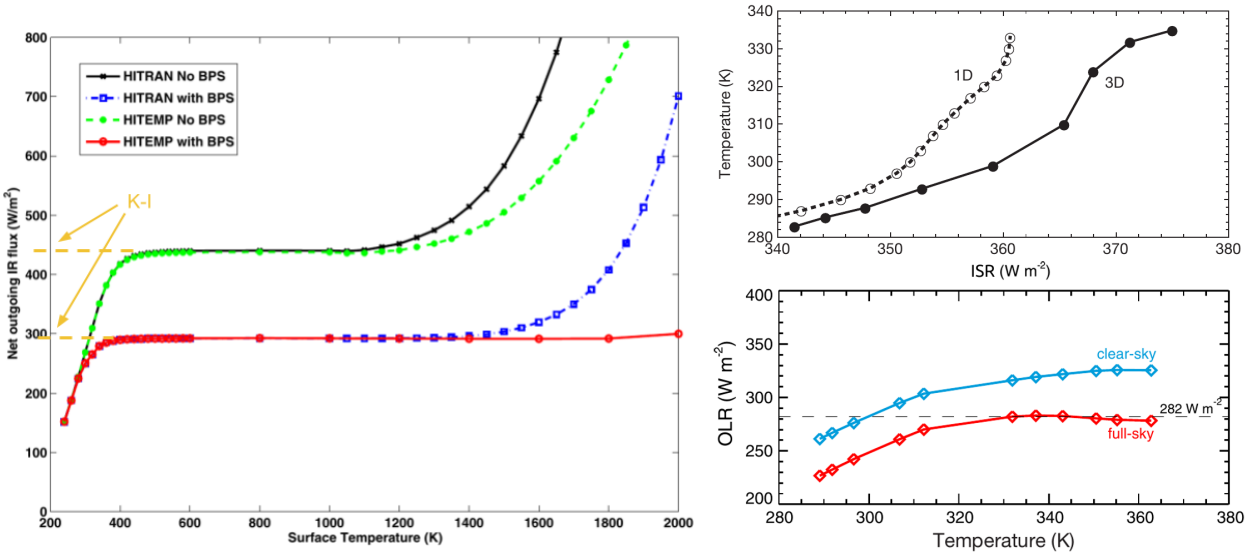

Figure 2.7: The relation between the the OLR and the surface temperature T_s for different models in literature. The onset of the RG state is marked by the decoupling between these two quantities. Left panel: single-column RT calculations by Kopparapu et al. (2013a). Four different models with varying prescriptions regarding water vapor absorption are shown. These models use either the HITRAN 2008 (Rothman et al., 2009) or the HITEMP 2010 (Rothman et al., 2010) spectroscopical databases and either include or not the continuum opacity as modeled by Paynter & Ramaswamy (2011, BPS). In these works *k-correlated* opacity tables have been calculated using KSPECTRUM and while RT calculations have been done using the Kasting (1988) model. Upper right panel: single-column and GCM results by Leconte et al. (2013). Both models use the HITRAN 2008 data for line opacity and the CKD model Clough et al. (1989) for the water vapor continuum. The "3D" and the "1D" curves have been calculated using, respectively, the full LMDG model (Hourdin et al., 2006) and only the RT module of LMDG. Note that in this panel T_s is on the y-axis and it is expressed as a function of the ISR. Lower right panel: GCM results by Wolf & Toon (2015) with either no (clear-sky) or a 100% (full-sky) cloud coverage. They used the Community Earth System Model 1.2 integrated with the LBLRTM (Clough et al., 2005) RT code. Line opacity data comes from HITRAN 2004 (Rothman et al., 2005). The dashed line refers to the RG threshold calculated by Goldblatt et al. (2013).

iting OLR (see Fig. 2.7, left panel and compare also with the dashed line in the upper right panel). As shown by Yang et al. (2016), different H_2O prescriptions can produce variations up to $\sim 10\%$ in the OLR for the typical temperatures at which the RG activates. Since OLR must be in equilibrium with the absorbed radiation, this translates in an equal uncertainty on the ISR. Another problem tied to this is the choice of the correct RH horizontal and vertical distributions. Numerical experiments (Pierrehumbert et al., 2007) showed that on the Earth, due to the horizontal motions of air, the RH is usually below 50%. Observations (Telegadas & London, 1954) show that RH reduces with altitude, starting from relatively high (70-90%) values at the surface and reducing to low values near the tropopause (20%). This is also the case when the atmosphere is perturbed, like during a cyclone (Kunii et al., 2010). Finally, general circulation impacts the horizontal distribution, producing low humidity belts at the poleward ends of the Hadley cells.

There are even stronger uncertainties related to cloud formation and distribution. Clouds

have a double effect on climate, both increasing $\alpha_{\rm TOA}$ (thus reducing the absorbed stellar radiation) and decreasing the OLR. The net forcing can go both ways and depends on the height and width of the cloud deck, the average particle size and the interaction with other cloud decks and with the surface (Pierrehumbert, 2010, cap. 5.8). As an example, high clouds over a high albedo region have a net warming effect, due to the way the cloud albedo combines with the surface albedo. Another aspect of the problem is the fact that cloud formation depends on microphysical mechanisms that are not fully understood. In order to form, clouds require either the presence of condensation nuclei such as dust, volcanic ash or water droplets from the ocean's surface or a strongly super-saturated air[8] (RH=800% for Earth-like conditions, see e.g. Helling, 2019). Also the biosphere seems to contribute to cloud formation via the release of sulphate compounds (most notably, dimethyl sulphide) that can, again, act as condensation nuclei (Charlson et al., 1987; Rap et al., 2013; Park et al., 2021). This is especially true under conditions that are far different from those present on the current Earth, as at the inception of the RG. Differences in cloud models strongly impact the outcome of 3-D GCM simulations, producing discordant results about the RG threshold. This can be seen in the two right panels of Fig. 2.7. For the Earth, Leconte et al. (2013) found it to be equal to ∼375 $\rm Wm^{-2}$ (upper panel, rightmost point of the solid curve), while Wolf & Toon (2015) found it equal to ∼415 $\rm Wm^{-2}$. These values are respectively 10.1% and 21.9% higher than the current Earth insolation of 340.5 $\rm Wm^{-2}$ (also called the Solar constant or $S_{\odot}$). The lower panel shows the impact of cloud cover in the Wolf & Toon (2015) model, which is ∼60 $\rm Wm^{-2}$ or 20% of the total OLR near the RG limit. Very recently, Turbet et al. (2021) demonstrated that the differential cloud formation on the day and night-side of a planet with an already steam-rich atmosphere (formed e.g. during planetary accretion or as a consequence of a large asteroid impact) can account for a net forcing of up to 120 $\rm Wm^{-2}$, potentially placing the planet in the very hot, steamy state produced by RG even if stellar irradiation is 8% below that of the current Earth (at 312 $\rm Wm^{-2}$).

The RG limit is also influenced by the stellar SED, given that shortwave photons are preferentially Rayleigh-scattered by the atmosphere. As such, the bluer spectrum of a more massive star allows for a higher insolation before the transition to this unstable state. Kopparapu et al. (2013a) calculated that the RG limit changes by nearly 20% with respect of their cloud-free single column calculations for an Earth analog (at 1.05 $S_{\odot}$), changing from ∼1.21 $S_{\odot}$ for a star with an effective temperature of 7000 K (F0) to ∼0.85 $S_{\odot}$ for one with 2500 K (M9).

Another, less destructive type of water vapor feedback-influenced state is the so called Moist Greenhouse (MG, Kasting et al., 1993b). The MG is a warm climate state that precedes the RG, in which the water-rich atmosphere is below the K-I limit (thus thermally stable) but subject to a large amount of water loss to space. This happens because of the disappearance of the cold trap at the tropopause, which lets a considerable amount of H_2O to seep into upper stratosphere, where it can be photodissociated. The MG insolation limit is calculated considering the rate of water loss that would dissipate the entire Earth inventory of water over 4.5 Gyr and further increases of insolation would speed up the process to less than a Gyr (Gómez-Leal et al., 2018). The single-column calculations of Kopparapu et al. (2013a)

[8]The condensation curve found by using the Clausius-Clapeyron relation (see Chapter 3) is exact when the surface tension of the liquid that forms from the phase transition is zero, which is true e.g. when we consider the deposition of water molecules on a flat surface. If we study the formation of a spherical droplet in the free air, this is no longer true. The extra energy required takes the form of a higher partial pressure required for condensation.

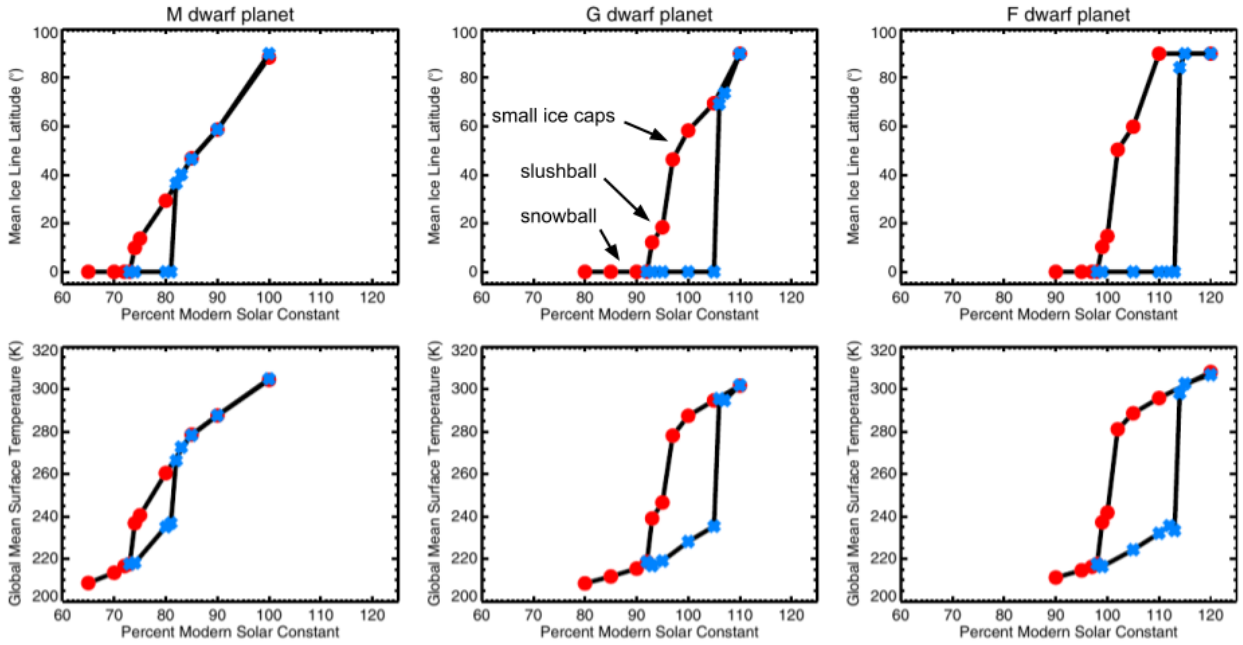

Figure 2.8: Hysteresis loops in the T_s-$\mathcal{I}$ (lower panels) and ice line-$\mathcal{I}$ (upper panels) for an Earth analog illuminated by AD Leonis (M3.5) on the left, by the Sun (G2) on the centre and by σ Bootis (F4). Red dots and blue asterisks correspond, respectively, to simulation runs with a warm start where insolation has been progressively reduced and runs with a cold start where insolation has been progressively increased. Credit: Shields et al. (2014).

produced a MG state at 1.015 $S_\odot$, while GCM models tend to give higher values, from 1.15 $S_\odot$ (Gómez-Leal et al., 2018) to 1.19 $S_\odot$ (Wolf & Toon, 2015). As for the RG limit, also the MG limit is influenced by the stellar SED, with redder stars able to induce it at lower levels of insolation.

Under the current Earth conditions, the water vapor feedback is stronger than the Planck feedback in the tropical regions but not globally, meaning that it cannot transition the planet to a RG state. Analyzing the Earth data about the El Niño Southern Oscillation (ENSO) events, which is a periodical change in the wind patterns of the South Pacific, Dessler & Wong (2009) found a value for the water vapor feedback parameter $\lambda_{\rm wv}$ in the range of 3.7-4.7 $\mathrm{Wm^{-2}K^{-1}}$ in the short term (a year). On the other hand, GCM simulations of century-long global warming (Soden & Held, 2006) found a lower value, in the range of 1.6-2.1 $\mathrm{Wm^{-2}K^{-1}}$.

2.4.2 Ice-albedo feedback and the climate multi-stability

Liquid water has generally a very low albedo (0.02 when hit perpendicularly by light, Huang et al., 2019), but when temperature drops and it solidifies into ice, it becomes far more reflective. Depending on the width of the glaciated layer, its albedo transitions rapidly from that of the liquid water to ∼0.6 for a 30 cm-thick ice (Pirazzini et al., 2006). As such, a positive feedback loop emerges, where low temperatures favors the formation of a reflective layer of ice that further reduces the temperature. The lowering of the surface temperature reverberates along the atmospheric column, condensing out water vapor in form of snow, which has an even higher albedo (up to 0.97 in the visible for fresh, dry snow, Hannula & Pulliainen, 2019). On a planetary level, the growth of the ice caps caused by any decrease in

the average T_s progressively reduces the absorbed solar radiation by increasing $\alpha_{\rm TOA}$ term. At high latitudes, the increase of the ice coverage has a negligible impact on the total radiation absorbed, due to the fact that only a small part of the total stellar radiation $\mathcal{I}$ impinges on the poles. However, as the ice caps extend to lower latitudes, an increasing fraction of $\mathcal{I}$ is reflected back into space. This further reduce T_s. There exists a limiting value of the ice caps extension that, if overstepped, causes a rapid transition into a completely glaciated state with very low surface temperatures called Snowball State. The limiting value for the ice line[9] varies from $\sim 50^o$ of latitude in the simplest EBMs (Budyko, 1969; Sellers, 1969) to 30-35^o in more sophisticated EBMs (Caldeira & Kasting, 1992; Ikeda & Tajika, 1999; Shields et al., 2013). In 3-D GCMs (Shields et al., 2013) the glaciation process is slightly smoother, with a first rapid increase of the ice caps extension from 50^o to 15^o and a second equally rapid one to the true Snowball. The intermediate state with large ice shelves and a small, deglaciated equatorial band is known as Slushball (Fairchild & Kennedy, 2007). The estimated decrease in $\mathcal{I}$ that gives rise to this state ranges from 3% (Budyko, 1969) to 10% (Shields et al., 2013) in both EBMs and GCMs, and depends on the details of the meridional transport and ice albedo modelization. This is also strongly influenced by the SED of the incoming light, with cooler, redder stars able to sustain a partially ice-free state at lower levels of $\mathcal{I}$ ($\sim 0.75\ S_\odot$) than hotter, bluer ones (Shields et al., 2014).

Once completely glaciated, an Earth analog would exhibit a very low surface temperature even at current levels of insolation and atmospheric GHGs because of the high surface albedo. In order to deglaciate, it would need a strong increase in the radiative forcing and when such a condition is met, a rapid transition would occur to a completely (or nearly completely) ice-free, high-temperature planet. This behaviour produce an hysteresis loop in the T_s-$\mathcal{I}$ plane and the coexistence of multiple stable climate states for a given value of insolation is known as climate multi-stability (see Fig. 2.8). The climate state of the planet would then be determined by its past temperature and the transitions between one state to another would be the product of strong, large scale upsets. Concerning the Earth, one of these upsets could have been the Great Oxidation Event (GOE, Holland, 2002), when oxygen mixing ratio in the Earth atmosphere increased from that of a trace gas (1-10 ppm) to several thousands ppm ($\sim$1% of the present atmospheric level or PAL) due to the combined effects of the spread of oxygenic photosynthetic organisms, the saturation of surface oxygen sinks, the decreased emissions of reducing gases from the mantle and the increased burial of organic carbon (Lyons et al., 2014). The presence of oxygen sharply reduced the lifetime of atmospheric CH_4 and thus its concentration, triggering a Snowball state known as Huronian or Paleoproterozoic glaciation (Kirschvink, 1992; Evans et al., 1997) between 2.4 and 2.1 Gyr ago. Subsequently, the planet would have exited from the Snowball state thanks to the collapse of the oxygen-producing biosphere and the accumulation of CO_2 and CH_4 in the atmosphere (Teitler et al., 2014), even though the concentrations needed are hotly debated (Pierrehumbert, 2005, discussed this problem in relation to the Neoproterozoic Snowball glaciations, between 1.0 and 0.54 Gyr ago).

Under the current Earth conditions, the ice-albedo feedback is relatively small with respect to the Planck or to the water vapor feedback. Using data and modeling employed for climate change calculations in the IPCC 4$^{\rm th}$ Assessment Report, Winton (2006) has estimated it to be equal to 0.2-0.4 $\rm Wm^{-2}K^{-1}$.

Ice-albedo feedback is not the only mechanism that can generate climate multi-stability. In fact, all positive feedbacks are associated with tipping points and act as attractors toward

[9]The minimum latitude at which permanent ice is found.

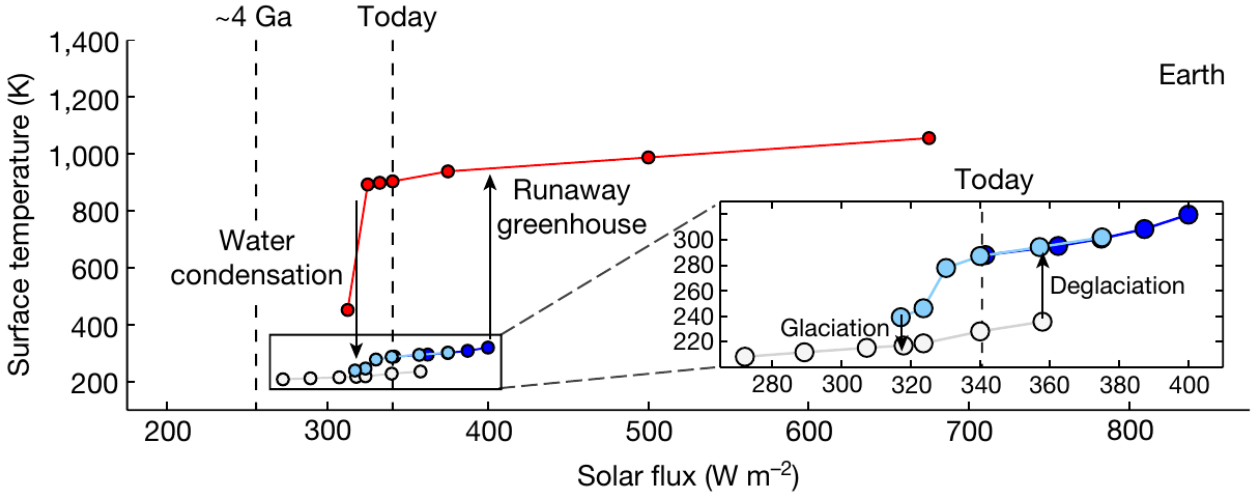

Figure 2.9: Hysteresis loops in the T_s-$\mathcal{I}$ for an Earth analog. Blue points are taken from Leconte et al. (2013), azure and white points are taken from Shields et al. (2014) and represent the deglaciated and the Snowball branches, respectively. Credit: Turbet et al. (2021).

specific climate states. An example is the already mentioned differential cloud formation on day and night side of hot planets with H_2O dominated atmospheres. Turbet et al. (2021) showed that at current levels of insolation, Earth has actually three stable states: a Snowball state, a temperate state and a very hot and steamy state in which the water reservoir is completely vaporized (see Fig. 2.9). Other surface-atmosphere feedbacks, related to the growth of a vegetation canopy, have been invoked to explain local climate multi-stability in arid and semi-arid regions of Earth (Charney et al., 1975; Baudena et al., 2008). In this case, both the surface albedo and the hydrological cycle are modified by the runaway growth (or collapse) of the plant cover. This concept has subsequently been applied also to an entire planet, showing that this kind of feedback can influence the global climate (Cresto Aleina et al., 2013).

2.4.3 Maximum greenhouse and the outer edge of the CHZ

At variance with the inner edge of the CHZ, for which an uncontrollable water vapor feedback is sufficient to doom life as we know it, the outer edge of the CHZ is not defined solely by the conditions that induce the complete glaciation of the planet. In other words, the ice-albedo feedback is not sufficient by itself to cause the complete extinction of life, as it is testified by the numerous Snowball states that Earth very likely endured. In fact, if a sufficient amount of GHGs accumulate in the atmosphere, the Snowball state can be reverted. During a Snowball state this is likely to occur, given the strongly reduced silicate weathering and biological activity on one end, and the nearly constant emission of volcanic gases on the other. Therefore, the question becomes how much radiative forcing can be produced by the atmospheric GHGs. In principle, this could be extremely large, making even free-floating planets able to sustain surface liquid water by geothermal flux alone thanks to thousands of bars of H_2 (Stevenson, 1999). However, a more realistic scenario for Earth-like, star-bound planets involving CO_2-dominated atmospheres has a stringent upper limit to the maximum greenhouse that can be produced due to combination of two factors, namely the condensation of CO_2, that limits the amount of gas that can be present in the atmospheric column, and the increased α_{TOA} due to Rayleigh scattering and CO_2 clouds formation. The former limit is encountered at a surface

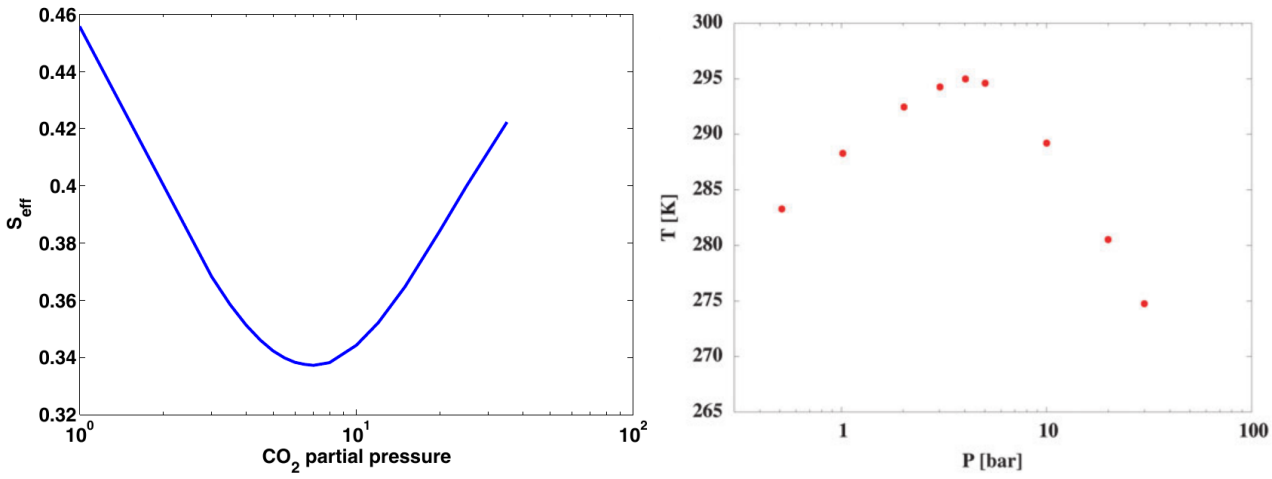

Figure 2.10: Left panel: the insolation (in $S_\odot$ units) necessary to maintain a surface temperature above 273 K for a 1-bar N_2 atmosphere with a variable amount of CO_2 and a 100% H_2O relative humidity, as calculated by Kopparapu et al. (2013a). Right panel: the surface temperature as a function of the surface pressure for an Earth-like atmosphere at fixed insolation of 1.0 $S_\odot$, as calculated by Keles et al. (2018).

CO_2 partial pressure of 34.7 bar, which corresponds to the saturation pressure at the freezing point of water. Adding further CO_2 would led to surface-level condensation without any increase in the greenhouse forcing. The latter concerns the fact that CO_2 is a very efficient Rayleigh scatterer. This causes the $\alpha_{\rm TOA}$ to increase nearly linearly with $\log P_s$ while the OLR forcing reaches an asymptote at around 10 bars due to complete saturation of the infrared absorption bands. At that point, any addition of CO_2 to the atmosphere decreases the absorbed solar radiation without decreasing the OLR, thus cooling the surface. This is shown in Fig. 2.10, left panel, from which is clear that any increase in the CO_2 pressure above $\sim$8 bar actually decreases the surface temperature due to the increased Rayleigh scattering. The minimum of the curve in known as Maximum Greenhouse (MG) and is usually taken as definition of the outer edge of the CHZ. Kasting et al. (1993b) found a value of 0.36 $S_\odot$ for the MG limit, a value confirmed also by Kopparapu et al. (2013a,b) using updated RT prescriptions. Both of these models were clear-sky and referred to an Earth-like planet in orbit around a Sun-like star. Including the effect of clouds further complicates the problem. First of all, they increase the $\alpha_{\rm TOA}$, thus helping to reduce the absorbed stellar radiation. However, despite being largely transparent in the infrared, CO_2 droplets and ice particles are efficient at scattering thermal radiation and as such can lead to a decrease of the OLR. The latter effect seems to be larger in magnitude, thus lowering the MG limits in models that include clouds. Forget & Pierrehumbert (1997) found an outer CHZ edge for the solar system at 2.4 AU, corresponding to $\sim$0.17 $S_\odot$, while Kitzmann (2017) revised it upward to $\sim$0.25 $S_\odot$.

The MG values reported above refer to an atmosphere where CO_2 and H_2O are the only infrared active gases. However, even small concentrations of other GHGs can contribute to expand outward the HZ by further reducing the OLR. The challenges in this case are (i) finding what equilibrium concentrations can be reached in a realistic scenario and (ii) analyzing the compatibility of these scenarios with the evolution of life-as-we-know-it. Ramirez & Kaltenegger (2017) studied the effect of volcanically released H_2 and shown that the outer edge can be extended up to 2.2 AU (0.20 $S_\odot$) under realistic assumptions regarding the

chemical state of early Mars and Earth mantles and a diffusion-limited hydrogen escape to space. According to their calculations, in the case of an Earth-like planet the MG conditions are reached in a ∼2.86 bar atmosphere with 1 bar of CO_2, 1 bar of N_2 and ∼0.86 bar of H_2 (30% of the dry part). They also calculated the increase in HZ width for different stellar spectral types, concluding that it amounts to 30-60% for M-A type stars (early-type being more advantaged). Ramirez & Kaltenegger (2018) analyzed instead the influence of CH_4, finding that it can widen the HZ up to 1.81 AU. This value has been found for a MG atmosphere with a methane partial pressure equal to 10% that of CO_2, which is near the lower limit for the formation of organic hazes (Trainer et al., 2006; DeWitt et al., 2009) that would increase TOA albedo, thus offsetting the greenhouse effect. Again, the increase is larger for hotter stars, while for stars cooler than 4500 K (mid-K type) the anti-greenhouse effect produced by methane absorption of the IR portion of the incoming stellar light actually shrinks the HZ. The maximum change in the position of the HZ outer edge is in the order of ∼20% in both cases. However, subsequent laboratory measurements by Turbet et al. (2019) showed that Ramirez & Kaltenegger (2018) overestimated the CO_2-CH_4 far-infrared absorption, thus producing an HZ outer limit which is too high. While hazes tend to reduce the absorbed stellar radiation, photochemically-produced organic molecules at ∼0.1 CH_4/CO_2 ratio such as ethane (C_2H_6) can help heating up the planet further, as shown by Haqq-Misra et al. (2008). Finally, Airapetian et al. (2016) calculated the equilibrium concentrations for an early Earth (N_2-CO_2-CH_4) atmosphere of nitrous oxide (N_2O) and hydrogen cyanide (HCN), as produced by the increased UV flux of the young Sun. Despite being present in small (few ppms at maximum) concentrations, they can still reduce the OLR by several Wm^{-2}, moving outward the HZ edge in the early phases of the planetary system life.

The presence of a clear minimum in the insolation required to maintain a given temperature on the planetary surface (or the presence of a maximum in T_s for a given insolation) as a function of pressure is not a feature unique to CO_2-dominated atmospheres. Keles et al. (2018) showed that this happens also for Earth-like, nitrogen-dominated atmospheres. In Fig. 2.10, right panel, the surface temperature variation as a function of the surface pressure is shown. It should be borne in mind that also GHGs (especially CO_2, CH_4 and N_2O) have been scaled with pressure, properly accounting for equilibrium chemistry at substantially different pressures than that of the real Earth. In this case, the maximum greenhouse is reached at 4 bars.

Chapter 3

Atmospheric radiative transfer

In this Chapter I will backtrack the path that, from line strengths and shapes obtained from spectroscopic repositories like HITRAN, leads to the solution of the RT equation. I begin with a very brief overview of the two main radiative transfer paradigms, namely the line-by-line and the k-correlated methods. Then I introduce the mathematical framework within which HELIOS and HELIOS-K operate, as described in their respective papers (cited below). I describe how scattering and absorption cross sections are calculated from the HITRAN line parameters. Finally, I present how the absorption continuum, which is the extra opacity that cannot be explained solely by absorption lines, has been calculated for two important molecular species, namely CO_2 and H_2O.

The second section of this Chapter lists in detail my contributions to the radiative transfer calculation procedure presented in this Thesis.

3.1 Radiative transfer models

The planetary energy budget plays the biggest role in determining the general physical state of a planet, as it has been shown in Chapter 2. This budget depends on three quantities: the Incoming Shortwave Radiation, the Outgoing Longwave Radiation and the Top-Of-Atmosphere albedo. The ISR depends on the orbital parameters of the planet and the physical characteristics of the host star. The OLR and the TOA albedo, on the other hand, depend on the radiative transfer (RT) properties of the atmosphere (and of the surface, for the latter). ISR and OLR are slightly misleading terms, given that the first one also includes the power emitted by the star as infrared radiation, and the second one may include a significant visible light component if the considered planet is very hot. Anyway, it is evident that the RT plays an essential role in both EBMs and GCMs models. The modelization of the atmospheric RT is also essential for achieving one of the main goals of present-day astronomy, namely to retrieve the chemical composition of exoplanetary atmospheres from their spectra (Madhusudhan et al., 2011; Line et al., 2013).

There exists a variety of specialized RT codes (Briegleb, 1992; Clough et al., 2005) and each of them carry on its task differently, but there are two main strategies: the opacity calculation is performed either on a small number of broad spectral bands via the k-distribution method (Goody et al., 1989; Lacis & Oinas, 1991), or line-by-line. In the latter case, the opacity is directly evaluated at each point in frequency while in the former case the spectrum is divided into several bands and a Lebesgue integration on the cumulative distribution function of the opacity inside each band is performed to derive an average value. The advantage of the

k-distribution method is computational: in the line-by-line case, the profiles of $10^5 - 10^6$ lines must be calculated on a very fine frequency grid with potentially $10^7 - 10^8$ points, which requires a lot of computational power and storage space. However, while being sound and solid, the k-distribution method cannot reach the accuracy of line-by-line calculations. Regardless of the specific strategy used to attain it, the goal of RT codes is to compute the transmission function of the atmosphere, usually dominated by Rayleigh scattering in the optical region and by absorption in the infrared region.

My PhD work consisted in adapting the GPU-based codes HELIOS (Malik et al., 2017, 2019a,b) and HELIOS-K (Grimm & Heng, 2015; Grimm et al., 2021) for studying Earth-like planets. These codes are part of the Exoclimes Simulation Platform (ESP[1]) of the University of Bern and were originally devised for the study of hot Jupiter-like planets. HELIOS-K is an opacity calculation tool that can operate both in line-by-line and in k-distribution mode, producing opacity functions from line lists provided by repositories such as HITRAN[2] (Gordon et al., 2022), HITEMP[3] (Rothman et al., 2010), ExoMol[4] (Tennyson et al., 2020), Kurucz (Kurucz & Bell, 1995), NIST (Kramida et al., 2019) and VALD3[5] (Ryabchikova et al., 2015). The output of HELIOS-K can then be used in HELIOS, which is a one-dimensional atmospheric RT code operating in the two-stream approximation. The specific goal of this part of the work is to calculate the OLR and the TOA albedo for atmospheric compositions of interest for studies of planetary habitability. In practice, we optimized the calculations for planetary atmospheres with variable amounts of H_2O, CO_2, CH_4, O_2, and N_2, taking into account upgraded formulations for the line and continuum opacities. Where these codes lacked the appropriate physical recipes, we introduced them by adding custom-built scripts. Since this new procedure derives from HELIOS, which is named after the Greek god of Sun, we chose for it the name EOS, as the goddess of Dawn and one of the sisters of Helios.

3.2 The EOS procedure

EOS is not a single code, but rather a set of codes that works together to produce the desired result from physically sensible inputs. As such, in this thesis EOS is referred to as a "procedure". The central and most important components of this procedure are the opacity calculator HELIOS-K and the radiative transfer code HELIOS, which are then complemented by (i) a script for the addition of the continuum absorption features described in Section 3.6, (ii) several atmospheric P-T profile generators that make use of the equation presented in Section 2.2, (iii) a chemical abundances calculator, (iv) post-processing analysis tools for calculating the OLR and the TOA albedo and (v) an infrastructure of wrappers to run efficiently the entire pipeline of codes. Moreover, HELIOS has been modified with respect of the publicly available version in the ESP repository in order to better suit the needs of this study. The most relevant change concerns the expansion of the set of species for which Rayleigh scattering cross-sections are computed. Other minor modifications regard the hard-coded structure of the grids over which the calculations are performed and the output format. Fig. 3.1 summarizes the steps in the EOS procedure and underlines their paternity. The physical recipes regarding the atmospheric profile and chemical composition implemented in

[1] https://github.com/exoclime
[2] https://hitran.org/
[3] https://hitran.org/hitemp/
[4] https://www.exomol.com/
[5] https://http://vald.astro.uu.se//

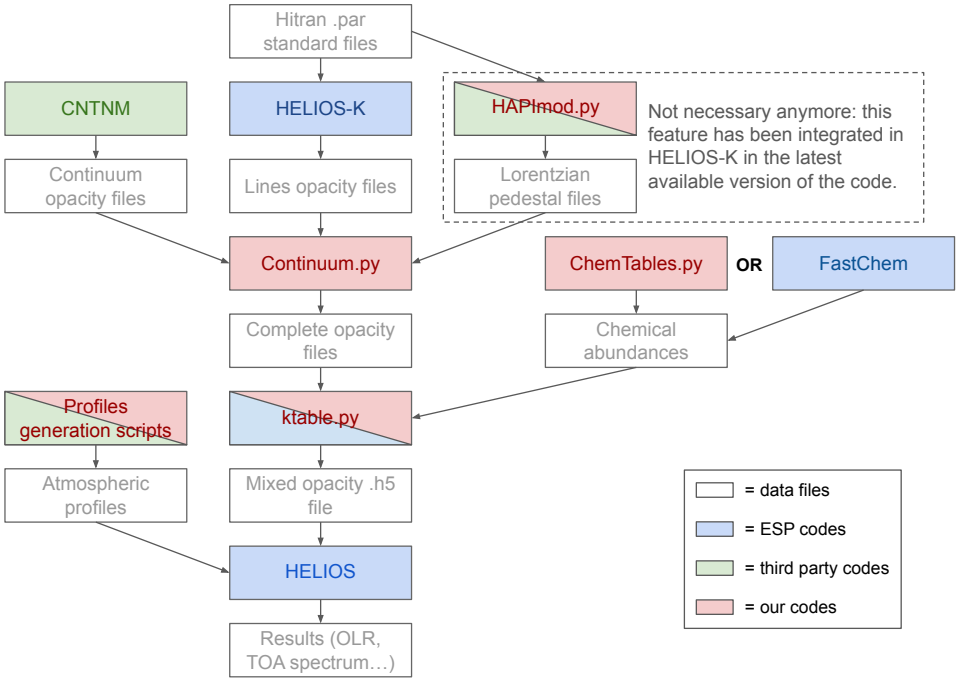

Figure 3.1: The workflow of EOS procedure to generate TOA fluxes for terrestrial-type atmospheres with HELIOS. The color-code is described in the legend of the figure. Double-colored cells refer to codes that have been developed by others but modified by us. The third party codes used are: CNTNM (a module of LBLRTM, see Clough et al., 2005), HAPI (Kochanov et al., 2016) and the MoistAdiabat class in the CliMT suite by Rodrigo Caballero.

this procedure have been introduced in Chapter 2, while those regarding the radiative transfer properties of the gas are reported in the next sections of this Chapter. The computational steps of EOS are briefly described below.

As a first step, we download the line parameters and the partition function files from HITRAN2016 (Gordon et al., 2017) for the following species of interest: H_2O, CO_2, CH_4, O_2 and N_2. These data are then used by HELIOS-K to calculate the absorption coefficients required in the subsequent part of the procedure. Both self- and foreign-broadening due to gas pressure has been evaluated by specifying the correct mixing ratio, but it must be kept in mind that foreign-broadening data in HITRAN are calculated using dry air as background gas. This means that it is actually evaluated for a nitrogen-oxygen background, which make results for CO_2-dominated atmosphere uncertain in principle. However, no better alternatives are available. For H_2O, CH_4, O_2 and N_2 I used Voigt profiles truncated at 25 cm^{-1}, while for CO_2 I tested several options: (i) a pure Voigt profile truncated at 25 cm^{-1}, (ii) a sub-Lorentzian profile using the parameters given by Perrin & Hartmann (1989) truncated at 500 cm^{-1} and (iii) a sub-Lorentzian profile using the parameters of Tonkov et al. (1996) truncated at 350 cm^{-1} (as indicated in their paper). When modeling Earth-like atmospheres, we used only the first setup, while for CO_2-rich and -dominated atmospheres we tested all three possibilities and adopted the option (ii) as a reference, as it is generally done in literature. Moreover, CO_2 CIAs has been calculated assuming this kind of profile for CO_2 lines, thus this choice is necessary to assure self-consistency.

As a second step, we add the CO_2 and the H_2O continua to the respective species files, calculated as described in Section 3.6.1 and 3.6.2. This is done via the script Continuum.

As a technical note, we remark that the H_2O continuum, as calculated by the MT-CKD model, includes the so-called Lorentzian pedestals, which therefore must be subtracted from the absorption coefficient of the lines. The Lorentzian pedestal of a line corresponds to the absorption coefficient of that line at 25 cm^{-1} from its centre. Previous versions of HELIOS-K did not have a built-in option for this subtraction, therefore we modified the HAPI (HITRAN Application Programming Interface)[6] script to calculate the Lorentzian pedestals from the `.par` standard line parameters file. We called it HAPImod. The latest version of HELIOS-K integrates this calculation and as such, HAPImod is no longer needed. The results obtained via the two different calculations are the same, thus adding robustness to this treatment. Details on the gas opacity calculations will be given in Section 3.5.

As a third step, we use the HELIOS tool ktable to produce line-by-line mixed opacity tables in the 0-30000 cm^{-1} range and with a $\lambda/\Delta\lambda$ resolution of 3000. We tested two main sets of atmospheres: (i) an Earth-like one, dominated by N_2 and O_2 and with CO_2, CH_4 and H_2O as minor components and (ii) a CO_2-dominated atmosphere with H_2O as a minor component. The volume mixing ratios have been calculated on a pressure-temperature grid by the tool ChemTables.

As a fourth step, we launch the main HELIOS code in its *post-processing* mode (that will be described in Section 3.3.1), in which the user can specify the vertical pressure-temperature structure of the atmosphere. This is necessary to ensure full control on the input variables (among others, the surface temperature T_s) needed to produce the OLR and the TOA albedo lookup tables. The vertical structure of the atmosphere is calculated by two sets of codes. For Earth-like atmospheres, we integrate Eq. 2.24 using the MoistAdiabat class in the CliMT suite by Rodrigo Caballero, also used in Pierrehumbert (2010) and described in Section 2.2.4. Instead, for CO_2-dominated cases, we wrote an ex-novo script that numerically integrated Eq. 2.26, detailed in Section 2.2.5.

Finally, as a fifth step, the bulk quantities in term of top-of-atmosphere fluxes are derived by integrating the results of HELIOS runs, in particular the line-by-line outgoing flux file called TOA_flux_eclipse.

3.3 RT equations in HELIOS

The goal of an atmospheric RT model is to solve the RT equation (Chandrasekar, 1960; Mihalas, 1970):

$$\mu \frac{dI_\lambda}{d\tau_\lambda} = I_\lambda - S_\lambda \tag{3.1}$$

where μ is the cosine of the incoming radiation incident (also called zenith) angle with respect to the normal, I_λ is the monochromatic intensity, τ_λ is the optical depth calculated from TOA and S_λ is the source function that accounts for both the shortwave radiation scattered into the line of sight from other directions and the thermal radiation emitted locally.

The atmosphere is divided in a number of layers and HELIOS calculates the monochromatic fluxes at both interfaces of each atmospheric layer, and in the layer's centre, as shown in the left panel of Fig. 3.2. Absorption and non-isotropic scattering are considered both for the incoming and the outgoing radiation. Each layer has an average temperature and an internal linear temperature gradient. The zenith angle is evaluated considering the sphericity

[6] https://hitran.org/hapi/

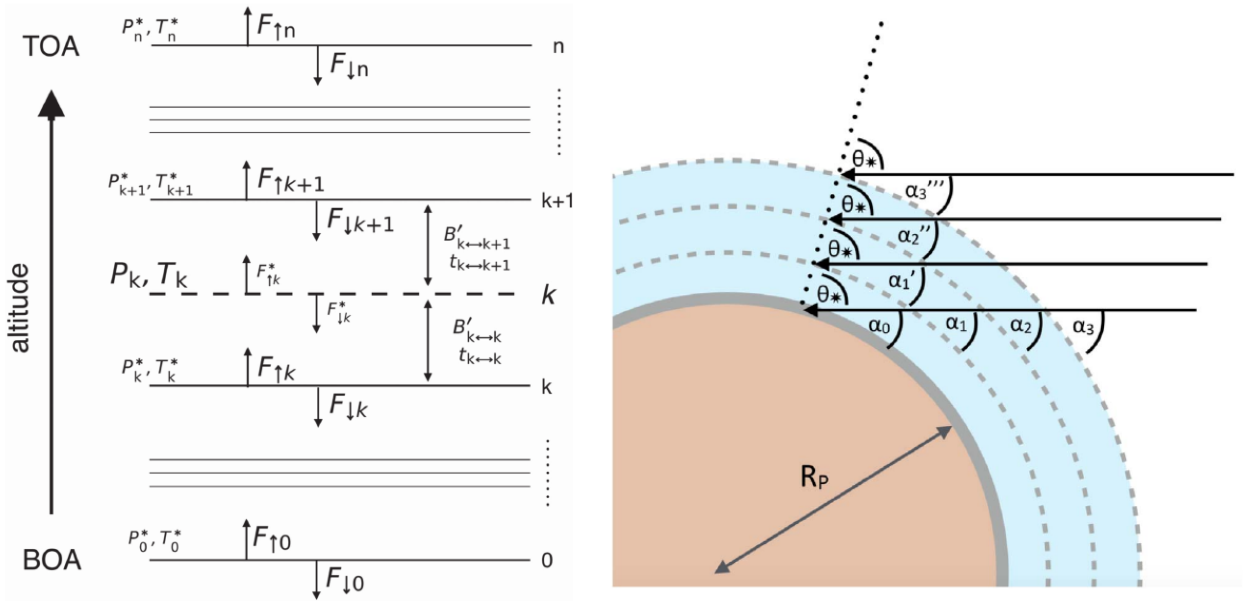

Figure 3.2: Left panel: the atmospheric pressure gird used in HELIOS for RT calculations. Fluxes are evaluated at the interface, while the self-emission is calculated at the layer centre. Credit: Malik et al. (2017). Right panel: the angle at which stellar radiation impinges on the atmosphere, corrected for the sphericity of the planet. Credit: Malik et al. (2019a).

of the planet, thus varies from layer to layer. In particular, it is slightly larger near the surface than at the TOA (right panel of Fig. 3.2). The mathematical treatments for the diffuse (F) and directional ($F^{\rm dir}$) fluxes employed in HELIOS are detailed in Heng et al. (2014) and Heng et al. (2018), respectively. Letting $\mu_\star$ be the cosine of the incoming stellar radiation, the equations for the outgoing ('↑') and incoming ('↓') fluxes at the lower interface of the ith layer are:

$$F_{i,\uparrow} = \frac{1}{\chi}\left(\psi F_{i-1,\uparrow} - \xi F_{i,\downarrow} + 2\pi\epsilon\mathcal{B}_\uparrow + \frac{1}{\mu_\star}\mathcal{I}_\uparrow\right) \tag{3.2}$$

$$F_{i,\downarrow} = \frac{1}{\chi}\left(\psi F_{i+1,\downarrow} - \xi F_{i,\uparrow} + 2\pi\epsilon\mathcal{B}_\downarrow + \frac{1}{\mu_\star}\mathcal{I}_\downarrow\right)$$

where:

$$\mathcal{B}_\uparrow = (\chi+\xi)B_i - \psi B_{i-1} + \frac{\epsilon}{1-\omega_0\, g_0}(\chi-\xi-\psi)B', \tag{3.3}$$

$$\mathcal{I}_\uparrow = \psi\mathcal{G}_+ F_{i-1}^{\rm dir} - (\xi\mathcal{G}_- + \chi\mathcal{G}_+)F_i^{\rm dir},$$

$$\mathcal{B}_\downarrow = (\chi+\xi)B_i - \psi B_{i+1} + \frac{\epsilon}{1-\omega_0\, g_0}(\xi-\chi+\psi)B',$$

$$\mathcal{I}_\downarrow = \psi\mathcal{G}_- F_{i+1}^{\rm dir} - (\chi\mathcal{G}_- + \xi\mathcal{G}_+)F_i^{\rm dir}$$

and B is the blackbody intensity within the layer. Note that there is a typographical error in Eq. (9) of Malik et al. (2019a). In their expression for $\mathcal{B}_\uparrow$, the $-\xi B_{i-1}$ term should be a $-\psi B_{i-1}$. The direct beam flux moves only downward and it is calculated as:

$$F_i^{\rm dir} = -\mu_\star F_\star e^{\tau_i/\mu_\star} \tag{3.4}$$

where $F_\star$ is the ISR, which can be modeled as both a blackbody or a real star spectrum, and τ_i is the optical depth from the TOA to the ith layer. $F_0^{\rm dir}$ is thus the residual direct beam

flux that impacts the planetary surface, of which a fraction P_s (the surface albedo) is reflected in the form of diffuse radiation and the remainder is absorbed. The auxiliary quantities used in Eqs. 3.2 and 3.3 are defined as follows:

$$\chi = \zeta_-^2 \mathcal{T} - \zeta_+^2 \tag{3.5}$$

$$\xi = \zeta_+ \zeta_- (1 - \mathcal{T}^2)$$

$$\psi = (\zeta_-^2 - \zeta_+^2)\mathcal{T}$$

$$\zeta_\pm = \frac{1}{2}\left(1 \pm \sqrt{\frac{1-\omega_0}{1-\omega_0\, g_0}}\right)$$

$$\mathcal{G}_\pm = \frac{1}{2}\left[\mathcal{L}\left(\frac{1}{\epsilon} \pm \frac{1}{\mu_\star(1-\omega_0\, g_0)}\right) \pm \frac{\omega_0\, g_0\, \mu_\star}{1-\omega_0\, g_0}\right]$$

$$\mathcal{L} = \frac{(1-\omega_0)(1-\omega_0\, g_0) - 1}{1/\mu_\star^2 - 1/\epsilon^2 (1-\omega_0)(1-\omega_0\, g_0)}$$

$$B' = \frac{\Delta B}{\Delta \tau}$$

In order to calculate these quantities, four physical variables must be evaluated in each layer, namely ϵ, ω_0, g_0 and $\Delta\tau$. The first one, ϵ, is called first Eddington coefficient and is defined as the ratio between the first and second moment of the intensity. It describes how much diffuse is the radiation and spans the range between 0.5 (fully isotropic) and 1.0 (fully directional on the vertical axis). The second variable, ω_0, is the single-scattering albedo and is defined as $k_{\text{sca}}/(k_{\text{sca}} + k_{\text{abs}})$, where k_{sca} and k_{abs} are the molecular cross sections of the gas mixture for Rayleigh scattering and absorption, respectively. The third variable, g_0, is the asymmetry parameter (see Eq. 2.9) and describes the preferred direction in which radiation is scattered. It spans the range from -1 (fully backward scattering) to +1 (fully forward scattering); if $g_0 = 0$ the scattering is isotropic. Finally, $\Delta\tau$ is the optical thickness of the layer, which is also employed to calculate the transmission function: $\mathcal{T}$:

$$\mathcal{T} = \exp\left[-\epsilon^{-1}\sqrt{(1-\omega_0\, g_0)(1-\omega_0)}\Delta\tau\right] \tag{3.6}$$

The optical thickness is the product of the scattering and absorption cross sections of the gas mixture multiplied by the columnar density u:

$$\tau = (k_{\text{sca}} + k_{\text{abs}})\, u = (k_{\text{sca}} + k_{\text{abs}}) \int_0^l \rho(l')\, dl' \tag{3.7}$$

where ρ is the volumetric density along the geometrical optical path l inside the layer.

In HELIOS, ω_0 and $\Delta\tau$ are calculated on the spot on the basis of the characteristics of the atmosphere, while ϵ and g_0 are kept constant. In particular, we chose $\epsilon = 0.5$ and $g_0 = 0$. The first assumption is justified by the fact that we are dealing with diffuse radiation, both in terms of thermal emission from the planet and the atmosphere (for the calculation of the OLR) and in terms of the light scattered by the air or reflected by the surface (for the calculation of the TOA albedo). This is consistent with the hemispheric mean closure (Toon et al., 1989)[7]. The second assumption is justified by the fact that, in our tests, we considered

[7] A widely used assumption made to close the system of RT equations in the two-stream approximation. Scattered flux is averaged over two hemispheres, corresponding to the forward (to the surface) and backward (to space) directions.

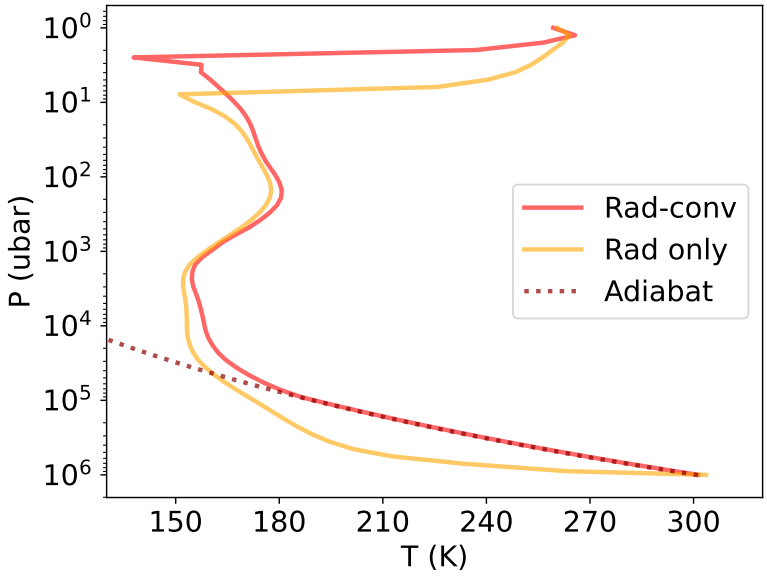

Figure 3.3: Vertical P-T profiles for the tropical Earth atmosphere calculated by HELIOS in *iterative* mode. Yellow line: radiative-only equilibrium (no convection). Red line: radiative-convective equilibrium. Dashed line: convective instability curve (note that it is not a true moist adiabat as calculated in Chapter 2, but has a slope equal to that of a moist adiabat). The tropopause is higher (∼0.01 bar vs ∼0.1 bar) in altitude and far colder (∼160 K vs ∼190 K) than that of the real Earth. This is caused by the lack of ozone in this model.

only the Rayleigh scattering by gas molecules and not the Mie scattering by particulate. In other words, we computed clear-sky results, without considering the effects of clouds or suspended dust. The effect of clouds is added at the level of the climate model (ESTM1 and 2 in this work, see Sections 2.1.2 and 5.1.5).

3.3.1 Operating HELIOS: iterative vs post-processing mode

HELIOS has two main operational modes: the *iterative* one and the *post-processing* one. Under the *iterative* mode, the user must specify an insolation, a zenith angle and a convective lapse rate. The code then tries to find the vertical P-T profile of the atmosphere and the surface temperature in order to balance the OLR with the specified ISR. If, in a given portion of the atmosphere, the temperature difference between two layers exceeds the convective lapse rate, the code automatically adjust it to the latter value. The calculation is iterated (hence the name) up to the point that the entire atmosphere is in radiative-convective equilibrium, thus finding a self-consistent solution for a given insolation. An example of the solutions found in this way can be seen in Fig. 3.3. The radiative-only solution is steeper in the lower, optically thick part of the atmosphere (i.e. the troposphere) and this activates convective motions that put the P-T profile on a moist adiabat. In the upper, thinner part of the atmosphere the radiative-only and the radiative-convective profiles converge and show the inversion due to shortwave absorption. On the other hand, under the *post-processing* mode, the user specifies the vertical P-T profile and the surface temperature and retrieves the TOA spectrum of the planet. No iteration is done to actually find the radiative-convective equilibrium, and the result is not checked for energy conservation neither layer-by-layer nor globally (i.e at

the TOA). This forces the user to be very careful in the selection of the input parameters, that must be physically self-consistent for the situation that they want to simulate. This is particularly evident in the case of the P-T atmospheric profiles, that must be generated to mimick an approximate radiative-convective equilibrium.

Operating HELIOS in *post-processing* mode means to waste part of the potential of the code. In fact, while the imposed P-T atmospheric profiles are built on solid theoretical grounds and a rich literature, they are tied to specific types of atmospheres and, in order to be generalized, would require calculations performed in the *iterative* mode. On the other hand, the *post-processing* mode has two indisputable advantages: (i) it has no convergence problems and (ii) it allows the user a far greater control on the input, especially when the results are intended to be tabulated for subsequent usage in a climate model. In fact, this is necessary if we want to follow the Kasting's *reverse procedure*, in which the OLR and the TOA albedo are calculated as a function of the surface temperature, and then an instellation that satisfy the energy balance is found as a result[8]. For this reason, during my PhD we mainly used HELIOS in this mode. All the results presented here have been obtained in this way. The EOS procedure is not incompatible with the *iterative* mode though, and a methodology that includes both will be the subject of future work.

OLR and TOA albedo calculations were performed by following two different set of steps. Concerning the former, we set a specific surface temperature, P-T vertical atmospheric and compositional profile and turned off the instellation term. Using this input HELIOS calculates the TOA emission spectrum of the planet. Since the thermal emission from the planet is the only contributor to this spectrum, the OLR can be computed by simple integration over the entire wavelength range. This corresponds to the red curve in Fig. 3.4. Concerning the TOA albedo, a few extra steps are required:

(i) We run HELIOS with the instellation term turned off, as we do to calculate the OLR.

(ii) We then run again HELIOS with the instellation term turned on. The TOA emission calculated by HELIOS now includes both the thermal emission from the planet and the reflected light from the star (the yellow curve in Fig. 3.4). The wavelength-independent surface albedo must be specified in this case, since it contributes to the total TOA albedo.

(iii) We subtract the spectrum obtained at (i) to the spectrum obtained at (ii). This difference is the light reflected by the planet as a result of the Rayleigh scattering in the atmosphere and the surface albedo.

(iv) We integrate the subtracted spectrum obtained at (iii) and divide the result for the total instellation. This gives us a TOA albedo that can be utilized in the energy balance equation.

The resultant TOA albedo is expected to be independent of the total instellation, for a fixed SED. This has been verified several times for the current procedure.

[8]The *forward* prodecure would imply to impose a given instellation and then find a surface temperature. While this is the most logic way to proceed, it is actually harder to implement, since the surface temperture enters the energy balance equation only indirectly, through the OLR and the TOA albedo.

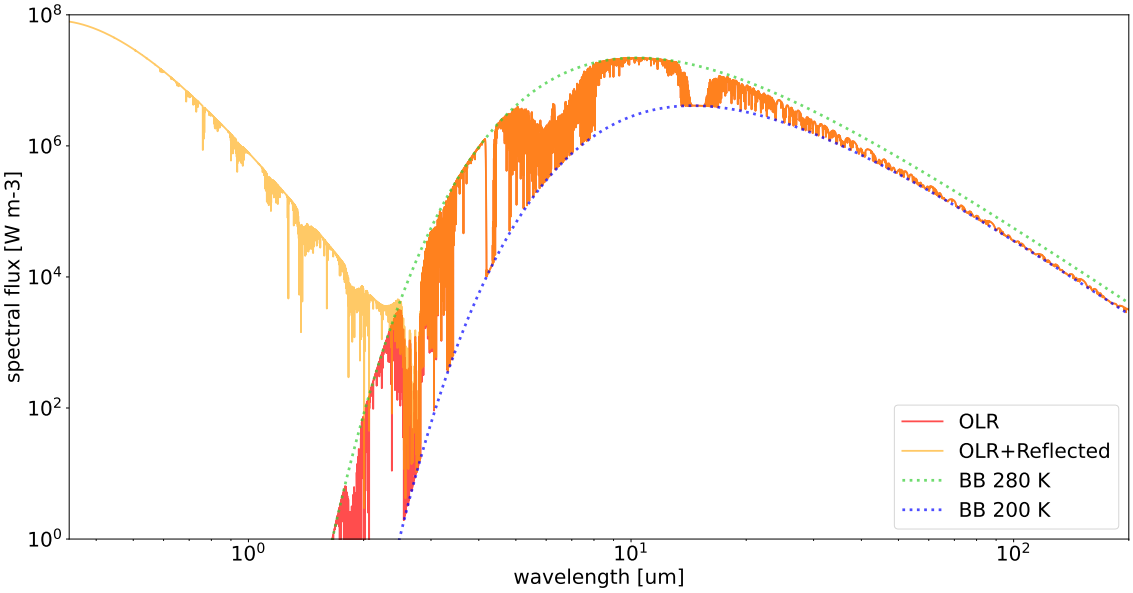

Figure 3.4: Top of atmosphere SED for an Earth-like planet with a surface temperature of 280 K, a tropopause at 200 K and a surf albedo of 0. The red line represents the OLR only, while the yellow line represents the sum of OLR and the reflected stellar radiation due to atmospheric scattering. The dotted lines describes the blackbody curves for a 280 K and a 200 K emitter.

3.4 Scattering cross sections

Since we run clear-sky RT calculations, the scattering opacity of the atmosphere is considered to be entirely caused by the Rayleigh scattering on gas molecules. As described in Sneep & Ubachs (2005), the cross section for this process is:

$$k_{\mathrm{sca}}(\lambda) = \frac{24\pi^3}{n_{\mathrm{ref}}^2 \lambda^4} \left(\frac{\tilde{n}_\lambda^2 - 1}{\tilde{n}_\lambda^2 + 2} \right)^2 K_\lambda \tag{3.8}$$

where $\tilde{n}_\lambda$ is the wavelength-dependent refractive index, n_{ref} is the number density at which the refractive index has been calculated and K_λ is the King depolarization correction factor (King, 1923).

The functional forms for $\tilde{n}_\lambda$ and K_λ are taken from the literature. For N_2, O_2 and CO_2 I referred to Sneep & Ubachs (2005) and Thalman et al. (2014), and for H_2O to Murphy (1977), Schiebener et al. (1990) and Wagner & Kretzschmar (2008). We did not consider the Rayleigh scattering on CH_4 since it has very low concentrations (of the order of one part per billion in volume) or it is absent altogether in the atmospheres that we tested. However, the formulation for CH_4 scattering has been included in the code using the coefficients reported in Sneep & Ubachs (2005) and will be used in future calculations. The dependence of the Rayleigh scattering cross sections used in this work on the wavelength is reported in Fig. 3.5, left panel. It can be noted that the scattering efficiency of CH_4 and CO_2 is ~3 times higher than those of N_2 and O_2. The H_2O scattering efficiency is even lower, and in fact this contribute (together with enhanced absorption) to decrease the clear-sky top-of-atmosphere albedo in warmer water-bearing habitable planets, as it will be shown in the next Chapter.

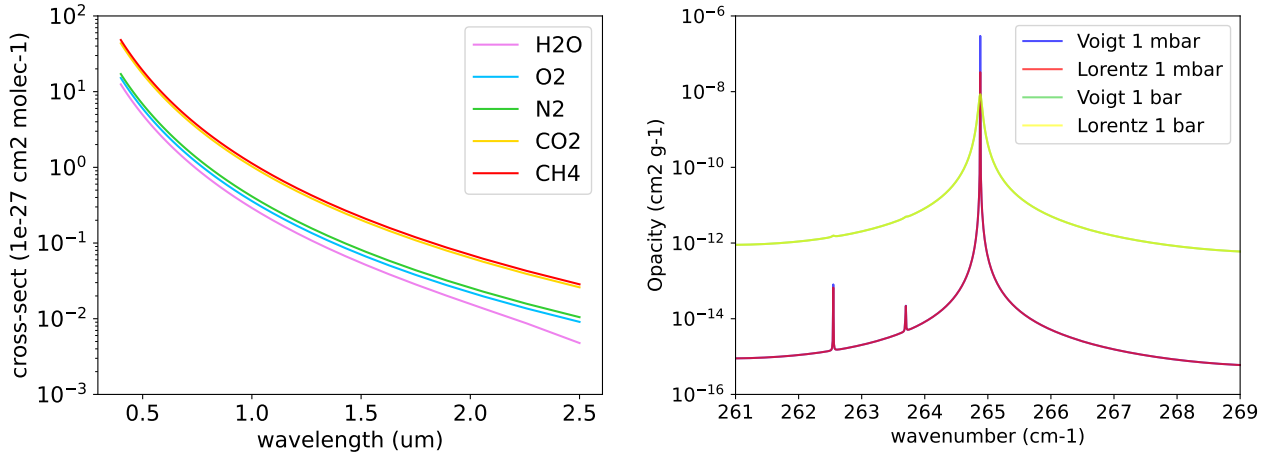

Figure 3.5: Left panel: the Rayleigh scattering cross sections for the molecular species considered in this work as a function of the wavelength. Right panel: the detail of a single self-broadened N_2 line at 300 K calculated using either a Voigt profile for 1 mbar (blue) and 1 bar (green) or a Lorentzian profile for 1 mbar (red) and 1 bar (yellow). The yellow and green lines are nearly perfectly superimposed.

3.5 Absorption cross sections

Photons at frequencies below those of ultraviolet radiation interact with molecules by exciting electrons in the molecular orbitals. When this happens, the photon is absorbed and thus removed by the radiation field. Since electrons can occupy only specific energetic levels inside a molecule, a photon can be absorbed only if its energy is just enough to make the electron jump from its low, stable energy state (the ground state) to its excited, high energy state. Therefore, if a certain volume of gas is illuminated by a beam of photons with different energies, only those that correspond to specific electronic transitions for the chemical species that made up that gas will be removed from the line-of-sight, thus producing dark lines in the light spectrum (absorption lines). Moreover, excited states are not stable and electrons are prone to return to their ground state. If given enough time, the electron de-excites itself by emitting a photon of the same frequency of that absorbed in a random direction. Thus, observing a volume of gas out of the direction of the illuminating beam, it is possible to see bright lines over a dark continuum (emission lines). Excitation and de-excitation can also happen via collision between molecules. As such, a hot gas against a colder background will show emission lines even if no light beams are present. On the other hand, a fraction of the absorbed energy when a radiation field is present is transformed into heat and contributes to increase the temperature of the gas. Finally, de-excitation of an electron can also be stimulated by the presence of a photon with the same frequency of the transition. This process, called stimulated emission, can produce highly monochromatic and coherent radiation beams and constitute the basis of the laser technology. However, in order to be efficient, this process needs a sufficiently large fraction of gas particles in the same excited state, which happens only under peculiar circumstances that are not relevant in our case.

Absorption processes are particularly relevant in the study of planetary atmospheres of cool, Earth-like planets. The probability of a photon of being absorbed when passing through a certain volume of gas is described by the absorption cross section (also called absorption coefficient), which for an individual line centered at frequency ν_0 can be calculated at each

frequency ν as follows:

$$k_{\rm abs}(\nu) = Sf(\nu - \nu_0, \gamma) \tag{3.9}$$

where S is the line strength, $f(\nu_0 - \nu, \gamma)$ is the line shape function and γ, using a formalism employed also in the HITRAN database, takes into account the effects of line broadening due to pressure and temperature effects.

Following e.g. Hill et al. (2013), the line strength S is calculated as:

$$S = \frac{A}{8\pi c\mu}\frac{g'}{\nu_0^2 Q(T)}\exp\left(-\frac{hc}{k_B T}E''\right)\left[1-\exp\left(-\frac{hc}{k_B T}\nu_0\right)\right] \tag{3.10}$$

where A is the Einstein coefficient for spontaneous emission, c is the speed of light, E'' is the energy of the lower-energy state in cm^{-1}, g' is the statistical weight of the upper-energy state, $Q(T)$ is the partition function and h is the Planck constant. The A values tabulated in HITRAN include electric dipole, magnetic dipole and eletric quadrupole transitions.

The line shape function is determined by a mix of intrinsic (related to the specific transition) and external (related to the environment in which that particle is immersed in) factors. First of all, the excited state has a finite duration in time. As such, due to the uncertainty principle, the photons emitted during de-excitation will show a Lorentzian distribution in energy (and thus frequency). This is called natural broadening and depends on the properties of the transition. Second, particles move with velocities distributed as a Maxwell curve. Therefore, the photons are never emitted at rest with respect to the observer and thus are Doppler-shifted. If thermal motion is taken into consideration, the energy distribution will be Gaussian. The line spread due to this phenomenon is called thermal broadening. Third, gas particles collide with each other, exciting and de-exciting in the process. Collisions have a finite duration in time and thus the uncertainty principle applies once more, producing again a Lorentzian distribution. This effect is called pressure broadening.

Depending on the physical state of the gas under study, different effects will dominate, producing different type of line shapes. Extremely thin and hot gas, such as the one found in stellar atmospheres will be dominated by Doppler broadening and will have nearly Gaussian-shaped lines. On the other hand, gases in cool and dense planetary atmospheres show quasi-Lorentzian profiles. In order to account for both the thermal and the pressure broadening and improving the accuracy of the model, it is possible to convolve the Lorentzian and the Gaussian profile, thus obtaining the so-called Voigt profile. For a Voigt profile centered at $\nu = 0$ the equation reads:

$$V(\nu, \sigma, \gamma) = \int_{-\infty}^{+\infty} G(\nu', \sigma) L(\nu - \nu', \gamma) d\nu' \tag{3.11}$$

where:

$$G(\nu, \sigma) = \frac{1}{\sqrt{2\pi\sigma^2}}\exp\frac{-\nu^2}{2\sigma^2} \quad L = (\nu, \gamma)\frac{1}{\pi}\frac{\gamma}{\nu^2 + \gamma^2} \tag{3.12}$$

The Voigt profile is extremely popular in literature for dealing with both planetary and stellar atmospheres (Pierrehumbert, 2010). The integral must be calculated numerically, but reduces to the Lorentzian distribution when the distance from the line centre is larger than few half-widths. The similarity between the Lorentzian and Voigtian profile rapidly increases with pressure, as it is possible to see in the case of N_2 in Fig. 3.5, right panel. Already at 1 mbar the difference between the two profiles can be noted only in the line centre, at $\lesssim$0.1 cm^{-1}, while at 1 bar is practically negligible.

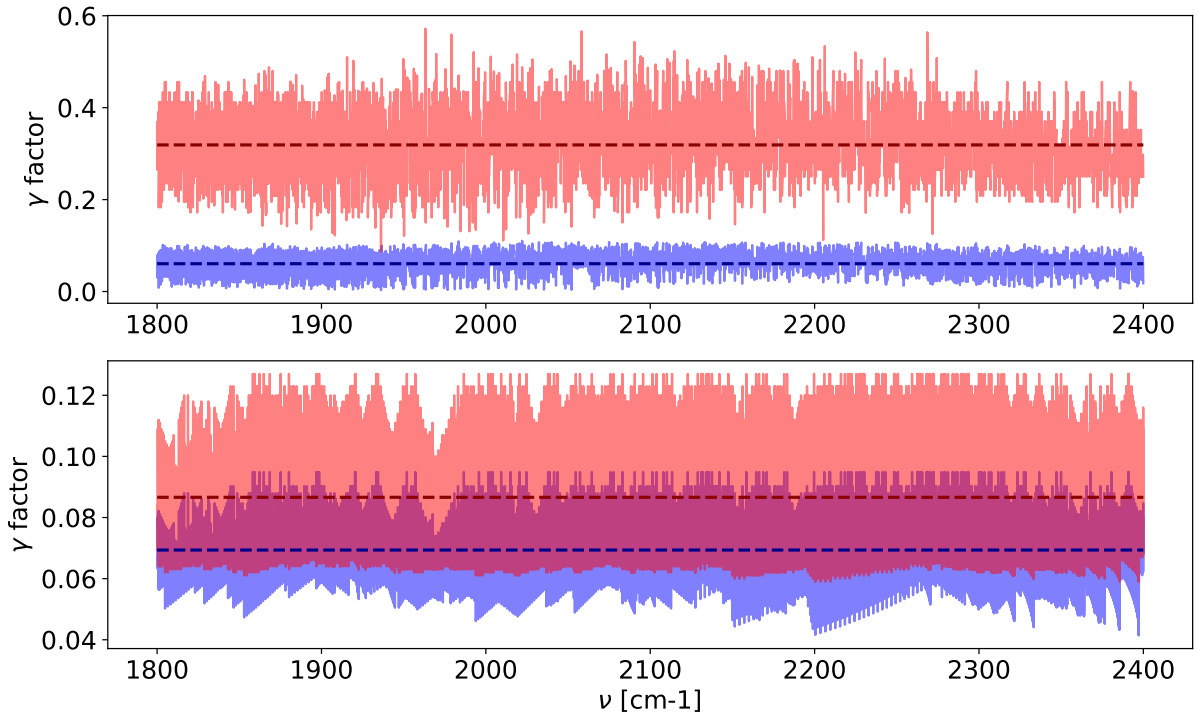

Figure 3.6: The self- (in red) and foreign-pressure (in blue) broadening factors in the 1800-2400 cm^{-1} bands for two important greenhouse gases: H_2O (top panel) and CO_2 (bottom panel). Average values in the considered band are reported as dashed horizontal lines. Note that the y-axis scale is different in the two cases.

There exists also other line shape functions, such as those of van Vleck & Weisskopf (1945), Galatry (1961), Rautian & Sobel'man (1967) and Ngo et al. (2013). These studies have been motivated by the discrepancies between the Voigt profile and the true shapes of isolated lines in several gases (e.g. H_2O, see de Vizia et al., 2011) and made efforts to incorporate several improvements in the line shape treatment. The deviations from the Voigt profile are driven by the effects of velocity changes during and after the collision between molecules and the dependence on speed of broadening parameters. These deviations are especially visible in the wings of the line and could be very important on the bulk absorption of an atmosphere. The deviations from the Voigt profile are especially important in the study of CO_2-dominated atmospheres. A model for the far-wings behaviour of the CO_2 will be presented in Section 3.5.1.

The Lorentzian part of the Voigt profile contains the information regarding the natural and pressure-induced broadening and it is relevant in the study of most of the total gas opacity. Therefore, starting from a few half-widths from the line centre, the absorption coefficient (neglecting the line centre pressure-induced shift) can be effectively written as:

$$k_{\text{abs}}(\nu) = S f_L(\nu - \nu_0, \gamma) = \frac{S}{\pi} \frac{\gamma(P,T)}{\gamma(P,T)^2 + (\nu - \nu_0)^2} \tag{3.13}$$

The factor γ, which is the half-width at half-maximum (HWHM) of the Lorentz distribution,

is then calculated as:

$$\begin{aligned}\gamma(P,T) &= \gamma_{\rm nat} + \gamma_{\rm self}(P,T) + \gamma_{\rm for}(P,T) = \\ &= \frac{A}{4\pi c} + \left(\frac{T}{T_{\rm ref}}\right)^{-n}\left(\tilde{\gamma}_{\rm self}(P_{\rm ref},T_{\rm ref})\frac{P_{\rm self}}{P_{\rm ref}} + \tilde{\gamma}_{\rm for}(P_{\rm ref},T_{\rm ref})\frac{P-P_{\rm self}}{P_{\rm ref}}\right)\end{aligned} \tag{3.14}$$

The first term represents the natural width of the line, while the second and the third terms represent the pressure broadening due to collisions with molecules of the same species and collision with molecules of other species, respectively. These last two terms are given for a reference temperature $T_{\rm ref}$ and pressure $P_{\rm ref}$ and scaled to other P and T values according to the equation. Both the broadening coefficents $\tilde{\gamma}$ and the exponent n are empirical and derived from laboratory measurements.

It must be noted that, in theory, each couple of molecules has its own $\tilde{\gamma}$ value, and as such the $\tilde{\gamma}_{\rm for}$ term should really be a summation over all the possible binary combinations of species in the considered mixture, weighted by their molar fractions. However, even the calculation for a relatively simple mixture of gas would require a large number of laboratory measurements that are not currently available. Therefore, publicly available repositories usually give only a single value for $\tilde{\gamma}_{\rm for}$, derived in the case of dry Earth air. This is the case, for example, of the standard HITRAN tables in the `.par` format (Rothman et al., 2005) read by HELIOS-K. A side effect of this lack of data is the fact that it is useless to calculate the opacity of N_2 under different mixing ratios, since $\tilde{\gamma}_{\rm for}$ is nearly equal to $\tilde{\gamma}_{\rm self}$ for it. Concerning the other gases, *foreign broadening* is basically equal to *broadening under a N_2 atmosphere*. Despite having only a single $\tilde{\gamma}_{\rm for}$ value, it is still important to set the mixing ratio correctly during HELIOS-K opacity calculations. As it is possible to see in Fig. 3.6, differences between self- and foreign-induced pressure broadening are quite large. In particular, for H_2O the $\tilde{\gamma}_{\rm self}/\tilde{\gamma}_{\rm for}$ ratio is $\sim$5 averaging over the entire 0-30000 cm$-$1 range, while for CO_2 and CH_4 it is equal to $\sim$1.3.

In this work, the solution of the RT equation via the two stream approximation (included the non-discussed treatment of isotropic and non-isotropic scattering) and the calculation of the optical depth of the gas mixture for a given composition is performed by HELIOS. On the other hand, the calculation of the absorption coefficients for each chemical species is handled by HELIOS-K.

In the rest of this section we discuss the main physical recipes adopted in EOS in order to adapt HELIOS and HELIOS-K to the study of the atmospheres of habitable planets. Following classic studies of circumstellar habitability (Kasting et al., 1993b) we focus on Earth-like atmospheres with variable amounts of water vapor, and CO_2-dominated atmospheres. The former are related to the emergence of the runaway greenhouse feedback and are important for the study of the inner edge of the circumstellar habitable zone (CHZ), whereas the latter are relevant for the study of the outer edge of the CHZ. In this context it is essential to investigate the opacity features of water and carbon dioxide.

3.5.1 Carbon dioxide line wings

One problem with the use of Voigt profiles is the well-known sub-Lorentzian behaviour of the far line wings of CO_2 (Winters, 1964): above a certain distance from the line centre, the opacity of the CO_2 absorption lines is lower than what expected by applying Eq. 3.13. A common way to model the deviation from the ideal line shape consists in multiplying the Lorentz distribution f_L by some other exponentially-decreasing $\chi(|\nu-\nu_0|,P,T)$ function for

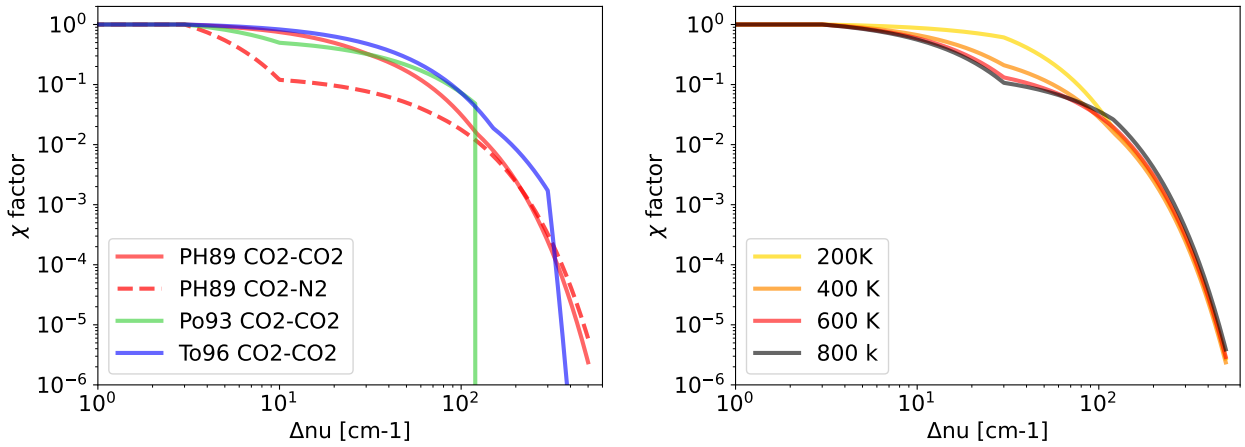

Figure 3.7: Left: the χ factor for different sub-Lorentzian formulations for the CO_2 line wings at 296 K. Solid lines represent the pure CO_2 broadening, while the dashed line represents N_2-broadened CO_2 lines. In red are reported the models of Perrin & Hartmann (1989) for the 4.3 μm band lines, in green the model of Pollack et al. (1993) fitted from data published by Burch et al. (1969) for the 2.7 μm band lines and in blue the model of Tonkov et al. (1996) for the 2.3 μm window region. Right: the χ factor value as derived by Perrin & Hartmann (1989) in the pure CO_2 case for different gas temperatures. The behaviour is similar in the CO_2-N_2 case.

distances from the line centre above a given threshold (also called critical distance and written as $\Delta\nu_c$, Burch et al., 1969). Letting $|\nu - \nu_0| = \Delta\nu$, for a single-component gas this takes the following form:

$$f(\Delta\nu, P, T) = \begin{cases} f_L(\Delta\nu, P, T) & \Delta\nu < \Delta\nu_c \\ f_L(\Delta\nu, P, T)\chi(\Delta\nu, T) & \Delta\nu \geqslant \Delta\nu_c \end{cases} \tag{3.15}$$

Whereas for a mixture of gases the $\nu \geqslant \nu_c$ case becomes:

$$f(\Delta\nu, P, T) = \frac{1}{\pi} \frac{\gamma_{\text{self}}(P,T)\chi_{\text{self}}(\Delta\nu, T) + \gamma_{\text{for}}(P,T)\chi_{\text{for}}(\Delta\nu, T)}{\gamma(P,T)^2 + \Delta\nu^2} \tag{3.16}$$

where γ is defined as in Eq. 3.14 and γ_{nat}, which for Earth-like conditions is much smaller than both the pressure induced terms, has been dropped in the numerator. The critical distance from the line centre $\Delta\nu_c$ has usually a value of 3 cm^{-1} (Burch et al., 1969; Perrin & Hartmann, 1989).

Many different $\chi(\Delta\nu, T)$ functions have been proposed, both empirical and theoretical (Ma et al., 1999). A widely known empirical formulation is the one proposed by Perrin & Hartmann (1989), who experimentally studied the sub-Lorentzian behaviour of the CO_2 lines in the 4.3 μm band for a large interval of temperatures and pressures. They proposed the following 4-case function:

$$\chi(\Delta\nu, T) = \begin{cases} 1 & \Delta\nu \leqslant \sigma_1 \\ \exp(-b_1(\Delta\nu - \sigma_1)) & \sigma_1 < \Delta\nu \leqslant \sigma_2 \\ \exp(-b_1(\sigma_2 - \sigma_1) - b_2(\Delta\nu - \sigma_2)) & \sigma_2 < \Delta\nu \leqslant \sigma_3 \\ \exp(-b_1(\sigma_2 - \sigma_1) - b_2(\sigma_3 - \sigma_2) - b_3(\Delta\nu - \sigma_3)) & \Delta\nu > \sigma_3 \end{cases} \tag{3.17}$$

where $\sigma_1 = \Delta\nu_c$ and the b_i terms contain the temperature dependence as:

$$b_i(T) = \alpha_i + \beta_i \exp(-\epsilon_i T) \tag{3.18}$$

The authors provide the values for α_i, β_i, ϵ_i and σ_i for CO_2-CO_2 and CO_2-N_2 mixtures.

Other groups (Bezard et al., 1990; Pollack et al., 1993; Tonkov et al., 1996) used similar schemes but found different values (see Fig. 3.7, left panel). Such discrepancies are caused by the fact that lines in different spectral bands are more or less sub-Lorentzian than in the 4.3 μm band. In particular, they become progressively less sub-Lorentzian with increasing wavenumber and as such, different models should be used in different regions. However, in the current version HELIOS-K does not allow this and given that the global impact on the energy balance would have been small, we have decided to apply only one model at time over the entire wavenumber range. Moreover, different groups (e.g. Tonkov et al., 1996) conducted their observations at room temperature only (296 K) and thus did not give the dependence of the line profile on temperature.

Another aspect that must be considered is the wing truncation distance from the line centre. This is less of an issue when a sub-Lorentzian χ function is applied with respect of the pure Voigt case, but this choice can still influence the final output (Haus & Arnold, 2010). Proposed values range from 120 cm^{-1} to no truncation whatsoever, but Wordsworth et al. (2010b) verified that choosing 500 cm^{-1} even for pure Voigt profiles produced only a negligible difference with respect to untruncated spectra, while being computationally more efficient.

For CO_2-dominated atmospheres we adopted the prescriptions of Perrin & Hartmann (1989), while for Earth-like atmospheres we kept a Voigtian profile truncated at 25 cm^{-1}. In the former case, we also tested the effects on the OLR and TOA albedo of the Tonkov et al. (1996) χ values. In Section 4.2.2 we will show how different sub-Lorentzian far wings and truncation prescriptions impact the final results for a CO_2-dominated atmosphere. This will help to check this kind of uncertainties inherent to RT models and how they reflect on climate simulations.

3.6 Continuum opacity

Besides the molecular transitions described by groups of spectral lines, different chemical species also have absorption continua, which are called in this way because they vary slowly in frequency. The contribution to the total opacity that comes from these continua is particularly important in the spectral windows, i.e. in the regions of the electromagnetic spectrum where there are few or no allowed transitions. They are characterized by a quadratic dependence on pressure, which makes them the principal contributor to a given species' opacity in mid- and high-pressure environments. The mechanisms responsible for the continuum absorption are not fully understood, and at least three different theories have been proposed and applied to different specific cases.

The first one explains the continuum opacity as the product of collision-induced dipole absorption, usually abbreviated in CIA. This is commonly invoked for non-polar molecules such as CO_2 (Gruszka & Borysow, 1997, 1998) or N_2 (Borysow & Frommhold, 1986), while it has been criticized when applied to polar species (see e.g. Vigasin, 2014).

The second theory considers the continuum as produced by stable and meta-stable dimers formed during molecular collisions. It is usually applied to polar molecules such as water

(Ptashnik et al., 2011), but has also been used to explain the absorption in the 1100-1800 cm^{-1} region of CO_2 (Baranov & Vigasin, 1999; Baranov et al., 2004). Strong support for this explanation, at least in the H_2O case, comes from the partial resolution of dimers' spectrum in the microwave region (Tretyakov et al., 2013; Serov et al., 2014).

The third possibility explains the continuum as the sum of super-Lorentzian mid wings (10-100 cm^{-1} from the line centre) and sub-Lorentzian far wings contributions from nearby allowed transitions. This has also formed the basis for the original CKD continuum model of H_2O (Clough et al., 1989), even though it is more of a practical approach, rather than a physical explanation.

In regard of the first two explanations, Shine et al. (2016) also note that it can be difficult to clearly separate the contributions of CIA from those of dimers, especially in the absence of a full understanding of the quantum chemistry of bound and quasi-bound molecular complexes, at least for water.

In general, continuum opacity can be modeled as the second-order contribution in density to the monochromatic optical depth. As such the total absorption coefficient will then be

$$k_{\text{abs}}(\nu) = k_{\text{lin}}(\nu) + k_{\text{cnt}}(\nu, n) = \ = k_{\text{lin}}(\nu) + \tilde{k}^{\text{self}}_{\text{cnt}}(\nu, T) n_{\text{self}} + \tilde{k}^{\text{for}}_{\text{cnt}}(\nu, T) n_{\text{for}} \tag{3.19}$$

where $k_{\text{lin}}(\nu)$ is the absorption due to the allowed transitions modeled as in Eq. 3.13 and $k_{\text{cnt}}(\nu, n)$ is the molar density-dependent continuum contribution. As in the case of pressure broadening and the χ function, there is a distinction between self-induced continuum and the (usually smaller) foreign-induced continuum. Once again, a precise absorption model should consider all the possible binary combinations of molecules in the gas mixture, but this is usually not possible given the lack of data. However, an increasing number of both theoretical (e.g. Wordsworth et al., 2017; Karman et al., 2018) and empirical (e.g. Turbet et al., 2020; Tran et al., 2022) models for foreign continuum opacities in different bands are being made available in literature. Some of these are available in a special repository on HITRAN (Karman et al., 2019). The specific recipes adopted in this work are reported in the following subsections.

3.6.1 Carbon dioxide continuum

Foundational works on early-Mars and early-Earth climates such as Kasting et al. (1984b) and Kasting (1991), hereafter K91, used a parameterized continuum model derived by Pollack et al. (1980) and tested against microwave and far infrared observations made by the Pioneer Venus spacecraft (Ho et al., 1971; Moore, 1971). This model has been deemed to be too opaque in the 250-500 cm^{-1} region and too transparent in the 1300-1400 cm^{-1} (Wordsworth et al., 2010b).

More recent data on the CO_2 self-continuum, as measured by laboratory experiments, numerical simulations and Venus observations, have been collected by HITRAN. The self-continuum is tabulated for four different bands: 0-750 cm^{-1} (Gruszka & Borysow, 1997, 1998), 1000-1800 cm^{-1} (Baranov & Vigasin, 1999), 2510-2850 cm^{-1} (Baranov et al., 2003) and 2850-3250 cm^{-1} (Baranov, 2018). The continuum in the first band is caused by induced electric dipoles, while those in the second and third bands have been linked to dimer formations. The continuum in the fourth band has not yet been fully explained, though it can be reconstructed by relaxing the selection rules for quantum numbers, suggesting a break in the molecular symmetry (see the discussion in Baranov, 2018). Data for each band do not span the same interval in temperature. For example, the continuum absorption for the first of these bands

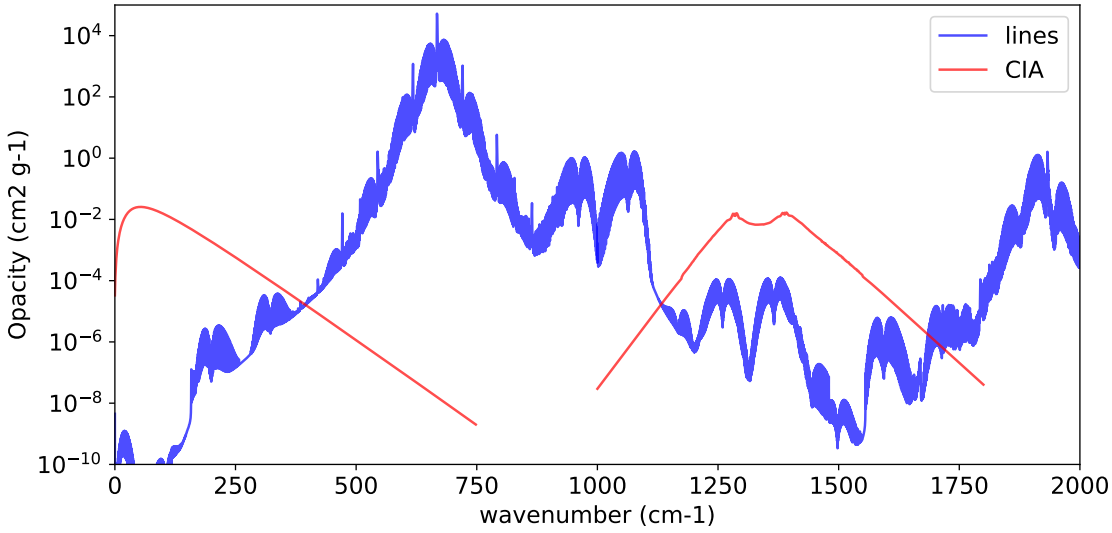

Figure 3.8: The line absorption (blue) and continuum (red) absorption for CO_2, calculated at 1 bar and 300 K. The line profile is that of (Perrin & Hartmann, 1989), truncated at 500 cm^{-1} from each line centre. Only self-broadening and CO_2-CO_2 CIA have been considered here.

is given for 10 points in the 200-800 K range, while for the last one only a single point at 298 K is available. In our work, given the non-negligible dependence of the continuum opacity on temperature, and for a more meaningful comparison with the results obtained by Wordsworth et al. (2010b), we have chosen to use only the 0-750 cm^{-1} and the 1000-1800 cm^{-1} bands continua. As in that work, we will label this model of continuum as "GBB" (Gruszka-Borysow-Baranov). The GBB CO_2 continuum has also been adopted by Kopparapu et al. (2013a) for his re-evaluation of the HZ edges. It is interesting to note that the combined effect of the changes introduced in that work with respect to Kasting et al. (1993b) does not seem to change the estimated position of the Maximum Greenhouse outer edge (see Table 1 in Kopparapu et al., 2013b). The line and continuum absorption of for a 1 bar of pure CO_2 at 300 K is shown in Fig. 3.8.

3.6.2 Water vapor continuum

As showed e.g. in Kopparapu et al. (2013a,b), correctly accounting for the water vapor continuum is of paramount importance for a meaningful modeling of Earth-like planets and for climate predictions on our own planet. An early model adopted in Kasting (1988), used also in Kasting et al. (1993b), is based on Fels-Goody random band model (Fels, 1979; Goody, 1964), computed on synthetic spectra published in McClatchey et al. (1971).

Clough et al. (1989) developed a super-Lorentzian treatment to account for the continuum opacity of the H_2O absorption lines, called the CKD model. More recently, Mlawer et al. (2012) expanded this model to incorporate the effects of the foreign-induced continuum, in what is known as the MT-CKD model. Both the CKD and the improved MT-CKD models are widely used in a variety of climate and weather simulations. Another formulation, prominently used in Kopparapu et al. (2013a), is the BPS model by Paynter & Ramaswamy (2011). This diverges slightly from the MT-CKD model on a conceptual basis because the contin-

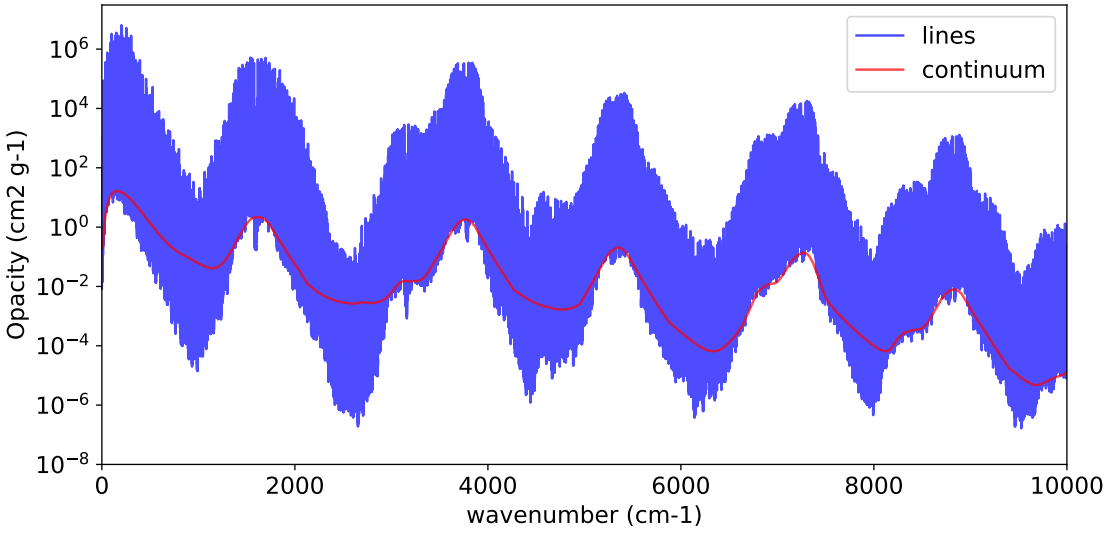

Figure 3.9: The line (blue) and continuum (red) absorption for H_2O, calculated at 0.01 bar and 300 K. The Voigt profile truncated at 25 cm^{-1} from the line centres has been used. Only self-broadening and self-continuum have been considered here.

uum absorption comes directly from empirical data and is independent from the analytical formulation of line profiles.

For this work we have adopted the latest version (3.4) of the MT-CKD model, where the continuum of water vapor is calculated by the CNTNM code, which is a standalone version of the continuum calculation module of the LBLRTM. The continuum is tabulated in the 0-10000 cm^{-1} frequency range and in the 200-400 K temperature range. In Fig. 3.9 is shown the opacity for self-broadened lines and the self-continuum for 0.01 bars of water vapor at 300 K.

3.7 GPU-based calculations

The necessity of processing digital data in order to generate a display image is an old one. The first chips dedicated exclusively to produce digital images were developed and commercialized during the '70 (Barron & Glorioso, 1973) in response to the growing demands of the video-game industry. One of them was the Television Interface Adaptor (TIA) built around the Alphanumeric Television Interface Controller (ANTIC) in the Atari 2600 *console*[9] which lacked any buffer memory and thus had to process images on the spot. These early *GPUs* (Graphical Processor Units) were not Turing complete, being unable to write computed data back to (or lacking completely) any memory, and were only partially programmable. The expanding requests of the consumer market forced manufacturers to increase both the computing capacity and the flexibility of the GPUs. In 1986, Texas Instruments Inc. released the TMS34010 chip, which was the first fully programmable GPU, thus being able to run any general-purpose program. Another step was made in 1999, when Nvidia Corp. commercialized the GeForce 256 graphic card as the first Graphical *Processing* Unit with full hardware-accelerated matrix manipulation for 3D graphics. Finally, in 2007, Nvidia intro-

[9]A mini-computer designed specifically to run video-games

duced independently programmable *stream processors* on its GeForce 8 series of GPUs, which made their products functionally equivalent to multi-core CPUs, and contextually released the first version of CUDA (Compute Unified Device Architecture), a programming framework that allows to run codes written in C and optimized for working with Nvidia products (Sanders & Kandrot, 2010). In 2009 the Khronos Group launched OpenCL, which is another GPGPU (General-Purpose GPU) computing framework based on the C language with the advantages of being open-source and cross-platform. CUDA and OpenCL allowed the growth of the GPGPU programming for scientific applications. At the present date, both of the largest GPU manufacturers (Nvidia and AMD Inc.) produce GPGPU-capable graphic cards with $\gtrsim 10^3$ stream processors with a relatively low cost per processor (around 1 $) and are widely available on the consumer market.

A modern GPU is composed by a large number of computational cores known as stream processors. Each of these computational cores is far slower than a corresponding CPU core, both in terms of computation cycles per second (clock frequency) and in number of floating-point operation per cycle. The specifics vary from model to model but modern, commercially available CPU cores can generally handle $20-60$ single-precision floating-points operations per cycle and execute $3-5\times10^9$ cycles per second. GPU cores, on the other hand, handle 1 or less operations per cycle and are capable of $1-2\times10^9$ cycles/s. However, CPUs are composed by 2-8 cores, while GPUs are composed by 10^3-10^4 cores. This allows to efficiently run highly parallelized codes. GPUs are not entirely independent, since they require the presence of a CPU for the assignment of tasks, and thus the actual processing power of the machine is influenced by the interplay between both these components.

In order to efficiently utilize the computational capabilities of GPUs a good management of the interaction between the storage memory and the graphic card is fundamental. Depending on the specific type of calculations, high-end commercial GPUs have a potential data throughput that exceeds that of the buses which connect them to the rest of the computer. Another problem is related to the access time to the storage memory itself, which can be mitigated adopting the proper strategies during the construction of the code (for example, by loading the data to manipulate into the Video RAM[10] of the graphic card itself). There exist two class of storage devices for modern computers, namely Hard Disk Drives (HDDs) and Solid State Drives (SSDs). HDDs store data on magnetizable rotating disks, while SSDs store data changing the electric charge state on floating gate transistors (a technology called flash memory). Reading-writing time is a factor of 3 to 4 faster for the SSD with respect to the HDD thanks to the fact that the former has no physically moving parts. The input/output speed for HDD is typically 80-160 MB/s, while for SSD is 240-600 MB/s, 600MB/s being the upper transfer speed limit for the Serial Advanced Technology Attachment (SATA) version 3.0 connector. However, since the storage cost per GB is roughly twice that of HDDs and that SSDs have a limited lifespan due to the wearing off of the flash memory cells, HDDs are widely used as the main memory storage devices on personal computers.

For this thesis, we utilized two personal computers of the Observatory of Trieste to run HELIOS and HELIOS-K: Angrenost and Magellanus. Angrenost features an Intel i7-3770 CPU, an Nvidia GTX 1080 Ti graphic card, a 7200 rpm HP/Seagate HDD with 4 TB of capacity and a 1 TB Samsung SSD. Magellanus features an Intel Xeon Silver 4108 CPU, two Nvidia RTX 2080 graphic cards (even though only one at a time was actually used), a 7200 rpm HP/Seagate HDD with 4 TB of capacity and a 500 GB Crucial SSD. Since the SSD space on Angrenost was larger, the output from its GPU was written directly on it, while on

[10] Random Access Memory

Magellanus it was redirected to the HDD. The two machines offered similar performances, being able to compute $\sim$ 30 GB of lines in $\sim$ 20 minutes using HELIOS-K and a single post-processing atmosphere in $\sim$ 30 s using HELIOS. In both cases, the reading-writing time is included. In particular, the calculations of CO_2-dominated atmospheres has been carried out on Angrenost, while those relative to Earth-like atmospheres has been computed on Magellanus.

Chapter 4

Testing EOS

In this Chapter we present the most relevant tests that we performed on EOS. These tests can be categorized in two large groups. The first group concerns the response of EOS to changes of input variables. The second group concerns how EOS compare, for a given input, to other radiative transfer models in literature. These are discussed, respectively, in Section 4.1 and 4.2. In Table 4.1 we list the name and main features of the test cases compared in the rest of the Chapter.

For a given atmosphere, the OLR is studied as a function of T_s and the TOA albedo is studied as a function of T_s and z. The dependence of TOA albedo on T_s is relevant in moist atmospheres due to the presence of H_2O absorption bands in the near infrared. The increased amount of H_2O at higher T_s thus reduces the amount of light scattered, in turn reducing the TOA albedo. Expressing the OLR and the TOA albedo as a function of T_s is required to compile lookup tables of these quantities to be used in climate simulations (in particular, the ESTM1 and 2). As briefly discussed in Section 3.3.1, this is mandated by the Kasting's *reverse procedure* onto which both versions of the ESTM model is built.

4.1 Robustness and sensitivity of the model

In this Section we show how the OLR and TOA albedo calculated with our procedure are affected by variations of simulation parameters and physical input variables. We begin by studying the influence of two computational parameters, namely the number of layers and the TOA pressure. Then we present the effects of changing the lapse rate formulation and the tropopause prescription. Finally we show the effects of changing chemical composition. For CO_2, we also explore the influence of different sub-Lorentzian line shape prescriptions.

4.1.1 Changes in computational variables

First of all, we probed the stability of the EOS results with respect to variations of computational variables. We devised four tests to be conducted on the same specific atmosphere, namely the *Saturated Modern Earth* one with 360 ppm of CO_2, 1.8 ppm of CH_4 and a RH=100% (see Table 4.1). In each test the dry BOA pressure was set to 1 bar, the total BOA pressure was varied according to the temperature-dependent contribution of water vapor and we adopted a moist adiabat lapse rate topped by a 200 K isothermal stratosphere (see Section 2.2.4). We then proceeded as follows.

Table 4.1: A summary of the test cases studied in this Chapter. The CO_2-dominated models have been tested for different CO_2 partial pressures. The total surface pressure has been varied according to the temperature dependence of the H_2O partial pressure. Entries in the the fourth and fifth columns are in volume fractions. The sixth column gives the relative humidity. The last column reports the prescriptions adopted for the CO_2 line opacity. Note that in Section 4.1.4 we investigated two sub-cases of the *Dry CO_2-dominated* atmosphere, by varying the CO_2 line prescriptions.

Name	N_2 fraction	O_2 fraction	CO_2 fraction	CH_4 fraction	H_2O RH	CO_2 line prescription	CO_2 CIA
Pre-industrial Earth	0.79	0.21	280×10^{-6}	0.6×10^{-6}	60%	Voigt, 25 cm^{-1}	no
Dry Modern Earth	0.79	0.21	360×10^{-6}	1.8×10^{-6}	no	Voigt, 25 cm^{-1}	no
Modern Earth 1	0.79	0.21	360×10^{-6}	1.8×10^{-6}	50%	Voigt, 25 cm^{-1}	no
Modern Earth 2	0.79	0.21	360×10^{-6}	1.8×10^{-6}	60%	Voigt, 25 cm^{-1}	no
Saturated Modern Earth	0.79	0.21	360×10^{-6}	1.8×10^{-6}	100%	Voigt, 25 cm^{-1}	no
Post-industrial Earth	0.79	0.21	1152×10^{-6}	no	60%	Voigt, 25 cm^{-1}	no
Dry CO_2-dominated 1	no	no	1.0	no	no	PH89[a], 500 cm^{-1}	GBB[b]
Dry CO_2-dominated 2	no	no	1.0	no	no	T96[c], 350 cm^{-1}	GBB
Moist CO_2-dominated 1	no	no	1.0	no	100%	PH89[a], 500 cm^{-1}	GBB
Moist CO_2-dominated 2	no	no	1.0	no	100%	T96, 350 cm^{-1}	GBB
Moist CO_2-dominated 3	no	no	1.0	no	100%	Voigt, 25 cm^{-1}	GBB
Dry Archean Earth 1[d]	0.615	no	0.385	no	no	PH89[a], 500 cm^{-1}	GBB
Dry Archean Earth 2[d]	0.615	no	0.385	100×10^{-6}	no	PH89[a], 500 cm^{-1}	GBB
Dry Archean Earth 3[d]	0.615	no	0.385	1000×10^{-6}	no	PH89[a], 500 cm^{-1}	GBB

a. Perrin & Hartmann (1989).
a. Gruszka-Borysow-Baranov, see Section 3.6.1.
c. Tonkov et al. (1996).
d. Abundances have been chosen to match the CO_2-N_2 atmosphere tested in Halevy et al. (2009) (see Section 4.2.2.

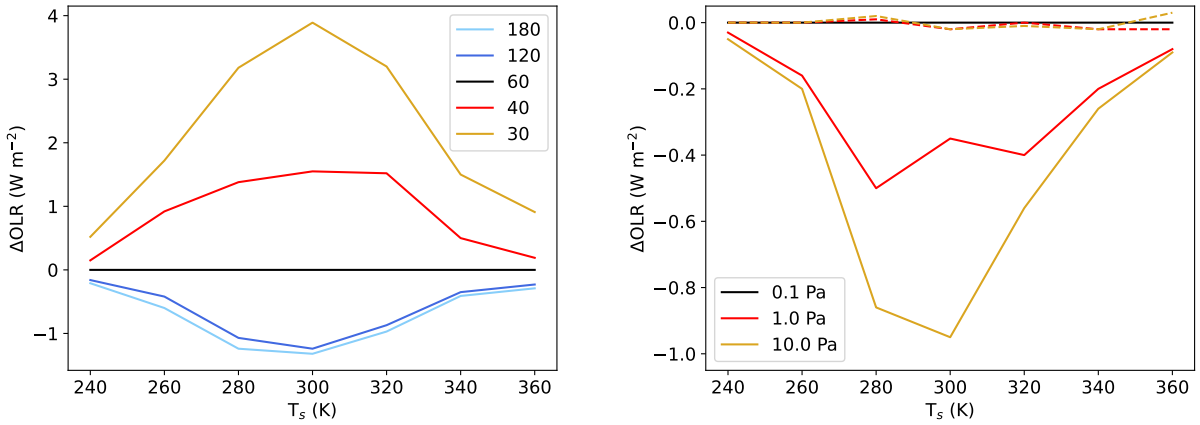

Figure 4.1: The absolute deviation (in W m^{-2}) from the OLR of our reference model for Earth atmosphere (in black) as a function of temperature. On the left hand panel we show models with different layer densities, reported in the legend as the total number of layers used each simulation. On the right hand panel models with different TOA pressures are shown. Solid lines refer to models with a fixed number of total layers (60 in this case), while dashed lines refer to models with a fixed layer density (10 per order of magnitude in this case).

Layer density

In the first test we changed the layer density (i.e., the number of layers per order of magnitude of pressure) in the simulation. We ran HELIOS using 30, 40, 60, 120 and 180 atmospheric layers, for 7 points in temperature in the 240-360 K interval. The 60-layer model was taken as a reference. Since the contribution of the water vapor to the total BOA pressure is modest, the number of layers is independent of the surface temperature. The results can be seen in Fig. 4.1, left panel. First, we note that reducing the density of layers has the effect of increasing the OLR, especially at intermediate (280-320 K) temperatures. For the 30-layer (5 layers per order of magnitude) the largest deviation from the reference model is found at 300 K. This deviation amounts to 3.9 W m^{-2}, corresponding to +1.8%. For the lowest and highest point in temperature, the deviation reduces to less than 1 W m^{-2}, which corresponds to +0.6% and +0.3%, respectively. Second, we note that increasing the density of layers produces smaller variations in the OLR. As an example, using 40 instead of 30 layers changes the OLR at 300 K by more than 2 W m^{-2}, while using 180 instead of 120 layers yields a difference of $\sim$ 0.2 W m^{-2}. Therefore, doubling or tripling the number of layers above the advised value of 10 layers per order of magnitude produces in general only marginal variations, in the order of 1 W m^{-2} or -0.3% in the worst case.

We were also interested in studying how the TOA albedo varied when the layer density of the model is changed. Therefore, we calculated the shortwave reflected radiation when the atmosphere is illuminated by a blackbody at 5780 K, representing a G2-type star. For the surface, we have chosen a surface albedo α_s equal to 0.25 and independent of the wavelength. The results for different numbers of layers and in terms of $\Delta\alpha_{\rm TOA}/\alpha_{\rm TOA}$ percentage points are shown in Fig. 4.2. Differently from the OLR, whose peak deviation is located at mid-range temperatures, the maximum deviation of TOA albedo can be found at low temperatures, as can be seen in the right panel. The deviations, both for our 30-layer and for our 180-layer model, reduce to less than 0.1% at higher temperatures. In the left panel the dependence

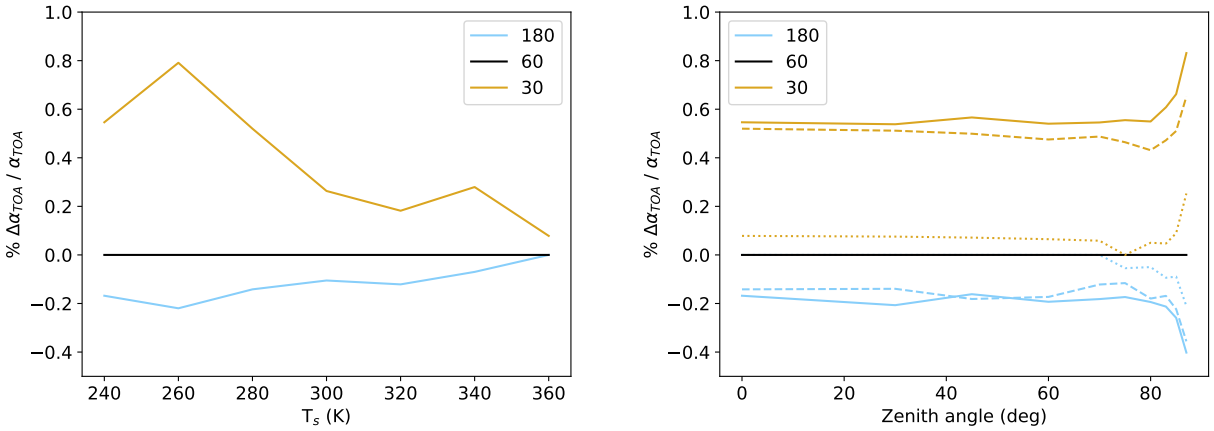

Figure 4.2: The relative deviation (in % points) from the TOA albedo of our reference model for Earth atmosphere (in black) of 30-layer (yellow lines) and 180-layer (light blue lines) models. On the left hand panel the dependence on temperature for 0º zenith angle is shown. On the right hand panel the dependence on zenith angle for three temperatures is shown: 240 K (solid), 280 K (dashed) and 360 K (dotted).

of TOA albedo deviations from the ISR zenith angle z is shown for three different values of T_s: 240 K (solid), 280 K (dashed) and 360 K (dotted). We note that: (i) the deviations become larger for higher values of z and (ii), at all z the deviations reduce when temperature is increased. In any case, in the temperature range considered, the maximum deviation found is $< 1\%$ for all values of z. As for the OLR, we stress that by increasing the number of layers above 10 per order of magnitude the improvements in accuracy become smaller and smaller.

Uppermost layer pressure

In the second test (Fig. 4.1, right panel), we have varied the pressure of the uppermost layer of the model, which for short we will call TOA pressure. Alongside the reference 0.1 Pa value, we have tried 1 and 10 Pa, either leaving constant the total number of layers (60, solid lines), or leaving constant the density of layers (10 per order of magnitude, dashed lines). First of all, increasing the TOA pressure when using a constant number of layers has the effect of decreasing the OLR, by ~ 1 W m^{-2} in the worst case. This is somewhat counter-intuitive given that we are removing the outer part of the atmosphere from the calculations and therefore reducing the overall opacity of the column, but it can be explained in light of the results found in the previous paragraph. In fact, in this case we are indirectly increasing the density of layers in the lower part of atmosphere, much like we have done in the first test. On the other hand, keeping a constant density of layers nearly cancels these deviations, meaning that the choice of the TOA pressure is not particularly relevant, at least for an Earth-like chemical composition and within the tested temperature interval.

We then studied the TOA albedo variations in response to a change in the TOA pressure. In particular, we tested the case with a 10 Pa TOA pressure, first keeping constant the number of layers and then changing this number in such a way to have the same layer density as in the 0.1 Pa reference model. Increasing the TOA pressure while leaving constant the total number of layers produced a very slight ($\sim 0.1\%$) reduction of the TOA albedo at low temperatures and no reduction at high temperatures for a fixed z. Given that the differences are small, we

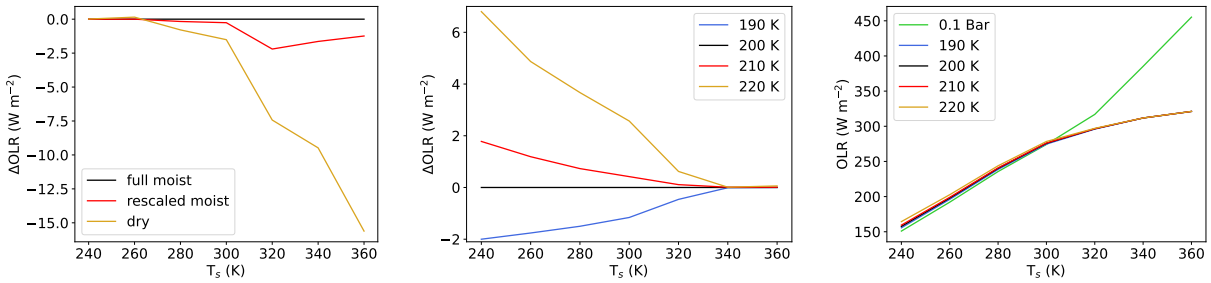

Figure 4.3: Comparison of the OLR predicted by different models of lapse rate (left panel) and tropopause prescriptions (central and right panels), as indicated in the legends. In the first two panels we display the absolute deviations, ΔOLR, with respect to the reference model (full moist lapse rate and tropopause at 200 K). In the right panel we display the absolute value of the OLR. The 0.1 bar fixed-pressure tropopause case (in green) strongly deviates from the fixed-temperature cases.

do not include a plot for this test. Higher values of z presented a more pronounced deviation. When we adjusted the number of layers to have same layer density as in the reference model the aforementioned effects disappeared.

4.1.2 Changes in the atmospheric structure

We then focused on the effects of changing prescriptions about the lapse rate and the tropopause position. In order to do so, we conducted two OLR tests and two TOA albedo tests on the same *Saturated Modern Earth* atmosphere described in the previous subsection, using the reference model case values for the layer density (10 per order of magnitude) and the TOA pressure (0.1 Pa).

Lapse rates

In the first test, to study the impact on the OLR, we applied three different P-T atmospheric profiles, produced using a dry adiabatic, a moist adiabatic and the moist rescaled adiabatic lapse rate described in Section 2.2.4. Strictly speaking, the models with a moist rescaled lapse rate and with a dry adiabatic lapse rate are not self-consistent, because they refer to situations where H_2O is accounted for in the opacity calculations, but not in the determination of the vertical P-T structure of the atmosphere. On the other hand, the saturated moist lapse rate, which is commonly adopted throughout literature, despite being internally consistent, is not realistic since the average relative humidity of planetary atmospheres is lower than 100%. With these caveats in mind, this test is useful to single out the influence of the lapse rate on the OLR, other factors being equal. The results are presented in Fig. 4.3, left panel. Changes in the lapse rates have maximum influence at high temperatures, where the atmosphere is richer in water vapor. At lower temperatures ($T \lesssim 300$ K) even adopting a dry lapse rate, the OLR is reduced by less than 2 W m^{-2} ($\sim 0.6\%$) with respect to our reference model (in black). Finally, our rescaled moist lapse rate produces results that are largely in line with those of a theoretical moist lapse rate, with peak differences of the order of ~ 3 W m^{-2} for mid-to-high temperatures. Based on these results, in the standard application of our procedure we adopt the rescaled lapse rate rather than the moist or dry adiabat.

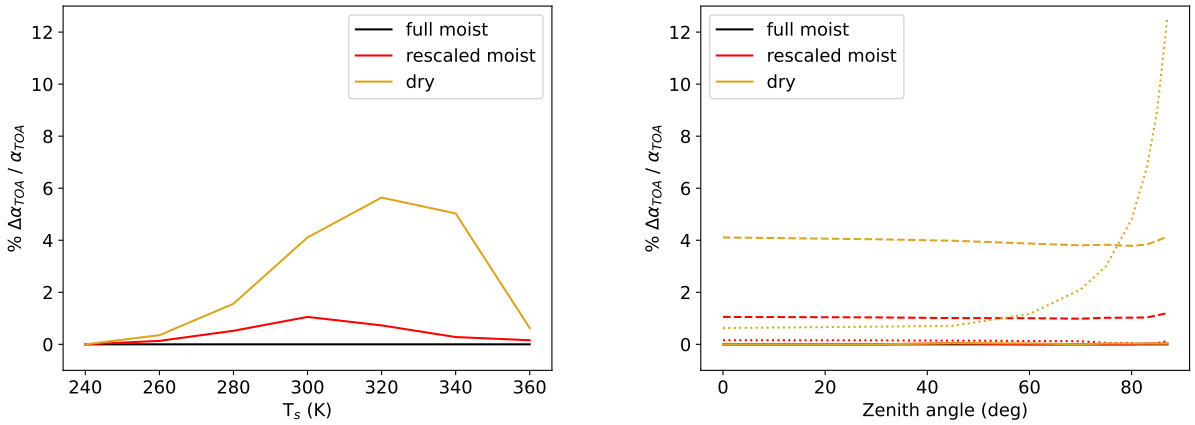

Figure 4.4: The relative deviation (in % points) from the TOA albedo of our reference model (ideal moist adiabatic lapse rate) of the dry adiabatic and the moist rescaled adiabatic lapse rate models. Left panel: the dependence on temperature for 0° zenith angle is shown. On the right panel the dependence on zenith angle for three temperatures is shown: 240 K (solid), 280 K (dashed) and 360 K (dotted).

As in the previous subsection, we were interested also in studying the effects of the lapse rate changes on the TOA albedo. Therefore we did another test in which we illuminated the three atmospheres described above with a G2 star like blackbody. The wavelength-independent surface albedo was set to 0.25. The results, in term of percent deviation from our reference case, are shown in Fig. 4.4. On the left panel, the dependence on temperature is shown. As it is possible to see, the deviation is negligible at low T_s and low ($< 1\%$) at very high T_s, while it is large at medium-to-high T_s (300-340 K). On the right panel the dependence of $\alpha_{\rm TOA}$ on zenith angle is shown. As in most of the other cases presented in this Chapter, the deviation is larger for high zenith angles. This can be explained by the fact that, at high zenith angles, the optical path through the simulated atmosphere is longer, thus magnifying the differences between models.

Tropopause position and stratospheric temperature

We then tried five different prescriptions for the tropopause position to study the effects on the OLR. Four of them are based on temperature and place the tropopause at the pressure corresponding to 190, 200, 210 or 220 K. The fifth prescription is taken from the work of Robinson & Catling (2014), who identified a common 0.1 bar position for the tropopauses of the Solar System planets. In this case, the tropopause is placed at the level corresponding to 0.1 bar. In all cases the overlying stratosphere has the same temperature of the tropopause. The results for the first four cases are shown in Fig. 4.3, central panel. The maximum deviations from our reference model (namely the one with a 200 K tropopause) are found for the lowest temperature, while over 320 K the deviations becomes negligible (i.e. less than 1 W m^{-2}, or 0.3%). This behaviour is expected since, under these prescriptions, at high surface temperatures the tropopause is so high ($10^{-3} - 10^{-4}$ bar) to be irrelevant on the final radiative balance of the atmosphere. On the other hand, the 0.1 bar tropopause prescription produces very different results, as it is possible to see in the right panel of Fig. 4.3. First of all, the deviations from our reference model are much larger both at low and at high

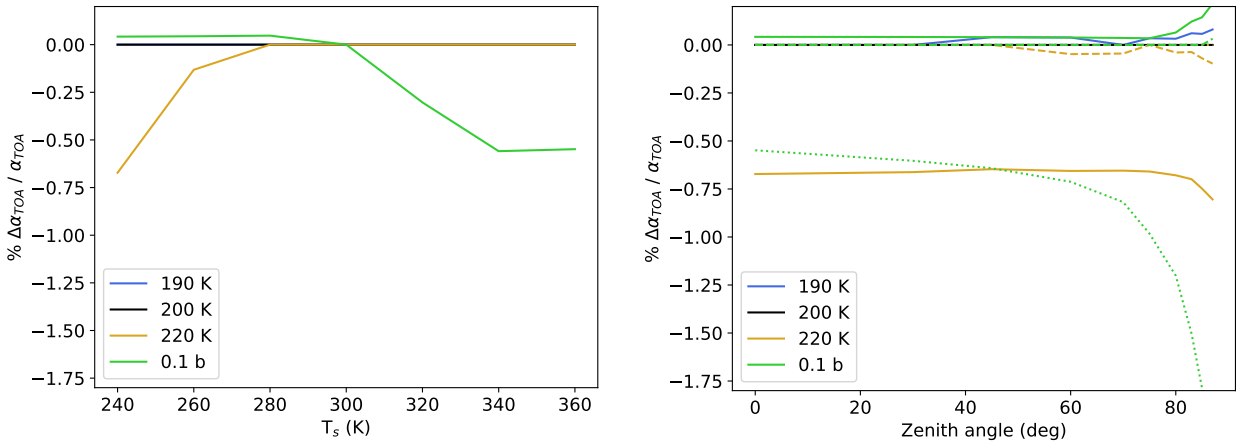

Figure 4.5: The relative deviation (in % points) from the TOA albedo of our reference model (200 K, in black) of 190 K (in blue) and 220 K (in yellow) models. Left panel: the dependence on temperature, for 0° zenith angle. The gray line and the black line are coincident. Right panel: the dependence on zenith angle for three temperatures: 240 (solid), 280 (dashed) and 360 (dotted). Grey dashed and dotted lines and the black line are coincident.

temperatures, going from -6 W m^{-2} at 240 K to +134 W m^{-2} at 360 K. In particular, it is relatively small (some units of W m^{-2}) and negative in the 240-300 K range, and large (tens of W m^{-2}) and positive from 320 K onward. The second thing we note is the steeper OLR vs T_s at high T_s under the 0.1 bar prescription. This is contrary to what is expected when T rises approaching the onset of the runaway greenhouse instability (see Section 2.4.1): the troposphere becomes increasingly opaque to IR radiation, thus reducing the slope of the OLR as a function of T_s. Above some critical point, the OLR flattens and T_s is allowed to increase freely up to the point in which the surface begins to radiate in the visible part of the spectrum (see e.g. Fig. 2.7, left panel). In our treatment this behaviour is reproduced when the tropopause is defined at constant temperature but not when it is defined at constant pressure. In this latter case the tropopause temperature becomes dependent on the surface temperature. Since the infrared photosphere of hot, H_2O-rich atmospheres is far above the 0.1 bar level, this prescription leads to a continual rise of the OLR with increasing surface temperature. If this situation were realistic, a runaway greenhouse would not be possible. However, the onset of the runaway greenhouse instability is predicted by a variety of models, including 3D GCMs, and is widely used to define the inner edge of the CHZ. The ability of reproducing such a feature is fundamental, therefore the fixed-pressure tropopause can be considered unfit to describe the climate and habitability of liquid-water bearing planets. In light of the above arguments we do not consider further the case of a tropopause at fixed pressure.

As before, we also studied the variations in the TOA albedo when the tropopause prescriptions change as described in the previous paragraph. In Fig. 4.5, left panel, the percent deviations from our reference case (i.e., the one with a 200 K tropopause, black line) for the other tested prescriptions are presented as a function of surface temperature. We note three things. First, the effect using a fixed-temperature tropopause with a different temperature is maximum (0.7%) at low surface temperatures and decreases rapidly at higher T_s (yellow line). Second, using a 190 K tropopause yielded a deviation lower than 0.1 % and therefore cannot be see on the plot. Third, when a 0.1 bar tropopause is chosen, the relation with temperature

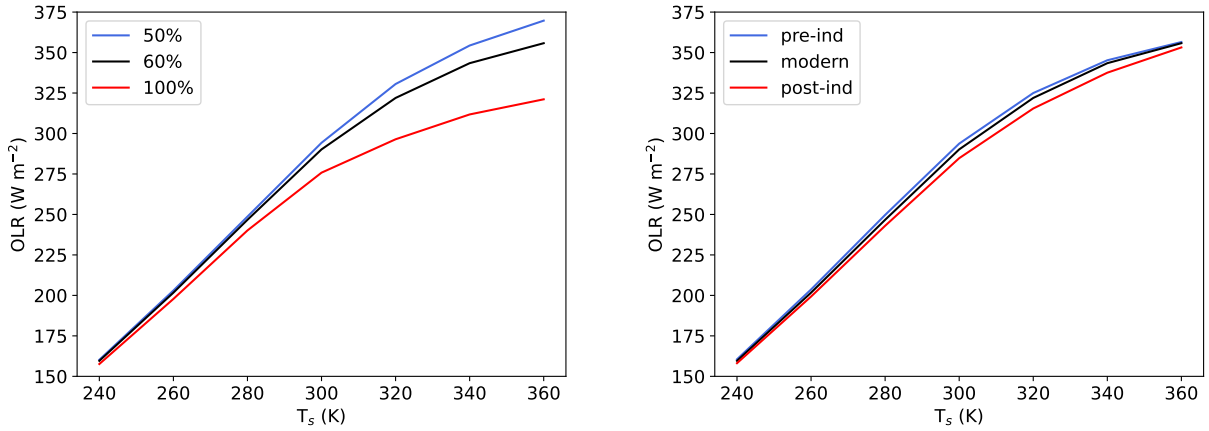

Figure 4.6: The effects on the OLR of varying the relative humidity (left panel) or the CO_2 and CH_4 dry molar fractions (right panel). The reference model (in black) is the same in both panels and have RH=60%, 360 ppm of CO_2 and 1.8 ppm of CH_4.

is inverted: the deviation is low at low temperatures and maximum at high temperatures. On the right panel of Fig. 4.5 the percent deviation from the reference case is shown as a function of the zenith angle. As expected, deviations are negligible in the $0^o - 75^o$ range and then increase, but remain small ($\sim$ 0.1% points). The only exception is the 0.1 bar troposphere case at 360 K (green line), which grows far more markedly to deviations larger than 2% for high zenith angles.

4.1.3 Changes in the atmospheric composition

The most relevant effects on the OLR and TOA albedo come from the atmospheric composition. In order to quantify them, we have devised two tests for the OLR and two tests for the TOA albedo, illuminating the described atmospheres with a G2-like blackbody.

Relative humidity

In the first test, we varied the RH value of the atmosphere, testing three values: 50%, 60% and 100%, which correspond to the *Modern Earth 1*, *Modern Earth 2* and *Saturated Modern Earth* cases of Table 4.1. The results are shown in Fig. 4.6, left panel. As expected, deviations start quite low at 240 K, with a difference between the 50% and the 100% case of 2.6 W m^{-2} of 1.6% and then grow quickly, becoming equal to 8.5 W m^{-2} at 280 K, to 34.1 W m^{-2} at 320 K and to 48.5 W m^{-2} at 360 K. This behaviour is caused by the nearly exponential increase of the water vapor content of the atmosphere as a function of temperature and its primary role as a greenhouse gas. Even a more modest increase, such as that present between the 50% and the 60% case is sufficient to produce a 0.6 W m^{-2} OLR decrease at 240 K which grows to 1.9 W m^{-2} at 280 K and to 13.9 W m^{-2} at 360 K.

We then proceeded by studying the impact of changing the relative humidity on the TOA albedo. The results can be seen in Fig. 4.7, left panel. Variations of TOA albedo are anti-correlated with the water vapor content in the atmosphere, mostly due to the larger absorption of water molecules in the near infrared. These differences are low at low temperatures (+0.2% for the drier case, -0.7% for the wetter case), increase at 340 K (+3.0% for the drier case,

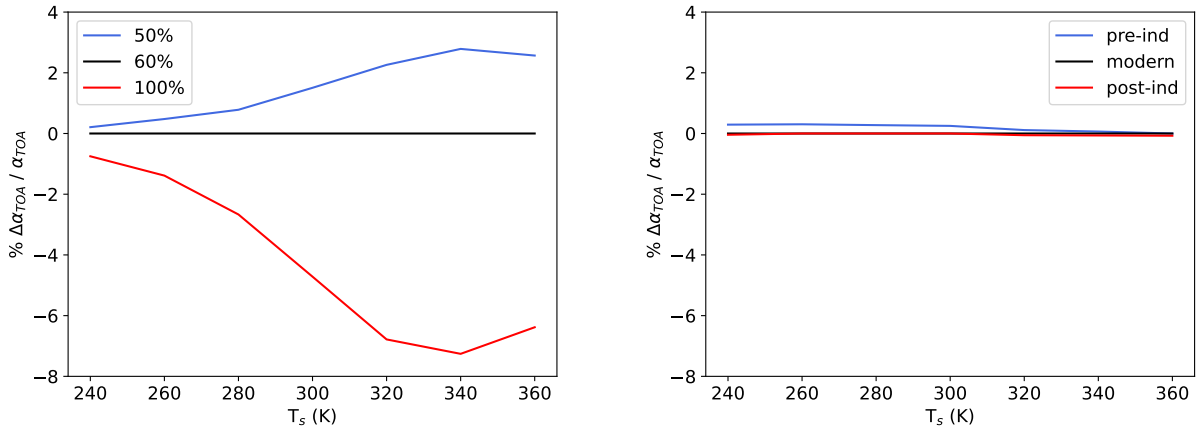

Figure 4.7: The relative deviation (in % points) from the TOA albedo of our chemical composition reference model (RH=60%, pCO2=360 ppmv and pCH4=1.8 ppmv) for different values of relative humidity (left) and CO2/CH4 abundances (right). Both are plotted as a function of surface temperature.

-7.3% for the wetter case) and then fall slightly at 360 K. We also tested how the TOA albedo changes as a function of the zenith angle (Fig. 4.8, left panel) and we found that, for higher angles, the deviations are nearly constant when T_s is low and become smaller when T_s is high. This is particularly evident for the 360 K case, where deviations reduce from +2.6% to +1.4% for the drier case, and from -6.4% to -3.5% for the wetter case.

CO_2 and CH_4 concentrations

In the second test, we varied the CO_2 and CH_4 content of the atmosphere. We tested three cases: a *Pre-industrial Earth* with 280 ppm of CO_2 and 0.6 ppm of CH_4, a mid-1990 Earth (i.e. the *Modern Earth 2* case) with 360 ppm of CO_2 and 1.8 ppm of CH_4 and a scenario typically explored in climate simulations with 1152 ppm of CO_2 and no CH_4, that here we call *Post-industrial Earth*. In this last one, the CO_2 level is chosen as to simulate a 4 times increase of the pre-industrial CO_2-equivalent (288 ppm) level, where CO_2-equivalent stands for the quantity of CO_2 that produces the same OLR of a mixture of CO_2 plus other greenhouse gases (like CH_4). The results are shown in the right panel of Fig. 4.6. The maximum deviations are found at 300 K for the pre-industrial case (+3.5 W m^{-2}) and at 320 K for the post-industrial case (-6.5 W m^{-2}). At high temperatures, the infrared opacity features of CO_2 and CH_4 are swamped by the stronger bands and continua of water vapor, which is the same throughout the models, thus reducing the relevance of those gases in the OLR computation and making the models to converge. On the other hand, at low temperatures, the deviations are lower in absolute terms but nearly proportional to the total OLR.

The relation between the OLR and the concentrations of CO_2 and CH_4 in an Earth-like atmosphere is very well studied since the rising concentrations of these GHGs are the main drivers of the anthropogenic climate change on our planet (Masson-Delmotte et al., 2021). Case-specific calculations to address this topic allow us to make a first intercomparison between our model and others. In particular here we consider the results of Etminan et al. (2016), which propose three relations derived by fitting RT calculations that model the dependence of the radiative forcing on CO_2, CH_4 and N_2O concentrations. These have already

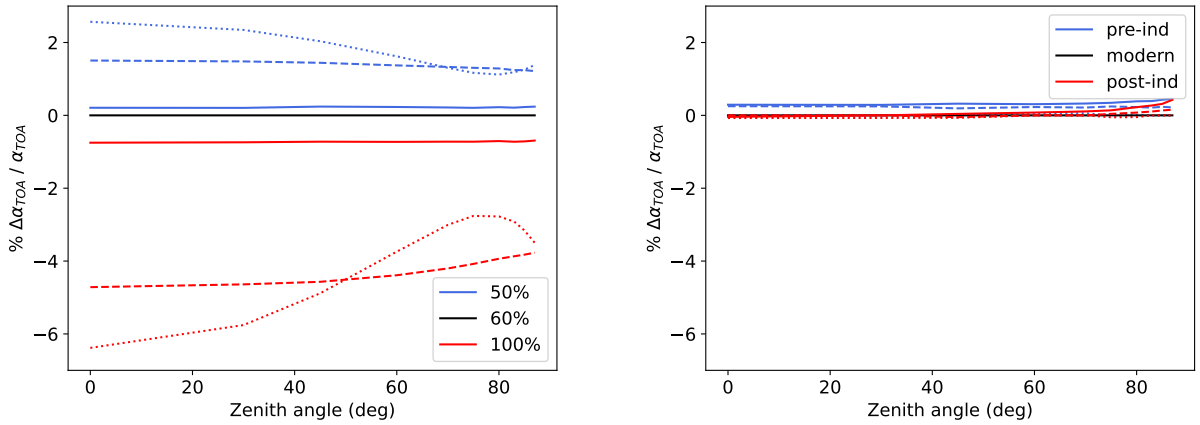

Figure 4.8: The relative deviation (in % points) from the TOA albedo of our chemical composition reference model (RH=60%, pCO2=360 ppmv and pCH4=1.8 ppmv) for different values of relative humidity (left) and CO2/CH4 abundances (right). Both are plotted as a function of the incident zenith angle for three values of the surface temperature: 240 K (solid), 280 K (dashed) and 360 K (dotted).

been presented in Section 2.1.3 (Eqs. 2.15). By employing them, it is possible to calculate the radiative forcing between the *Pre-industrial Earth* case and the two other cases (*Modern Earth 2* and *Post-industrial Earth*), obtaining 2.1 Wm^{-2} and 7.2 Wm^{-2}, respectively. If we now calculate the OLR difference between our models for the average Earth temperature (288 K), which is equivalent to the radiative forcing as expressed in Eqs. 2.15, we obtain 3.0 and 6.8 Wm^{-2}. These small differences (∼0.4% in relative terms) indicate that EOS calculations are able to reproduce the effect of trace gases concentrations changes with a degree of precision comparable to that of models specifically designed to study the Earth atmosphere.

To complete our analysis, we studied how changes of CO_2 and CH_4 concentrations in trace amounts may affect the TOA albedo. As can be seen in Fig. 4.7, right panel, the effects of such changes are very small, especially when compared to the effects of relative humidity changes. The maximum deviations are found for low T_s and are equal to +0.3% for the *Pre-industrial Earth* case and to -0.1% for the post-industrial one. Above 300 K, they become undetectable. When higher zenith angles are considered (Fig. 4.8, right panel), two different things happen. For the Pre-industrial case, the positive difference at low T_s (240 K run) is slightly amplified, changing from +0.3% (at z=0^o) to +0.5% (at z=87^o). This is caused entirely by the lower CO_2 absorption, whose effect is amplified when the atmospheric optical path becomes larger at higher zenith angles. Instead, at higher T_s, this amplification becomes unnoticeable due to the dominant role of the water vapor opacity. On the other hand, for the *Post-industrial Earth* case, the negative difference at low zenith angles become a positive difference at high zenith angles. Taking the 240 K run, the deviation evolves from -0.1% to +0.4%. For higher T_s, the effect becomes less strong, but still detectable. This increase of the TOA albedo can be explained by the fact that CO_2 is a very good scatterer compared to the main component of Earth-like atmospheres (N_2), and for long optical paths the CO_2 scattering may overcome the CO_2 absorption. In these cases, CO_2 is a trace gas and its effect on the albedo is very small, but for CO_2-dominated atmospheres the enhancement in the TOA albedo at high CO_2 partial pressures is so strong that it can overcome the increased greenhouse effect, thus cooling the surface. This is a well-known effect linked to the definition of the maximum greenhouse limit,

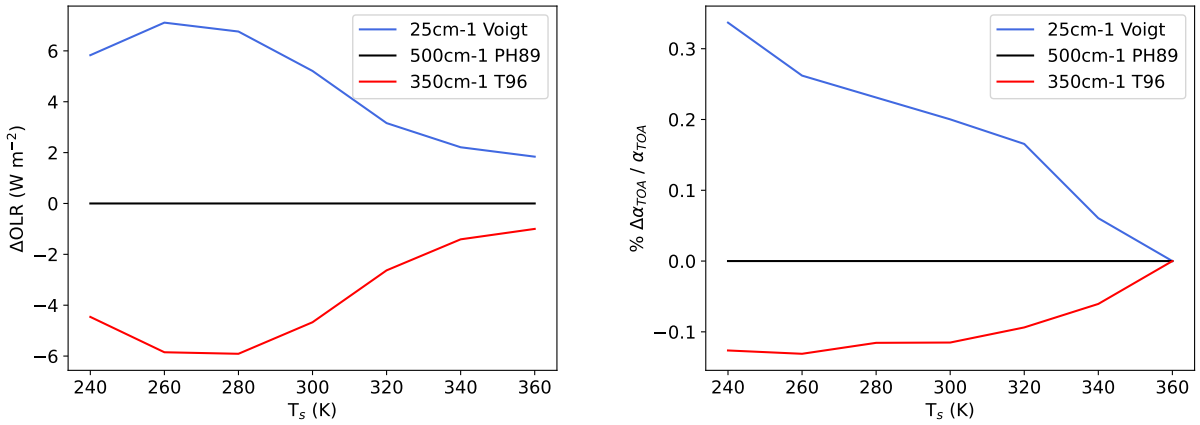

Figure 4.9: The effects of varying CO_2 line profile prescriptions on the OLR (left panel) and TOA albedo (right panel). Both model cases use a 1 bar atmosphere of CO_2 with a water vapor humidity of 100%.

which acts as outer limit for the circumstellar habitable zone (see Section 2.4.3).

4.1.4 Changes in the carbon dioxide line profiles

As described in Section 3.5.1, CO_2 offers a special challenge in terms of absorption line profiles description. We tested three possible prescriptions for the CO_2 lines: a Perrin & Hartmann (1989) profile truncated at 500 cm^{-1}, a Tonkov et al. (1996) profile truncated at 350 cm^{-1} and a Voigt profile truncated at 25 cm^{-1}. In all cases the CIA was considered. These cases are labeled *Moist CO_2-dominated 1, 2* and *3*, respectively. We carried on two tests to assess the effects of changing such prescriptions on the OLR and TOA albedo. In both tests we chose a 1-bar CO_2 atmosphere with a water vapor relative humidity of 100%. The vertical P-T profile was calculated as in Section 2.2.5.

In the first test we investigated the OLR and the results are shown in Fig. 4.9, left panel. The truncated Voigt profile is less opaque, allowing for an increase in the OLR at low temperatures of 5.8-7.1 W m^{-2}, which is a 4.7% increase with respect to the reference (the one adopting the Perrin & Hartmann, 1989, profiles) model OLR. The Tonkov et al. (1996) profile is instead more opaque causing a decrease of the OLR by 4.5-5.8 W m^{-2} (i.e. −4.2%). At higher T_s the H_2O absorption becomes increasingly important and the effects of different profiles decline to less than 0.5%. We also removed the CIA absorption to assess its impact on the OLR. In all three cases, we find very similar results: between 240 and 300 K, the OLR increases by 5-7% with respect to the same model with continuum absorption, while at higher T_s the difference reduces to less than one percent (not shown in figure).

In the second test we recorded the TOA albedo in the presence of an incoming radiation from our standard G2-star like blackbody. The results are shown in Fig. 4.9, right panel. In this case, the relative differences between the different cases are basically negligible, peaking at 0.3% for the Voigt profile at 240 K. The deviation produced by the Tonkov et al. (1996) prescriptions are even less marked, peaking at 0.1%. Finally, an increase in the zenith angle slightly reduces the deviations at all temperatures.

4.2 Comparison with other RT models

In this Section we will show how EOS compares with other radiative transfer models in literature. The goal is showing the ability of our procedure to reproduce well studied cases in order to validate it. More specifically, we tested the cases of a moist saturated Earth-like atmosphere, typically considered in the analysis of the inner edge of the HZ, and of CO_2-dominated atmosphere typically considered in the analysis of the outer edge of the HZ.

4.2.1 Earth-like atmospheric models

Concerning the Earth-like atmospheres we considered five of the seven models discussed by Yang et al. (2016), namely CAM3, SMART, SBDART, LBLRTM and LMDG. In addition, we considered predictions of CCM3 calculated by us as described in Vladilo et al. (2015). Finally, we also included the results published by Williams & Kasting (1997) and by Kopparapu et al. (2013a), hereafter *WK97* and *KOP13* respectively. The main characteristics of the models used as comparison tests are summarized in Table 4.2 and discussed below.

Radiative transfer specifics

CCM3 (Kiehl et al., 1998) and CAM3 (Collins et al., 2002) are band models that adopts 19 intervals for the incoming stellar radiation. Opacities are formulated in terms of absorbivity $\mathcal{A}$ and emissivity $\mathcal{E}$ as delineated in Manabe & Möller (1961). In practice, $\mathcal{A}$ and $\mathcal{E}$ are computed from line-by-line models for a variety of homogenoeous atmospheric slabs, each with different temperatures, pressures and composition. The actual stratified atmosphere is substituted with the pre-computed slab that better matches the overall properties of the real atmosphere, and its $\mathcal{A}$ and $\mathcal{E}$ are then used to calculate transmitted, emitted and diffused flux in each band. The H_2O continuum is included via the CKD formulation (Clough et al., 1989). Wavelength intervals have been chosen to maximise the precision for calculations involving an Earth-like atmosphere illuminated by a Sun-like star, which is not an issue in the present study but might be when trying to apply these models to cases substantially different (e.g. planets illuminated by M-type stars).

KOP13, LMDG (Wordsworth et al., 2010a) and SBDART (Yang et al., 2000) are again band models. *KOP13* and LMDG adopt, respectively, 28 and 36 spectral intervals. SBDART performs its calculations on a much finer grid with 369 spectral intervals. Opacities are calculated using the correlated-k approximation starting from line-by-line computations performed using KSPECTRUM and then deriving the opacity distribution function with in-house scripts. In LMDG and SBDART, the H_2O continuum is included using the CKD formulation, while *KOP13* adopted the BPS scheme (Paynter & Ramaswamy, 2011). *KOP13* and LMDG have been used to model the RT properties of atmospheres under a wide range SEDs, including M-type dwarfs, thus it can be expected to be not as calibrated on the Earth case as CCM3 and CAM3. SBDART has a sufficiently high resolution to naturally avoid this issue.

LBLRTM (Clough et al., 2005) and SMART (Meadows & Crisp, 1996) are instead line-by-line models. Both of them can calculate line opacities with precisions down to 0.001 cm^{-1} (but Yang et al., 2016, do not specify the precision used in their study). Interestingly, instead of the standard Voigt line profile, SMART adopts a van Vleck-Weisskopf (VVW, van Vleck & Weisskopf, 1945) line shape, which has a slightly higher absorption in the radio and

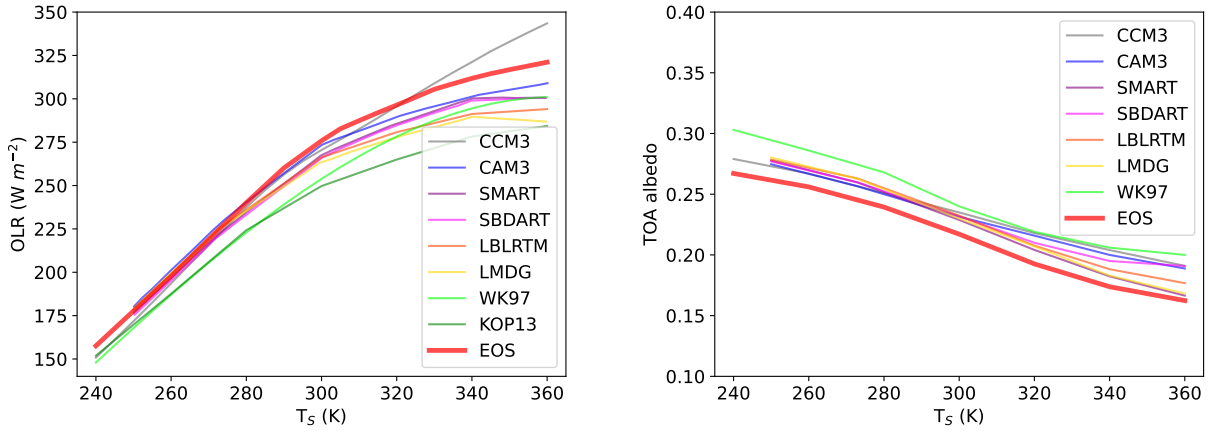

Figure 4.10: The dependence on surface temperature of OLR (left panel) and TOA albedo (right panel) for 8 different RT codes, plus EOS (thick red line). Data relative to CAM3, SMART, SBDART, LBLRTM and LMDG has been taken from Yang et al. (2016), while data relative to CCM3 has been produced by us.

microwave region[1]. The H_2O continuum is treated via the MT_CKD model in LBLRTM, while in SMART it is included directly in the line profile by multiplying the VVW profile by a wavelength-dependent χ factor, thus producing substantially super-Lorentzian line wings. Being line-by-line, these models should not be particularly restricted in treating cases even wildly different from an Earth-twin.

Finally, *WK97* used the band model detailed in Kasting et al. (1984b), Kasting et al. (1984a) and Kasting (1988) to run a large grid of calculations and fitted the resulting OLR and TOA albedo in polynomial form. Theirs is the oldest among the models cross-tested here. Opacity calculations have been performed using an exponential sum on data of the AFGL (McClatchey et al., 1971). Water continuum is modeled with ad hoc formulations fitted on observational data. For the treatment of the incoming stellar radiation, the Kasting model uses a slightly higher number of spectral intervals with respect to the other low-resolution band models described above.

Chemical makeup of the atmosphere

For CAM3, SMART, SBDART, LBLRTM and LMDG the atmosphere is composed by 1 bar of N_2, 376 ppm of CO_2 and temperature dependent quantity of H_2O, calculated with a relative humidity of 100%. In all these models the surface pressure was adjusted to consider the vapor pressure of H_2O, but the CO_2 mixing ratio was not adjusted to account for the changes in the atmospheric gas mix. Therefore, high temperature points have a higher mass of CO_2 in the atmospheric column. However, Yang et al. (2016) estimate that the effect of this error on the OLR should be about 2.1 W m^{-2} in the worst case (the 360 K point), which is $\sim 0.7\%$ of the total OLR averaged through those models. The TOA pressure was set to 10 Pa and the number of atmospheric layers to 301, with the exception of LBLRTM which has 150 longwave layers and 75 shortwave layers and SMART which has 75 layers. The atmospheric vertical structure is the same as described in Section 2.2.4 and shown in Fig. 2.3.

[1]This line profile has been derived under the assuption that collisions cause molecules to polarize following a Boltzmann distribution, rather than at random.

Table 4.2: A summary of the RT models used to compare EOS results regarding Earth-like atmospheres. Information concerning CAM3, LBLRTM, LMDG, SBDART and SMART have been taken from Yang et al. (2016). Information concerning CCM3 has been taken from Kiehl et al. (1998). *WK97* and *KOP13* are not codes, but rather refer to the specific models employed in Williams & Kasting (1997) and Kopparapu et al. (2013a), respectively. Information concerning the former has been collected from Kasting et al. (1984b), Kasting et al. (1984a) and Kasting (1988). The chemical composition of the adopted atmosphere is nearly identical in all the models and consisted of 1 bar of N_2, an amount of H_2O dependent on the surface temperature (RH=100%) and CO_2 and CH_4 as reported in column 2.

Model	CO_2/CH_4 [ppm]	HITRAN	Layers	Intervals	Absorption	H_2O cont.	Scattering
CAM3[a]	376/0.0	2000	301	19	absorp./emis.	CKD 2.4	Briegleb (1992)
CCM3[a]	380/1.8	1996	26	19	absorp./emis.	CKD 2.3	Briegleb (1992)
KOP13	330/0.0	2008	101	28	correlated-k	BPS	Toon et al. (1989)
LBLRTM	376/0.0	2008	150[b]	$>10^4$	line-by-line	MT_CKD 2.5	Moncet & Clough (1997)
LMDG	376/0.0	2008	301	36	correlated-k	CKD 2.4	Toon et al. (1989)
SBDART	376/0.0	1996	301	369	correlated-k	CKD 2.3	Stamnes et al. (1988)
SMART	376/0.0	2010	75	$>10^4$	line-by-line	χ-factors	Stamnes et al. (1988)
WK97	376/0.0	none[c]	20	62	exponential sum	Goody model[d]	Toon et al. (1989)
EOS	360/1.8	2016	60	$>10^4$	line-by-line	MT_CKD 3.4	Heng et al. (2018)

a. These are actually the names of 3D GCM codes. Here only the results from the RT modules are considered, as calculated using the CliMT toolkit by Rodrigo Caballero.

b. 150 levels for longwave calculations, 75 levels for shortwave calculations.

c. It uses the coefficients in the AFGL tapes (McClatchey et al., 1971).

d. The Goody random band model is presented in (Goody, 1964). The band parameters for H_2O absorption has been taken from Rodgers & Walshaw (1966) and Goldman & Kyle (1968).

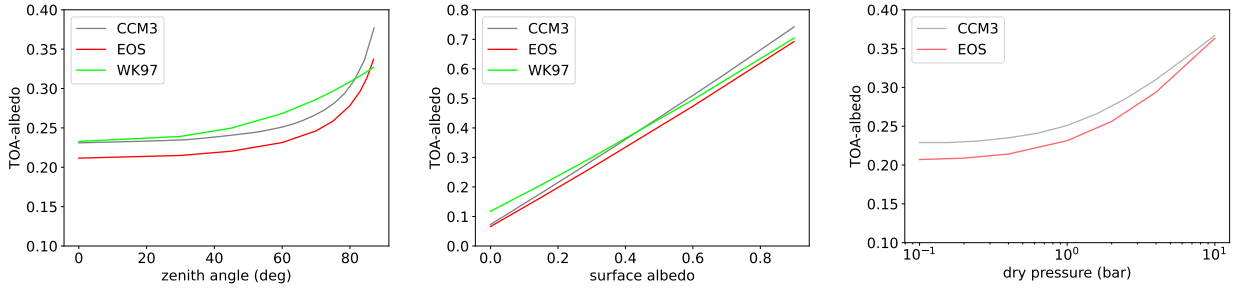

Figure 4.11: The dependence of TOA albedo on the incident zenith angle (left panel), the surface albedo (central panel) and the surface dry pressure (right panel). On the latter one, given the limits of the WK97 polynomial formulation, we cannot compare their results with ours.

For CCM3 the atmosphere is composed of 380 ppm of CO_2, 1.8 ppm of CH_4 and variable H_2O with a relative humidity of 100%. Adopting a value of 28 for the CO_2-equivalent[2] of methane gas (Masson-Delmotte et al., 2021) gives a total amount of CO_2-equivalent for the CCM3 model of 430 ppm.

WK97 used an atmosphere composed of 1 bar of N_2 and saturated with H_2O. The partial pressure of CO_2 is an input of the polynomial that we have chosen in such a way to obtain a volume mixing ratio of 376 ppm, as in the models described by Yang et al. (2016). Regarding the vertical P-T structure, WK97 adopted a fixed tropospheric lapse rate equal to 6.5 K km^{-1} and a temperature for the tropopause that is dependent on T_s (see Eq. 2.32). As a result, their model underestimates the OLR with respect to the other models at low T_s and slightly overestimates it at high T_s. On the basis of our previous results (see Fig. 4.3, central panel), OLR differences should be of the order of units of W m^{-2}, while TOA albedo differences should be negligible.

For the calculation of the inner edge of the habitable zone, KOP13 used an atmosphere composed of 1 bar of N_2, 330 ppmv of CO_2 and saturated with H_2O. Their model atmosphere is divided into 101 layers. The vertical P-T structure is given by a moist pseudoadiabat, as described in the appendix A of Kasting (1988), overlain by a 200 K isothermal stratosphere.

Finally, for EOS we adopted the reference *Saturated Modern Earth* atmosphere described in Section 2.2.4: 360 ppm of CO_2, 1.8 ppm of CH_4 and 100% relative humidity. The minor differences of trace greenhouse gas concentrations between different models are expected to produce completely negligible effects in the TOA albedo and very small differences in the OLR. In particular, for the latter we estimated a deviation of $\sim$ 0.5 W m^{-2}, given that a doubling of CO_2 concentration produces a forcing of 4 W m^{-2} (Collins et al., 2006).

Comparison of the results

Regarding the OLR, the results are shown in Fig. 4.10, left panel. As can be seen, for low temperatures (less than 280 K) EOS gives values that are perfectly in line with those obtained by other codes. At 250 K (lowest temperature point for the data taken from Yang et al., 2016), the highest OLR is given by CAM3 (180.3 W m^{-2}), the lowest by CCM3 (171.8 W m^{-2}), while EOS gives an intermediate result (177.7 W m^{-2}). Differences between all models start to arise when T_s increases above 280 K, presumably as a result of the differences in the treatment of the

[2]See Section 2.1.3 for an explanation of the concept of CO_2-equivalent.

water vapor absorption. At very high T_s the slope of the OLR vs T_s flattens in most models, including EOS, a behaviour that is expected at the onset of the runaway greenhouse instability (see previous discussion in Section 4.1.2). Only CCM3 shows a steady rise of the OLR with increasing T_s, probably due to its outdated prescriptions. In some of the models tested by KOP13, precisely in those lacking the prescriptions of the H_2O continuum absorption, the flattening of the slope takes place at temperatures that are higher than in their reference models. Clearly, the treatment of the effects of water vapor at high T_s is extremely difficult and model dependent. EOS, with its updated prescriptions, is able to capture these effects at high T_s, but with an OLR that is higher than that predicted by the codes compared in Yang et al. (2016). A satisfactory explanation of this difference would require a thorough analysis of each one of the RT codes described in that paper, which is something beyond the scope of this work. However, the adoption of EOS predictions in ESTM2 has allowed us to reproduce a variety of zonally-averaged observables of the current Earth climate while keeping the other ESTM2 parameters well in the range of Earth observational data (see the next Chapter). This encourages us to believe that the quantities calculated by EOS are physically sound.

Regarding the TOA albedo under a G2-like blackbody insolation, the results are shown in Fig. 4.10, right panel. All models, including EOS, predict a decreasing of TOA albedo as T_s increases. The EOS albedos are slightly lower than those predicted by the other codes, but the differences are small, typically in the order of $\simeq -0.02$, and -0.04 in the worst cases. In this comparison, we have not included the results of KOP13 because they used a different value for the surface albedo (0.32). Using CCM3 and the WK97 polynomials, we were able to compare also the EOS-calculated albedos as a function of the zenith angle, the surface albedo and the surface dry pressure. These additional results are shown in Fig. 4.11. As it is possible to see, all the trends are reproduced. Part of this small offset can be explained by two known differences between EOS and the other codes, namely (i) the fact that EOS corrects the zenith distance for the sphericity of the planet (for both Fig. 4.10, right panel and Fig. 4.11, left panel) and (ii) the usage of a slightly hotter blackbody for the results of (Yang et al., 2016) and CCM3 (for Fig. 4.10, right panel). However, these two factors only account for a reduction in the EOS albedo of 0.002-0.004, or, 10% of the total discrepancy. The remaining part of the offset might be due to differences in the gas opacities. Specifically, if our gas opacity is slightly higher in the visible and in the near infrared, and slightly lower in the mid and far infrared, we would obtain both a higher OLR and a lower TOA albedo[3]. We are not in the position to test this hypothesis, since it would require accessing the detailed opacity tables used by Yang et al. (2016). In any case, the difference with the other models is small and we believe that the EOS results are reliable because, once inserted in the ESTM2, they are capable to match very well the observational data of the Earth climate system, as we show in the next Chapter.

4.2.2 CO_2-dominated atmospheric models

In this second round of tests we compared the predictions of the OLR and TOA albedo of CO_2-dominated atmospheres obtained with EOS with similar predictions obtained from other codes. In particular, we considered the five cases labeled as *Dry CO_2-dominated 1* and *2* and

[3]An increased absorption in the visible/near infrared would reduce the scattered light and thus the TOA albedo. This would also reduce the OLR. However, since the fraction of thermal radiation emitted by the planet in visible/near infrared is small, the OLR reduction in this part of the spectrum can easily be swamped by an OLR increase in mid/far infrared if the absorption in these bands is reduced.

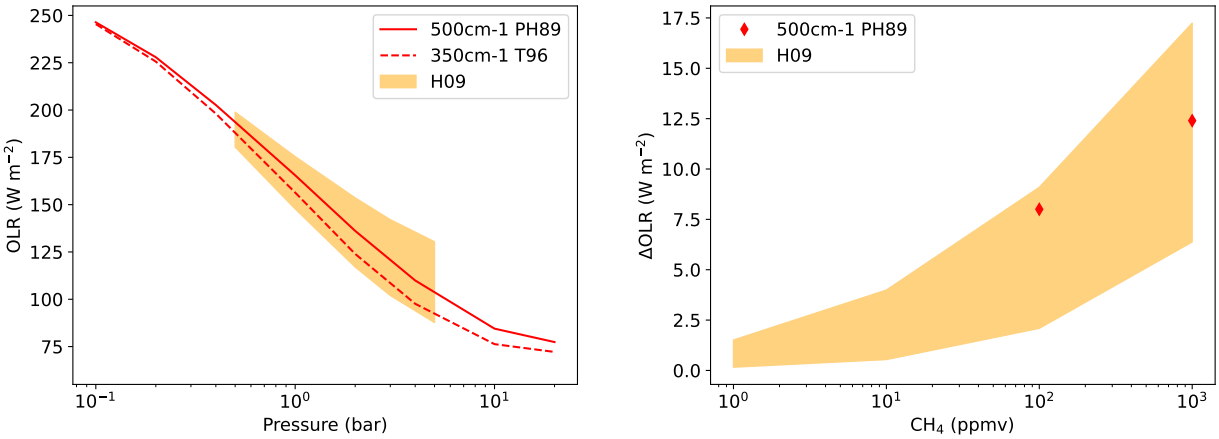

Figure 4.12: Left panel: the dependence of the OLR on the surface pressure for a dry CO_2 dominated Martian atmosphere. Right panel: the dependence of the OLR on CH_4 concentration for a dry CO_2-N_2 Earth atmosphere as described in the text. In both cases the surface temperature has been fixed to 273 K. Yellow areas represent the envelope of the predictions of the Halevy et al. (2009) models. Red lines on the left and red diamonds on the right represent the results from EOS.

Moist CO_2-dominated 1, 2 and *3*. The vertical profiles are constructed as explained in Section 2.2.5. For consistency with previous published work, we explored the dependence of the OLR and TOA albedo on the CO_2 surface partial pressure, rather than the surface temperature. In practice, the surface pressure of the dry part (i.e. carbon dioxide) was varied between 0.1 and 20 bar while keeping constant the surface temperature at $T = 273$ K. In some of the cases presented below, we also changed the surface gravity acceleration to match that of Mars (38% of the Earth's one).

Pure CO_2 case

In the first test we compared our *Dry CO_2-dominated 1* and *2* cases with the models presented in Halevy et al. (2009). These authors explored: (1) the effects of different prescriptions for the CO_2 line profiles and CIA and (2) the forcing due to addition of various other greenhouse gases (like H_2O, CH_4, N_2O etc.). They performed their calculations both for a pure CO_2 atmosphere under a Martian gravity and for a CO_2-N_2 atmosphere under an Earth gravity, varying in both cases the CO_2 pressure. Here we focus on the former, for which they investigated the 0.5-5 bar interval.

Concerning the CO_2 prescriptions, Halevy et al. (2009) models are different from ours in several ways. First of all, line profiles are modeled using the Voigt distribution up to 40 Doppler half-witdhs from the line centre, and using the VVW distribution farther away. The line profile is also multiplied by a $\chi(\nu)$ factor to include the sub-Lorentzian behaviour of the wings. Rather than a single sub-Lorentzian formulation for the entire spectrum, they adopt 4 different $\chi(\nu)$ functions taken from Le Doucen et al. (1985), Perrin & Hartmann (1989), Tonkov et al. (1996) and Meadows & Crisp (1996) to model, respectively, the CO_2 lines in the 0-2300 cm^{-1}, 2300-3000 cm^{-1}, 3000-6000 cm^{-1} and >6000 cm^{-1} bands. Three combinations of line truncations and CIA models are tested, labeled labeled "CA", "MTCKD" and "GBKM". The features of each of these models are summarized below.

(i) The "MTCKD" model adopts a 25 cm^{-1} line cutoff. Foreign continuum of CO_2 is taken from the MT_CKD 2.0 model in LBLRTM. The self-continuum, not calculated by the same code, is considered equal to the foreign continuum multiplied by 1.3.

(ii) The "GBKM" model adopts a 500 cm^{-1} line cutoff. Foreign and self-continuum of CO_2 are considered by taking a collage of several empirical formulations. Gruszka & Borysow (1997) and Gruszka & Borysow (1998) are used in the 0-300 cm^{-1} band, Kasting et al. (1984b) is used in the 1150-1850 cm^{-1} band and (Moore, 1971) in the 4000-4600 cm^{-1} band.

(iii) The "CA" model adopts a 1000 cm^{-1} line cutoff. Foreign and self-continuum of CO_2 are not considered separately from the lines but rather included in the χ factor used to treat the sub-Lorentzian behaviour of the far wings. This methodology is derived from Meadows & Crisp (1996).

It is clear that it is not possible to make a direct comparison with our recipes. Thus, in its place, we decided to consider the Halevy et al. (2009) models as an envelope, and to check our ability to match it. The results are shown in Fig. 4.12, left panel. Halevy predictions are represented by the yellow area, while our predictions using the Perrin & Hartmann (1989) and Tonkov et al. (1996) models are represented by the solid and dashed red lines respectively. As it is possible to see, in the pressure range considered here EOS fares well, despite its simpler modelization. Both the *Dry CO_2-dominated 1* and the *Dry CO_2-dominated 2* case reproduces the dependence of the OLR on the surface pressure as found by Halevy et al. (2009). It is interesting to note that our *Dry CO_2-dominated 1* matches very closely their "MTCKD" model (not shown).

CO_2-CH_4 case

In the second test we compared our *Dry Archean Earth 1, 2* and *3* cases with the results of Halevy et al. (2009). Alongside the pure, Martian CO_2 atmosphere described in the previous paragraph, they also studied how an Earth CO_2-N_2 atmosphere with p_{CO2} = 0.5 bars and p_{N2} = 0.8 bars responded to the addition of increasing quantities of other GHGs. They evaluated the effect of NH_3, N_2O, H_2S, SO_2 and CH_4 at concentrations of 1, 10, 100 and 1000 ppmv, and of H_2O at a relative humidity of 20%, 50% and 80%.

We focus in particular on the dependence of forcing on CH_4 concentration. The results are shown in Fig. 4.12, right panel. Again, it must be noted that a direct comparison between their models and EOS is not possible due to the differences in the line shape and CIA recipes adopted, both for CO_2 and CH_4 and for this reason, we chose to represent them as an envelope (in yellow). The red diamonds represent, respectively, the forcing produced by the *Dry Archean Earth 2* and *3* cases with respect to the *Dry Archean Earth 1* case. Again, our results match those of Halevy et al. (2009), even though the spread in their forcings underline clearly the persisting issues in this field. In this case, their "MTCKD" passes near the upper edge of the yellow envelope. We note that, also in this case, EOS results seems to match the "MTCKD" model better than the others.

CO_2-H_2O case

In the third test we compared our *Moist CO_2-dominated 1* and *2* cases with those of Kasting (1991), who considered a water vapor saturated, CO_2-dominated Martian atmosphere with

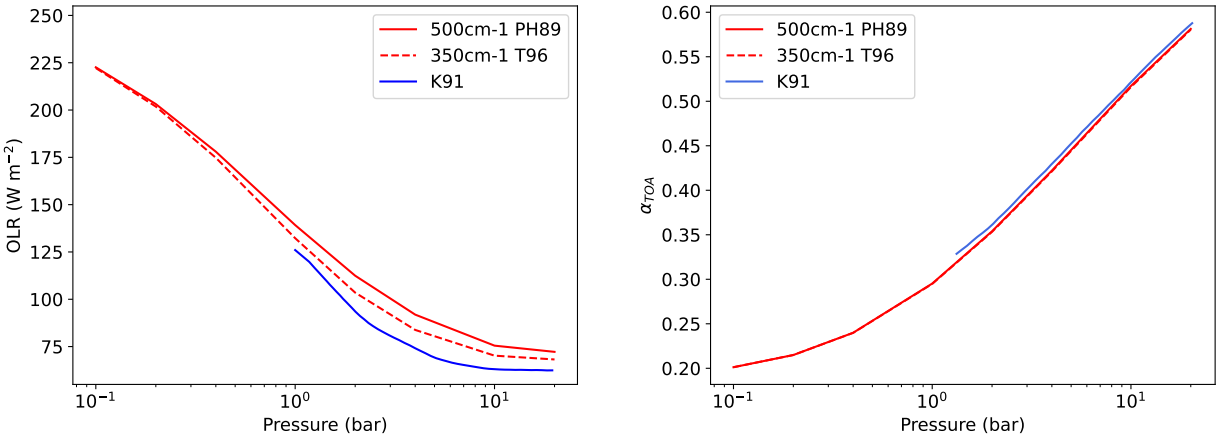

Figure 4.13: The dependence of the OLR (left) and TOA albedo (right) on the surface pressure for a H_2O saturated, CO_2-dominated Martian atmosphere. In both cases the surface temperature has been fixed to 273 K. For TOA albedo calculations, a surface albedo equal to 0.215 and a a zenith angle of 60° have been chosen. Kasting (1991) results: blue lines. EOS results: red lines.

CO_2 surface pressures between 1 and 34.7 bar. The upper value corresponds to the pressure at which CO_2 condenses when $T = 273\,\mathrm{K}$, which is the surface temperature. We tested both the OLR and the TOA albedo, and the result of this comparison is shown in Fig. 4.13.

Concerning the OLR (left panel), EOS tends to produce a slightly larger OLR in both of the tested cases This is true for the enrire pressure interval considered. However, this is expected, since, according to Wordsworth et al. (2010b), the Kasting (1991) model overestimates CO_2 opacity due to outdated CIA prescriptions. The estimated offset is around 14 W m^{-2} for a surface temperature of 250 K, a surface pressure of 2 bars and no water vapor. This offset cannot be directly translated to the case under analysis here, because of the presence of water vapor and because of the different surface temperature adopted by Wordsworth et al. (2010b), but gives a zeroth-order estimate of the magnitude of this effect. The average differences between EOS results and K91 results are equal to 14.7 W m^{-2} for the Perrin & Hartmann (1989) line case and to 7.8 W m^{-2} for the Tonkov et al. (1996) case.

Concerning the TOA albedo (right panel), EOS matches very well the curve obtained by Kasting (1991). As in the Earth-like atmosphere case studied in Section 4.2.1, we found a slightly lower TOA albedo (∼3% at worst) than that of the other model. The offset is far less pronounced than in the OLR since the most important difference between EOS and the Kasting (1991) model, at least for the case under study here, are the CIA prescriptions in the far-IR. The difference between the *Moist CO_2-dominated 1* and the *Moist CO_2-dominated 2* cases are very modest and amounts to ∼0.2% at worst, in line with what has been found in Section 4.1.4. Remarkably, this relative difference is nearly constant between 0.1 and 20 bars.

Chapter 5

The EOS-ESTM model: description and validation

This Chapter is composed by two parts. In the first one, I present the updates implemented in ESTM as a part of the larger work on coupling EOS to ESTM to obtain a new and powerful tool for the analysis of the surface conditions of rocky planets. In the second one, I show how our model results compare with a variety of observational Earth quantities. The good match between data and model constitute a validation of the physical prescriptions adopted here, especially since each of them have also been tested separately. It is also an indirect validation of the RT results produced by EOS. The results presented here have been obtained in the framework of the collaboration within the Trieste group on exoclimates. The parts of the work described in detail below are the ones where I gave an important contribution. The complete recalibration and comparison work is presented in Biasiotti, Simonetti et al. (2022).

5.1 The new ESTM

EOS is a standalone tool that can be used both to directly probe the extent of the circumstellar habitable zone via the energy balance equation and to link these calculations to predicted emission spectra. However, one of the original goals behind its development was to provide more flexible, precise and up-to-date OLR and TOA albedo lookup tables to ESTM. Since ESTM is a 2D climate model, it represents a vast enhancement in the study of the physical state of planetary surfaces with respect to single-column models (as used, e.g., in the reference work by Kopparapu et al., 2013a). Thus, as part of my PhD activity I contributed by improving the parameterization of the climate system employed in ESTM. This new version of the code, updated using the EOS results and new prescriptions for land albedo, cloud properties and ice formation has been presented and validated in Biasiotti, Simonetti et al. (2022). Below I describe the new features present in this version of the code, that we will call ESTM2 hereafter. The previous version of the code (ESTM1, Vladilo et al., 2015) is described in Chapter 2.

5.1.1 Land albedo

In ESTM1, the albedo of lands was independent of the stellar zenith angle z. At variance with this choice, ESTM2 drops the Lambertian approximation and adopts the formulation

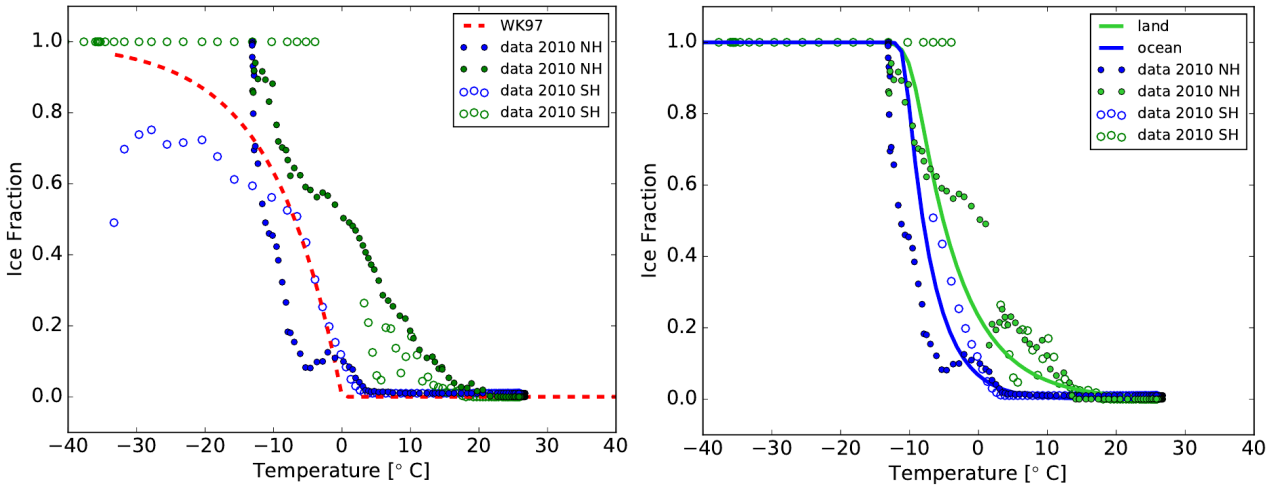

Figure 5.1: Mean annual ice fraction cover for Earth over lands (green) and oceans (blue). Dots refer to the northern hemisphere and circles to the southern hemisphere. Temperature data have been taken from ERA5 and ice fraction from the Terra and Aqua spacecrafts. Left panel: the Williams & Kasting (1997, WK97) relation adopted in ESTM1 against the uncorrected dataset. Right panel: the new logistic relations for land and ocean ices plotted against the corrected dataset. In the corrected dataset the land ice fraction has been adjusted to exclude orographic glaciers at low latitudes and ocean data at the edge of Antarctica have been removed. Credit: Biasiotti, Simonetti et al. (2022).

proposed by Briegleb (1992):

$$\alpha_{\rm srf}(\mu) = \alpha_{\rm srf}(0.5)\frac{1+d_B}{1+d_B\mu} \tag{5.1}$$

where $\alpha_{\rm srf}(0.5)$ is the measured albedo of a generic surface at $\mu = 0.5$ ($z = 60°$) and the parameter d_B regulates its dependence on the zenith angle. In their work, Briegleb et al. found that several widespread Earth surface types can be categorized in two classes, one with a *weak* z-dependence and another with a *strong* z-dependence, for which d_B is equal to 0.1 and 0.4, respectively. The former can be used to describe forested land and tundra, while the latter is suitable for grasslands, shrublands and sandy deserts. In ESTM2 we adopted a single land albedo equal to 0.20 with a *weak* dependence, that was found to better match the observational albedo profile of Earth (Coakley, 2003). This value can be changed to model planets with different surface characteristics.

5.1.2 Ice formation

The relation adopted in ESTM1 for ice formation (see eq. 2.12, Williams & Kasting, 1997) fails to reproduce two features of the observed ice fraction on Earth. First of all, it predicts a fully frozen ($f_{\rm i} = 1$) surface only for very low mean annual surface temperatures ($\bar{T}_s < -40$ °C), while experimental data shows that this condition is reached for $\bar{T}_s \simeq -12$ °C (Fig. 5.1, left panel). Second, it is unable to capture the relatively slow rising $f_{\rm i}$ at $\bar{T}_s > 0$ °C. Moreover, by considering separately the ice formation over ocean and land it becomes clear that there are two different functional dependencies that cannot be captured by a simple exponential function. To solve these issues in ESTM2, we paid special attention to re-calibrate this

Parameter	Description	Value
Land		
$T_{\circ,lnd}$	Turning point	265.15 K
θ_{lnd}	Growth rate	1.2
ξ_{lnd}	Shape parameter	8.0
Ocean		
$T_{\circ,ocn}$	Turning point	263.15 K
θ_{ocn}	Growth rate	3.0
ξ_{ocn}	Shape parameter	12.0

Table 5.1: Parameters adopted for new ice coverage function 5.2.

important aspect of the model by searching for (i) a new set of experimental data appropriately reduced and (ii) a new and more flexible functional dependence on the surface temperature.

Concerning (i), the latitudinal distribution of ice on the Earth surface has been derived from the NASA's Terra and Aqua spacecrafts[1] in the period 2005-2015 and linked to temperture by associating it to the latitudinal distribution of temperatures obtained from the ERA5 dataset in the same period. This exercise has been done separately for lands and oceans. The impact of the orography in the formation of low latitude glaciers has been mitigated by calculating the fraction of land above the mean local freezing level (i.e. the altitude at which the temperature falls below 273 K due to the lapse rate) and subtracting it from the ice fraction at low latitudes ($\phi < 60°$). The impact of specific oceanographic conditions such as the polynyas[2] (Stringer & Groves, 1991) near the coastline of Antarctica have been dealt with by considering only data from the northern hemisphere.

Concerning (ii), we adopted a more flexible *generalized logistic function* (Richard, 1959):

$$f_{\mathrm{i,srf}}(\overline{T}_s) = \frac{1}{\left[1 + \xi_{\mathrm{srf}}\, e^{\theta_{\mathrm{srf}}\,(\overline{T}_s - T_{\circ,\mathrm{srf}})}\right]^{1/\xi_{\mathrm{srf}}}} \tag{5.2}$$

where $\overline{T}_s$ is the zonal temperature averaged over a time τ_{ice} representative of the time scale of ice growth and melting, $T_{\circ,\mathrm{srf}}$ is the temperature turning point, θ_{srf} is the growth rate and ξ_{srf} is the shape parameter. The index *srf* refers to the type of surface over which we are calculating $f_{\mathrm{i,srf}}$, where *ocn* stands for oceans and *lnd* stands for lands. τ_{ice} has been chosen to be equal to 12 months, for consistency with the observational data. The values for these parameters, reported in Table 5.1, have been tuned to both reproduce the ice fraction data in Fig 5.1, right panel and the mean latitudinal ice fraction distribution in (see Fig. 5.3, lower right panel).

5.1.3 Ice albedo

In the ESTM1 a single albedo (equal to 0.70) for all kind of frozen surface was adopted, with no dependence on the zenith angle of the incident light. ESTM2 both drops the Lambertian idealization by adopting Eq. 5.1 and distinguishes between the formation location of ice. Concerning the former, a *weak* z-dependence is considered, in line with observational data

[1] https://modis.gsfc.nasa.gov/

[2] The combined effects of katabatic winds from the mountainous interior of Antarctica and ocean currents form mesoscale areas of open water surrounded by sea ice.

from Briegleb (1992). Concerning the latter, stable ices formed on land by snow deposition and on ocean by seawater freezing are associated to two different $\alpha_{\mathrm{srf}}(0.5)$, respectively equal to 0.70 and 0.55. These values are in the range found by experimental measurements and provide a good match to the latitudinal zonal profile of Earth albedo.

An additional problem when considering the contribution of ice to the planetary albedo is related to the distinction between permanent and transient ice. In the ESTM1 this problem has been tackled by triggering a special condition when a given latitudinal zone is below 273 K for more than half of the orbital period (see the last paragraph of Section 2.1.2). In ESTM2, that condition has been removed and has been substituted by an estimation of the patchiness of ice coverage in the temperature range at which the transition between completely frozen and completely unfrozen surfaces occurs. The fractional ice coverage $f_{\mathrm{i,x}}$ can be considered a reasonable tracker of this patchiness, thus the following relation has been adopted:

$$\alpha_{\mathrm{i,srf}}(\overline{T}_s) = \alpha_{\mathrm{srf}} + (\alpha_{\mathrm{i,srf}}^{\mathrm{stab}} - \alpha_{\mathrm{srf}}) f_{\mathrm{i,srf}}(\overline{T}_s) \tag{5.3}$$

where *srf* can refer to either *lnd* or *ocn*, $\alpha_{\mathrm{i,srf}}^{\mathrm{stab}}$ is the albedo of stable ice reported in the previous paragraph and α_{srf} is the albedo of the underlying land or ocean. The resultant $\alpha_{\mathrm{i,srf}}(\overline{T}_s)$ is calculated for $\mu = 0.5$ and is then used in Eq. 5.1 to obtain the actual T- and z-dependent ice albedo.

Finally, concerning the thermal inertia of ice, ESTM2 follows the same approach used for the albedo. For oceans, which provide the main contribution to the planetary thermal inertia, the following relation has been adopted:

$$C_{\mathrm{i,ocn}}(\overline{T}_s) = C_{\mathrm{ocn}} + (C_{\mathrm{i,ocn}}^{\mathrm{stab}} - C_{\mathrm{ocn}}) f_{\mathrm{i,ocn}}(\overline{T}_s) \tag{5.4}$$

where $C_{\mathrm{i,ocn}}^{\mathrm{stab}}$ is the thermal inertia of stable ice over ocean. On the other hand, for land the contribution is very small overall and there is no need to adopt a scaling relation. Thus, $C_{\mathrm{i,lnd}}^{\mathrm{stab}} = C_{\mathrm{lnd}}$.

5.1.4 Cloud fraction

The complexity of the microphysics of cloud formation and the lack of fluidodynamics capabilities prevent ESTM2 to model in detail the distribution and properties of clouds. However, ignoring completely their contributions to the OLR and the TOA albedo by running clear-sky simulations would have caused large errors and prevented a meaningful comparison with Earth observational data. As such, some simple parameterizations have been adopted.

The cloud fraction is calculated both in ESTM1 and 2 by using the expression:

$$f_{\mathrm{c}} = f_{\mathrm{ocn}}[(1 - f_{\mathrm{ocn}}) f_{\mathrm{c,ocn}} + f_{\mathrm{i,ocn}} f_{\mathrm{c,i}}] + f_{\mathrm{lnd}}[(1 - f_{\mathrm{i,lnd}}) f_{\mathrm{c,lnd}} + f_{\mathrm{i,lnd}} f_{\mathrm{c,i}}] \tag{5.5}$$

where $f_{\mathrm{c,ocn}}$, $f_{\mathrm{c,lnd}}$ and $f_{\mathrm{c,i}}$ are representative values of the cloud coverage over ocean, lands and ice, respectively. In ESTM2, $f_{\mathrm{c,ocn}}$ and $f_{\mathrm{c,lnd}}$ have been fixed to the average observational values for Earth as found by King et al. (2013), which are equal to 0.72 and 0.55, respectively. Instead, $f_{\mathrm{c,i}}$ has been made dependent on the temperature. In fact, the cloud fraction is strongly influenced by the availability of both cloud condensation nuclei and by water vapor in the atmospheric column. Both these factors are expected to decrease on planets with a lower average temperature and larger planetary ice fractions. In the limit case of a Snowball climate state, a substantial reduction of the cloud coverage is expected, even though 3D GCM simulations predict that clouds do not completely disappear (Le Hir et al., 2010; Hu et al.,

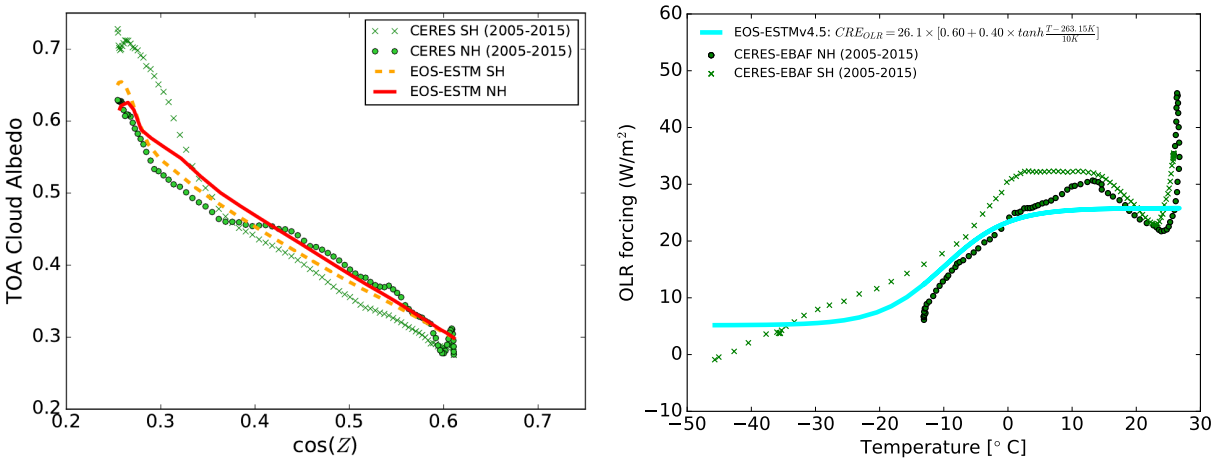

Figure 5.2: Left panel: the cloud albedo as a function of μ. Green crosses and circles are, respectively, the observational data for Southern and Northern hemisphere reduced using Eq. 5.7. Red-solid and orange-dashed lines are ESTM2 results as obtained applying Eq. 5.8, for Southern and Northern hemisphere, respectively. Credit: Biasiotti, Simonetti et al. (2022). Right panel: observational data on cloud OLR forcing as a function of T_s. Circles and crosses represent zonal yearly averages.

2011; Abbot, 2014). In order to test different scenarios, the parameter f_c^{sb} (representative of the cloud coverage for a hard Snowball state) has been introduced and the cloud fraction over ice is now related to the global ice fraction $\langle f_i \rangle$. When $\langle f_t exti \angle = 1$ the model gives $f_{c,i} = f_c^{sb}$. In practice, the adopted expression reads:

$$f_{c,i} = (f_{c,i,\oplus} - f_c^{sb}) \left(\frac{1 - \langle f_i \rangle}{1 - \langle f_i \rangle_\oplus} \right) + f_c^{sb} \tag{5.6}$$

where $f_{c,i,\oplus} = 0.56$ is the cloud coverage over ice calibrated on Earth Northern hemisphere data. Southern hemisphere data has not been used due to the peculiar orography of Antarctica, where most of the Southern hemisphere ice resides. It can also be noted that the Earth model is not affected by the choice of f_c^{sb}, since $f_{c,i} = f_{c,i,\oplus}$ when $\langle f_i \rangle = \langle f_i \rangle_\oplus$. As per default we adopt $f_c^{sb} = 0$.

5.1.5 Cloud albedo

Cloud albedo in ESTM1 was modeled via a two-sloped function of z. In the areas covered by clouds, their albedo substituted that of the underlying surface. That approach was suggested by Cess (1976), who derived their relation from the dataset of Ellis & Haar (1976). In order to upgrade this prescription in ESTM2, the first step consisted in searching a more recent and complete set of observations. To this purpose, the zonal TOA albedo data from the CERES-EBAF spacecraft (Loeb et al., 2018) were selected and reduced using the expression:

$$\alpha_{clo}^{obs} = \frac{\alpha^{obs} - \alpha_{clear}^{obs}(1 - f_c)}{f_c} \tag{5.7}$$

where α^{obs} are the zonal TOA albedo data from CERES and α_{clear}^{obs} are the zonal clear-sky albedo data for the same zone. In this manner it was possible to disentagle the contributions

from clouds on one hand and atmospheric Rayleigh scattering and the surface on the other. To derive the experimental μ dependence, $\alpha_{\rm clo}^{\rm obs}$ was then associated with the average value of μ over with data were tabulated, which is one year.

These new data were then used to fit the following relation:

$$\alpha_{\rm clo}(\mu) = \alpha_{\rm clo}(0.5) + m_{\rm clo}(\mu - 0.5) \tag{5.8}$$

where $m_{\rm clo} = -0.67$ is the slope and $\alpha_{\rm clo}(0.5) = 0.44$ is the cloud albedo at $\mu = 0.5$ ($z = 60^\circ$). In practice, these are free parameters that have been tuned to match the cloud albedo data from the CERES-EBAS spacecraft shown in Fig. 5.2, left panel. This parameterization was adopted to make the calculation of cloud albedo consistent with those of land, ocean and ice albedos, which are all expressed as a smooth function of μ and $\alpha_{\rm srf}(0.5)$.

Another upgrade concerned the dependence of the effective cloud albedo $\alpha'_{\rm clo}$ on the albedo of the underlying surface. This is especially important for the polar clouds that have a relatively high short-wavelength transmittance, thus making the final albedo of the cloudy fraction dependent on the highly reflective ices on the surface. This effect is cleary visible in the data as a change in the slope of the $\alpha_{\rm clo}$ vs μ at low μ (i.e., high z): this transition happens at latitudes where the surface albedo increases steeply due to the presence of the ice caps. To incorporate this effect, ESTM2 adopts the relation proposed by Thompson & Barron (1981). The effective cloud albedo is thus equal to:

$$\alpha'_{\rm clo} = \alpha_{\rm clo} + \frac{(1-\alpha_{\rm clo})(1-\alpha^*_{\rm clo})}{\alpha^*_{\rm clo}} \left(\frac{1}{1 - \mathcal{T}^2_{\rm clo}\, \alpha^*_{\rm srf}\, \alpha^*_{\rm clo}} - 1 \right) \tag{5.9}$$

where $\alpha_{\rm clo}$ is the cloud albedo over a completely unreflective surface, $\alpha^*_{\rm clo}$ is the cloud albedo for diffure radiation, $\alpha^*_{\rm srf}$ is the surface albedo for diffuse radiation and $\mathcal{T}_{\rm clo}$ is the cloud shortwave transmittance. The values of diffuse albedo are estimated from the corresponding direct reflection albedo calculated at $\mu = 0.5$, while $\mathcal{T}_{\rm clo}$ is estimated with the function:

$$\mathcal{T}_{\rm clo} = 0.90 - 0.05 \tanh\left(\frac{T_s - 263.15}{10} \right) \tag{5.10}$$

which provides a smooth transition between the typical transmittance of a thin polar cloud (∼0.95, see Thompson & Barron, 1981) and the lower transmittance of thicker, low latitude clouds. In this case, the temperature that it is considered is the instantaneous one, rather than the yearly average. Since at low latitudes the surface albedo is low, the term $\mathcal{T}^2_{\rm clo}\, \alpha^*_{\rm srf}\, \alpha^*_{\rm clo}$ is small and the exact choice of $\mathcal{T}_{\rm clo}$ has only a modest impact on the calculation of $\alpha^*_{\rm clo}$.

The comparison between ESTM2 results and observational data can be seen in Fig. 5.2, left panel. The match is especially good for the Northern hemisphere in the polar regions and in the Southern hemisphere at mid latitudes, which are less influenced by the orographic features of Antarctica.

5.1.6 Cloud OLR forcing

In ESTM1, the cloud OLR forcing (CRE) has been taken as constant and fixed to the average value of modern terrestrial clouds. However, this approach is unsatisfactory, since CRE measurements present a large seasonal and latitudinal scatter (see e.g. Fig. 10 in Hartmann et al., 1992). In fact, while clouds remain optically thick in the thermal IR down to very low condensed water columnar masses (~ 50 g m^{-2}, Pierrehumbert, 2010), their impact on OLR

depend on the altitude of their tops, which vary both seasonally and latitudinally. Data shows a general reduction of the CRE as a function of the surface temperature (see Fig. 5.2, right panel). On polar regions, the forcing can be down to 90% lower than the average value, while on the Tropics in can be up to 100% higher. To reproduce these features one needs a 3D GCM with treatment of the cloud formation and circulation. However, as an improvement over the previous versions, we introduced a distiction for clouds over polar regions. In fact, under the constant CRE scheme it was impossible to reproduce the average Earth latitudinal OLR over the poles, irrespectively of the RT prescriptions adopted (CCM3 or EOS). Matching the data would have required a change in the clear-sky OLR vs T_s slope that is not seen in any of the RT codes showed in Chapter 4: the linearity of the clear-sky OLR in T_s has been pointed out in several other works (see e.g. Koll & Cronin, 2018). In ESTM2 it is thus adopted the following expression:

$$CRE = CRE_{\circ}\left[0.60 - 0.40\tanh\left(\frac{T_s - 263.15}{10}\right)\right] \tag{5.11}$$

where $CRE_{\circ}$ is a representative value calibrated on the Earth model to reproduce the average cloud forcing over the entire planet. The temperature considered is the instantaneous one. By dropping the CRE at low T_s, this prescription improves significantly the match with Earth observational data.

5.2 Validation against modern Earth data

In order to test the reliability of the radiative fluxes obtained with the EOS procedure, the OLR and TOA albedo tables obtained with EOS were employed to calculate the present-day climate of the Earth using ESTM2. While EOS can be used to study the RT properties of any atmosphere, we focused on the modern Earth case due to large availability of high quality experimental data. This allowed us to compare most of the parameters adopted in the climate model with observational quantities. While a small amount of tuning of the free parameters has been done, the very good agreement between simulated and observed quantities make us confident in the recipes adopted both in ESTM2 and in EOS. Unless differently specified, all the experimental data used in the validation procedure are averaged for the 2005-2015 period.

5.2.1 Input parameters

For this set of tests, aimed at reproducing the current Earth climate state, we adopted the Earth planetary parameters in ESTM2 and the Earth atmospheric parameters in EOS. Concerning the former, the instellation was set to 1361 $\mathrm{Wm^{-2}}$(to be compared with the measured CERES value of 1361.16 $\mathrm{Wm^{-2}}$), the orbital eccentricity to 0.016710, the axis obliquity to 23.439°, the surface gravity acceleration to 9.81 $\mathrm{ms^{-2}}$ and the Earth latitudinal distribution of lands.

Concerning the latter, we adopted a modified moist adiabat (as presented in Chapter 2) with a constant relative humidity of 60%, a stratospheric temperature of 200 K and a surface dry pressure of 1.00×10^5 Pa. The atmosphere included N_2, O_2, CO_2, CH_4 and H_2O as radiatively active species, with the concentrations of CO_2 and CH_4 set, respectively, to 350 ppmv and 1.7 ppmv. These values are slightly lower than those measured in the 2005-2015 period (390 and 1.8, respectively), because it must be considered that, due to anthropogenic

greenhouse emissions, Earth is currently out of radiative equilibrium. This imbalance amounts to ~ 0.6 Wm^{-2}and makes the Earth climate to lag with respect to the instantaneous GHGs concentrations. Since we perform equilibrium calculations, we corrected for this effect by applying Eq. 2.14 to retrieve the amount of GHGs related to the measured imbalance. At the emission rate of that time, this corresponds to a ~ 15 year lag. Radiative transfer calculations were performed on a 60-layer atmospheric column logarithmically spaced in pressure, from the ~ 1 bar surface to the 1 μbar TOA level (10 layers per order of magnitude). The OLR was evaluated as a function of T every 20 K below 280 K, every 10 K between 280 K and 310 K and every 5 K up to 360 K. The TOA albedo was evaluated every 20 K in the entire T range up to 360 K, for $Z \in (0°, 30°, 45°, 60°, 70°, 75°, 80°, 83°, 85°, 87°, 88°, 89°)$ and for $a_{\rm srf} \in (0.0, 0.15, 0.30, 0.60, 0.90)$. The TOA albedo at 90° is extrapolated by means of a third order polynomial fitted on the EOS-calculated values for the previous three Z angles. The TOA albedo at $a_x = 1.0$ is set to 1.0, but it is never reached during climate simulations. We adopted a non-equally spaced grid in order to sample more precisely the regions in which the OLR and the TOA albedo change their slopes. Multilinear interpolation on both OLR and TOA albedo tables is then carried out by ESTM2.

5.2.2 Results

The validation of the coupled EOS-ESTM2 model has been done by considering two broad set of variables, both averaged over one orbital period: global and zonal. Concerning the global variables, the results are shown in Table 5.2. Observations are reported in the third column whereas model results are shown in the fourth column. The agreement is very good, with relative differences below 2% for albedo and ~ 0.4% for the OLR, and together with the rest of the set of data consitutes an indirect validation of EOS.

Concerning zonal quantities, the results are shown in Figure 5.3. Going clockwise from the upper left panel the surface temperature, the TOA albedo, the OLR and the ice fraction profiles are presented. The agreement of the surface temperature curve (top left panel) is excellent, with an area-weighted rms deviation of 1.0 K for the Northern hemisphere. The main difference arise above the South Polar cap, where the observed temperature is ~ 20 K lower than predicted due to the lack of orography of the model.This difference is consistent with the ~ 2 km thickness of the ice sheet and a dry lapse rate of ~ 10 K/km.

The albedo curve (top right panel) shows an excellent agreement in the Northern Hemisphere at mid-high latitudes, where the gradual change of the albedo of transient ice provided by Eq. 5.4 yields a better match to the data than in the ESTM1. In the equatorial regions the agreement is reasonable, considering the existence of albedo factors that can only be treated in 3D models, such as the atmospheric circulation, which affects the clouds distribution. In the Antarctic region, the model underestimates the albedo due to the lack of orography.

The OLR profile (bottom left panel) shows a general agreement, with strong deviations in Antarctica and in the tropical regions. The OLR excess predicted by the model over Antarctic regions is due to the temperature excess that we have already discussed. The bumps of OLR emission measured at the edges of tropical regions are connected with the presence of large deserts and of low clouds with warm tops, while the reduced equatorial OLR is connected with the presence of deep convective clouds with cold tops (see e.g. Hartmann, 2016). Neither of these two features can be captured by our model (or other 2D models). The good match between model and observations in the North polar region is an improvement with respect to the ESTM1, and is due to the fact that the scaling factor presented in Eq. 5.11 rises the

Table 5.2: Earth satellite data and results of the Earth reference model, using ESTM2 coupled with the RT lookup tables produced either by EOS (column 4) or CCM3 (column 5, "CCM3 new"). We also included the results obtained by ESTM1 coupled with CCM3 (column 6, "CCM3 old"). Data in columns 3 and 4 have been taken from Biasiotti, Simonetti et al. (2022). Data in column 5 have been generated for this work. Data in column 6 have been taken from Vladilo et al. (2015).

Quantity	Description	Observations	EOS	CCM3 new	CCM3 old	Units
$\langle T_s \rangle$	Global surface temperature	287.5[a]	288.7	277.2	nd	K
$\langle T_s \rangle_{\mathtt{NH}}$	Mean surface temperature of Northern hemisphere	288.4[a]	288.5	275.8	288.6	K
$\Delta T_{\mathtt{PE}}$	North Pole-Equator temperature difference	38.9[a]	41.1	52.8	41.7	K
$\langle h \rangle_{\mathtt{NH}}$	Fraction of habitable surface (Northern hemisphere)	0.866[b]	0.855	0.648	0.858	...
$\langle A \rangle$	Global top-of-atmosphere albedo	0.314[c]	0.315	0.396	nd	...
$\langle A \rangle_{\mathtt{NH}}$	Mean top-of-atmosphere albedo of Northern hemisphere	0.310[c]	0.314	0.408	0.323	...
$\langle OLR \rangle$	Global outgoing longwave radiation	240.2[c]	241.4	217.7	nd	Wm^{-2}
$\langle OLR \rangle_{\mathtt{NH}}$	Mean outgoing longwave radiation of Northern hemisphere	240.8[c]	241.6	215.6	237.6	Wm^{-2}
$\langle f \rangle_c$	Global cloud fraction	0.674[c]	0.666	0.618	0.670	..
$\langle f \rangle_{c,\mathtt{NH}}$	Mean cloud fraction of Northern hemisphere	0.644[c]	0.646	0.599	nd	..
$\langle CRE \rangle$	Global cloud forcing	25.8[c]	25.5	23.1	26.4[d]	Wm^{-2}
$\Phi_{\mathtt{max}}$	Peak of atmospheric transport at mid latitudes	5.0[e]	5.0	6.0	4.9	PW

a. Average ERA5 temperatures in the period 2005-2015.
b. Average fraction of planet surface with temperature satisfying the liquid water criterion, i.e. that is unfrozen year long.
c. Average CERES-EBAF data in the period 2005-2015.
d. IN ESTM1, this quantity is fixed a priori to the value found by Stephens et al. (2012).
e. Datum from Trenberth & Caron (2001).

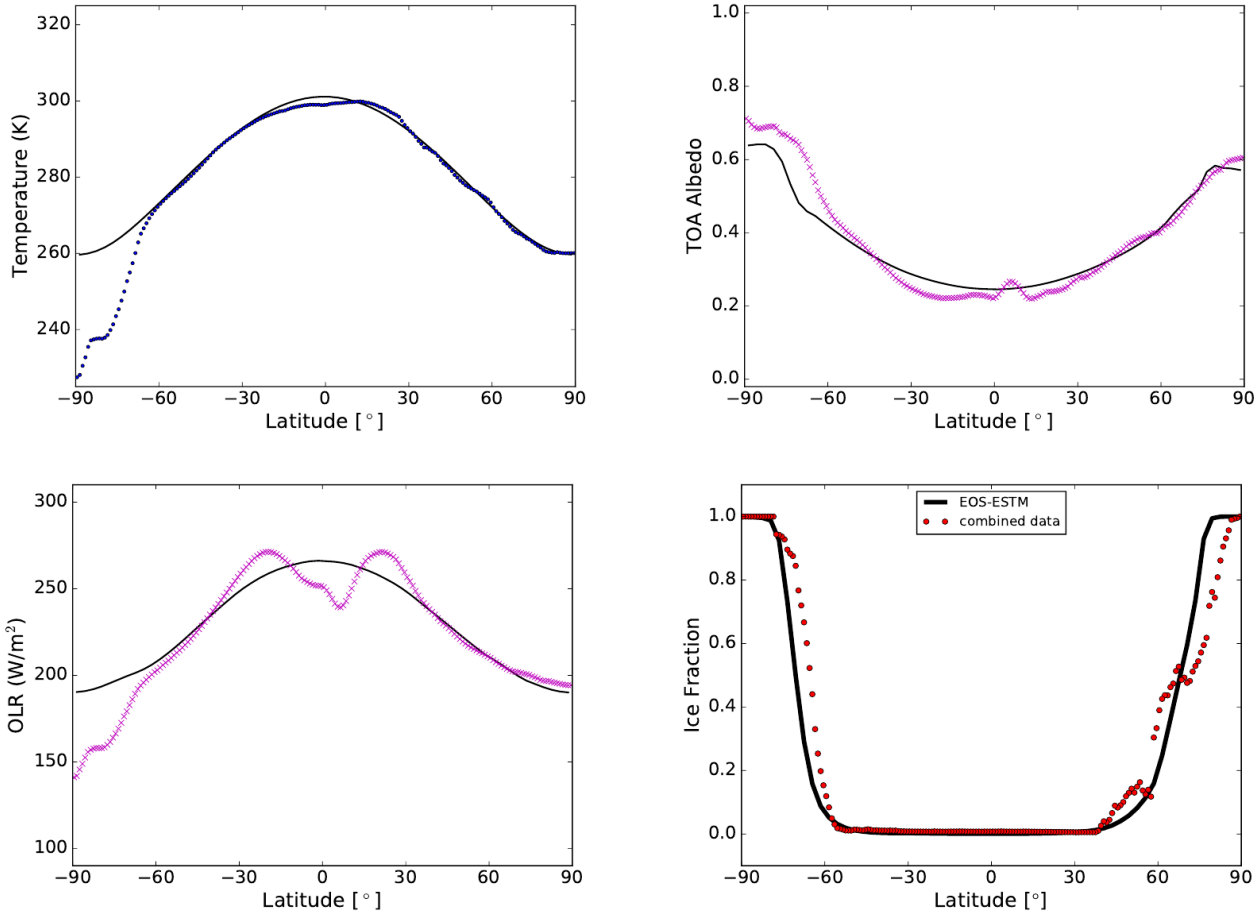

Figure 5.3: Mean annual latitude profiles of four quantities as predicted by the reference Earth model (solid lines). Top left panel: the temperature profile, compared with ERA5 temperatures averaged in the period 2005-2015 (blue dots). Top right panel: the albedo profile, compared with CERES-EBAF data averaged in the period 2005-2015 (pink crosses). Bottom left panel: the OLR profile, compared with CERES-EBAF data averaged in the period 2005-2015 (pink crosses). Bottom right panel: the ice fraction profile compared with Terra and Aqua spacecrafts coverage data, averaged in the period 2005-2015. Credit: Biasiotti, Simonetti et al. (2022).

planetary OLR emitted from frozen regions.

In the bottom-right panel we show a diagnostic test on ice coverage that was not performed by Vladilo et al. (2015). The mean annual zonal coverage of ice predicted is in general agreement with the area-weighted lands and oceans data (red dots). This implies that the new algorithm that we have introduced, based on Eq. 5.2, is able to capture the main characteristics of ice coverage, using the dependence on a single parameter, namely the surface temperature. A future improvement of this parameterization will be a treatment of the physics of ice formation and melting that in addition to the dependence on temperature, may account for the timescale of these processes.

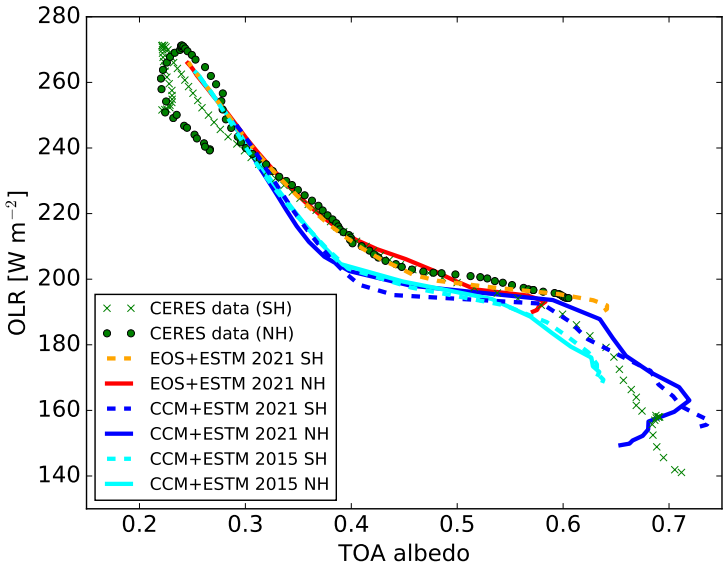

Figure 5.4: Mean annual values of OLR and TOA albedo of the present-day Earth at different latitudes for the Northern and Southern hemispheres. Green circles and crosses: experimental data obtained with the CERES satellite averaged over the period 2005-2015 for the Northern and Southern hemisphere, respectively. Solid lines: model predictions for the Earth Northern hemisphere. Dashed lines: model predictions for the Southern hemisphere. Colors codifies the ESTM version and the RT model adopted: red/orange for EOS+ESTM2, blue for CCM3+ESTM2 and light blue for CCM3+ESTM1.

5.2.3 Disentagling EOS and ESTM contributions

A question that now may arise is: how much merit does EOS have in reproducing the Earth climate? This is a legitimate question in the light of the parameterizations adopted in ESTM. Even though the specific recipes for surface albedos, ice formation etc. have been tested one by one against observational data, there remains a certain amount of fine tuning. Does this fine tuning allow for the indirect validation of any RT model, and not only EOS? A thorough answer to this question would have needed a PhD thesis of its own. However, a partial investigation have been done by comparing the results from ESTM2 when coupled to two different RT models, namely EOS and CCM3. CCM3 has been used in the previous version of the ESTM, thus allowing also to study how the enhancements presented in Section 5.1 impact the results. In other words, it allows us to partially disentangle the contributions from EOS and ESTM in matching the observational data.

For this comparison, we have run three models: ESTM1 coupled with CCM3, ESTM2 coupled with CCM3 and ESTM2 coupled with EOS. The adopted atmospheric composition and structure for the RT models are the same. We then analyzed two sets of data: the global and Northern hemisphere averages reported in Table 5.2 on one hand, and the OLR vs TOA albedo trend on the other. Again, the results have been compared with observational data and with each other.

Concerning the first set of data, it is clear that using the new formulations adopted in ESTM2, the CCM3 RT model is unable to reproduce satisfactorily any of the variables considered. Due to the higher TOA albedo at every $(T_s, z, \alpha_{\text{srf}})$ point produced by CCM3

with respect to EOS, the Earth model finds an equilibrium at a consistently lower average surface temperature (277.2 K vs 288.7 K). This difference is amplified by the growth of larger ice caps, that further increases the overall planetary albedo in a perfect example of positive feedback (see Section 2.4.2). Larger, permanent ice caps also reduce the fraction of habitable surface by ∼25% and indirectly change the meridional transport efficiency, which increases the Pole-Equator temperature difference. Finally, due to the newly introduced feedback on cloud fraction and forcing (Sections 5.1.4 and 5.2.1), we observe a reduction of both these quantities, which again act as a positive feedback. Instead, employing the CCM3 lookup tables in ESTM1 produces better results. In this case, the equilibrium state found is near to that of the real Earth, even though the offset is larger for every quantity in Table 5.2 except the global cloud fraction. However, it shoud be considered that ESTM1 parameterization is more hardwired to the current Earth climate (since, for example, it fixes $\langle CRE \rangle$ to an Earth-specific value), which naturally results in a better agreement with observations. It should also be considered that ESTM1 uses a slightly higher insolation value, equal to 1362 Wm^{-2}.

Also the second set of data shows that the coupled EOS-ESTM model fares better than the others. The comparison can be seen in Fig. 5.4 Using CCM3 gives a steeper OLR vs TOA albedo relation even when the smoother prescriptions concerning ice albedo and fractions are adopted. There are two regions of this plot that none of the models can reproduce adequately, which are the strong OLR reduction at the South pole (the tail in the lower right part of the plot) and the reduction of the OLR at the ITCZ (upper left part of the plot). The first is, again, due to the orography of Antarctica, which reduces the surface temperature and thus the OLR. The second is caused by the formation of dense clouds with high altitude, cold tops in the ascending part of the Hadley cell that depresses the OLR. The blue curve (CCM3+ESTM2) do extend to lower OLR and higher albedos, but as it has been mentioned previously, this is caused by the fact that the planet falls into a consistently colder equilibrium state when these RT prescriptions are used.

Chapter 6

Habitability in binary star systems

In this Chapter I present my work on habitability in binary star systems. Binary stars are unique environments with very specific features that must be considered when searching for habitable planet candidates. Here, I show how we identified the sets of binary star orbital parameters that are best suited for the presence of a circumstellar or circumbinary planet in the system, as presented in Simonetti et al. (2020). In the next Chapter I will show how we applied EOS and ESTM to an exotic study case inspired by these results, namely a non-tidally locked planet around an M dwarf secondary that it is kept warm by instellation from the primary.

6.1 Habitability in binary systems: a Monte Carlo Approach

Most studies of habitability are focused on planetary systems orbiting single stars, in particular Solar twins hosting an Earth-like planet. However, the advancements in the characterization of exoplanetary systems have shown that our system is just a single possible outcome among many different architectures (Hatzes, 2016). The studies of planetary habitability must therefore take a broader perspective. In this respect, an important point to consider is that $\sim 50\%$ stars in the field are in binary or even multiple star systems (Duquennoy & Mayor, 1991; Kouwenhoven et al., 2007; Bergfors et al., 2010; Raghavan et al., 2010; Duchêne & Kraus, 2013; Tokovinin, 2014). Therefore, the impact of stellar binarity must be taken into account in studies of planetary formation and habitability (see, e.g., Pilat-Lohinger et al., 2019).

The efficiency of planetary formation in binary and multiple systems with respect to single stars is debated, since the presence of multiple stars may affect the protoplanetary disk. This is true both for the circumstellar case (Quintana et al., 2007; Jang-Condell, 2015; Thebault & Haghighipour, 2015; Rafikov & Silsbee, 2015a) and for the circumbinary case (Quintana & Lissauer, 2006; Bromley & Kenyon, 2015; Czekala et al., 2019). However, it is a fact that a relatively large number of planets in binary stellar systems have been discovered, both in circumstellar (e.g. Hatzes et al., 2003; Barnes et al., 2020) and in circumbinary (e.g. Doyle et al., 2011; Kostov et al., 2020) orbits. As of June 2020, based on the catalogue by Schwarz et al. (2016)[1], 150 exoplanets have been found in 102 binary systems and 36 exoplanets in 26 multiple star systems. Currently, exoplanet-hosting stars in binary systems amount to about

[1] http://www.univie.ac.at/adg/schwarz/multiple.html

$\sim 2\%$ of the total, but increasing the completeness of the sample this percentage could go up to $10 - 15\%$ (Raghavan et al., 2006; Mugrauer & Neuhäuser, 2009; Roell et al., 2012). The latter number provides the rationale for a systematic, statistical approach to assess the impact of stellar binarity on planetary habitability of the kind we address here.

Only planets in stable orbits can benefit from climatological conditions that allow the long-term persistence of liquid water. Therefore a prerequisite of planetary habitability in binary systems is the existence of regions of dynamical stability in the three-body system. The existence of dynamically stable regions is a simplification (for instance, stable planetary orbits could be forced to relatively high value of eccentricity, see Georgakarakos, 2006; Georgakarakos & Eggl, 2015) but it is nonetheless a good starting point. Numerical integrations of the general three-body problem indicate that regions of dynamical stability do exist in binary systems (Harrington, 1977; Rabl & Dvorak, 1988; Dvorak & Henrard, 1988; Dvorak et al., 1989; Holman & Wiegert, 1999; Doolin & Blundell, 2011; Quarles et al., 2018, 2020). Two main dynamical classes are possible: circumstellar orbits around one component of the system (S-type orbits) and circumbinary orbits around both stars (P-type orbits). For S-type orbits dynamical stability is achieved when the planetary semi-major axis is smaller than a critical value $a_{\rm crit,S}$, whereas for P-type orbits the stability region is found outwards of a critical value $a_{\rm crit,P}$. From dynamical simulations of 10^4 binary orbits, Holman & Wiegert (1999) extracted empirical expressions to estimate critical values of orbital stability as a function of the binary parameters. A reassessment of these calculations, based on a much larger number of simulations, covering 10^6 binary orbits and a broader space of dynamical configurations (e.g. non-coplanar planetary orbits), was recently performed by Quarles et al. (2018, 2020). The basic results concerning the location of the stability regions found by Holman & Wiegert (1999) are confirmed by these works. It should be noted that there is not a complete distinction between stable and unstable regions: islands of stability can exist inside otherwise unstable regions and vice versa due to the interplay between competing orbital resonances. However, these resonant configurations would probably be the exception rather than the rule. The same is true for L-type orbits around the L_4 and L_5 Lagrangian points of the binary system (Schwarz et al., 2012) which are only relevant for a minority of systems (Holman & Wiegert, 1999). In the present work we focus on the habitability of coplanar S-type and P-type orbits and we adopt the analytical expressions for $a_{\rm crit,P}$ and $a_{\rm crit,S}$ provided by Quarles et al. (2018) and Quarles et al. (2020), respectively.

The effects of insolation on the habitability of circumstellar and circumbinary regions in binary systems has been investigated by several authors (Kane & Hinkel, 2013; Kaltenegger & Haghighipour, 2013; Haghighipour & Kaltenegger, 2013; Cukier et al., 2019). A common approach of these studies is to combine the flux from the two stars by properly weighting each contribution so to define radiative HZs for binary systems. In some cases analytical expressions of the HZ incorporating the stability conditions have been derived (Eggl et al., 2012; Cuntz, 2014; Wang & Cuntz, 2017). In general it is found that radiative HZs intersecting the stability regions can exist. The habitability around low-mass stars could even improve in binary systems with respect to the single star case, because tidal breaking between the two stars is expected to reduce the magnetic dynamo action and thereby the stellar activity that leads to erosion of the planetary atmosphere (Mason et al., 2013, 2015; Zuluaga et al., 2016). Moreover, May & Rauscher (2016) and Haqq-Misra et al. (2019) demonstrated that atmospheric redistribution and surface heat capacity are able to contain surface temperature oscillations within less than few percent in a variety of cases. On the other hand, Popp & Eggl (2017) found that the periodic radiative forcing due to the binary orbital mechanics

have important effects on the planet's climate. In Yadavalli et al. (2020) this forcing is studied in relation also to other binary parameters, most importantly the mass ratio between the components. (Quarles et al., 2019) found that the tilt of the planetary rotation axis is particularly complex to stabilize in binary systems, a condition that can negatively affect the planetary habitability. Finally, circumstellar planets are subject to secular perturbations from the distant companion star which may undermine the dynamical stability of the radiative HZ in presence of a Jupiter-like planet external to the HZ (Bazso & Pilat-Lohinger, 2019).

Given the potential capability of binary stellar systems to host habitable exoplanets, we introduced a statistical approach aimed at quantifying the circumstellar and circumbinary properties of habitability as a function of the stellar and orbital parameters of the systems. Starting from a set of statistical distributions constrained by observations of binary stars, we generated a large number of binary systems by means of Monte Carlo simulations. We limited our attention to systems with main-sequence stars, the most interesting from the point of view of long-term habitability. For each system, we calculated the location and extension of the circumstellar and circumbinary regions with long-term habitability conditions, both in terms of insolation and dynamical stability.

6.2 Methods

The main steps of our methodology can be summarized as follows. First we generate a Monte Carlo sample of binary systems. For each system of the sample we then calculate the boundaries of circumbinary and circumstellar regions where (1) the planetary orbits are dynamically stable and (2) the insolation allows the long-term existence of surface liquid water. Finally we investigate the habitability of the circumstellar and circumbinary regions of the simulated sample as a function of binary system parameters.

6.2.1 Building the sample of binary systems

The sample of binary systems is generated by random sampling of probability density functions (PDFs) of stellar masses, orbital periods, mass ratios, and orbital eccentricities that we now describe in detail.

The primary star mass function

First, we draw the mass of the primary star ($m_{\rm A}$) of the system using a mass function (MF), $\xi(\log m)$, which represents the number of stars per unit volume per logarithmic mass interval $d\log m$. To this end we use empirical relations derived for stars of the Galactic disk (Chabrier, 2003). For $m \leqslant 1\,{\rm M}_\odot$ we adopt the log-normal distribution $\xi(\log m) = A\exp\{-(\log m - \log m_c)^2/2\sigma^2_{\log m}\}$ with $A = 0.086$ pc^{-3} $(\log {\rm M}_\odot)^{-1}$, $m_c = 0.079\,{\rm M}_\odot$, and $\sigma_{\log m} = 0.69$. For $m > 1\,{\rm M}_\odot$ we adopt the classic power law suggested by Salpeter (1955), $\xi(\log m) = A\,m^{-x}$. Since high-mass stars evolve significantly in the course of a Hubble time we use two different sets of parameters, one representative of the initial mass function (IMF) and the other of the present-day mass function (PDMF). In practice, we adopt $A = 4.43\times10^{-2}$ pc^{-3} $(\log {\rm M}_\odot)^{-1}$ and $x = 1.3$ for the IMF and $A = 4.4\times10^{-2}$ pc^{-3} $(\log {\rm M}_\odot)^{-1}$ and $x = 4.37$ for the PDMF (Chabrier, 2003). The stellar mass is drawn in the range $0.1 \leqslant m/({\rm M}_\odot) \leqslant 1.5$, which is within the range of validity of the above distributions (the parametrization of the PDMF that we use is valid up to $m = 3.5$ M$_\odot$). Stars with $m > 1.5$ M$_\odot$ are not considered

because they are less frequent and because they are less interesting for studies of habitability given the fact that their lifetime on the main sequence is small compared to the evolutionary timescales for terrestrial life as we know it.In Sec. 6.3.3 we explore the impact of a possible spectral type-dependent occurrence of primary stars in binaries different from that of single stars.

The distribution of stellar orbital periods

As a second step, we draw a value for the orbital period of the binary system in days, P_b, using the log-normal distribution suggested by Raghavan et al. (2010):

$$\xi(\log P_b) \propto \exp\{-(\log P_b - \log \overline{P_b})^2 / 2\sigma^2_{\log P_b}\} \tag{6.1}$$

with $\overline{P_b} = 3.69$ and $\sigma_{\log P_b} = 1.3$ for M-type primary stars and $\overline{P_b} = 5.03$ and $\sigma_{\log P_b} = 2.28$ for FGK-type primary stars. We use $m_\ell = 0.5\,\mathrm{M}_\odot$ as a threshold value between M-type stars and stars of earlier type. In both cases we limit our draws in the $[0.0 - 10.0]$ $\log P_b$ interval. The lower limit allows us to avoid Roche lobe overflows, while the upper limit is dictated by observations (e.g. Hartman & Lépine, 2020) which suggest that there is no clear cut in the long period tail of the distribution. After the generation of the mass of secondary star, which will be described in the next subsection, we use P_b to calculate the binary semi-major axis a_b using Newton's version of the third Kepler law.

The mass ratio distribution

As a third step, we draw a value of mass ratio of the two stars of the system, $q = m_B/m_A$, from a probability density distribution, $\xi(q)$. We explore three possibilities, namely:

1. a single slope power-law distribution, as reported by Duchêne & Kraus (2013, hereafter DK13) in their table 1;
2. a log-normal distribution, as suggested by Duquennoy & Mayor (1991, hereafter DM91);
3. a double slope power-law with an excess fraction of same mass stars, as suggested by Moe & Di Stefano (2017, hereafter MDS17).

In the first case, the distribution will have the form:

$$\xi(q) \propto q^\gamma \tag{6.2}$$

with $\gamma = 0.4$ for M-type stars and $\gamma = 0.3$ for FGK-stars, using again $m_\ell = 0.5\,\mathrm{M}_\odot$ as a conventional limit between M-type and FGK-type stars. This type of distribution favors larger values of q.

In the second case, the distribution will have the form:

$$\xi(q) \propto \exp[-(q - \overline{q})/2\sigma_q^2] \tag{6.3}$$

with $\overline{q} = 0.23$ and $\sigma_q = 0.42$ over the entire mass range. This type of distribution favors average-to-low values for q.

In the third case, the distribution will have the form:

$$\xi(q) \propto \begin{cases} q^{\gamma_L} & \text{if } q < 0.3 \\ q^{\gamma_H} & \text{if } 0.3 < q < 0.95 \\ q^{\gamma_H} + \text{Exc} & \text{if } q > 0.95 \end{cases} \tag{6.4}$$

where γ_L and γ_H are the slopes for low and high values of q, respectively, and Exc is the excess fraction of systems with same-mass stars, aka twins. This distribution is valid for F- and G-type stars, while for K- and M-type stars we will revert to DM91. For the slopes of the power law part of the distribution, $\xi_{\text{pwl}}(q)$, we have:

$$\gamma_L = 0.3 \tag{6.5}$$

$$\gamma_H = \begin{cases} -0.5 & \text{if } \log P_b < 5 \\ -0.5 - 0.3(\log P_b - 5) & \text{if } \log P_b \geqslant 5 \end{cases} \tag{6.6}$$

On the other hand, the excess fraction will be calculated as follows:

$$F_{\text{twin},0} = 0.3 - 0.15 \log\left(\frac{m}{M_\odot}\right) \tag{6.7}$$

$$F_{\text{twin}} = \begin{cases} F_{\text{twin},0} & \text{if } \log P_b < 1 \\ F_{\text{twin},0}\left(1 - \frac{\log P_b - 1}{7}\right) & \text{if } 1 < \log P_b < 8 \\ 0 & \text{if } \log P_b > 8 \end{cases} \tag{6.8}$$

$$\text{Exc} = \frac{F_{\text{twin}} \int_{0.3}^{1.0} \xi_{\text{pwl}}(q) dq}{1 - F_{\text{twin}}} \tag{6.9}$$

Eq. (6.7) gives the excess fraction (as intended in MDS17, see their Fig. 2) for short period binary systems and Eq. (6.8) scales this excess for higher periods. Finally, Eq. (6.9) gives the actual excess fraction of twins (i.e. the red area in Fig. 2 of MDS17) to be inserted in Eq. (6.4). It should be noted that we are extending to $\log P = 10$ the results of MDS17, that they derived for systems with periods up to $\log P = 8$. When $\log P_b < 5$ this distribution has two bumps, namely at $q = 0.3$ and at $q = 1.0$, and is flat overall. On the other hand, when $\log P_b > 5$ it becomes increasingly skewed towards the first bump and for high P_b is similar to the DM91 case, favoring average-to-low values of q.

After normalizing the distribution ($\int_0^1 \xi(q)\, dq = 1$), we use $\xi(q)$ to draw a value of q and calculate the mass of the secondary star as $m_{\text{B}} = q\, m_{\text{A}}$ from the value of m_{A} drawn in the first step (see 6.2.1). Since q has values in the $[0-1]$ range, m_{B} is guaranteed to be less than or equal to m_{A}.

The binary eccentricity distribution

We finally assign the orbital eccentricity, e_b, using another empirical distribution, $\xi(e_b)$. The eccentricity distribution is strongly affected by the orbital period: for P_b less than a certain value identified as the circularization period P_{circ} the orbits are circularized due to the long-term history of tidal interactions between the two stars (Duquennoy & Mayor, 1991). On the other hand, the eccentricity distribution shows a remarkably small dependence on the mass of the primary (Duchêne & Kraus, 2013). For our calculation, we test two different hypotheses:

1. a Gaussian distribution with $P_{\rm circ} = 20$ days ($\log P_b = 1.3$), as suggested by Stepinski & Black (2001, hereafter SB01);

2. a period-dependent power law distribution as suggested by MDS17.

In the first case, the function will have the form:

$$\xi(e_b) \propto \exp[-(e_b - \overline{e})^2/2\sigma_e^2] \tag{6.10}$$

$\overline{e} = 0.35$ and $\sigma_e = 0.2$ for all values of P_b above 20 days. This produces a sample with low-to-average eccentricities.

In the second case, the function will have the form:

$$\xi(e_b) \propto e^{\eta} \quad \text{with} \quad \eta = 0.6 - \frac{0.7}{\log P_b - 0.5} \tag{6.11}$$

This power law favors low eccentricities when $\log P_b < 5/3$ and favors high eccentricities when $\log P_b > 5/3$. Given that the distribution of periods produces far more binaries with $\log P_b > 5/3$, the average eccentricity of the sample will be skewed towards larger values than in the SB01 case. The circularization period adopted by MDS17 is $\log P_{\rm circ} = 0.3$, but their function is actually not normalizable if $\log P_b \leqslant 0.9375$. We therefore adopted a circularization period equal to $\log P_{\rm circ} = 0.94$, after testing that the final distribution of eccentricities is almost unaffected by this change. In fact, the fraction of systems generated with an eccentricity in the $[0.0 - 0.1]$ range is over 98% when $\log P_b = 0.94$, meaning that our results provide a good match to the observational data employed by MDS17 in their analysis. It should also be considered that MDS17 define a period-dependent maximum eccentricity, equal to:

$$e_{\rm max} = 1 - \left(\frac{P_b}{2 \text{ days}}\right)^{-2/3} \tag{6.12}$$

that further reduces the cases with high eccentricity when the orbital period is low, making even less critical our choice $\log P_{\rm circ} = 0.94$. As far as the upper end of the distribution is concerned, in our calculations we extrapolated Eq. (6.11) up to $\log P_b = 10$, that is the upper limit of period as described in sect. 6.2.1.

6.2.2 Boundaries of dynamical stability

The parameters $m_{\rm A}$, $\mu = m_{\rm B}/(m_{\rm A} + m_{\rm B})$, a_b, and e_b, drawn for each binary systems are used to explore which regions of parameter space are consistent with the existence of stable planetary orbits. To this end, we use the results of the study of orbital stability of planets in binary systems performed by Quarles et al. (2018) and Quarles et al. (2020). These authors derived empirical expressions for calculating the largest circumstellar orbit and the smallest circumbinary orbit where fully-interacting particles survive the length of the integration (10^5 binary periods). The semi-major axis of such critical planetary orbits are approximated as functions of e_b and μ. In units of the binary semi-major axis, the semi-major axis of the smallest, stable P-type orbit is:

$$\frac{a_{\rm crit,P}}{a_b} = 1.48 + 3.92\, e_b - 1.41\, e_b^2 + 5.14\, \mu + 0.33\, e_b\, \mu - 7.95\, \mu^2 - 4.89\, e_b^2 \mu^2 \tag{6.13}$$

whereas the semi-major axis of the largest, stable S-type orbit is:

$$\frac{a_{\rm crit,S}}{a_b} = 0.501 - 0.435\,\mu - 0.668\,e_b + 0.644\,\mu\,e_b + 0.152\,e_b^2 - 0.196\,\mu\,e_b^2 \quad . \tag{6.14}$$

This last expression is used for the circumstellar stability regions of both stars. For the primary, $a_{\rm crit,SA}$ is estimated adopting $\mu = m_{\rm B}/(m_{\rm A} + m_{\rm B})$, whereas for the secondary $a_{\rm crit,SB}$ is estimated adopting $\mu = m_{\rm A}/(m_{\rm A} + m_{\rm B})$. We use the above empirical expressions within the limits of validity given by Quarles et al. (2018, 2020), namely $e_b \leqslant 0.8$ and $\mu \in [0.01, 0.99]$.

6.2.3 Luminosity and effective temperature of the stars

After extracting the masses of the primary ($m_{\rm A}$) and secondary star ($m_{\rm B}$), the luminosities ($L_{\rm A}$ and $L_{\rm B}$) and effective temperatures ($T_{\rm A}$ and $T_{\rm B}$) are calculated using the PARSEC evolutionary tracks of main sequence stars by Bressan et al. (2012). The main sequence is the most interesting stage for planetary habitability thanks to the extremely low rate of luminosity evolution. For a given evolutionary track we use the mid point of the main sequence to assign the effective temperature and luminosity from a given stellar mass. We consider two different sets of tracks, one with solar metallicity ($Z = 0.017$) and one with subsolar metallicity ($Z = 0.008$), representative of stars in earlier stages of Galactic chemical evolution. To avoid extrapolation of stellar evolutionary tracks, we exclude cases with $m_{\rm B} < 0.08$ $M_\odot$, the mass threshold limit for hydrogen burning.

6.2.4 Boundaries of insolation

As in the case of single stars, the insolation boundaries of the circumbinary and circumstellar habitable zones of binaries systems depend not only on the integrated stellar flux, but also on the spectral energy distribution of the stellar radiation. The reason for this is that hotter stars emit a larger fraction of energy in the form of short-wavelength radiation that is reflected back to space from the planetary atmosphere via Rayleigh scattering. As a result, the Bond albedo of the planet increases with the effective temperature of the star (Selsis et al., 2007; Kopparapu et al., 2013a). This effect can be taken into account in binary systems by summing the fluxes of the two stars with spectral weight factors that take into account the SED of the star and the radiative properties of the planetary atmosphere (Kaltenegger & Haghighipour, 2013; Haghighipour & Kaltenegger, 2013). Following this approach we can estimate the combined flux of the two stars with the expression

$$F_{\rm eff,x} = w(T_1, \mathcal{R}_x)\frac{L_1}{r_{\rm p\text{-}1}^2} + w(T_2, \mathcal{R}_x)\frac{L_2}{r_{\rm p\text{-}2}^2} \quad , \tag{6.15}$$

where L_i is the luminosity of each of the two stars ($i = 1, 2$) and $r_{{\rm p}\text{-}i}$ the distance between the planet and each star. The term $w(T_i, \mathcal{R})$ is a spectral weight dependent on the effective temperature of each star, T_i, and on a set of atmospheric parameters, $\mathcal{R}_x$, that specify the radiative properties of the planetary atmosphere (e.g. clouds, atmospheric composition, stratification, surface pressure, etc.).

To define the insolation boundaries in a binary system, we calculate at which distance from the stars, $r_{\rm p\text{-}1}$ and $r_{\rm p\text{-}2}$, the effective flux 6.15 matches the flux received by a planet at the inner and outer edge (x = in, out) of the classic HZ around a single star (Kasting et al., 1993b). In practice, we impose the condition: $F_{\rm eff,x} = L_{\rm Sun}/l_{\rm x\text{-}Sun}^2$, where $l_{\rm x\text{-}Sun}$ is the inner or

Constant value	Runaway Greenhouse	Maximum Greenhouse	Recent Venus	Early Mars
$F_{\rm x}$ ($S_\oplus$)	1.0385	0.3507	1.7763	0.3207
$l_{\text{x-Sun}}$ (AU)	0.9813	1.6882	0.7503	1.7658
$a_{\rm x}$	1.2456×10^{-4}	5.9578×10^{-5}	1.4335×10^{-4}	5.4471×10^{-5}
$b_{\rm x}$	1.4612×10^{-8}	1.6707×10^{-9}	3.3954×10^{-9}	1.5275×10^{-9}
$c_{\rm x}$	-7.6345×10^{-12}	-3.0058×10^{-12}	-7.6364×10^{-12}	-2.1709×10^{-12}
$d_{\rm x}$	-1.7511×10^{-15}	-5.1925×10^{-16}	-1.1950×10^{-15}	-3.8282×10^{-16}

Table 6.1: Flux limits and coefficients of Eq. (6.17) from (Kopparapu et al., 2013b). Fluxes are in units of the mean orbital Earth insolation, $S_\oplus$.

outer edge of the HZ around the Sun. We adopt the parametrization of $l_{\text{x-Sun}}$ limits provided by Kopparapu et al. (2013a,b). These limits are calculated with single-column atmospheric models considering Runaway Greenhouse (RG) conditions for the inner edge and Maximum Greenhouse for the outer edge. The radiative atmospheric parameters, $\mathcal{R}_{\rm x}$, mimic an H_2O-dominated atmosphere at the inner edge and a CO_2-dominated atmosphere at the outer edge. In addition, two empirical limits are considered, namely the Recent Venus (RV) and Early Mars (EM), inferred from the possible existence of liquid water on Venus (up to 1 Gyr ago) and Mars (up to 3.5 Gyr ago), respectively. The flux limits for these four edges, taken from Kopparapu et al. (2013b), are listed in the first row of Table 6.1. The corresponding values of $l_{\text{x-Sun}}$ (AU) that we adopt are listed in the second row of the same table. As far as the spectral weights are concerned, following Kaltenegger & Haghighipour (2013), we adopt the equation

$$w(T_i, \mathcal{R}_{\rm x}) = [1 + \alpha_{\rm x}(T_i, \mathcal{R}_{\rm x})\, l^2_{\text{x-Sun}}]^{-1} \tag{6.16}$$

where

$$\alpha_{\rm x}(T_i, \mathcal{R}_{\rm x}) = a_{\rm x}\tilde{T}_i + b_{\rm x}\tilde{T}_i^2 + c_{\rm x}\tilde{T}_i^3 + d_{\rm x}\tilde{T}_i^4 \tag{6.17}$$

with $\tilde{T}_i = T_i - 5780$ K. The term $\alpha_{\rm x}(T_i, \mathcal{R}_{\rm x})$ captures the dependence of the planetary Bond albedo on the stellar effective temperature for a given set of atmospheric planetary conditions, $\mathcal{R}_{\rm x}$. Higher stellar effective temperatures give weights (6.16) smaller than 1, while for lower stellar effective temperatures the opposite is true. The coefficients $a_{\rm x}$, $b_{\rm x}$, $c_{\rm x}$, $d_{\rm x}$, derived from a 4-th order fit in T_i (Kopparapu et al., 2013a,b), are also shown in Table 6.1. These coefficients are valid for main sequence stars in the range of effective temperature $2600 < T_i < 7300$ K.

To derive the circumbinary and circumstellar boundaries of insolation we consider circular planetary orbits with constant orbital radius $r_{\text{p-1}} = a_1$ around the host star (hereafter "star 1"). The case of eccentric planetary orbits is discussed later (Section 6.3.5). We limit our attention to planetary orbits that lie inside, or in the proximity, of the regions of dynamical stability.

For circumbinary (P-type) orbits the critical semi-major axis of dynamical stability, $a_{\text{crit,P}}$, is larger than the typical distance between the two stars, $r_{12} \simeq a_b$. Since stable orbits have $a_1 > a_{\text{crit,P}}$, we assume that in the circumbinary region of dynamical stability the planet will be sufficiently distant from from both stars to justify the approximation $r_{\text{p-2}} \simeq r_{\text{p-1}}$. With this approximation the condition $F_{\text{eff,x}} = L_{\rm Sun}/l^2_{\text{x-Sun}}$ yields:

$$w(T_1, \mathcal{R}_{\rm x})\frac{L_1}{a^2_{\text{x,cb}}} + w(T_2, \mathcal{R}_{\rm x})\frac{L_2}{a^2_{\text{x,cb}}} = \frac{L_{\rm Sun}}{l^2_{\text{x-Sun}}} \quad , \tag{6.18}$$

where $a_{\rm x,cb}$ is the inner or outer edge of the radiative HZ in the circumbinary region. From this we obtain:

$$a_{\rm x,cb} = \left[w(T_1, \mathcal{R}_{\rm x})\, \widetilde{L}_1 + w(T_2, \mathcal{R}_{\rm x}))\, \widetilde{L}_2 \right]^{1/2} l_{\text{x-Sun}} \tag{6.19}$$

where $\widetilde{L}_i = L_i / L_{\rm Sun}$. This equation is valid if $a_{\rm x,cb}$ is sufficiently close to the circumbinary region of dynamical stability so that $a_{\rm crit,P}/a_b \gg 1$ and $r_{\text{p-2}} \simeq r_{\text{p-1}}$. From our simulations we find that this is generally true.

For circumstellar (S-type) orbits, the mean orbital insolation from the host star is constant, but the flux received from the other star (hereafter "star 2") evolves in time according to the instantaneous $r_{\text{p-2}} = r_{\text{p-2}}(t)$. In a reference frame centered in star 1, we have:

$$r_{\text{p-2}} = [r^2_{\text{p-1}} + r^2_{12} + 2 r_{\text{p-1}} r_{12}(\nu) \cos\theta]^{1/2} \tag{6.20}$$

where ν is the true anomaly (i.e. the position angle of star 2 along the stellar orbit with respect of the periastron) and θ is the position angle of the planet orbiting star 1. A sketch of this astrocentric configuration can be seen in the bottom panel of fig.1 in (Kaltenegger & Haghighipour, 2013). To derive $r_{\text{p-2}}(t)$ we express θ and ν as functions of t. For circular orbits around the host star, $\theta = (2\pi/P_p)t + \theta_0$, where P_p is the orbital period of the planet. On the other hand, ν does not increase linearly with time. To solve this problem, we replace the true anomaly with eccentric anomaly, E. This angle can be calculated using Kepler's equation

$$E(t) - e_b \sin E(t) = M(t) \quad , \tag{6.21}$$

where the mean anomaly $M(t) = (2\pi/P_b)t + M_0$, increases linearly with time and P_b is the orbital period of the star 2. With this formalism the distance between the two stars is

$$r_{12}(t) = a_b[1 - e_b \cos E(t)] \quad . \tag{6.22}$$

We solve this equation numerically[2] and insert the result in Eq. (6.20) to obtain $r_{\text{p-2}}(t)$. Having derived $r_{\text{p-2}}(t)$, we use Eq. (6.15) to calculate the instantaneous value of the circumstellar radiative boundary, $a_{\rm x,cs1}$, that satisfies the condition $F_{\rm eff,x} = L_{\rm Sun}/l^2_{\text{x-Sun}}$. Given the dependence of $r_{\text{p-2}}$ on $r_{\text{p-1}}$, shown in (6.20), the solution is found using numerical methods. The results are strongly dependent on the eccentricity e_b and the semi-major axis a_b of the binary system. When e_b is high and a_b is small, the boundary varies dramatically in time and it is meaningless to derive a representative value of the circumstellar radiative boundary. Luckily, these cases are automatically excluded from our analysis of habitability because, when such conditions hold, $a_{\rm x,cs1}(t)$ overlaps invariably the region of dynamical instability. In practice, when $a_{\rm x,cs1}(t) \geqslant a_{\rm crit,S1}$ during portion of the orbital period, we tag the case as dynamically unstable. Instead, for the majority of systems extracted, we find $a_{\rm x,cs1}(t) < a_{\rm crit,S1}$ during the whole orbital period. When this condition holds, the relative contribution of star 2 to the total insolation evolves smoothly or is negligible, because e_b is small or/and a_b is large. In this case we derive a mean value of $a_{\rm x,cs1}(t)$ by averaging the time-dependent terms of Eq. (6.15). This approach is sufficient for our purpose, given the statistical nature of our calculations. From the condition $F_{\rm eff,x} = L_{\rm Sun}/l^2_{\text{x-Sun}}$ we obtain

$$w(T_1, \mathcal{R}_x)\frac{L_1}{r^2_{\text{p-1}}} + w(T_1, \mathcal{R}_x)\frac{L_1}{\Delta t}\int_0^{\Delta t} \frac{dt}{r^2_{\text{p-2}}(t)} = \frac{L_{\rm Sun}}{l^2_{\rm Sun}} \quad . \tag{6.23}$$

[2] See Vladilo et al. (2015, appendix A.5) for details on the numerical solution of Eqs. (6.21) and (6.22)

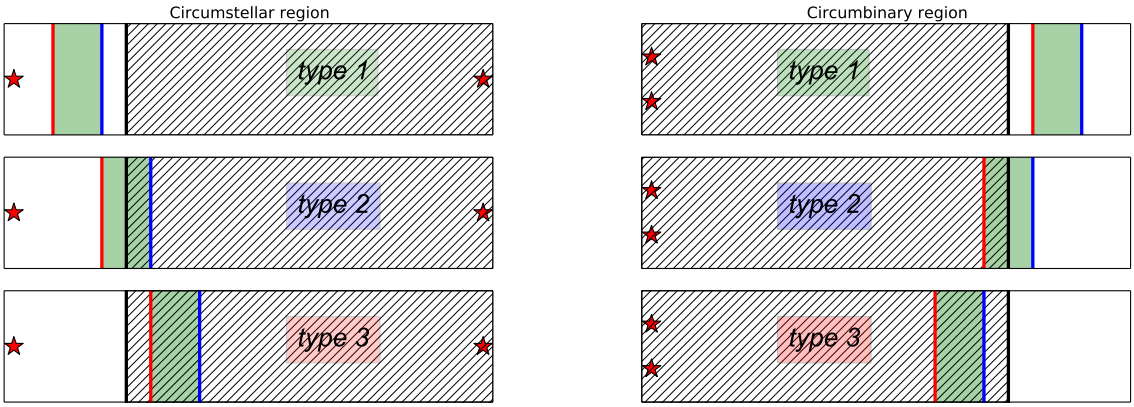

Figure 6.1: Sketch of possible types of habitability conditions in binary systems. Left panels: circumstellar regions, with the host star to the left and the companion star to the right. Right panels: circumbinary regions, with the pair of stars to the left. Green areas: radiative HZs. Red lines: inner edges of insolation, $a_{\rm inn,cs}$ (left) and $a_{\rm inn,cb}$ (right). Blue lines: outer edges of insolation, $a_{\rm out,cs}$ (left) and $a_{\rm out,cb}$ (right). Solid lines: boundaries of dynamical stability, $a_{\rm crit,S}$ (left) and $a_{\rm crit,P}$ (right); hatched areas: instability regions.

We solve this equation numerically in the unknown $r_{\rm p\text{-}1}$, taking into account the dependence of $r_{\rm p\text{-}2}$ on $r_{\rm p\text{-}1}$. The solution $r_{\rm p\text{-}1} = a_{\rm x,cs1}$ is adopted as the circumstellar radiative boundary. In the numerical integration we adopt a variable time step sufficiently small to sample properly the planetary and stellar periods (i.e. $\delta t \ll \min(P_b, P_p)$) and an integration interval Δt sufficiently long to obtain a stable solution. In this way the estimate of $a_{\rm x,cs1}$ is not affected by the choice of the initial conditions θ_0 and M_0. As an additional test of dynamical stability, we checked if the planet enters the Hill radius of the star 2 in the course of the binary orbital evolution. This test shows that the Hill radius criterion is always less stringent than the criterion $a_{\rm x,cs1} \geqslant a_{\rm crit,S1}$. We therefore implemented only this last one, as explained above, to discriminate unstable cases for our analysis of habitability. Finally, in order to save computational time, when $a_b \gg a_p$ we approximate (6.23) with the equation

$$w(T_1, \mathcal{R}_x)\frac{L_1}{r_{\rm p\text{-}1}^2} + w(T_1, \mathcal{R}_x)\frac{L_2}{a_b(1-e_b^2)^2} = \frac{L_{\rm Sun}}{l_{\rm Sun}^2} \tag{6.24}$$

that we solve analytically. This approximation is justified when $a_b \gg a_p$ because in this case the distance between the planet and star 2 is virtually identical to the distance between the two stars and the mean insolation from star 2 equals that received by a planet orbiting star 2 with semimajor axis a_b and eccentricity e_b.[3] After some testing, we found that $a_{\rm crit,S1} > 10 \times a_{\rm MG,cs1}$ is a good criterion for using Eq. (6.24) instead of Eq. (6.23).

6.2.5 Binary habitable zones

By comparing dynamical boundaries with insolation boundaries one can test if binary systems have circumstellar and/or circumbinary zones that are habitable in the long term (Cuntz,

[3]In our case the problem is symmetric, with a source in Keplerian orbit around the planet, but the mean orbital insolation (Williams & Pollard, 2002) is obviously the same.

Model	$\xi(\log m)$	$\xi(q)$	$\xi(e_b)$	Z	e_p	$f_{\rm hab,SA}$	$\overline{w}_{\rm SA}$	$f_{\rm hab,SB}$	$\overline{w}_{\rm SB}$	$f_{\rm hab,P}$	$\overline{w}_{\rm P}$
A	IMF	DK13	SB01	0.017	0.0	0.843	0.955	0.869	0.970	0.035	0.930
B	PDMF	DK13	SB01	0.017	0.0	0.848	0.955	0.874	0.969	0.034	0.929
C	IMF	DM91	SB01	0.017	0.0	0.835	0.955	0.874	0.979	0.039	0.885
D	PDMF	DM91	SB01	0.017	0.0	0.839	0.955	0.877	0.977	0.036	0.882
E	IMF	DK13	SB01	0.008	0.0	0.832	0.954	0.859	0.969	0.038	0.941
F	PDMF	DK13	SB01	0.008	0.0	0.836	0.954	0.863	0.968	0.036	0.935
G	IMF	DM91	SB01	0.008	0.0	0.824	0.953	0.864	0.979	0.043	0.899
H	PDMF	DM91	SB01	0.008	0.0	0.829	0.952	0.869	0.977	0.039	0.888
I	IMF	MDS17	MDS17	0.017	0.0	0.792	0.947	0.838	0.969	0.045	0.918
J	PDMF	MDS17	MDS17	0.017	0.0	0.796	0.945	0.841	0.967	0.043	0.910
K	IMF	MDS17	MDS17	0.008	0.0	0.779	0.944	0.828	0.967	0.048	0.931
L	PDMF	MDS17	MDS17	0.008	0.0	0.783	0.943	0.831	0.966	0.045	0.925

Table 6.2: Average statistical properties of habitability of the Monte Carlo samples of binary systems generated as explained in Section 6.2.1. The first 6 columns of the Table define the model that has been used to perform the simulations. The last 6 columns show the global indices of circumstellar and circumbinary habitability defined in Section 6.3. IMF: initial mass function; PDMF: present-day mass function (Chabrier, 2003). Metallicity of the adopted stellar evolutionary track Bressan et al. (2012).

2014, 2015). In Fig. 6.1 we sketch three types of habitability conditions than can be present in circumstellar and circumbinary regions (left and right panels, respectively). In what we call here "type 1" habitability, the whole radiative HZ is dynamically stable (top panels). Circumstellar and circumbinary "type 1" habitability is equivalent to Cuntz' "S-type" and "P-type", respectively. In "type 2", only part of the radiative HZ is dynamically stable (middle panels). Circumstellar and circumbinary "type 2" habitability is equivalent to Cuntz' "ST-type" and "PT-type", respectively. In "type 3", the region is uninhabitable because the whole radiative HZ is dynamically unstable (bottom panels). In accordance with Cuntz' analysis, we define the spatial extension of the circumbinary HZ as given by:

$$\Delta\ell_{\rm P} = \max(a_{\rm crit,P}, a_{\rm out,cb}) - \max(a_{\rm crit,P}, a_{\rm inn,cb}) \quad . \tag{6.25}$$

When $\Delta\ell_{\rm P} = 0$, the binary system is uninhabitable for P-type orbits (type 3 condition, right panel of Fig. 6.1). This condition holds when $a_{\rm crit,P} > a_{\rm out,cb}$, in which case planets in dynamically stable P-type orbits will be in a snowball state. Similarly, the spatial extension of the circumstellar HZ around each star is given by:

$$\Delta\ell_{\rm S\star} = \min(a_{\rm crit,S\star}, a_{\rm out,cs\star}) - \min(a_{\rm crit,S\star}, a_{\rm inn,cs\star}) \quad , \tag{6.26}$$

where $\star$ =A and B for the primary and secondary, respectively. When $\Delta\ell_{\rm S\star} = 0$ the binary system is uninhabitable for S-type orbits around one of the two stars (type 3 condition, left panel of Fig. 6.1). This condition holds when $a_{\rm crit,S\star} < a_{\rm inn,cs\star}$, in which case planets in dynamically stable S-type orbits have an insolation above the runaway greenhouse limit.

It should be remarked that $\Delta\ell_{\rm S\star}$ and $\Delta\ell_{\rm P\star}$ vary with time according to the instantaneous location of the planet and the stars. This makes somewhat tricky to evaluate a continuously habitable zone. Where these variations are more pronounced, namely studying circumstellar cases in relatively close binaries, we calculate the time-averaged extension of the HZ (see Sect. 6.2.4). A part from these cases, insolation variations due to stellar motions are either small enough to be basically negligible (e.g., for S-type HZs in wide binaries) or frequent enough to smooth out over orbital periods relevant for our problem (e.g. for all P-type HZs).

In the next section we present the statistical results that we obtain with our methodology, taking also into account our current understanding of planetary formation in binary systems. The interpretation of our results in light of observational surveys of exoplanets in binary systems is presented in Section 6.4.

6.3 Results

To run the Monte Carlo simulations we considered different models, each model being defined by a specific set of distribution functions and stellar evolutionary tracks described in the previous section. The adopted prescriptions of the models are specified in the first 6 columns of Table 6.2. For each model we performed a Monte Carlo extraction rejecting the cases with parameters outside the assigned ranges. Specifically, we rejected cases with mass of the secondary below the substellar threshold (0.08 $M_\odot$) and parameters μ and e_b outside the range of validity of the prescriptions (6.13) and (6.14) given by Quarles et al. (2018, 2020). The extraction procedure was iterated until an assigned number of systems, $N_\circ$, was generated. To assess the statistical robustness of the results, we compared the results obtained for increasing values of $N_\circ$, typically 10^4, 10^5, and, for some models (namely A, B, C, D and F), 10^6.

As a first step to study the results obtained from our procedure we introduced two indices aimed at characterizing the mean habitability of each sample. The first index, $f_{\rm hab}$, is the fraction of systems, out of the total number $N_\circ$, for which the circumbinary or circumstellar regions are habitable. Specifically, the fraction of systems with habitable circumbinary regions, $f_{\rm hab,P}$, is calculated counting the systems for which $\Delta\ell_{\rm P} > 0$. The fractions of systems with habitable circumstellar regions around the primary and the secondary, $f_{\rm hab,SA}$ and $f_{\rm hab,SB}$, are obtained counting the cases in which $\Delta\ell_{\rm SA} > 0$ and $\Delta\ell_{\rm SB} > 0$, respectively.

The second index, $\overline{w}$, is a mean, normalized width of circumstellar or circumbinary HZs. We calculate this index normalizing the widths (6.25) and (6.26) to the width $\Delta\ell_\circ(m_1)$ of the HZ around a single star with mass m_1 (i.e. the mass of the host star). For circumbinary regions we set $m_1 = m_A$ and calculate the circumbinary index $\overline{w}_{\rm P}$ by averaging the ratio $w_{\rm P} = \Delta\ell_{\rm P}/\Delta\ell_\circ(m_A)$ for the systems for which $\Delta\ell_{\rm P} > 0$. Similarly, we calculate the circumstellar indices $\overline{w}_{\rm SA}$ and $\overline{w}_{\rm SB}$ by averaging the ratios $w_{\rm SA} = \Delta\ell_{\rm SA}/\Delta\ell_\circ(m_A)$ and $w_{\rm SB} = \Delta\ell_{\rm SB}/\Delta\ell_\circ(m_B)$ for the systems for which $\Delta\ell_{\rm SA} > 0$ and $\Delta\ell_{\rm SB} > 0$, respectively.

For both of these indexes, we found that the runs with 10^5 extractions yield results that differ by less than 0.1% compared to the test runs performed with 10^6 extractions. Also the distributions of different HZ types versus binary parameters are largely unaffected. Therefore we adopted the less-time consuming samples with 10^5 to compare results obtained from different models. In the last 6 columns of Table 6.2 we list the indices $f_{\rm hab}$ and $\overline{w}$ obtained by running a set of simulations with $N_\circ = 10^5$ for each model. All calculations were performed using the climatological boundaries of habitability RG (runaway greenhouse) and MG (maximum greenhouse).

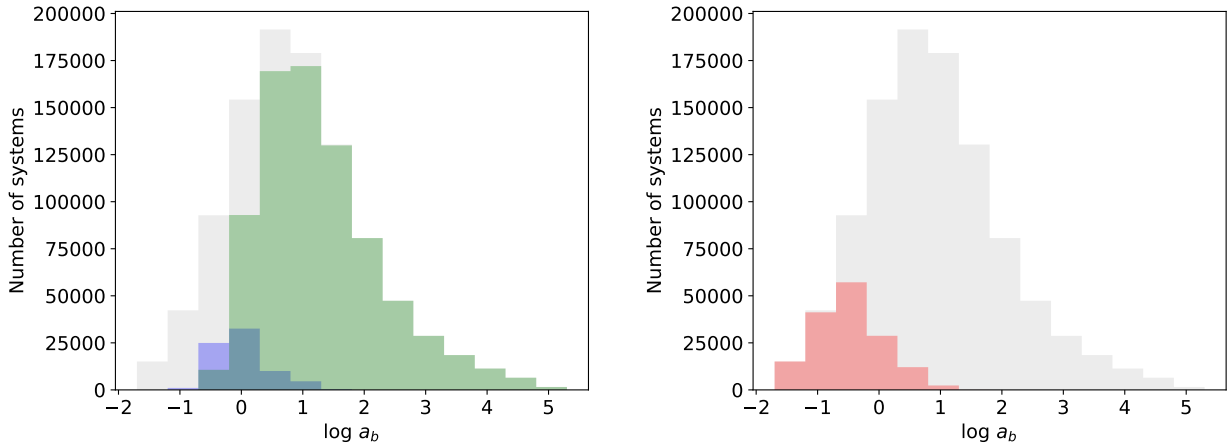

Figure 6.2: Habitability of circumstellar regions around the primary star in binary systems. Gray histogram: number of binary systems versus binary semi-major axis (AU) for the whole sample generated with Model A (Table 6.2). Left panel: systems with $\Delta\ell_{\rm SA} > 0$ counted according to their conditions of habitability; green and blue histograms: type-1 and type-2 conditions. Red histogram in the right panel: systems with uninhabitable regions around the primary (type-3 condition). See Fig. 6.1.

The results collected in Table 6.2 indicate that the average properties of habitability are very different for the circumstellar and the circumbinary regions. The main difference is that circumstellar regions are habitable in most systems, whereas circumbinary regions are uninhabitable in a large fraction of the full Monte Carlo sample. Specifically, for the circumstellar region around the primary all models yield $f_{\rm hab,SA} \simeq 78 - 85\%$, with a mean,

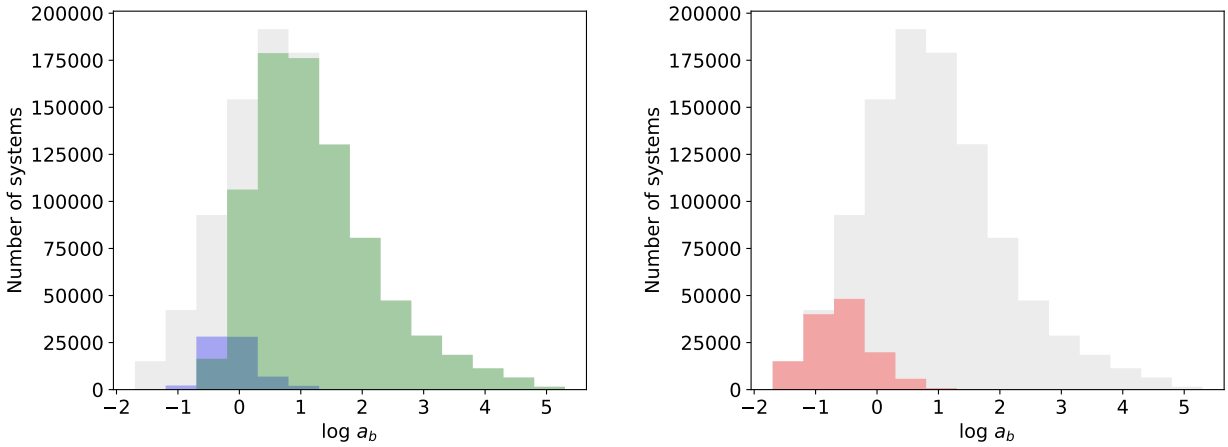

Figure 6.3: Habitability of circumstellar regions around the secondary star in binary systems. Same sample of binary systems and same color coding of the histograms as in Fig. 6.2.

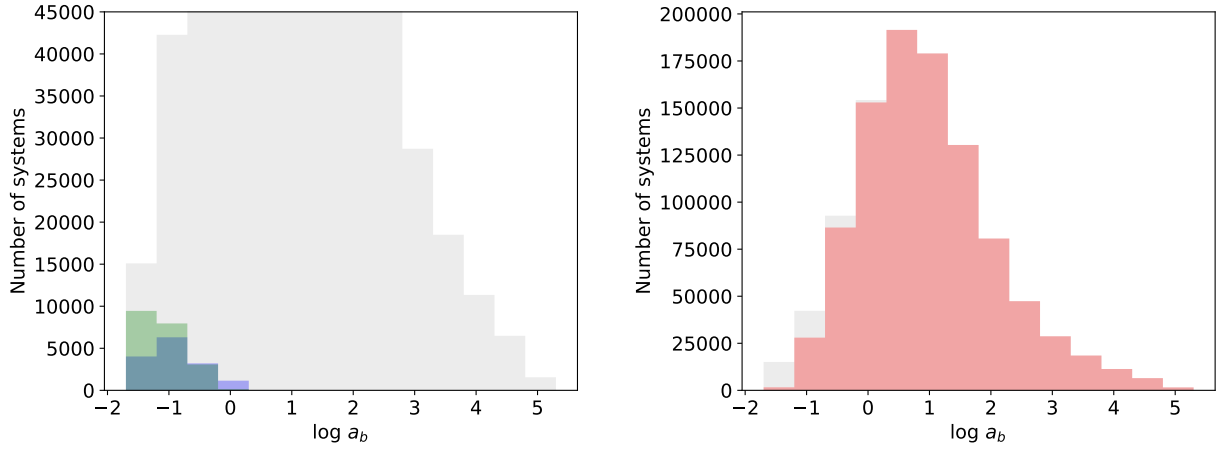

Figure 6.4: Habitability of circumbinary regions in binary stellar systems. Gray histogram: whole sample of systems as in Fig. 6.2. Left: expanded figure of systems with $\Delta\ell_{\rm P} > 0$. Right: systems with $\Delta\ell_{\rm P} = 0$. Same color coding of the histograms as in Fig. 6.2.

normalized width of the HZ, $\overline{w}_{\rm SA} \simeq 0.95$. For the circumstellar region around the secondary, the habitable fraction is slightly higher, with $f_{\rm hab,SB} \sim 84-88\%$ and the mean, normalized width is slightly larger, with $\overline{w}_{\rm SB} \sim 0.97$. On the contrary, the circumbinary region has type-3 conditions in the majority of cases, yielding an average fraction of habitable circumbinary regions $f_{\rm hab,P} \simeq 3-5\%$. However, for the circumbinary regions that are habitable, the mean, normalized width is quite high, $\overline{w}_{\rm P} \sim 0.88-0.94$. In other words, circumbinary HZs are less numerous, but not less extended. As we discuss below, the fraction of habitable circumbinary regions is much higher in specific intervals of binary and stellar parameters. The fact that the mean widths of the HZs are almost equal to those around a single star implies that habitability conditions of type-2, where part of the radiative HZ is dynamically unstable, are not common. In fact, the detailed analysis that we present below shows that the HZs in binary systems can be even more extended than in the case of a single star.

To cast light on the average statistical results summarized above, we investigated how the systems with type-1, type-2, and type-3 conditions of habitability are distributed as a function of the binary semi-major axis. In Fig. 6.2 we show the number of systems binned in constant logarithmic steps of a_b for a sample obtained from model A (gray histogram) and for different sub-samples selected according to the habitability conditions around the primary star. In the left panel one can see that there is a majority of cases of type-1 habitability, with a maximum at $a_b \simeq 10\,{\rm AU}$ (green histogram), and a minority of cases with type-2 conditions, with a maximum at $a_b \simeq 1\,{\rm AU}$ (blue histogram). In the right panel one can see that the systems with uninhabitable circumprimary regions are a minority, with a maximum at at $a_b \simeq 0.3\,{\rm AU}$ (red histogram). Similar results are found for the circumstellar regions around the secondary, shown in Fig. 6.3. A close comparison with Fig. 6.2 shows that circumsecondary regions are slightly more habitable than circumprimary regions. This difference is not due to statistical fluctuations, but to intrinsically different conditions of habitability that we discuss below.

The situation for circumbinary regions, shown in Fig. 6.4, is completely different. In the right panel one can see that the large majority of circumbinary regions is uninhabitable (type-3 conditions), with a maximum of cases at $\simeq 3\,{\rm AU}$ (red histogram). This maximum corresponds to the maximum of the period distribution of the entire sample. In the left panel we show the systems with type-1 (green histogram) and type-2 (blue histogram) conditions of habitability, where the former has a maximum for closest binary systems bin at $\simeq 0.02-0.06\,{\rm AU}$ and the latter has a maximum at $\simeq 0.1\,{\rm AU}$. These findings were expected, since they generally reproduce the results of the seminal work on protoplanetary disks in binary systems by Artymowicz & Lubow (1994). Results similar to those shown in Figs. 6.2, 6.3 and 6.4 are found for all models.

To cast light on the extension of the HZs in binary systems, in Fig. 6.5 we plot the 2D histograms of the extension of the HZ around the primary. On the left panel, it is possible to see the absolute width $\Delta\ell_{\rm SA}$ (in AU) for type-2 habitability conditions. It underlines the great range of widths of circumstellar HZs in binary systems, which spans from a negligible fraction of AU up to a few AU in the considered range of parameters. This spread is expected due the fact that the boundary of dynamical instability can interrupt the radiative HZ at any location, according to all possible combinations of binary system parameters. There is a visible left-right density gradient induced by the primary mass distribution, which produces more small mass stars. An abrupt change at $m_\ell = 0.5\,{\rm M}_\odot$ is also visible and it is caused by the different distribution of binary periods below and above this threshold. On the right panel, we show the normalized width $w_{\rm SA}$ of type-1 HZs, with type-2 systems that sport a $w_{\rm SA} \geqslant 1.0$ superimposed as blue crosses. As it is possible to see, the widths of most type-1

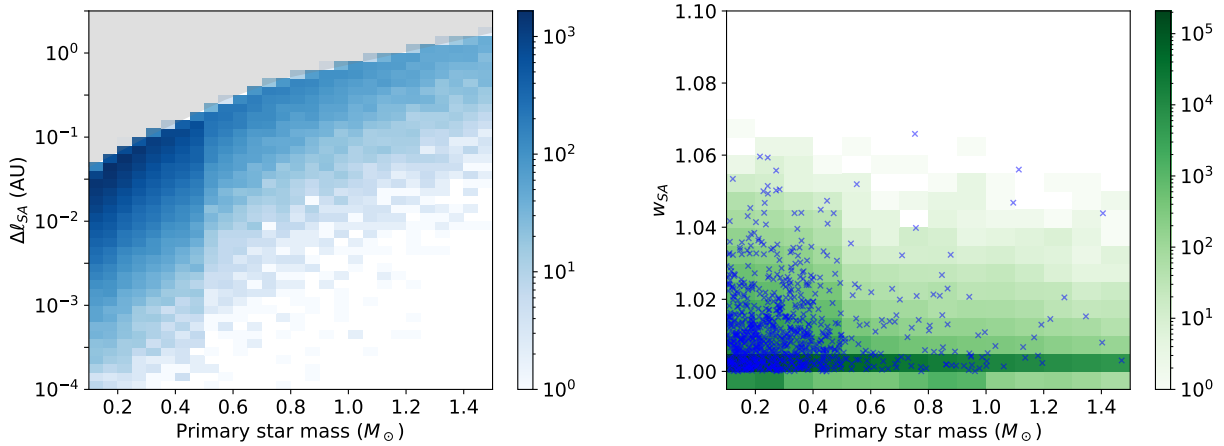

Figure 6.5: Extension of the circumstellar HZs around the primary star in binary systems. Left panel: 2D histogram of $\Delta\ell_{\rm SA}$ vs star mass for type-2 (blue) habitability condition (see Fig. 6.1). The gray-shaded area in the topmost part of the plot is empty due to the definition of the radiative HZ for a given star. Right panel: 2D histogram of $w_{\rm SA}$ vs star mass for type-1 (green) habitability condition, zoomed on the y-axis for better readability. Superimposed blue crosses represent type-2 cases with $w_{\rm SA} \geqslant 1.0$. Results obtained for Model A (Table 6.2), from a simulation with $N_\circ = 10^6$.

HZ are essentially equal to those around single stars (the string of dark green bins in the lower part of the panel) and depends on the fact that secondary stars usually play a minor role. On the other hand, there is a small number of systems with slightly enhanced HZ, in the order of some percent points. Also a small subset ($< 0.1\%$) of type-2 cases is interested by this effect.

Concerning the width of the HZ around the secondary star, in the left panel of Fig. 6.6 we plot $w_{\rm SB} = \Delta\ell_{\rm SB}/\Delta\ell_\circ(m_B)$ versus m_B. As in the primary star case analyzed above, most of the secondary stars sport HZs with comparable extensions as those around single stars of the same mass. Also in this case there are several instances of HZs wider than in the case of a single star, both for type-1 and type-2 habitability conditions. However, around secondary stars the enhancement effect is far more pronounced, especially for low mass stars with late type companions, where $w_{\rm SB}$ can be as large as 7.4 and 5.8 for type-2 and type-1 HZs, respectively. An inspection of the systems where this result is found shows that this effect is due to the strong radiative flux of the primary which, in some cases, shifts outwards the insolation outer edge of the secondary. This effect explains why the circumstellar habitability around the secondary tends to be slightly larger than that around the primary, as we have seen when comparing Figs. 6.2 and 6.3.

Concerning the width of circumbinary HZs, in the right panel of Fig. 6.6 we plot the normalized width, $w_{\rm P} = \Delta\ell_{\rm P}/\Delta\ell_\circ(m_A)$, versus mass ratio $q = m_{\rm B}/m_{\rm A}$. One can see that also the circumbinary HZ can be wider than in the case of a single star, especially when the two stars have similar masses. This may happen not only for type-1 habitability conditions, but even when the radiative HZ is interrupted by the edge of dynamical instability (blue crosses). This effect becomes stronger with increasing mass ratio because the increasing contribution of radiative flux of the companion shifts the outer edge of the radiative HZ beyond the boundary of dynamical stability. The fraction of systems where this effect takes place is very small in the Monte Carlo sample. However, the effect leads to a significant extension of the circumbinary

HZ in binary systems with stars of similar mass.

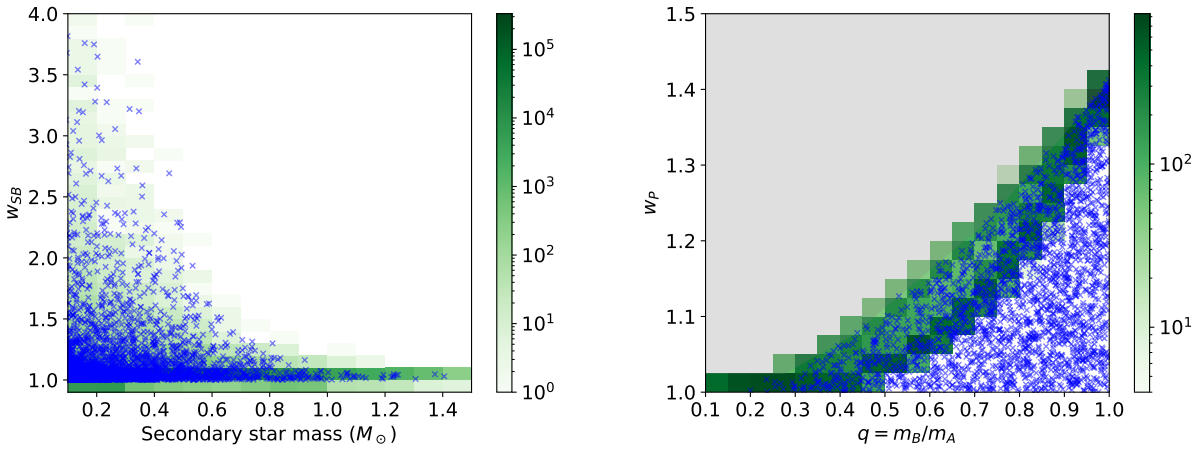

Figure 6.6: Normalized width of HZs in binary systems. Left panel: 2D histogram of the normalized width of the circumstellar HZ around the secondary, $w_{\rm SB}$, versus mass of the secondary, $m_{\rm B}$. Right panel: 2D histogram of the normalized width of the circumbinary HZ, $w_{\rm P}$, versus mass ratio $q = m_{\rm B}/m_{\rm A}$. Green shades: type-1 conditions of habitability. Blue crosses: type-2 conditions of habitability with $w_{\rm SB}$ or $w_{\rm P} \geqslant 1.0$. The gray-shaded area is inaccessible due to the definition of radiative HZ. Same sample as in Fig. 6.5.

6.3.1 Constraints from planetary formation

In Table 6.2 and subsequent figures, we have analyzed the statistical properties of a general population of binaries under various hypotheses, regardless of the effective ability of a given binary configuration to give rise to a planetary system. While the details about planetary formation processes in binary systems are still under debate and fall out of the scope of the present work, we cannot ignore the influence that they may have on the statistics of habitable binaries. To deal with this issue, we extracted various sub-samples from each run, imposing limits on the binary semi-major axis, which seems to be the main factor in determining the limits of planetary formation in binaries. The results of this analysis, shown in columns 2, 3, 4 and 5 of Table 6.3, are discussed below.

Planetary formation in circumstellar orbits

The ability to form planets from a circumstellar protoplanetary disk perturbed by a companion star is a topic investigated both numerically (Quintana et al., 2007), analytically (Rafikov & Silsbee, 2015b,a; Silsbee & Rafikov, 2015) and observationally (Kraus et al., 2016). Theoretical models indicate that the formation and growth of Earth-mass planets in the radiative HZ of a G-type primary star is generally allowed when $a_b \gtrsim 10$ AU. However, they also allow for the formation of close-in planets when $a_b = 5$ AU (Quintana et al., 2007) or the formation in the radiative HZ when certain specific conditions on orbital parameters are met (Rafikov & Silsbee, 2015a). From the observational point of view, Kraus et al. (2016) found a dearth of planet candidates around binaries with $a_b \leqslant 50$ AU and no candidates below $a_b \sim 10$ AU. Finally, (Barnes et al., 2020) identified a circumstellar super-Earth around HD 42936, whose binary separation is 1.22 AU. Here we consider this latter system as an outlier and we adopt

Model	$f_{\rm hab,SA}^{>10\,\rm AU}$	$f_{\rm hab,SB}^{>10\,\rm AU}$	$f_{\rm hab,P}^{<1.0\,\rm AU}$	$f_{\rm hab,P}^{<0.3\,\rm AU}$	$f_{\rm hab,SA}^{\rm half\ M}$	$f_{\rm hab,SB}^{\rm half\ M}$	$f_{\rm hab,P}^{\rm half\ M}$
A	0.998	0.999	0.171	0.368	0.831	0.860	0.043
B	0.999	1.000	0.159	0.354	0.836	0.864	0.040
C	0.997	1.000	0.200	0.418	0.822	0.865	0.047
D	0.999	1.000	0.183	0.399	0.829	0.871	0.044
E	0.997	0.999	0.185	0.389	0.819	0.851	0.047
F	0.999	1.000	0.172	0.376	0.824	0.855	0.044
G	0.997	1.000	0.214	0.440	0.809	0.855	0.052
H	0.999	1.000	0.198	0.425	0.816	0.860	0.048
I	0.994	0.998	0.210	0.415	0.779	0.829	0.055
J	0.996	0.999	0.196	0.401	0.785	0.834	0.052
K	0.992	0.998	0.226	0.440	0.765	0.819	0.060
L	0.995	0.999	0.211	0.423	0.772	0.824	0.056

Table 6.3: Statistical properties of habitability of the sub-samples obtained by considering: (i) limiting values in the binary semi-major axis a_b for circumstellar and circumbinary planetary formation (columns 2 to 5) and (ii) different multiplicity fractions for M-type and FGK-type stars (columns 6 to 8). The properties of the whole sample for each model are shown in Table 6.2.

a tentative lower limit of $a_b > 10$ AU for circumstellar planetary formation. We extract a sub-sample with this cutoff for each of our models and we analyse the results. As it is possible to see in Table 6.3 (columns 2 and 3), the adoption of this cutoff increases $f_{\rm hab,SA}$ and $f_{\rm hab,SB}$ to near 100% for every model. Therefore, the constraints of dynamical stability of already formed planets are less stringent than those of circumstellar planetary formation. These latter constraints, albeit still uncertain at the present time, suggest that every binary configuration where circumstellar planets can be formed allows habitable circumstellar planets to exist.

Planetary formation in circumbinary orbits

Planetary formation in circumbinary protoplanetary disks also has some issues. Quintana & Lissauer (2006) investigated this topic via numerical simulations finding that, for binary apastrons $\lesssim 0.2$ AU, planetary formation proceeds in the same way as around single stars, while for apastrons > 0.3 AU the formation of Earth-like planets at 1 AU is less likely. On the observational side, Trilling et al. (2007) found that a large fraction of young binaries with separations < 3 AU have circumbinary disks, with at least some instances of dynamically stable ones for $a_b > 1$ AU. Alves et al. (2019) demonstrated the undergoing dissipation of the circumbinary disk around Barnard 59, whose separation is ~ 20 AU. Finally, the widest circumbinary planet-hosting binary known up to date has $a_b = 0.23$ AU (Welsh et al., 2015). Clearly, it is difficult to establish a hard upper limit in a_b for circumbinary planetary formation at the present time. Given that the fraction of circumbinary planet-hosting systems is strongly dependent on the adopted cutoff, we extracted two sub-samples, one with $a_b < 1.0$ AU and another with $a_b < 0.3$ AU. In these two sub-samples $f_{\rm hab,P}$ increases considerably, from $3-5\%$ of the complete sample, up to $16-23\%$ or $35-44\%$ (columns 4 and 5 in Table 6.3, respectively).

In any case, even the most selective sub-sample still leaves the potentially habitable, circumbinary planet-hosting systems in minority. This points to an intrinsic paucity of cir-

cumbinary habitable planets, regardless of the specific hypotheses about the q, a_b and e_b distributions.

Alongside the upper limit in the binary star separation, some authors pointed also to the possible existence of a lower limit for this variable. Martin et al. (2015) and Martin (2018) underlined a paucity of exoplanet detections in very close binary stars with periods of less than 5 days. They suggest that the presence of a third, undetected faint companion in some of the members of the sample could have skewed their conclusion. On the other hand, Fleming et al. (2018) explained this dearth through an interplay of successive angular momentum transfers (between the two stars and the newly formed planets) and magnetic braking. Circumbinary planets would then exist only for systems with P_b over 5 days. If we adopt this lower limit for binary star separation we find a reduction of $20-25\%$ of $f_{\rm hab,P}$ across all our models. This fact, once again, reinforces our conclusion that circumbinary habitable planets are rare.

6.3.2 Effects of the short-period binary excess

From a reanalysis of the Kepler Eclipsing Binary Catalog, Kirk et al. (2016) found an excess of very-short period (in the $0.3-1$ day interval in P_b) binary systems that is not captured by the log-normal distribution that we have adopted (see Sect. 6.2.1). This excess amounts to $\sim 0.5\%$ of the total population. Given that most of the binaries with $P_b < 10$ days host type-1 circumbinary HZs, this in turn increases the fraction $f_{hab,P}$. This does not affect our conclusions since the increase is quite modest across our models, affecting only the last decimal digit of the values in Table 6.2. It is important to recall that in such close systems, a variety of complex phenomena set in, like e.g. Roche lobe overflows, which can substantially change the radiative properties of the stars involved. Our code is not equipped for studying these particular environments.

6.3.3 Binary occurrence rate versus spectral type of the primary

In the methodology that we designed to generate samples of binaries we extract the mass of the primary star from the IMF or the PDMF distributions described in Section 6.2.1. In doing so, we implicitly assume that the occurrence rate of binaries is the same across different spectral types (FGKM) of the primary. This is the simplest approximation given the uncertainties surrounding this topic. However, there are clues that this could not be the case. The synthesis of results analysed by Raghavan et al. (2010) indicate that the occurrence rate of binaries increases with mass, with multiplicity fraction of $42-48\%$ in the F6-K3 range, compared to $11-42\%$ for M-dwarfs (Fischer & Marcy, 1992; Reid & Gizis, 1997). Moe & Di Stefano (2017) observed a similar trend in the O-G range. Considering the uncertain distinction between the binary and the higher-order multiplicity fractions, it is difficult to quantify these trends. To assess the impact of a possible dearth of binary systems with red dwarf primaries, we extracted a subset from each of the main samples, removing half of the systems with M-type primaries. As a result, we find that the circumstellar habitability fractions $f_{\rm hab,SA}$ and $f_{\rm hab,SB}$ of the subsets (Table 6.3, columns 6 and 7) are very similar to those of the whole samples (Table 6.2). The circumbinary habitability fractions $f_{\rm hab,P}$ of the subsets tend to increase, but remain very low, in the order of $4-6\%$ (Table 6.3, column 8).

Finally, we combined the constraints on a_b for planetary formation with the reduction in the binary occurrence rate for M-type primaries. In this case, we do not report the results in the table. For circumstellar habitability, both $f_{\rm hab,SA}$ and $f_{\rm hab,SB}$ are virtually identical

to those reported in columns 2 and 3 of Table 6.3 in all models. On the oher hand, the fractions of circumbinary habitability tend to increase slightly for both of the adopted limits for planetary formation. Even in this scenario, $f_{\rm hab,P}$ is generally $\lesssim 50\%$, confirming the paucity of circumbinary configurations suitable for life. The higher results in this regard are achieved by models G and K, that reach a $f_{\rm hab,P}$ value equal to 54% and 55%, respectively. This analysis suggests that our results are weakly affected by the uncertainties of the stellar orbital parameters and occurrence rates in binary systems.

6.3.4 Model dependence of the results

The fact that the properties of circumbinary and circumstellar habitability in binary systems are similar for most models lends support to the robustness of the main conclusions that we have summarized above. To cast light on the model dependence of our procedure, we now discuss some minor, but systematic differences that are seen when comparing the results obtained from different models.

Distribution functions

When passing from the IMF to the PDMF, keeping fixed the other prescriptions, our results tend to give slightly higher habitability to circumstellar regions and slightly lower habitability to circumbinary regions. This can be seen in Table 6.2, where a change from IMF to PDMF yields an increase of habitable fractions $f_{\rm hab,SA}$ and $f_{\rm hab,SB}$ and a small but systematic rise of $\overline{w}_{\rm SA}$ and $\overline{w}_{\rm SB}$. Conversely, for circumbinary regions we see a small decrease of $\overline{w}_{\rm P}$ and a small decrease of the habitable fraction $f_{\rm hab,P}$. These changes can be interpreted in terms of: (1) the lower contribution of high-mass stars in the PDMF and (2) the strong dependence of stellar luminosity on stellar mass on the main sequence. The lower fraction of high-luminosity stars in the PDMF implies that, on average, the radiative HZ will get closer to the stars. As a result, the radiative HZ will get closer to the circumstellar region of stability, increasing the habitability of S-type orbits, and closer to the circumbinary region of instability, decreasing the habitability of P-type orbits.

As for the distribution of mass ratios, $\xi(q)$, it is possible to see a minor but systematic increase in the circumstellar habitable fractions $f_{\rm hab,SA}$ and $f_{\rm hab,SB}$ when we use the top-heavy DK13 power-law instead of the log-normal, low-q centered function of DM91. This is unexpected, given that systems with similar-sized stars should have narrower dynamical stability zones around the primary and further out inner HZ edges around the secondary, other things being equal.

As far as the distribution function of eccentricities of stellar orbits, $\xi(e_b)$, is concerned, using the results of Moe & Di Stefano (2017) yields an higher value for $f_{\rm hab,P}$ and a smaller value for both $f_{\rm hab,SA}$ and $f_{\rm hab,SB}$ than using the Stepinski & Black (2001) prescription. In this case, it is not easy to disentangle the effect of changing $\xi(e_b)$ from the effect of changing $\xi(q)$. Even if MDS17 $\xi(q)$ gives rise to a final q distribution that is largely similar to the DM91 one, the former introduces a correlation with P_b that is absent in the latter. Nonetheless, a detailed analysis of the sample shows that the increase in the circumbinary habitable fraction is caused by the correlation between binary eccentricity and period that favors the generation of low eccentricity systems when the period is small. This in turn allows for smaller possible planetary semi-major axes. On the other hand, for larger binary periods, larger eccentricities are favored, and this cause the small reduction of the circumstellar habitable fractions around both stars.

Model[a]	e_p	$f_{\rm hab,SA}$	$\overline{w}_{\rm SA}$	$f_{\rm hab,SB}$	$\overline{w}_{\rm SB}$	$f_{\rm hab,P}$	$\overline{w}_{\rm P}$	Reference for $a_{\rm crit}$
A	0.0	0.843	0.955	0.869	0.970	0.035	0.930	Quarles et al. (2018, 2020)
A	0.0	0.857	0.960	0.885	0.974	0.031	0.939	Holman & Wiegert (1999)
B	0.0	0.848	0.955	0.874	0.969	0.034	0.929	Quarles et al. (2018, 2020)
B	0.0	0.863	0.960	0.889	0.973	0.029	0.932	Holman & Wiegert (1999)
C	0.0	0.835	0.955	0.874	0.979	0.039	0.885	Quarles et al. (2018, 2020)
C	0.0	0.848	0.959	0.888	0.983	0.034	0.895	Holman & Wiegert (1999)
D	0.0	0.839	0.955	0.877	0.977	0.036	0.882	Quarles et al. (2018, 2020)
D	0.0	0.854	0.959	0.892	0.981	0.031	0.886	Holman & Wiegert (1999)

Table 6.4: Comparison of the indices of habitability obtained by adopting the recipes for $a_{\rm crit}$ from Quarles et al. (2018, 2020) and the original expressions from Holman & Wiegert (1999).Distribution functions adopted in each model are shown in Table 6.2. $N_\circ = 10^5$.

The above considerations on the adopted distribution functions are also valid for the subsamples defined in 6.3.1 and 6.3.3, as it is possible to see in Table 6.3. In particular, for S-type orbits, most of the variations are swamped by the fact that both $f_{\rm hab,SA}$ and $f_{\rm hab,SB}$ have values near unity, while for $f_{\rm hab,P}$ they are amplified and more clearly visible, especially when the planetary formation limits are considered.

Boundaries of dynamical stability

The exact location of the boundaries of dynamical stability $a_{\rm crit}$ play an essential role in our calculations. The determination of the regions of dynamical instability depends on the accuracy of the N-body simulations performed by different authors. Our results are based on the analytical expressions (6.13) and (6.14) derived by Quarles et al. (2018, 2020) from a large database of simulations, each simulation covering 10^5 orbital periods of the binary system. To assess the impact of the uncertainties related to the definition of the regions of stability, we repeated our calculations adopting the original analytical expressions derived by Holman & Wiegert (1999) from a more limited set of N-body simulations covering 10^4 orbital periods. The indices of habitability obtained from the two different recipes of $a_{\rm crit}$ are compared in Table 6.4. One can see that the results match well, the differences being consistent with the statistical uncertainties. This is true also for the subsamples described in Sections 6.3.1 and 6.3.3 (not reported in Table 6.4).

Insolation boundaries of the radiative HZ

The results presented in Table 6.2 have been derived using the climatological limits RG and MG. Adopting the empirical limits RV and EM we find a slightly higher habitability, but the results do not change significantly. In circumbinary regions, where the habitability is very sensitive to the location of the outer edge of insolation, the differences are particularly small because the MG edge is quite close to the EM edge (Table 6.1). Indeed, we find that the fraction of habitable circumbinary regions increases typically by $\sim 0.1 - 0.2\%$ adopting the empirical limit EM. The differences are more marked in the circumstellar regions, which are particularly sensitive to the location of the inner edge, because the RV is significantly closer to the star than the RG edge (Table 6.1). We find that the fraction of habitable circumstellar regions increases by $\sim 2 - 3\%$ adopting the empirical limit RV. These differences do not affect

the conclusions of the present work. In the rest of this Chapter we use the results obtained from the climatological limits RG and MG as a reference for our discussion. Similarly modest variations are found in the a_b-limited and the binary M-dwarf halved samples described in Sections 6.3.1 and 6.3.3.

6.3.5 Eccentricity of planetary orbits

The eccentricity of planetary orbits affects the habitability of binary stellar systems both in terms of insolation and in terms of dynamical stability. In terms of insolation, we know that the mean stellar flux received by a planet moving in an elliptic orbit with eccentricity $e_p > 0$ is enhanced by a factor $(1 - e_p^2)^{-1/2}$ compared to the case of circular orbits (see, e.g., Williams & Pollard, 2002; Vladilo et al., 2013). As we have already emphasized, in binary systems an enhancement of insolation has opposite effects of habitability in circumstellar and circumbinary regions. In circumstellar regions the larger insolation yields a larger frequency of type 3 habitability conditions, whereas in circumbinary regions a larger frequency of type 1 conditions. Therefore we expect a decrease of circumstellar habitability and an increase of circumbinary habitability with increasing e_p. Even though planetary eccentricity may be forced to low values both by dynamical stability considerations and by momentum exchange between the stars and the planet, in order to quantify the potential impact on insolation, we repeated our simulations applying a correction term $(1 - e_p^2)^{-1/2}$ to the stellar luminosities. For P-type orbits, we applied this correction to both stars since stable planetary orbits are far from both stars. For S-type orbits, we applied the insolation enhancement only to the host star. Results for model A with increasing value of e_p are shown in Table 6.5. With increasing planetary eccentricity one can see, as expected, a decrease of $f_{\rm hab,SA}$ and $f_{\rm hab,SB}$ and an increase of $f_{\rm hab,P}$. Correspondingly, we see variations of the normalized width of the HZs, with a decrease of $\overline{w}_{\rm SA}$ and $\overline{w}_{\rm SB}$ and an increase of $\overline{w}_{\rm P}$. The same happens in the subsamples described in Sections 6.3.1 and 6.3.3 (not reported in Table 6.5). These changes are modest, at least up to $e_p \simeq 0.6$. However, the dynamical stability of configurations with $e_p \gtrsim 0.6$ are critical in most of the cases. Planetary orbital eccentricity, if not damped out by momentum exchange, may hardly increase the habitability of circumbinary regions, in any case only up to the critical conditions of stability.

6.4 Discussion

We now discuss the potential impact of our results on searches for habitable planets in binary systems. First we investigate which observable properties of binary systems can be used to optimize searches for the highest conditions of circumstellar or circumbinary habitability. Then we discuss potential applications to known exoplanets and for planning future searches of exoplanets.

6.4.1 Searching for binary systems with habitable zones

Trends with binary system properties

The stellar separation has a strong influence on the binary habitability because the boundaries of dynamical stability scale with the semi-major axis of the binary system, a_b, as shown in Eqs. (6.13) and (6.14). In circumstellar regions, when a_b is sufficiently small the largest stable

orbit will be so close to the star to have an insolation above the Runaway Greenhouse limit. In circumbinary regions, when a_b is sufficiently small, stable orbits of P type will be so close to both stars that the planets will have sufficient insolation to escape the snowball state. The impact of these effects can be seen in Fig. 6.7, where we show the fraction of systems with type-1,-2 and -3 conditions of habitability plotted in constant bins of $\log a_b$. One can see that the fraction of circumprimary type-1 regions increases with a_b, from $\simeq 0$ at $a_b < 0.1$ AU up to $\simeq 1$ at $a_b > 10$ AU, with a sharp rise at $a_b \simeq 1$ AU. In addition, there is a small fraction of systems with type-2 conditions between $\simeq 0.1$ and $\simeq 3$ AU. If we include the constraints of planetary formation (Section 6.3.1), nearly any system that can form planets also has a dynamically stable radiative HZ. One can see that circumsecondary (thin dark lines) and circumprimary (thick light lines) habitability show similar values and trends. In the right panel we show the results for circumbinary regions, where the behaviour is opposite to that of circumstellar regions. Specifically, circumbinary habitability starts very high at $a_b < 0.1$ AU, but then declines sharply with increasing a_b. Since the limit for planetary formation in circumbinary orbits seems to lie in the $0.3 - 1.0$ AU range, this result shows that a sizeable number of systems able to form circumbinary planets cannot support a stable radiative HZ. This fact clearly differentiates P-type habitability from S-type habitability.

In Fig. 6.8 we show the impact of the mass ratio, $q = m_{\rm B}/m_{\rm A}$, on the relative number of circumstellar and circumbinary HZs. In the left panel one can see that the fraction of cases with type-1 conditions around the primary shows a modest rise with increasing q, with a maximum value $\simeq 0.8$ when both stars have the same mass (thick light lines). For the circum-secondary regions the fractions of different types of habitability conditions is almost independent of q (thin dark lines). Also the fractions of circumbinary HZs show no significant trend with q, apart from a very modest increase towards smaller mass ratios. This result, which concerns the number of systems in a given condition, should not be confused with the result concerning the extension of the circumbinary HZ which becomes larger with increasing q, as we have already seen in Fig. 6.6. Therefore, the mass ratio is not a strong discriminant as far as the relative number of cases in different habitability conditions is concerned, but it does have an impact on the extension of the HZs.

In Fig. 6.9 we show the impact of the stellar orbital eccentricity, e_b, on the relative number of binary HZs. For circumstellar regions around the primary (left panel, thick light lines) one can see a sudden, initial rise of the fraction of HZs with increasing e_b, followed by a smooth decline. Similar results are found for regions around the secondary (left panel, thin dark lines). Also in this case we find an opposite behaviour in circumbinary regions (right panel), with a sudden decrease of the fraction of HZs when e_b increases above 0.0. The sudden changes above 0.0 are due to the fact that the stellar orbits are assumed to be circularized ($e_b = 0$) at short orbital periods. This means that at $e_b = 0$ the semimajor axis is very small and so, as discussed above, circumstellar regions become less habitable, whereas circumbinary regions more habitable. As soon as a_b gets larger, e_b can assume any value, including larger values, and this creates a sudden change of habitability. This happens regardless of the specific choice of $\xi(e_b)$ and is magnified by the use of normalized bins. On top of this effect, there is a trend due to the fact that the boundaries of dynamical stability vary with e_b according to Eqs. (6.13) and (6.14). With increasing e_b the circumstellar edge $a_{\rm crit,S}$ gets closer to the host star, whereas the circumbinary edge $a_{\rm crit,P}$ is shifted outwards. As a result both the circumstellar and the circumbinary regions become less habitable, but this effect is modest.

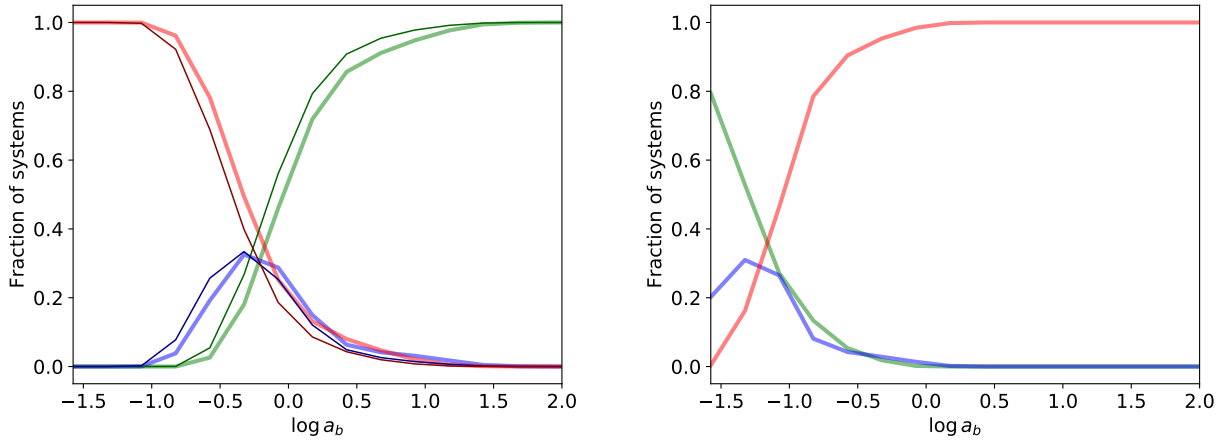

Figure 6.7: Fraction of systems with different conditions of habitability as a function of binary semimajor axis. In each bin of $\log a_b$ the number of systems with type-1 (green), type-2 (blue) and type-3 (red) conditions of habitability is normalized to the total number of systems in the same bin. The plots are truncated to $\log a_b = 2$ to better highlight the trends. Left panel: circumstellar regions around the primary (thick light lines) and the secondary star (thin dark lines). Right panel: circumbinary regions. Same Monte Carlo sample as in Fig. 6.2.

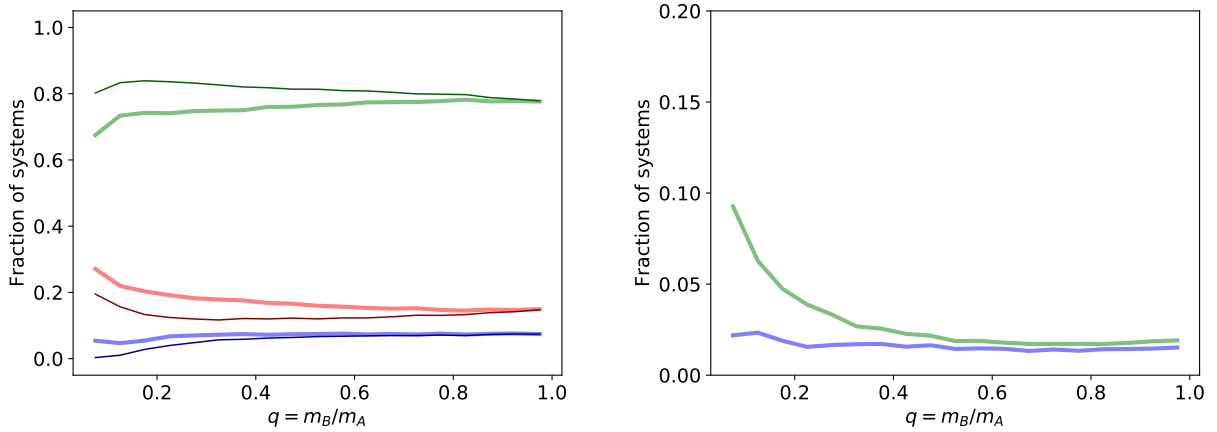

Figure 6.8: Fraction of systems with different conditions of habitability as a function of mass ratio, $q = m_{\rm B}/m_{\rm A}$. In each bin of q the number of systems with type-1 (green), type-2 (blue) and type-3 (red) conditions of habitability is normalized to the total number of systems in the same bin. Left panel: circumstellar regions around the primary (thick light lines) and the secondary star (thin dark lines). Right panel: circumbinary regions (type-3 HZ are omitted to better highlight the trend for type-1 and 2 HZs). Same Monte Carlo sample as in Fig. 6.2.

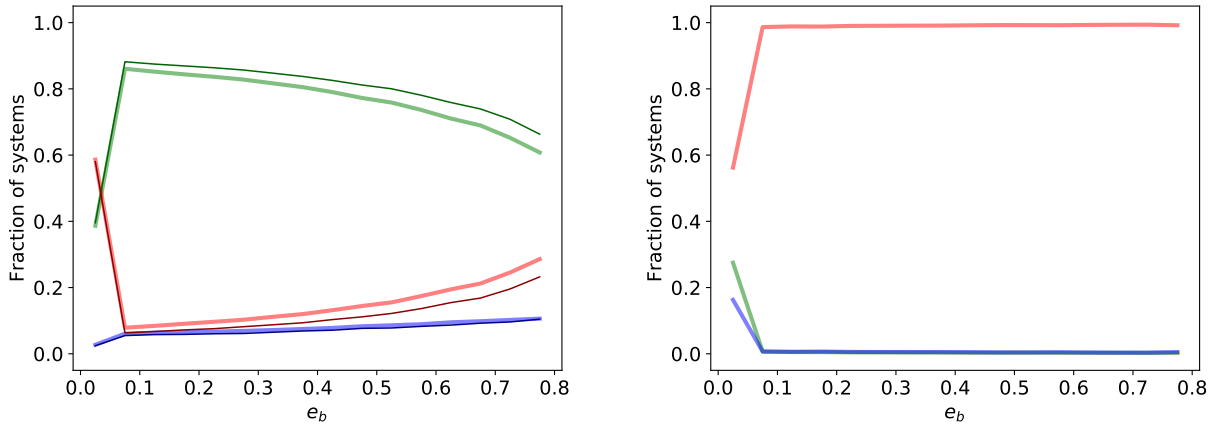

Figure 6.9: Fraction of systems with different conditions of habitability as a function of the binary orbital eccentricity. In each bin of e_b the number of systems with type-1 (green), type-2 (blue) and type-3 (red) conditions of habitability is normalized to the total number of systems in the same bin. Left panel: circumstellar regions around the primary (thick light lines) and the secondary star (thin dark lines). Right panel: circumbinary regions. Same Monte Carlo sample as in Fig. 6.2.

Trends with stellar spectral type

By applying our methodology we can quantify the habitability of binary systems as a function of stellar mass. In Fig. 6.10, we show the mean values of the indices of habitability $f_{\rm hab}$ and $\overline{w}$ averaged in four bins of mass of the primary, m_A, corresponding to the range of masses of M-, K-, G- and F-type stars. In the left panel we show the fraction of habitable regions $f_{\rm hab,SA}$, $f_{\rm hab,SB}$ and $f_{\rm hab,P}$ and in the right panel the normalized width of the HZ, $\overline{w}_{\rm SA}$, $\overline{w}_{\rm SB}$, and $\overline{w}_{\rm P}$. The left panel shows that the number of circumstellar HZs decreases with increasing stellar mass, whereas the number of circumbinary HZs increases with stellar mass. The right panel shows that at higher stellar masses there is an increase of the normalized width of circumbinary HZs. The strong dependence of stellar luminosity on stellar mass provides an interpretation of these trends in terms of an outwards shift of the radiative HZ (Fig. 6.1). Indeed, as the radiative HZ shift outwards, we expect a larger chance of of type-3 conditions in circumstellar regions (e.g., a decrease of habitable fractions $f_{\rm hab,SA}$, $f_{\rm hab,SB}$) and a larger chance of type-1 habitability in circumbinary regions (i.e, an increase of $f_{\rm hab,P}$). The probability of finding habitable planets in S-type orbits increases for late-type host stars. Instead, the chance of finding habitable planets in P-type orbits increases for early-type host stars. Binary systems with $m_A > 1.5$ $M_\odot$, not treated in this work, would probably have better circumbinary habitability conditions.

Trends with stellar metallicity

Our results indicate that, for a given set of binary parameters, a decrease of stellar metallicity tends to give a lower habitability of circumstellar regions and a higher habitability of circumbinary regions. This can be seen in Table 6.2 by comparing the results obtained from models with identical distribution functions, but with different stellar metallicity. One can see that a decrease of metallicity from $Z = 0.017$ (the solar value) to $Z = 0.008$ yields lower

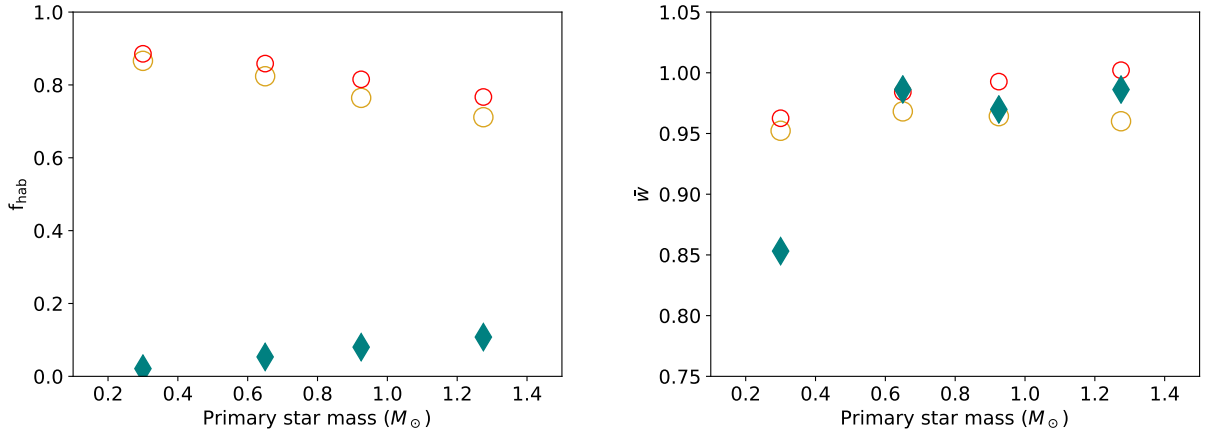

Figure 6.10: Indices of habitability of circumstellar and circumbinary regions averaged in four bins of mass corresponding to the range of masses of M-, K-, G- and F-type stars. Left panel: big and small circles: fraction $f_{\rm hab}$ of habitable circumstellar regions around the primary and secondary star, respectively; diamonds: fraction $f_{\rm P}$ of habitable circumbinary regions. Right panel: big and small circles: mean normalized widths $\overline{w}_{\rm S}$ of the circumstellar HZs around the primary and the secondary, respectively; diamonds: mean, normalized width $\overline{w}_{\rm P}$ of the circumbinary HZs. Results obtained from Model A (Table 6.2).

fractions of habitable circumstellar regions $f_{\rm hab,SA}$ and $f_{\rm hab,SB}$ and slightly higher fractions of habitable circumbinary regions $f_{\rm hab,P}$. These results can be interpreted considering that, for a given stellar mass, the luminosity in the main sequence increases with decreasing metallicity (see, e.g., Bressan et al., 2012). As a result, the radiative HZ shifts outwards, yielding a larger fraction of circumstellar conditions of type 3, as well as a larger fraction of circumbinary conditions of type 1. In all cases, the differences that we find are very small, but systematic. Concerning the average normalized widths of the HZs, we find slightly larger values of circumbinary widths $\overline{w}_{\rm P}$ at low metallicity, and negligible differences in the circumstellar widths $\overline{w}_{\rm SA}$ and $\overline{w}_{\rm SB}$.

In this context it is interesting to compare the results obtained from models with IMF and low-metallicity, representative of binary systems of an older stellar population (e.g. models E and G), and models with PDMF and solar metallicity, representative of present-day stellar populations (e.g. models B and D). All other model assumptions being the same, the results shown in Table 6.2 show that in the older stellar population (e.g. model E) the circumstellar habitability decreases and the circumbinary habitability increases compared to the present-day population (e.g. model B). The combined effect of changes of the mass distribution function, discussed in Section 6.3.4, and metallicity tend to reinforce these systematic trends.

6.4.2 Searching for habitable planets in P-type orbits

Optimal conditions for circumbinary habitability

The statistical results displayed in Table 6.2 predict a very small fraction of binary systems with circumbinary HZs. The main reason for this is the extremely wide distribution of orbital separations exhibited by binary stars, which can attain values up to $\sim 2 \times 10^5$ AU (e.g. Hartman & Lépine, 2020). However, if we focus on close binaries ($\log a_b < -1$), most ($\sim 75\%$)

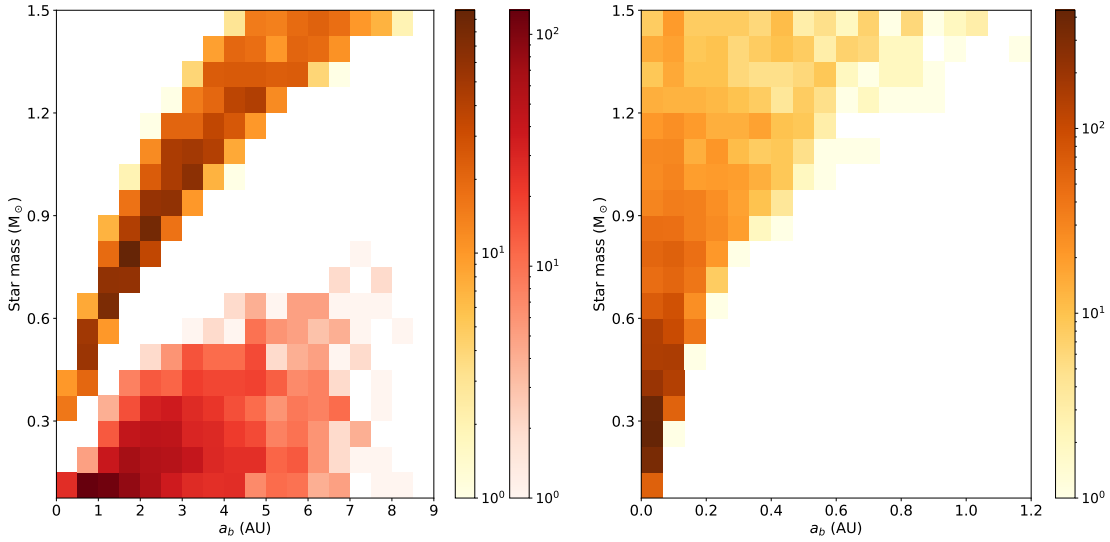

Figure 6.11: Density plot of star masses versus binary semimajor axis for selected samples of binary systems with optimal conditions of circumstellar (left) and circumbinary (right) habitability. Left panel: systems with $w_{\rm SB} > 1.3$. Right panel: systems with $w_{\rm P} > 1.3$. Yellow bins refer to the primary star mass, red bins refer to the secondary star mass. Sample obtained from a simulation with $N_\circ = 10^6$ of Model A (Table 6.2).

of the binary systems allow the existence of type-1 circumbinary regions (Fig. 6.7, right panel). Type-2 regions are possible for binaries with a separation of $\log a_b < 0.5$ ($P \lesssim 1000$ days for FGK-type twins), corresponding to 20% of the separation distribution. Only a small fraction of the systems in the $-1 < \log a_b < 0.5$ range has a combination of stellar and orbital parameters that actually supports habitability. As for the eccentricity, Fig. 6.9 clearly indicates that even a small increase above 0 strongly reduces the fraction of systems hosting circumbinary HZs. Therefore, we can identify two distinct populations: one of close, circularized binaries ($P < 30$ days), supportive of habitable circumbinary planets, and the other of wide, eccentric binaries ($P \geqslant 30$ days), mostly uninhabitable. On top of that, studies of planetary formation in circumbinary environments have raised concerns on the effective ability to form planets for binaries with $P \gtrsim 50$ days (see Section 6.3.1).

We can also observe (Fig. 6.6, right panel) that, for a small subset of the type-1 and type-2 binaries, the supplemental insolation of the secondary can produce a habitable zone wider than that allowed around a single star with the same mass of the primary star. The maximum enhancement of the width of the habitable zone (+41%) occurs for "twin-star" systems, where

Model[a]	e_p	$f_{\rm hab,SA}$	$\overline{w}_{\rm SA}$	$f_{\rm hab,SB}$	$\overline{w}_{\rm SB}$	$f_{\rm hab,P}$	$\overline{w}_{\rm P}$
A	0.0	0.843	0.955	0.869	0.970	0.035	0.930
A	0.3	0.841	0.954	0.868	0.969	0.036	0.936
A	0.6	0.832	0.951	0.860	0.966	0.038	0.942

Table 6.5: Impact of planetary orbital eccentricity, e_p, on the indices of habitability $f_{\rm hab}$ and $\overline{w}$ calculated with Model A. Model A is defined in Table 6.2. Results obtained for $N_\circ = 10^5$.

both stars have the same mass and hence the same luminosity. These twin-star, very close binaries have been already identified as especially conductive to life (Shevchenko, 2017) and our results support this conclusion, even though we must note that these systems seem to be very rare.

Concerning the mass of the primary star, Fig. 6.10 casts light on the requirements for optimal circumbinary habitability. While extended habitable zones are not a prerogative of massive primaries, it is clear that the strict binary separation prerequisite relaxes as mass increases. Higher mass primaries are able to sustain an appropriate level of insolation at larger distances, which in turn allow for less closed secondaries. In fact, all type-1 systems with $\log a_b > -0.5$ require a primary with $M > 0.8\,M_\odot$, namely a G-type star. The extension of the circumbinary HZ is favoured when we consider higher mass primaries. This can be seen in Fig. 6.11 (right panel), where we have selected the systems for which the circumbinary HZ is at least 1.3 times wider than in the case of a single central star with mass of the primary. Therefore, the mass of the primary can be considered a relevant statistical booster in the context of a rare scenario.

To summarize, even if the absolute number of binary systems with circumbinary HZs is low, by selecting close ($P < 10$ days), equal-mass binaries with G- and F-type primaries and low binary eccentricity we will find all the ingredients for increasing the circumbinary habitability.

Lessons from the current sample of exoplanets in P-type orbits

So far, there are 33 known binary systems with substellar companions in circumbinary orbits (The Extrasolar Planet Encyclopedia[6]): 12 of them have been detected via timing methods (applied to eclipsing binaries and pulsars), 10 via transit photometry, 8 via direct imaging, 2 via to microlensing and 1 thanks to radial velocity. When we exclude from the computation the objects with mass -or minimum mass- over 13 M_J (brown dwarfs), the detection by transit shrinks to 7, those by imaging to 4 and that by radial velocity (RV) to 0. In the case of Doppler surveys, past and present efforts have achieved typical measurement precision > 20 m s^{-1} (e.g., Martin et al. 2019, and references therein). The circumbinary planets uncovered by the transit method have typical masses akin to that of Saturn. The amplitude of the RV reflex motion induced by such companions at orbital distances beyond the critical value prescribed by dynamical stability considerations straddles the threshold of detectability for RV times-series with the above mentioned precision level. This might explain the lack of RV detections for this sample. Only 10 out of 33 systems are composed by Main Sequence stars and have their stellar and orbital parameters sufficiently constrained to conduct an analysis of their habitability. The circumbinary planets found around these systems have all been detected via the transit method. We now discuss the properties of this specific sample.

As can be seen in Table 6.6, the ten systems are well characterized and somewhat homogeneous in their properties. They all have separations comprised between 0.08 and 0.23 AU. Apart from Kepler-34, which exhibits a binary eccentricity of 0.52, they all have eccentricities lower than 0.16. Eight out of ten systems have a G-type primary (Kepler-16 has a K-type primary and Kepler-1647 has a F-type primary). Finally, their mass ratios are relatively high, with the largest disparity sported by Kepler-453 with $q = 0.21$. In other words, they generally comply with the conditions for finding circumbinary HZs (low a_b, low e_b, and relatively early-type primaries) and for widening the circumbinary HZs (relatively high mass ratios).

[6] http://www.exoplanet.eu

The detailed analysis of their circumbinary habitability confirms the existence of an overlap between radiative HZs and the regions of dynamical stability (Fig. 6.12).

At first sight, the fact that all the systems in Table 6.6 host circumbinary HZs seems at odds with the prediction that circumbinary HZs are extremely rare (Table 6.2). Even when we consider the limits on a_b for planetary formation and reduce the fraction of binaries with red dwarf primaries, we find that at least 1/2 of the systems does not support type-1 or 2 circumbinary HZs (Table 6.3). The detections collected in Table 6.6 point to the existence of observational biases that favor the detection of circumbinary planets in systems where the circumbinary habitability is possible. One obvious bias is that exoplanets are expected to be found in stable orbits, which means that circumbinary exoplanets must lie beyond the outer boundary of dynamical stability. At the same time, the geometrical probability of detecting exoplanets with the transit method increases with decreasing semimajor axis of the planetary orbit. The combination of these two biases means that circumbinary exoplanets can be detected with the transit method only if the outer boundary of dynamical stability, $a_{\rm crit,P}$, is sufficiently close to the stars. In turn, according to Eq. (6.13), the vicinity to the stars of $a_{\rm crit,P}$ implies that a_b must be small, which is exactly the condition that maximizes the existence of circumbinary HZs.

A more subtle bias emerges from the study of circumbinary planets around eclipsing binaries. It has been noted that this subset of planet-hosting binary systems is characterized by statistically larger than average periods (Martin et al., 2015; Martin, 2018). A proposed explanation of this bias involves the presence of a third, undetected faint companion in a large fraction of these systems. Another hypothesis by Fleming et al. (2018) explains it through an initial angular momentum transfer that widens a tight binary during the pre-MS stage and a successive magnetic braking that shrinks again the system. During the first stages of this process the closest circumbinary planets would be ejected. As a result, circumbinary planets would only be detected in wider systems ($P_b \gtrsim 5$ days), where this complex physical mechanism does not take place. If the systems have $P_b \lesssim 30$ days our predictions show that circumbinary HZs can still exist and be populated.

Finally, we note that the sample of known circumbinary planets is biased against the detection of small ($< 3\,M_\oplus$) objects. Detecting these planets via the transit method presents observational challenges, as the very shallow events exhibit transit timing variations (TTVs) on the order of days in magnitude, irregular depths and durations (Armstrong et al., 2013; Martin, 2020).

Analysis of the known circumbinary planet-hosting binaries

We now discuss the known circumbinary planet-hosting systems selected in the previous section one by one. Many of them have the habitability of their known circumbinary planets already explored (Haghighipour & Kaltenegger, 2013). Quarles et al. (2018) have assessed the possible existence of other, more interior planets in these systems, while Barbosa et al. (2020) discussed the formation of other planets besides those already discovered simulating their protoplanetary disk stage. Here, we apply Eq. (6.25) to insert them into the framework of our analysis of habitability. In addition, we investigate the possibility that undetected planets with terrestrial size may exist in the circumbinary habitable region.

The possible planet-planet interactions, that must be considered in order to evaluate the potential presence of Earth-sized planets in these systems, are treated under the conclusions derived by Quarles et al. (2018). For each known circumbinary exoplanet, they defined a

Name	M_A	M_B	a_b	e_b	ref
Kepler-16	0.689	0.203	0.224	0.159	Doyle et al. (2011)
Kepler-34	1.048	1.021	0.229	0.521	Welsh et al. (2012)
Kepler-35	0.890	0.810	0.176	0.142	Welsh et al. (2012)
Kepler-38	0.949	0.249	0.147	0.103	Orosz et al. (2012a)
Kepler-47	1.043	0.362	0.084	0.023	Orosz et al. (2012b)
Kepler-413	0.820	0.542	0.102	0.037	Kostov et al. (2014a,b)
Kepler-453	0.944	0.195	0.185	0.052	Welsh et al. (2015)
Kepler-1647	1.221	0.968	0.128	0.159	Kostov et al. (2016)
Kepler-1661	0.841	0.262	0.187	0.112	Socia et al. (2020)
TOI-1338	1.038	0.297	0.129	0.156	Kostov et al. (2020)

Table 6.6: The 10 currently known Main Sequence binary systems that host circumbinary planets. The masses in the second and third column are in solar units and the semimajor axis in the fourth column is in AU. It should be noted that other works include also Kepler-64 but, being actually a 4-component system, is not discussed in our study.

range of semimajor axes that would give rise to repeated close planetary encounters and the eventual destruction of the system architecture. These values are tested in massive numerical simulations and expressed in terms of planet-planet mutual Hill spheres (Chambers et al., 1996):

$$R_{H,m} = \frac{a_1 + a_2}{2}\left(\frac{m_1 + m_2}{3M_{int}}\right)^{1/3} \tag{6.27}$$

where a_1, a_2, m_1 and m_2 are, respectively, the semimajor axes and the masses of the innermost and outermost planet considered and M_{int} is the total mass interior to the outermost planet. The authors found that, in order to attain the long-term stability in all their tests, $a_2 - a_1 > \beta \times R_{H,m}$ with $\beta = 7$. This is a very conservative estimate, as they noted, and in some circumstances β can be as low as 5. However, in this work we will use the former value. This method gives us the opportunity to make a first-order assessment of the ability of a given binary system to host another planet in its HZ.

The combined results of our analysis of dynamical stability and habitability are summarized in Fig. 6.12. We now discuss individual cases.

Kepler-16 is the least habitable system in the sample, having a type-2 HZ with a reduced extension, $w_P = 0.29$, compared to a single-star HZ. This is caused by the interplay between the relatively large separation in this sample (0.22 AU) and the low luminosity of the two central stars. The system hosts a 0.33 $M_{\mathcal{Y}}$ planet right in the middle of its HZ, that makes quite unlikely the presence of another, Earth-sized planet in it.

Kepler-38, 47, 413, 453, 1661 and TOI-1338 have type-1 HZs, with w_P in the range from 1.0 to 1.08. These systems should present an environment remarkably similar to that of our own Solar System, especially when we consider that they all have G-type primaries. Kepler-38, Kepler-413 and TOI-1338 host respectively a 5.1 $M_\oplus$, a 0.21 $M_{\mathcal{Y}}$ and a 0.32 $M_{\mathcal{Y}}$ planet, all of them orbiting close to the inner edge of the respective dynamical stability zones and leaving the habitable zones entirely free for other possible bodies. Kepler-47 has three known planets with masses between 9 and 20 $M_\oplus$, two of them out of the HZ, being too close to the central stars to be habitable, and the third in the HZ but near its inner edge, possibly leaving room for another, cooler body in an outer orbit. Kepler-453 and Kepler-1661 both present

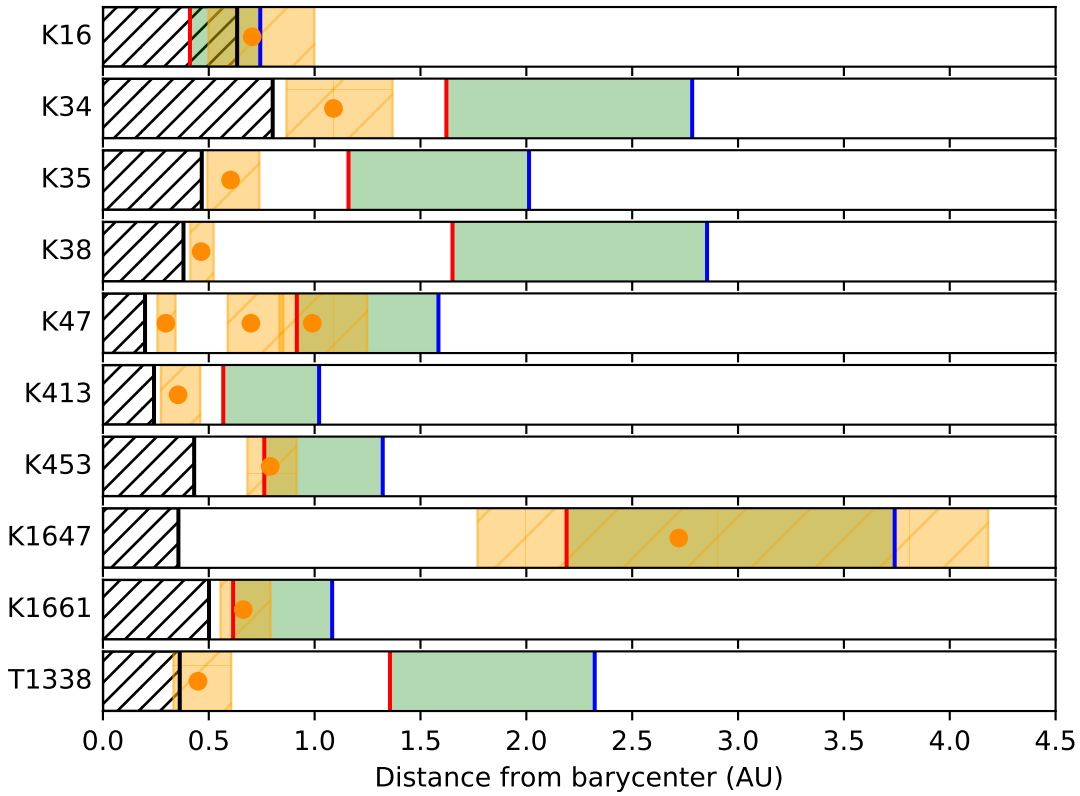

Figure 6.12: Combined analysis of the circumbinary regions hosting the Kepler and TESS exoplanets discovered so far. Orange dots: detected planets. Black hatched areas: region of dynamical instability. Red and blue lines: inner and outer edges of the radiation HZs. Orange areas: ranges of semimajor axes that cannot continuously host an additional Earth-sized (or larger) planet under the conditions derived by Quarles et al. (2018).

a similar situation, hosting respectively a 10 $M_\oplus$ and a 16 $M_\oplus$ planet in their HZ, near the inner edge.

Finally, Kepler-34, 35 and 1647 have extended type-1 HZs with w_P in the range from 1.1 to 1.36. Kepler-34 and Kepler-35 host respectively a 0.22 and a 0.13 $M_\jmath$ planet, both of them orbiting between the dynamical stability edge and the inner edge of the HZ. Once again, their HZ seem able to host Earth-sized planets. Considerations about disruption by planetary migration are not discussed here, but we note that such a mechanism may have prevented the formation or eliminated possible habitable bodies. Kepler-1647 hosts a 1.52 $M_\jmath$ planet in the central region of the HZ.

6.4.3 Searching for habitable planets in S-type orbits

Optimal conditions for circumstellar habitability

In contrast with the results related to circumbinary habitability, our Monte Carlo sampling (Tables 6.2 and 6.3) shows that planets in circumstellar orbits should encounter favourable conditions in most cases. The explanation for this fact is once again related to the extremely

wide distribution of binary semimajor axis. As it is possible to see in Fig. 6.11, the radiative influence of the secondary star rapidly decreases with increasing binary separation and for most of the systems is expected to be negligible. In particular, if we discriminate the systems where the circumstellar habitability conditions substantially deviates from the single-star case when $w > 1.1$, we find that only $\sim 1.2\%$ of the type-1 and 2 HZs around secondary and no HZ around primary fall in this category. If we raise the threshold to $w > 1.3$ (as in plot 6.11), the percentage of HZs around secondary reduces to $\lesssim 0.3\%$. In other words, we expect that most of the circumstellar planets in binary systems are subject to the same conditions of those in orbit around single stars.

On the other hand, close binary systems offer a range of exotic conditions that could result in vast enhancements of habitability, especially around secondary stars (as discussed in 6.4.3). This subset of binaries is also responsible for most of the trends that we observe in our habitability indexes. As it is possible to see in Fig. 6.10 (left panel), circumstellar habitability is favoured around low mass stars, both for the primary and the secondary. In particular, the mean extension $\overline{w}$ around the secondary is the largest on the entire mass range (right panel), although it must be noted that $\overline{w}$ is high in all cases, the lowest value being $\simeq 0.9$. Fig. 6.8 (left panel) hints that type-1 habitability around primary stars increases with the mass ratio between the components, while type-1 habitability around the secondary is substantially flat. A clearer trend is visible in Fig. 6.9, where type-1 habitability around both the primary and the secondary component is favoured by low eccentricies. At exactly $e = 0.0$ the fraction of type-1 HZ decreases significantly, but this is the effect of the correlation between eccentricity and orbital period introduced by the existence of a circularization period (see sect. 6.2.1): a consistent fraction of zero-eccentricity systems are also very close binaries that do not present dynamically stable S-type orbits sufficiently far away to the star. If only systems with $P_{\rm b} > P_{\rm circ}$ are included, the increasing trend in type-1 HZ width with decreasing eccentricity is uninterrupted. To conclude, apart from the wide binaries whose circumprimary or circumsecondary orbit can be studied as separated single stars, the best places for searching habitable exoplanets seems to be low mass systems with moderate separations and low eccentricites, that can offer enlarged HZs around secondary stars.

Even if the circumstellar habitability inside binary systems might not be impeded by dynamical instability, there are concerns regarding the disruption of the protoplanetary disk during the formation phase, as discussed in Section 6.3.1.

Analysis of the known circumstellar planet-hosting binaries

Currently, there are 90 known binary systems with projected separation under 1000 AU that host at least one planet in S-type orbit (the Extrasolar Planet Encyclopedia and the Schwarz et al. (2016) catalogue). Among them, 48 have been detected via radial velocity, 39 via primary transit photometry, 2 via microlensing and 1 via astrometry. This sample is larger than that of known circumbinary planets, but the stellar and orbital properties of these systems are somewhat less constrained. Most (63) of these systems have projected separations above 100 AU, possibly indicating a bias in favor of wide binaries. A physical explanation of this bias points to the difficulty to form planets in the gravitationally active environment influenced by the presence of a close companion star (Kraus et al., 2016). An explanation in terms of observational bias is that, for such large separations, the reflex motion induced by one star on the other is small and varies very little in time. This makes the probability of detecting exoplanets around any of the components no different from the probability of

Name	M_A	M_B	a_b	e_b	$w_{\rm SA}$	$w_{\rm SB}$	Method[b]	ref
HD 41004	0.7	0.4	23	0.2[a]	1.00	1.00	RV	Zucker et al. (2004)
HD 196885	1.33	0.45	21	0.42	1.00	1.02	RV	Correia et al. (2008)
γ Cephei	1.41	0.41	20.2	0.41	1.00	1.03	RV	Hatzes et al. (2003)
Gliese 86	0.83	0.49	19	0.40	1.00	1.00	RV	Queloz et al. (2000)
HD 176051[c]	1.07	0.71	18.9	0.54	1.00	1.01	AS	Muterspaugh et al. (2010)
Kepler-420[d]	0.99	0.70	5.3	0.31	0.16	1.01	TR	Santerne et al. (2014)
HD 42936	0.87	0.08	1.22	0.59	0.00	1.14	RV	Barnes et al. (2020)

Table 6.7: The 7 binary systems with circumstellar exoplanets currently known with component separations < 30 AU, Main Sequence components and sufficiently constrained stellar and orbital parameters. Masses are in solar units, a_b is AU. (a) assumed eccentricity. (b) RV: radial velocity, AS: astrometry, TR: transit. (c) unconfirmed. (d) the orbital properties of the binary companion, derived for an assumed distance of ~ 900 pc (Santerne et al., 2014), are uncertain. The Gaia DR2 astrometric solution reports a negative parallax, it has a large excess noise (2.44 mas), and the reduced unit weight error (RUWE) statistics is $\simeq 12$, indicating an unreliable solution (well-behaved solutions being those with RUWE < 1.4 (see e.g. Lindegren et al., 2018). This might be due to a combination of unmodeled orbital motion and confusion due to light contribution from the binary companion.

detecting exoplanets around single stars. In fact, in some instances, the binarity has been discovered after the detection of the planet. This fact makes also clear that this statistics is far from definitive. On one side, there are ongoing searches (e.g. Ziegler et al., 2017) for possible companions of stars currently considered single. On the other, some of the systems currently considered binary might be part of higher order multiplicity groups.

As explained in sect. 6.4.3, the influence of the one star on the other's HZ rapidly decreases with increasing separations. Therefore, in order to give them a closer look in the framework of our work, we have selected the 12 known binaries with $a_b < 30$ AU. We then excluded 5 of them for the lack of sufficient data (OGLE2013-BLG0341 and HD 7449), the presence of a non-Main Sequence primary (HD 59686 and HD 87646) and the misalignment of planetary and companion star orbital planes (Kepler-693). The 7 remaining systems and the method used for the detection of their planets are reported in table 6.7.

All the selected systems have late-type (M- or K- type) secondaries and relatively large eccentricities. Even if these conditions tend to favor circumstellar habitability, the effects of binarity on these systems are generally negligible. An enhancement in the order of $1-3\%$ is present in the widths of the secondary star HZs in 3 systems, while for the primary star HZs the effect is $< 0.2\%$ in every instance. Only the two systems with small stellar separations (HD 42936 and Kepler-420) show significant effects of binarity on their HZs. This fact stresses, again, the dominant role of stellar separation on the habitability of binary systems. In Kepler-420 the gravitational pull of the secondary reduces $w_{\rm SA}$ to 0.16, making it an uncommon example of type-2 HZ. Instead, the secondary star HZ is slightly enhanced. Finally, in HD 42936 the secondary orbits in the outer part of the primary star HZ. Therefore, there is no room for habitable planets around the most massive component. On the other hand, the secondary star has an enhanced type-2 HZ. The flux from the primary generally dominates the energy balance in the secondary HZ, and accounts for $\sim 47\%$ of the total energy that would be received by an hypothetical planet at exactly the inner edge of the HZ.

Searching for habitable planets around the secondary

The enlargement of the HZ around the secondary star (left panel in Fig. 6.6), resulting from the outwards shift of the outer edge of the radiative HZ (Section 6.3), is potentially interesting for observational searches of habitable planets in binary systems. For this reason, we performed several tests to understand in which range of binary parameters this effect is prominent. The only significant trends we found are shown in the left panel of Fig. 6.11, where we plot the systems for which the HZ is extended by more than 30% than the HZ of a single star of the same mass. One can see that the enlargement of the HZ takes place for small values of binary semi-major axis ($a_b \lesssim 8$ AU), when secondary stars are of M type (red dots with $m_B \lesssim 0.6$ M$_\odot$), and when the primaries have a well-defined range of masses as a function of a_b (yellow dots). Even if the fraction of systems with these properties is small ($\sim 0.1-0.3\%$ across different models), it would be extremely interesting to search for extended HZs around M-type stars. Since the enlargement of the HZ is due to the outward shift of the outer edge of insolation, with a proper selection of binary systems this configuration may provide a unique possibility to find habitable planets not affected by tidal locking around M-type stars.

6.5 Conclusions

We have designed a suite of Monte Carlo experiments aimed at generating large samples of binary stellar systems. The systems are extracted by random sampling of a set of PDFs of stellar masses and orbital parameters representative of binary stars in the main sequence, with masses in the range from 0.08 to 1.5 M$_\odot$. The simulated samples of binary stars are used to quantify the statistical properties of planetary habitability in binary systems. For each extracted system, we estimate the luminosity and effective temperature of the primary and secondary star using stellar evolutionary tracks calculated at two values of stellar metallicity (solar and 1/2 solar). From the dynamical data of each system and the application of algorithms obtained from N-body simulations (Quarles et al., 2018, 2020) we calculate the location and extension of regions of dynamical stability for planetary orbits. By weighting the radiative flux received by the two stars (Kaltenegger & Haghighipour, 2013; Haghighipour & Kaltenegger, 2013) we calculate the boundaries of the radiative HZs. We define three possible conditions of long-term habitability from the study of the intersection between dynamically stable regions and radiative HZs in the stellar orbital plane. If the intersection is complete, partial or null, the habitability is classified of type 1, 2, and 3, respectively. This definition is applied both to circumstellar, S-type orbits and to circumbinary, P-type orbits. To gauge the impact of stellar binarity on habitability, the extension of type-1 and type-2 HZs is compared to the extension of the classic HZ around a single star with the same mass of the host star. To assess the robustness of the results, the Monte Carlo experiments are repeated for different models, each model being defined by a specific set of PDFs. The results obtained from different models consistently support the following conclusions.

- In $\sim 95-97\%$ of all binary systems, circumbinary habitability is prevented by the lack of overlap between the radiative HZ and the dynamically stable region (type-3 condition). However, significant fractions of circumbinary HZs exist at the low-end tail of the distribution of stellar separations, when $a_b \lesssim 0.3$ AU.

- Circumstellar habitability is possible for $\sim 78-94\%$ of binary systems, in most cases with a complete overlap between the radiative HZ and the dynamically stable region

(type-1 condition). However, habitable circumstellar regions become rare when $a_b \lesssim 1\,\mathrm{AU}$.

- If we consider the sub-samples of systems where planetary formation is currently believed to be possible, we find that $99-100\%$ of systems with $a_b > 10\,\mathrm{AU}$ can feature circumstellar HZs, whereas $16-23\%$ (or $35-44\%$) of systems with $a_b < 0.3\,\mathrm{AU}$ (or $< 1.0\,\mathrm{AU}$) can feature circumbinary HZs. If we consider also a lower limit $P_b > 5$ days for circumbinary planetary formation, we find a reduction of $20-25\%$ of the circumbinary habitable fraction. Therefore, the conditions for circumbinary habitability are stringent even when planetary formation is taken into account.

- The habitability fractions are marginally affected by different hypotheses on the occurrence rate of binaries with primary stars of different spectral types. A factor-of-two reduction of the systems with M-type primaries does not change the circumstellar habitability and increases the circumbinary habitability by $4-6\%$.

- Cases in which the radiative HZ is interrupted by the boundary of dynamical instability (i.e., type-2 conditions of habitability) are rare and are found around $a_b \sim 1\,\mathrm{AU}$ in circumstellar regions and around $a_b \sim 0.1\,\mathrm{AU}$ in circumbinary regions.

- The eccentricity of stellar orbits, e_b, affects the habitability around binary stars. Both circumbinary and circumstellar habitability are favored at low e_b, but in the latter case this result is partially masked by the correlation between period and eccentricity introduced by the circularization period P_{circ}. This causes a drop at exactly $e_b = 0.0$.

- Stellar hosts of F and G spectral types yield slightly higher fractions of habitable circumbinary regions than hosts of K and M spectral types. Instead, the fraction of habitable circumstellar regions tends to increase for host stars of later spectral type.

- The impact of stellar metallicity on binary habitability is almost negligible, with a slight increase ($\lesssim 1\%$) of the fraction of habitable circumbinary regions when the metallicity decreases from solar to half the solar value.

- Owing to the radiative contribution of the companion star, circumstellar HZs around M-type secondary stars can be several times (up to one order of magnitude) more extended than in the case of a single star. Circumbinary HZs can be up to 41% more extended when the mass ratio of the two stars is $q = m_{\mathrm{B}}/m_{\mathrm{A}} \sim 1$.

- The ranges of a_b and stellar masses that allow the existence of extended HZs are well constrained (Fig. 6.11) and can be used to focus searches for habitable planets in binary systems. An intriguing, albeit hard to detect, possibility would be to search for extended HZs around M-type stars, with the outer edge located beyond the tidal-lock limit.

To set the predictions of our statistical analysis in an observational framework, we have investigated the properties of the binary systems where exoplanets have been discovered so far. Circumbinary HZs are found in all the systems that host transiting planets in P-type orbits. Different observational biases conspire to boost the detection of such systems despite the rarity of circumbinary HZs in the general population of binary stars. In most of the cases, circumbinary HZs in these systems may potentially host additional Earth-sized planets not detected so far. As far as the exoplanets in S-type orbits, at present time the quality of the

observational data of the binary systems hosting these exoplanets is insufficient to perform a general study of the habitability of circumstellar regions.

Chapter 7

Using EOS-ESTM: some study cases

In this Chapter I present three applications of the EOS RT model. First of all, I show how the coupled EOS-ESTM procedure has been used to probe the habitability of circumstellar planets in binary stars, as an initial follow-up to the statistical analysis presented in Chapter 6. Then, again using the EOS-ESTM model, the Archean Earth climate is analyzed by considering the most recent understanding on the surface pressure limits and the CO_2 abundance. Finally, I demostrate how EOS can be used to bridge the gap between climate modeling and future observations by presenting some of the synthetic emission spectra produced with our code.

The work on binary habitability has been done as part of the Master's Degree Thesis of Maria Di Paolo. Model calculations and analysis were performed between late Winter 2020 and early Spring 2021, and the Thesis was presented in June 2021. The work on the Archean Earth has been done as part of the Master's Degree Thesis of Riccardo Bevilaqua. Model calculations and analysis were performed in the first months of 2022, and the Thesis was presented in April 2022. In both cases and together with their Advisor (Prof. G. Vladilo), I tutored the students by contributing to the preliminary analysis process and I produced all the RT lookup tables necessary to run the climate simulation. The Di Paolo study, in particular, was directly inspired by and largely based on the work presented in Simonetti et al. (2020). While the results of these studies are still preliminar, these applications are included in the present work to show the extreme flexibility and efficiency of EOS and I thus include them in the present work.

7.1 Habitable planets in binary star systems

Under normal circumstances, the habitable zones (HZs) for M- and late K-type stars reside completely inside the tidal lock radius $r_{\rm tl}$ (Kasting et al., 1993b) for those stars, meaning that over timescales much shorter than the life of the system the planet spins down due to the tides induced by the parent star until $P_{\rm rot} = P_{\rm orb}$, becoming *tidally locked*. The tidal lock radius depends on the initial rotation rate and on the deceleration rate $d\omega_p/dt$ (ω_p being the angular velocity of the planet), which in turn depends on several planetary parameters (mass, radius, moment of inertia, the tidal dissipation function[1] and the second Love number[2]), on the stellar

[1]The tidal dissipation function (MacDonald, 1964; Goldreich & Soter, 1966) describes the departure of the planet from perfect elasticity, i.e. from energy conservation. It depends on the rheological properties of the planet and it is, in general, very poorly constrained.

[2]The first and second order Love numbers (Love, 1909) are used to summarize the susceptibility of the planet to deform in response to an external gravitational potential, and depends on both the elasticity and

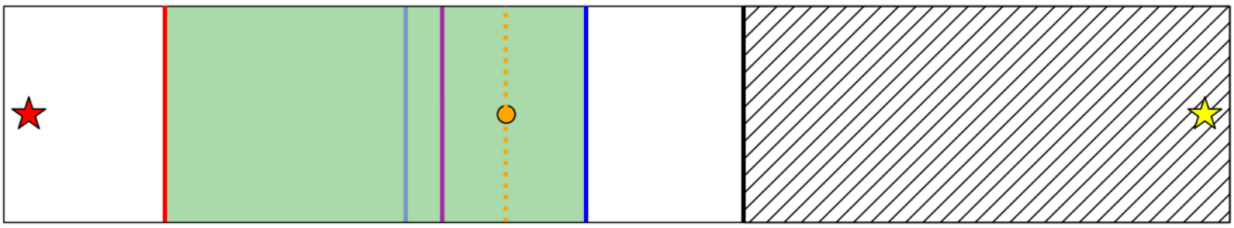

Figure 7.1: Sketch of the configuration of an extended circumstellar HZ in a binary star system. Red and yellow stars: secondary (B) and primary (A) components of the system. Orange circle: planet. Green region: circumstellar HZ around the secondary. Red and blue lines: inner and outer edge of the HZ, taking into account the insolation from both stars. Light blue line: outer edge when the contribution from the primary is neglected. Purple line: tidal lock radius. Orange dotted line: orbital radius of the planet around the secondary. Hatched area: dynamical instability region. Credit: Di Paolo et al., in preparation.

.

mass and on the orbital semi-major axis (see e.g. p.p. 130-178 of Murray & Dermott, 1999). This last quantity enters the relation as a_p^{-6}, thus producing a sharp transition between the region in which the planet becomes tidally locked in a very short amount of time ($\lesssim$ 100 Myr), and the region in which it is basically unaffected. On a tidally locked planet, one hemisphere is always illuminated by the star and the other hemisphere suffers a perennial night. These planets are characterized by a large thermal gradient between the substellar and the antistellar point, resulting in extreme weather patterns (see e.g. Wordsworth, 2015). This suggests the possibility that M-type stars might be unable to host habitable planets.

However, a circumstellar planet in a binary star system would receive energy not only from the parent star, but also from the binary companion. The increased instellation moves the circumstellar HZ outward. In a small but nonzero fraction of systems, this allow the HZ out edge radius to exceed the tidal lock radius also for late type stars (up to the coldest M5), opening the possibility for them to host non-tidally locked habitable planets. This situation is qualitatively depicted in Fig. 7.1: the non-locked planet (orange circle) would be outside the single-star HZ (the region between the red and the light blue line), but it is warmed up to habitable conditions once the flux from the other star is accounted for (darker blue line). This situation is most likely to happen around the least massive component, i.e. the secondary.

Th statistical analysis of the synthetic population of binary stellar systems discussed in Section 6.4.3 has shown the theoretical possibility for non-tidally locked habitable exoplanets to exist in circumstellar orbits around M-type secondaries. The occurrence rate of this configuration is low ($\sim$ 1.2%) but warranted a more thorough investigation, because binary systems are quite common and the HZ can be widened by a factor of 10. The HZ calculations in Simonetti et al. (2020) were based on the mean instellation received by the planet over one orbital period of the companion. However, such a companion can be on an eccentric orbit, causing substantial variations in the amount of energy received by the circumsecondary planet. Considering that climate systems show hysteresis (see Section 2.4), this case must be studied using a climate model, even if simplified as ESTM, in order to be able to track the evolution of surface planetary conditions when the total instellation varies during the orbital motion of the two stars. Below we present the preliminary results of this study which constitutes a practical application of the EOS-ESTM1 code. The full analysis will be included in a

the internal density profile of the body. They can be estimated by planetary interior models.

separate paper (Di Paolo et al., in preparation).

7.1.1 Target selection

The first step of the Di Paolo's analysis of habitability in widened circumsecondary HZs was to select two specific test cases. The first one, that we will call *system 1*, is representative of the averge features of these types of HZs. The second, that we call *system 2*, is representative of cases with a large widending of the HZ, which implies strong variations of the instellation along the orbit. These specimens were extracted from the synthetic population labeled as *Model A* (see Table 6.2). Quantities used for the selection are: (i) the outer edge of the HZ around the secondary accounting for the fluxes of both stars $a_{\mathrm{MG,SB}}$ and (ii) the outer edge without accounting for the flux of the primary star $a_{\mathrm{MG,SB}\circ}$.

In order to find the average features of the binary star systems of interest, a **first selection** was operated on the Monte Carlo sample by selecting the specimens that satisfied the following criteria:

- $r_{\mathrm{tl}} > a_{\mathrm{MG,SB}\circ}$, which means that the single-star HZ would host only tidally-locked planets;
- $r_{\mathrm{tl}} < a_{\mathrm{MG,SB}}$, which means that the widened HZ allows for non-tidally locked planets;
- be a type-1 HZ, which means that it does not overlap with the dynamical instability region;
- $\frac{a_{\mathrm{MG,SB}}}{a_{\mathrm{MG,SB}\circ}} \geqslant 1.01$, which excludes negligibly widened HZs.

This produced a smaller subsample consisting of 582 systems (∼0.06% of the original sample). The statistical analysis of these systems showed the following features:

(i) a flat distribution of the primary star masses M_A;

(ii) a distribution of the secondary star masses M_B peaked at 0.48 $\mathrm{M}_\odot$, with a large majority of the systems (∼85%) at $M_B \geqslant 0.44$ $\mathrm{M}_\odot$;

(iii) a Gaussian distribution in the binary eccentricity e_b that closely follows the Stepinski & Black (2001) distribution used to produce the original sample;

(iv) a distribution in the binary semi-major axis a_b peaked at 3.8 AU, with ∼80% of the systems in the $[2.0; 6.0]$ AU range.

Based on the shape of the distributions considered at (ii) and (iv), it was decided to operate a **second selection** by considering only systems with $2\,\mathrm{AU} \leqslant a_b \leqslant 6\,\mathrm{AU}$ and $M_B \geqslant 0.44$ $\mathrm{M}_\odot$, reducing the number of specimens to 345. By analyzing again the primary star mass and the binary eccentricity distributions it emerged that the former exhibited a shallow peak in the $[0.62; 0.86]$ $\mathrm{M}_\odot$ region, while the latter remained unchanged.

On this subsample, a **third, final selection** under two different sets of criteria was operated in order to select the two test cases (*system 1* and *system 2*) for the climate simulation. In the case of *system 1*, the following course of action was adopted:

1. The conditions on the M_B and a_b where further tightened around the respective distribution peaks found on a finer bin grid. As a result, 44 systems with $M_B \in [0.48; 0.485]$ $\mathrm{M}_\odot$ and $a_b \in [2.7; 3.7]$ AU were extracted.

Quantity	*system 1*	*system 2*	Units
M_B	0.48377	0.47208	$M_\odot$
M_A	0.5813	1.0977	$M_\odot$
L_B	0.031677	0.029141	$L_\odot$
L_A	0.072021	1.5183	$L_\odot$
T_B	3487	3458	K
T_A	3846	6074	K
a_b	3.2194	2.8300	AU
p_b	2044.5	1387.9	days
e_b	0.03257	0.08740	..
$a_{\mathrm{MG,SB}\circ}$	0.3596	0.3455	AU
$a_{\mathrm{MG,SB}}$	0.3646	0.4969	AU
$a_{\mathrm{crit,SB}}$	0.8156	0.5035	AU
r_{tl}	0.3608	0.3579	AU
a_p	0.361	0.380	AU

Table 7.1: Features of the selected test cases.

2. A new peak in the M_A distribution was identified in the $[0.58; 0.60]$ $M_\odot$ mass range, containing 8 systems.

In the case of *system 2* the procedure was as follows:

1. A stricter condition of the outward shift of the outer edge was applied, such that $a_{\mathrm{MG,SB}} \geqslant 1.1 a_{\mathrm{MG,SB}\circ}$.

2. The maximum instellation contribution of the primary star (i.e., when it is at the periastron) at r_{tl} and at $a_{\mathrm{MG,SB}}$ was evaluated. Then, the systems for which the total instellation at the former position was $\geqslant$150% that at the latter position were extracted. This condition ensures that the distance between the tidal lock radius and the outer edge of the HZ is substantial. 18 systems passed these conditions.

System 1 and *system 2* were then picked randomly among the respective surviving specimens. The characteristics of these systems are reported in Table 7.1. The last set of parameters that had to be decided concerned the features of the planet orbit in the two selected cases. To keep the analysis simple, it was opted for perfectly circular planetary orbits, coplanar with the binary star orbit. The planetary semi-major axis a_p was chosen in such a way to have $P_b = N \times P_{\mathrm{orb}}$ with $N \in \mathbb{N}$, which means that the binary orbital period is a multiple of the planetary orbital period. In both cases, the planet was positioned just outside the tidal lock radius, at the first value of a_p that satisfied the orbital period condition stated above.

The next step was to study the evolution over the ages of the two selected systems to fix a proper moment in the lifetime of these planets. This must be done since (i) both planets have been put outside but near the tidal lock radius, meaning that during their evolution their rotation rate will significantly decrease and (ii) stars undergo evolutionary processes that increase their power output during their permanence in the Main Sequence. For *system 1*, the stellar evolution of both components is slow since they are low mass, meaning that their luminosity is basically constant on a $\sim$10 Gyr timescale. Given that the initial rotation rate of the planet is itself a free parameter, it was actually not necessary to fix a specific

moment in the system lifetime. The rotation period of the planet in the *system 1* was thus fixed to 1.0 days.

On the other hand, the primary component in *system 2* is massive enough to experience a significant increase in luminosity. It was decided to consider three epochs: 3.5, 4.0 and 4.5 Gyr from the formation of the system. The first is the Main Sequence mid-point for the primary star and the third is roughly equal to the age of Earth. The second was chosen as an in-between value. With respect to the mid-point value, the luminosity of the star at 4.0 and 4.5 Gyr increases respectively by 6% and 13%. Fixing a specific epoch made necessary to study the evolution of the rotation period of the planet. In turn, several hypotheses were required to perform the integration of the deceleration rate $d\omega_p/dt$ to find a specific rotation period. This calculation was carried out by:

- supposing that the planet has formed at the same time of the stars;
- choosing an initial rotation period of 13.5 h and a tidal dissipation function value of 100 (as done by Kasting et al., 1993b, for a generic Earth-like planet);
- modeling the planet as an homogenous sphere with the same average density of Earth.

and as a result, the rotation period of the planet in *system 2* at the three considered epochs was equal to 1.23, 1.48 and 1.86 days, respectively.

Independently from the specific evolution of the system, both test planets are subjected to large variations in the instellation on the ∼year timescale due to the combined orbital motion around their parent star and the orbital motion of the binary companion. As reported at the beginning of this Section, this was actually one of the reasons that justified this work. The total excursion in the received flux can be evaluated considering two specific orbital geometries: (i) when the bodies are aligned in the secondary-planet-primary configuration and the primary star is at periastron and (ii) when the bodies are aligned in the primary-secondary-planet configuration and the primary star is at apastron. The former corresponds to the maximum total received flux $\mathcal{I}$, the latter to the minimum. For *system 1* $\Delta\mathcal{I} \sim 0.004$ $S_\odot$, while for *system 2* at 4.5 Gyr $\Delta\mathcal{I} \sim 0.210$ $S_\odot$. By considering that the flux received from the parent star is ~ 0.24 $S_\odot$ in the first case and ~ 0.20 $S_\odot$ in the second case, the relative excursion in the latter is nearly two orders of magnitude larger.

7.1.2 Choice of the ESTM parameters

The obliquity of the planet was set to zero in both cases and a constant ocean fraction, equal to 0.7, was adopted for all the latitudinal bands. Given the exotic configuration selected for this study, the following changes in the ESTM parameters were necessary:

(i) In the case of a single star, the latitudinal temperature profile of the planet is calculated in a certain number of points along the planetary orbit, for a certain number of orbits, until a stationary solution is found. In this case instead, a certain number of points on the primary star orbit are selected. Moreover, ESTM is to convergence *in each point* and the equilibrium state of the planet found at the point i is then used to initialize the simulation at the point $i + 1$. The process is repeated until both the planet and the primary star are again at the initial positions. The evolution of the total instellation during this period is depicted in Fig. 7.2 for *system 1* (panel a) and *system 2* (panel b).

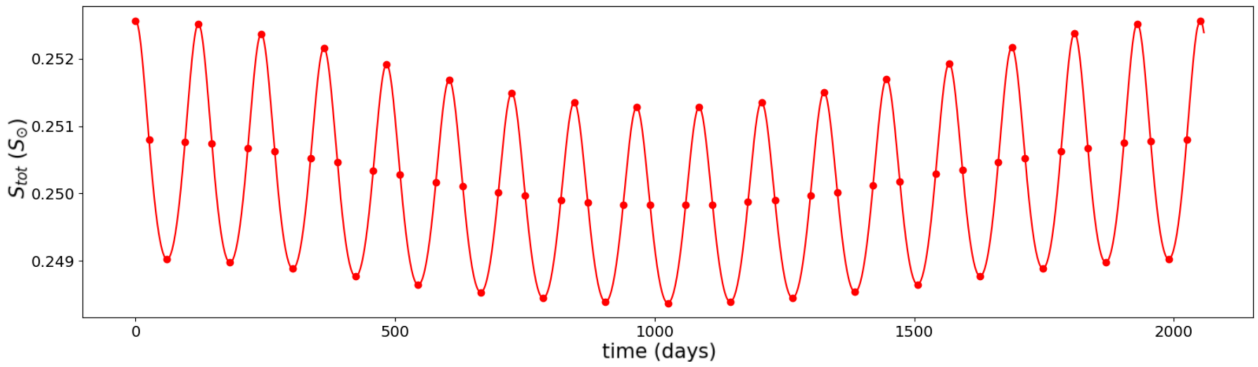

(a)

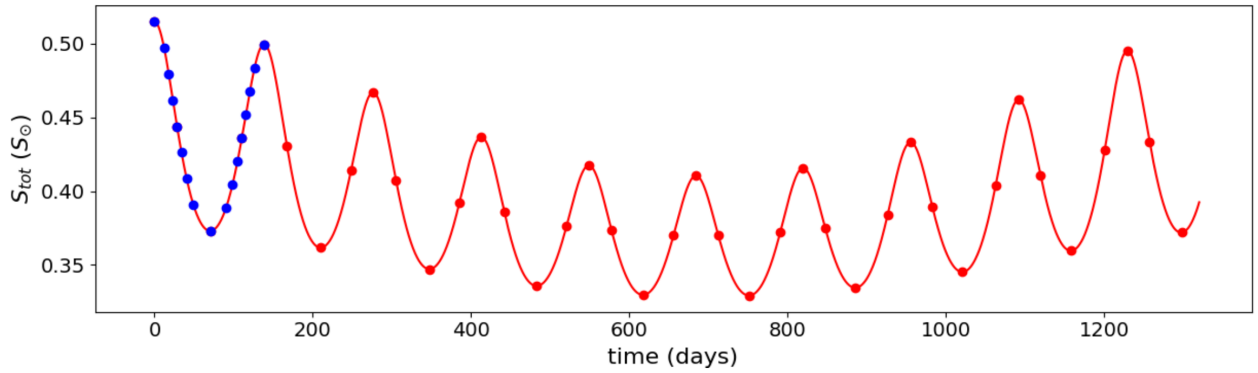

(b)

Figure 7.2: Temporal evolution of the total instellation received by the planet in the *system 1* (panel a) and in the *system 2* (panel b). The climate model has been run at the instants represented by the red and blue points along the curves. The final part of the curve in panel (b) is lacking but has been considered in the computations. Credit: Maria Di Paolo.

.

(ii) At variance with the standard ESTM1 version, here the albedo of ices over land ($\alpha_{\rm i,lnd}$) and oceans ($\alpha_{\rm i,ocn}$) were given two distinct values. They were set to 0.7 and 0.5, in order to represent the deposition of snow and the formation blue marine ice, respectively (see Tab. 2.1).

(iii) For one of the models (namely, *system 2* at 4.5 Gyr), a different set of ice albedos was tested, alongside the one reported at (ii). In fact, since the test planets receive either the entirety (*system 1*) or a large fraction (*system 2*) of the light with a SED different from that of the Sun, the albedo of ices should be re-evaluated accordingly. For this study, the results from Joshi & Haberle (2012)[3] were taken into consideration and used to derive new values for the marine ice and snow albedos when illuminated by an M2-type star. These values are 0.45 and 0.23, respectively. The actual values of $\alpha_{\rm i,lnd}$ and $\alpha_{\rm i,ocn}$ were calculated by a weighted average between these values and those reported at (ii), with fluxes from star A and B as weigths.

[3]They computed the snow and ice albedo under the spectrum of Gl 436 ($T_{\rm eff}$ = 3684 K) and GJ 1214 ($T_{\rm eff}$ = 3026 K). Since the B component in both systems have $T_{\rm eff} \sim$ 3450 K, the arithmetic mean of their results was taken.

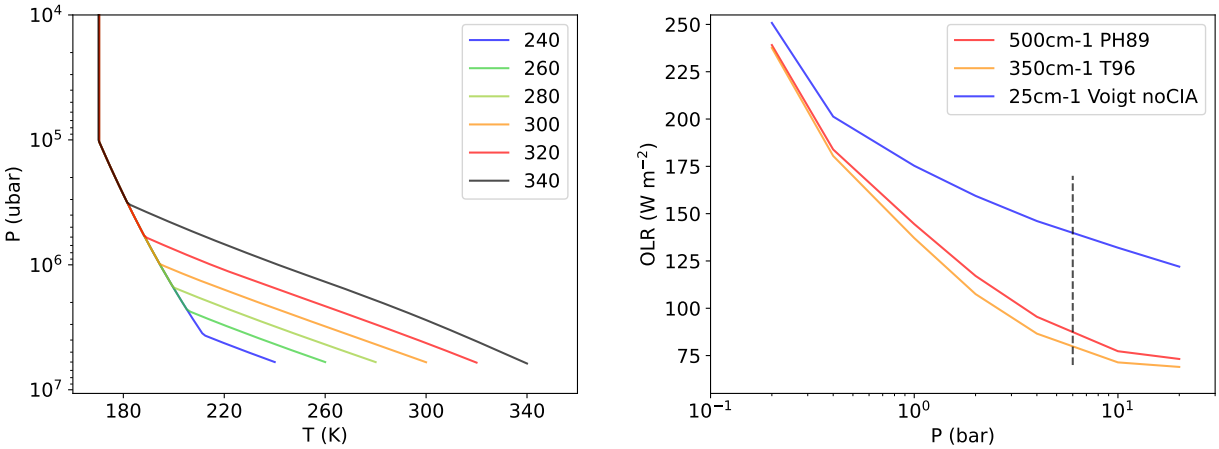

Figure 7.3: Left panel: some of the vertical pressure-temperature profiles used to model the atmosphere in this study case. Right panel: the OLR as a function of the surface pressure for a fixed surface temperture of 273 K, using different prescriptions for the CO_2 line profile and CIA. Red line: Perrin & Hartmann (1989) sub-Lorentzian profile truncated at 500 cm^{-1} and GBB CIA. Orange line: Tonkov et al. (1996) sub-Lorentzian profile truncated at 350 cm^{-1} and GBB CIA. Blue line: Voigt profile truncated at 25 cm^{-1}, no CIA. The vertical black dashed line identifies the 6.0 bar pressure. The chemical makeup and the vertical atmospheric profile are the same in all cases.

7.1.3 The RT model

Given that both the test planets lie in the outer part of the HZ, relatively dense CO_2-dominated atmospheres (ses Section 2.4.3) can be expected. It was thus decided to adopt for all tests a CO_2-H_2O atmosphere with a dry (i.e. CO_2) surface pressure of 6 bars and a variable H_2O pressure, calculated from the Clausius-Clapeyron relation (Eq. 2.21) by considering a 60% fixed relative humidity throughout the atmospheric column. The pressure grid adopted for RT calculations consisted in 68 layers (∼10 per order of magnitude), from the surface to the uppermost layer at 1 μbar. The pressure-temperature atmospheric profile was composed by a convective troposphere overlain by an isothermal stratosphere. The lapse rate in the troposphere was calculated by integrating Eq. 2.26. The tropopause was fixed at the 0.1 bar level, following the results of Robinson & Catling (2014). The temperature of the stratosphere, equal to that of the tropopause, is thus variable and related to the surface temperature, at least in principle. In Section 4.1.2 it was shown that this particular choice prevents the change of the OLR slope at high temperatures that is expected when the Runaway Greenhouse limit is approached, at least in relatively thin, Earth-like atmospheres. However, this is not true in this case. As it is possible to see in Fig. 7.3, left panel, the atmosphere used here is sufficiently deep to prevent this behaviour, at least up to $T_s \simeq 350$ K: the tropopause has the same temperature in all models (170.2 K).

Concerning the opacity prescription for gases, the work presented in this Section was conducted before the completion of EOS. In particular, the formulations to produce sub-Lorentzian absorption line wings in CO_2 and to add the CO_2 CIA features were still lacking. This means that the results presented below are only preliminary. However, they are useful to show both flexibility and the efficienty of the coupled EOS-ESTM calculations, that allows for a rapid exploration of varying climate conditions resulting from the change of instellation

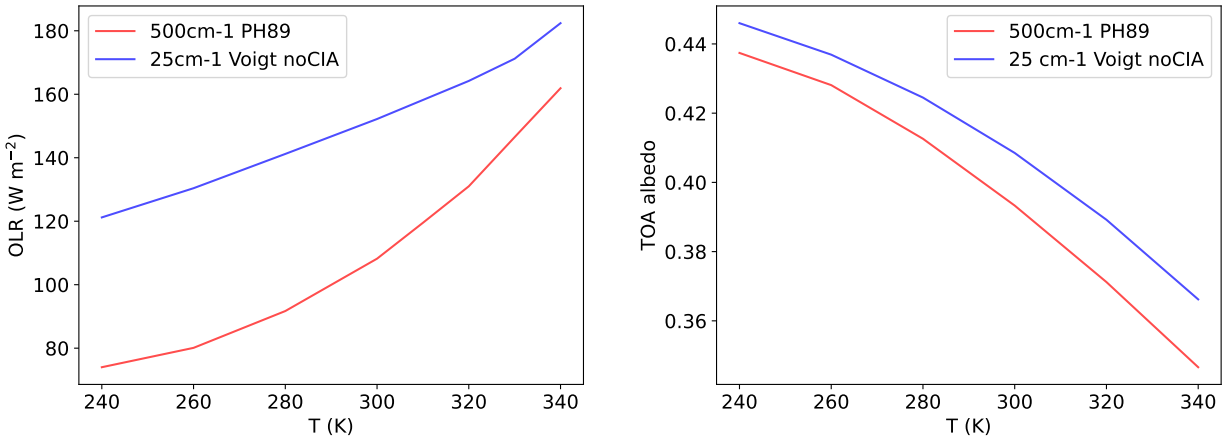

Figure 7.4: The dependence of the OLR and TOA albedo on the surface temperature for the atmosphere adopted in this study. Left panel: OLR. Right panel: TOA albedo for a stellar zenith angle of 60° and a surface albedo of 0.30. The instellation SED is that of a 5780 K blackbody, which models a G2-type star. Red line: Perrin & Hartmann (1989) sub-Lorentzian profile truncated at 500 cm^{-1} and GBB CIA. Blue line: Voigt profile truncated at 25 cm^{-1}, no CIA.

properties (intensity and SED) during the binary orbital period. The case study presented here will be subject of a re-analysis with the updated EOS RT (Di Paolo et al., in preparation).

The OLR

H_2O absorption is treated following the same standard used throughout the rest of this Thesis: lines are Voigtian and truncated at 25 cm^{-1} and the continuum has been calculated using the MT_CKD 3.4 model. However, in the RT calculations performed at that time the CO_2 lines were modeled via stardard Voigt profiles truncated at 25 cm^{-1} and the absorption contiuum for this gas was not considered. Because of the lacking CO_2 opacity, the OLR is higher at all points in the considered temperature range. In order to evaluate this effect, I run again the same atmosphere but using the lastest version of EOS. The comparison between the dependence of the OLR on the surface pressure (Fig. 7.3, right panel) and the surface temperature (Fig. 7.4, left panel) have been studied. By taking the Perrin & Hartmann (1989) model with the Gruszka-Borysow-Baranov (GBB) CIA (see Section 3.6.1) as the fiducial model (in red), it is possibile to see that, at low (< 280 K) temperatures, the OLR difference is $\sim$ 46 Wm^{-2}, while at high (> 330 K) temperatures it rapidly reduces to $\sim$ 20 Wm^{-2}. This behaviour is caused by the fact that the contribution to the atmospheric opacity from H_2O is much smaller in the former case than in the latter. Since the two models deviate in the treatment of CO_2, a larger spread is seen at low T_s. This means that the OLR is considerably overestimated, especially at low temperatures, leading to a colder simulated climate. Another feature that may be noticed is the fact that, for both models, the evolution of the slope with temperature is the opposite of what expected, being steeper at higher T_s. This is probably caused by the fact that the atmospheric opacity is dominated by CO_2 contributions both at low and at high T_s. In this regime, the OLR flattens at temperatures higher than in the case of a Earth-like atmosphere (see e.g. Fig. 4.6, left panel), and higher than the highest value considered here (340 K).

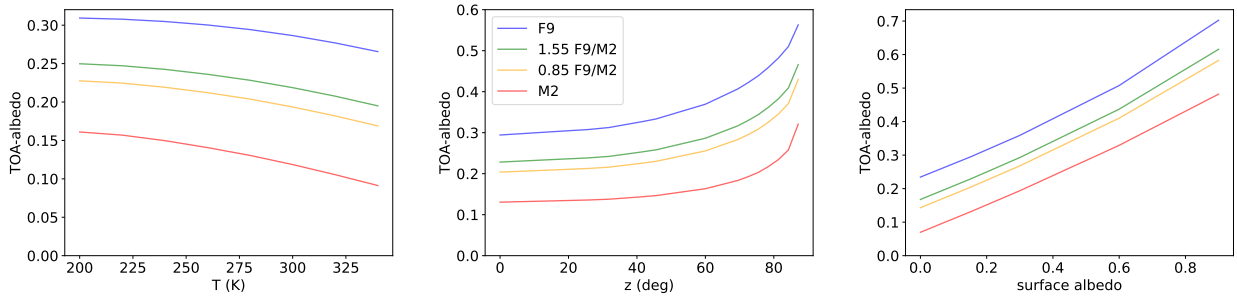

Figure 7.5: TOA albedo trends as a function of the three variables considered in EOS lookup tables. Left panel: TOA albedo as a function of the surface temperature, at $z = 0°$ and $\alpha_{\rm srf} = 0.15$. Central panel: TOA albedo as a function of the zenith angle, at $T_s = 280$ K and $\alpha_{\rm srf} = 0.15$. Right panel: TOA albedo as a function of the surface albedo, at $T_s = 280$ K and $z = 0°$. Colors codify the different blackbody SED chosen for the incoming light: F9 (blue), M2 (red) and combinations of the two weighted by flux (green: 1.55 F9/M2; orange: 0.85 F9/M2).

The TOA albedo

The adoption of different opacity prescriptions influences also the resultant TOA albedo $\alpha_{\rm TOA}$, albeit to a smaller degree. A smaller fraction of stellar light is absorbed, thus increasing the albedo. The TOA albedo as a function of surface temperature for a test planet illuminated by a G2-type star blackbody (at 5780 K) is reported in Fig. 7.4, right panel. The spread with respect to our fiducial model is in the order of ∼5 % and again the bias goes in the direction of making the planet colder.

A particular challenge of this work was the fact that the SED of the incoming radiation changes with time as a function of the relative distance between the planet and the primary star. While in *system 1* this effect is negligible (since the two stars have basically the same effective temperature), it cannot be ignored in *system 2*. A changing SED produces a changing TOA albedo, since the ratio between showrtwave and longwave photons varies, in turn varying the overall Rayleigh scattering efficiency of the atmosphere. Thus, for the *system 2* case, the TOA albedo lookup tables were calculated for four different SED: (i) a 6075 K blackbody representative of a F9-type star, (ii) a 3460 K blackbody representative of a M2-type star and two combined SEDs corresponding to a (iii) 1.55 F9/M2 mix and (iv) 0.85 F9/M2 mix. The two combined SEDs were obtained by flux-weighting the two blackbody curves and then scale them back to a specified integrated flux. These two extra SEDs are in fact intermediate cases between (i) and (ii) and correspond to the instellation at maximum and minimum, respectively (see the last paragraph in Section 7.1.1). For each point in which the surface temperature has been evaluated (Fig. 7.2), a linear interpolation on fluxes ratio has been performed to find the appropriate TOA albedo.

CO_2 clouds

From the change in the lapse rate of atmospheric profiles shown in the left panel of Fig. 7.3, it is evident that even at surface tempertures above 340 K CO_2 condensation happens somewhere in the upper troposphere. This implies the formation of a CO_2 cloud deck. A second, lower layer of water clouds is also espected to form at lower altitudes. While the latter is considered, albeit in a very simplistic form (see Section 2.1.2), the former is not. What does this model

Point #	3.5 Gyr			4.0 Gyr			4.5 Gyr		
	$\langle T \rangle$	$\langle A \rangle$	$\langle ice \rangle$	$\langle T \rangle$	$\langle A \rangle$	$\langle ice \rangle$	$\langle T \rangle$	$\langle A \rangle$	$\langle ice \rangle$
1	302.493	0.362054	0.00000	319.066	0.325814	0.00000	328.358	0.315701	0.00000
2	295.284	0.366539	0.0141265	309.968	0.335211	0.00000	319.409	0.325361	0.00000
3	287.410	0.373898	0.0644413	300.873	0.343992	0.00000	309.868	0.335182	0.00000
4	278.370	0.387718	0.0162886	291.991	0.352897	0.0200246	300.085	0.344649	0.00000
5	228.511	0.561361	0.985188	282.254	0.366938	0.100610	290.749	0.353676	0.0153391
6	224.906	0.562899	0.989817	229.181	0.553150	0.984616	280.161	0.369423	0.108862
7	221.611	0.563802	0.992773	225.079	0.557190	0.989931	227.918	0.554686	0.986940
8	218.291	0.564438	0.994884	220.928	0.560804	0.993447	223.446	0.558908	0.991752
9	215.163	0.564650	0.996297	217.183	0.563541	0.995553	219.277	0.562269	0.994630
10	217.905	0.564517	0.995087	220.495	0.561152	0.993736	223.001	0.559277	0.992124
11	220.829	0.564012	0.993341	224.004	0.558217	0.990993	226.966	0.555622	0.988161
12	223.834	0.563235	0.990895	227.889	0.554464	0.986543	231.220	0.551076	0.981675
13	226.965	0.562060	0.987391	231.885	0.550049	0.979668	236.247	0.544177	0.969235
14	230.069	0.560640	0.982591	236.843	0.542724	0.965942	243.383	0.530030	0.935548
15	233.878	0.557746	0.974091	244.317	0.526965	0.925585	303.385	0.341527	0.00000
16	238.232	0.552546	0.959043	303.170	0.341783	0.00000	312.257	0.332815	0.00000
17	245.332	0.538549	0.913219	311.312	0.333872	0.00000	321.021	0.323576	0.00000

Figure 7.6: Average global results of the ESTM simulations at the three epochs considered for *system 2*. Variables considered are the surface temperature, the albedo and the fractional ice coverage. Credit: Maria Di Paolo

miss by not including them? The answer to this question is related to the contribution of CO_2 clouds to the planet-contributed quantities in the energy balance equation: the OLR and the TOA albedo. CO_2 ice is mostly transparent to the IR radiation if compared to H_2O ice (see Kitzmann et al., 2013, and references therein). However, a cloud formed by typical CO_2 ice particles with diameters in the 10-100 μm range can scatter thermal infrared photons back to the planet and thus contributing to the atmospheric greenhouse effect. The same cloud would also scatter visible photons of the incoming stellar light, thus increasing the albedo. Forget & Pierrehumbert (1997) estimated that, for average particle radii larger than $\sim$6 μm, CO_2 clouds would have a net warming effect, at least when illuminated by a G2-type star. For a vast variety of cases, they predicted that these clouds would contribute potentially tens of K in the surface temperature. Later reanalysis of the topic by Kitzmann et al. (2013) and Kitzmann (2016) showed that the Forget & Pierrehumbert (1997) model overestimated this warming effect. A recalculation of the outer edge of the HZ for different stellar classes by Kitzmann (2017) showed that CO_2 clouds are nearly radiatively neutral for late-type stars, heating the surface only by 6 K at best. Thicker clouds would even have a net cooling effect. This means that for the case study under analysis here, clouds can probably be considered not relevant, at least in first approximation. The largest source of error remains the underestimated CO_2 gas opacity.

7.1.4 Results

The first step in running ESTM was to verify that the outcomes corresponding to the first sampled point (i.e. that of maximum possible instellation) did not depend on the surface

temperature set as the initial condition $T_{\rm start}$. This check must be made since, for a given instellation, multiple stable solutions exists (see the discussion in Section 2.4.2). In order to test this possibility, both test planets were initialized by varying $T_{\rm start}$ between 220 K and 280 K. All these tests yielded the same results, thus ruling out a Snowball-temperate bistability. A possible temperate-hot bistability such that discussed by Turbet et al. (2021) can still be present and will be checked in the future development of this work.

System 1

The test planet in *system 1* proved to be uninhabitable under the conditions set for this numerical experiment: the final global average temperature found by ESTM was equal to 193.5 K, with a fractional ice coverage of the surface equal to 1.0. Moreover, at that temperature, the vapor pressure of CO_2 is 0.93 bars, meaning that the 6-bar atmosphere set at the beginning would collapse as CO_2 snow on the surface, further reducing the greenhouse effect. The highly reflective frozen surface would instead prevent the planet of taking advantage of the simultaneous reduction of the Rayleigh scattering efficiency. Since these results refers to the orbital point in which the planet receives the maximum instellation, this Snowball condition is necessarily perpetual. Also, the two stars in this simulated system are late-type and thus do not significantly increase their luminosity in the first ∼10 Gyr.

As discussed in the previous Section, this result has been found by using a strongly underabsorbing atmosphere, so the habitability status reported here is debatable. In fact, by using the formulations presented in Section 6.2.4, the planet shoud be habitable. However, it is still possible that a combination of variable instellation and climate hysteresis might set the planet in an unrecoverable Snowball state that would lead to an atmospheric collapse even if CO_2 absorption is properly treated.

System 2

The test planet in *system 2* proved to be more interesting. In order to follow more closely the climate evolution, a finer grid of orbital points have been adopted for the first orbital period (the set of blue points in Fig. 7.2, panel b), between the first and the second maximum. The average planetary temperature and albedo and the ice fraction are reported in Fig. 7.6. As it is possible to see, in all cases there is a sharp transition between a nearly deglaciated and a nearly glaciated condition, largely due to the strong ice-albedo feedback. There are still variations of the average tempearture and albedo but are minor. The variations in the ice coverage are not realistic and caused by the fact that the relation between ice coverage and temperature (Eq. 2.12) tends asymptotically to 1.0. The transition to a Snowball state occurs at different points along the orbit: point 5 at 3.5 Gyr, point 6 at 4.0 Gyr and point 7 at 4.5 Gyr. In between the glaciated and the temperate state, a possible Slushball state can occur, in which a thin belt of water forms at the equator. Such a state occurs, for example, at point 17 (3.5 Gyr) and at point 15 (4.0 Gyr). The jointed temporal and latitudinal maps of the surface temperature and the ice distribution are shown in Fig. 7.7 and Fig. 7.9. We now discuss the climate evolution at different epochs.

In the first epoch (3.5 Gyr), the planet is unable to deglaciate even at the second maximum. This means that it will remain in a Snowball state until the next approach of the primary star to its periastron. At this epoch, the planet is thus able to host liquid water only for brief intervals of time between global glaciations. The temperate state last ∼30 days every orbit of the primary star (∼1400 days), equal to ∼2% of the time. The analysis of Slushball

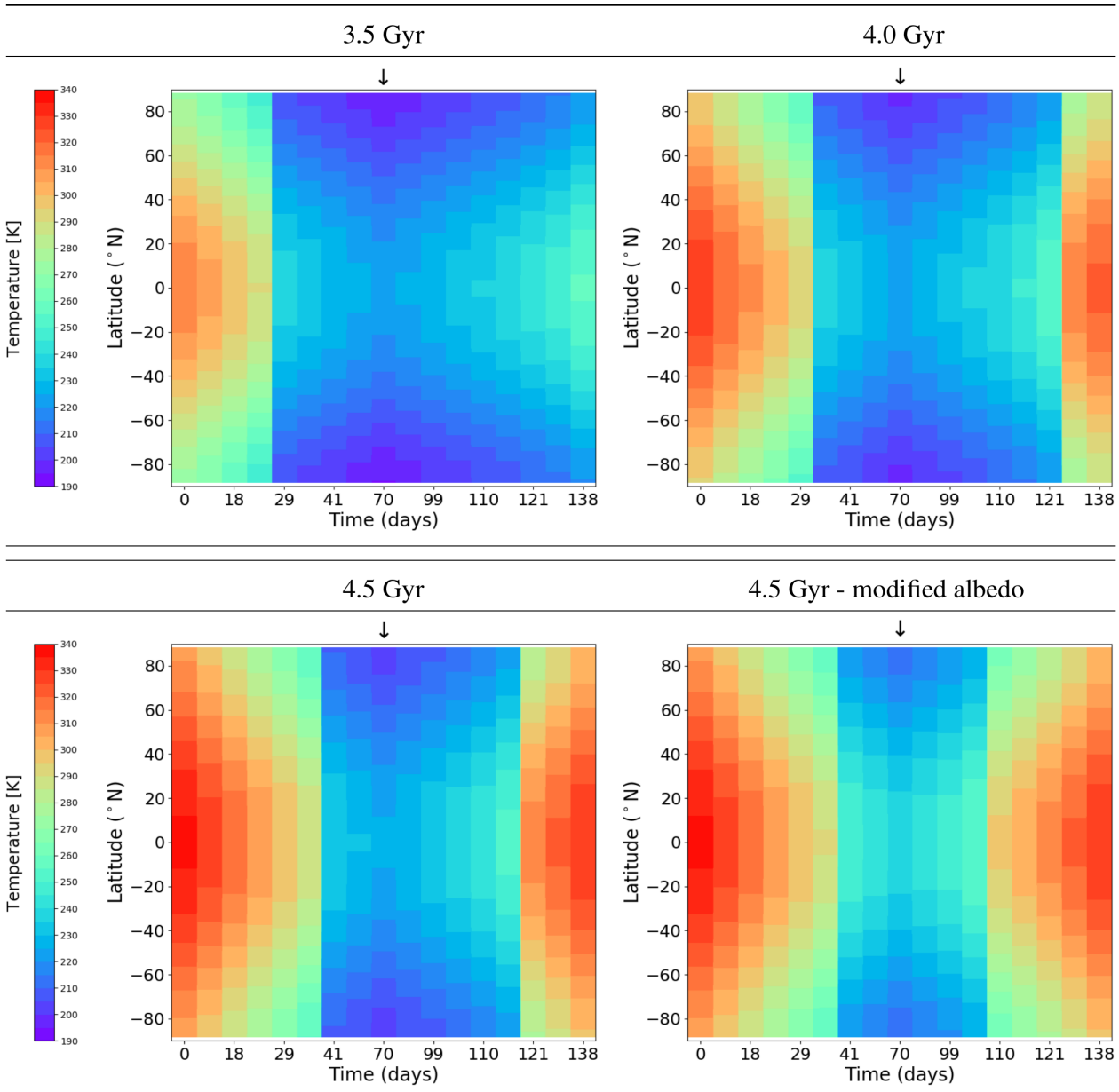

Figure 7.7: Temporal and latitudinal surface temperature maps of the *system 2* at the three considered epochs, and at the 4.5 Gyr case with the decreased ice albedo (to account for the different instellation SED). The arrows indicate the minimum instellation time. Credit: Maria Di Paolo.

states was not undertaken at that time, but it can be estimated, optimistically, to account for another ∼1% of the time.

In the second epoch (4.0 Gyr), the planet thaws before reaching the instellation level corresponding to the second maximum (point 16), thus producing a second, shorter temperate state along the orbit. The temperate period associated with the first maximum is also slightly longer (∼35 days). At the third maximum, instead, the planet remain largely glaciated. This does not surprise, since a rapid calculation shows that the instellation associated with the third maximum is lower than that at point 16. A new temperate state occurs instead at the last maximum before the primary star periastron. Fully habitable conditions are thus reached three times each binary star period. Two more maxima (the fourth and the second-to-last) are associated with possible Slushball states.

In the third epoch (4.5 Gyr) the planet thaws at point 15, which allows for a longer temperate period. The first maximum is, again, longer than in the previously analyzed epoch (∼40 days). At fourth temperate period can be found at the third maximum, while the instellation at the second-to-last remain too low. This brings the total amount of time passed in temperate state to ∼130 days, just short of 10% of the total time. Also this round of runs find that two maxima (the fifth and the second-to-last) are associated with Slushball states. Fig. 7.8 shows in more detail the state of the planet at the first maximum (left column), just before entering the first glaciation (central column) and in one of the points during the first glaciation (right column). For each instant, the latitudinal profiles for six quantities are depicted: the surface temeperature (first row), the TOA albedo and the ice fraction (second row), the OLR and the absorbed stellar radiation (i.e. $\mathcal{I} \times \alpha_{\rm TOA}$, third row) and the meridional energy flux due to dry and moist air (fourth row). The first and third rows of plots underline the heat redistribution efficiency of the test planet's CO_2 atmosphere with respect to that of Earth (see e.g. Fig. 5.3, upper and lower left panels). This is not unexpected: the meridional diffusion coefficient adopted depends on the surface pressure in the ESTM (Eq. 2.38), since thicker atmospheres have an easier time in leveling off temperature differences form regions with substantially different levels of instellation. The second row of plots show instead the relatively small impact of the TOA albedo due to ices, especially at high latitudes where the Rayleigh scattering from CO_2 produces very high $\alpha_{\rm TOA}$ values even in presence of a predominantly non reflective surface. The steep rise of the albedo in the $\gtrsim 87^\circ$ region (both North and South) is an artifact caused by the combined effect of imposing manually $\alpha_{\rm TOA} = 1$ at $z = 90^\circ$ and the fact that the last calculated $\alpha_{\rm TOA}$ value corresponds to $z = 87^\circ$. However, the limiting value corresponding to a total reflecion is never actually used in the code and the region interested by this anomalously high $\alpha_{\rm TOA}$ is too small to produce a significant change in the results. The fourth row of plots is interesting because they show the steep dependence of the moist latitudinal transport to the average surface temperature. Again, in the ESTM this effect is parameterized (and thus expected), but as argued in Section 2.3.1 this parameterization is grounded in solid numerical experiments performed with GCMs.

In the three cases discussed so far, an asymmetry can be noted between glaciation and deglaciation, with the second process requiring higher than expected instellations. The change in the ice fraction is also sharper, as can be noted in Fig. 7.9. This is a proof that climate hysteresis is working: the planet requires more energy to overcome the high albedo produced by the frozen surface. When this happens, though, the strong ice-albedo feedback provide for a rapid transition to an ice-free state.

Finally, as a fourth case, the 4.5 Gyr epoch planet has been probed again but this time adopting the modified ice albedo described at (iii) in Section 7.1.2. The obvious effect of

lowering the albedo of snow and ice is to heat up the planet. The temperature increase is zero during most of the temperate phase, since there is no ice present, while it amounts to ∼10 K during glaciations. Glaciations still occur and produces a climate transition, but are shorter. The less obvious effect is the increase in the symmetry between the freezing and thawing processes, both in the duration with respect to the time of minimum instellation and in the ice coverage of the outgoing/incoming temperate state. This signals a weaker ice-albedo feedback and caused by the fact that the formation of ice causes a smaller jump in the planetary albedo than before. A similar effect was also observed also by Shields et al. (2014) (see Fig. 2.8).

It can be expected that, with the continuous increase in instellation due to stellar evolution, the temperate phases would become even more prominent. However, a new problem that may arise is the possible transition to a Runaway State. At the first maximum in the 4.0 Gyr, it can be seen that the planet reaches equatorial temperatures around 340 K already (Fig. 7.7, upper right panel). The planet is still far away from the classical inner edge limit, but the dense CO_2-dominated atmosphere produces a stronger greenhouse effect than the 1-bar N_2-dominated one usually adopted for this last calculation. A possible mechanism to postpone this fate is a self-regulating change in the atmospheric composition: longer and hotter temperate periods could remove the excess CO_2 via carbonate-silicate weathering, reducing the CO_2 partial pressure over geological timescales. This, however, means that the temperate interglacial periods would remain short even at later evolutionary stages of the system. The large excursion in temperature and its implications for the habitability of the planet would have been present even if the CO_2 opacity were treated correctly. A more IR-opaque atmosphere would have produced longer temperate periods starting from an early epoch in the history of the system, but it would have also caused the equatorial temperatures to hit the 340 K mark earlier. The steeper slope of the red curve with respect to the blue one in the left panel of Fig. 7.4 can in theory mitigate the surface temperature variations by providing a stronger blackbody feedback (see Section 2.4), but the impact on the final climate state of the planet is difficult to evaluate a priori.

Also in this test case, the problem of the atmospheric collapse must be dealt with. In fact, during the glacial periods, an important fraction of the surface has a temperature lower than 220 K, which is the condensation temperature of CO_2 at 6 bars. While the planet will be heated up at the next instellation maximum, it is not clear if this would be sufficient to re-vaporize the CO_2 snow, especially under the thinner, less warming post-collapse atmosphere. For this type of analysis, it becomes important the timescale of this process, especially in relation to the (again, highly simplified) warming and cooling time of the planetary surface. This type of analysis would be paramount in the future re-evaluation of the topic.

7.2 Exploring the Archean Earth climate

Climate modeling is fundamental for studying the habitability not only of exoplanets, but also of Solar System planets in the distant past. Data derived from surviving geological records on Earth are fragmentary and require a unified frame to be interpreted. The same will be true when geological intestigations will be conducted on Mars and possibly Venus. As such, the paleoclimatology of Earth, Mars and Venus constitutes another natural field of application of the coupled EOS-ESTM procedure.

Particularly interesting from the point of view of astrobiology is the study of the Archean

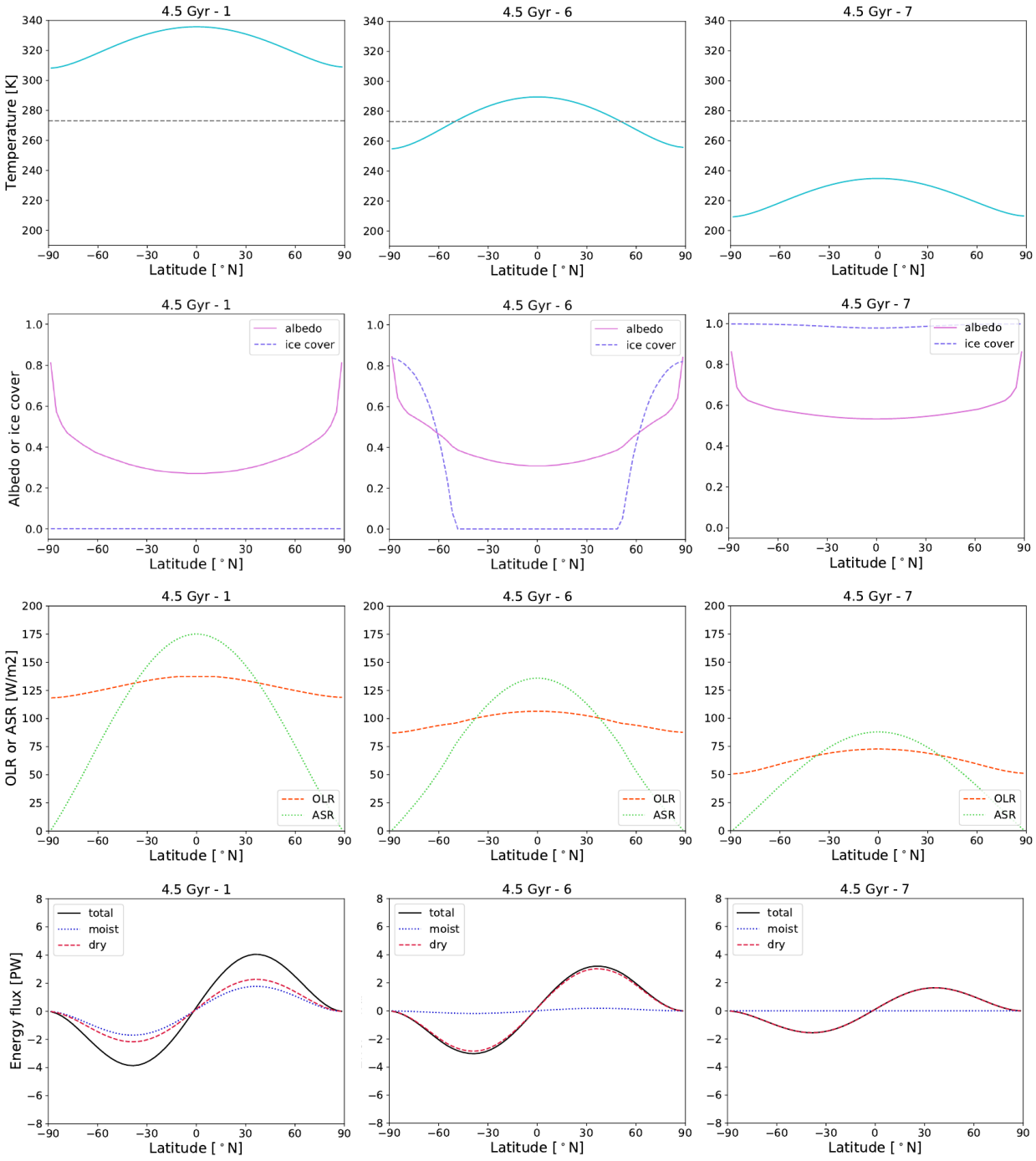

Figure 7.8: Latitudinal profiles for four climate quantities in the *system 2* case at the 4.5 Gyr epoch. Firt row: the temperature profile (cyan) with respect to the 273.15 K level (grey dashed). Second row: the ice fraction (blue dashed) and the TOA albedo (magenta). Third row: the OLR (dashed orange) and the asborbed stellar radiation (green dotted). Fourth row: the meridional moist (blue dotted), dry (red dashed) and total (black) heat fluxes. Columns refer to three different moments along the planetary orbit: the first maximum peak (left, point 1), the last partially deglaciated time (central, point 6) and the average conditions during the first glaciation (right, point 7). Credit: Maria Di Paolo.

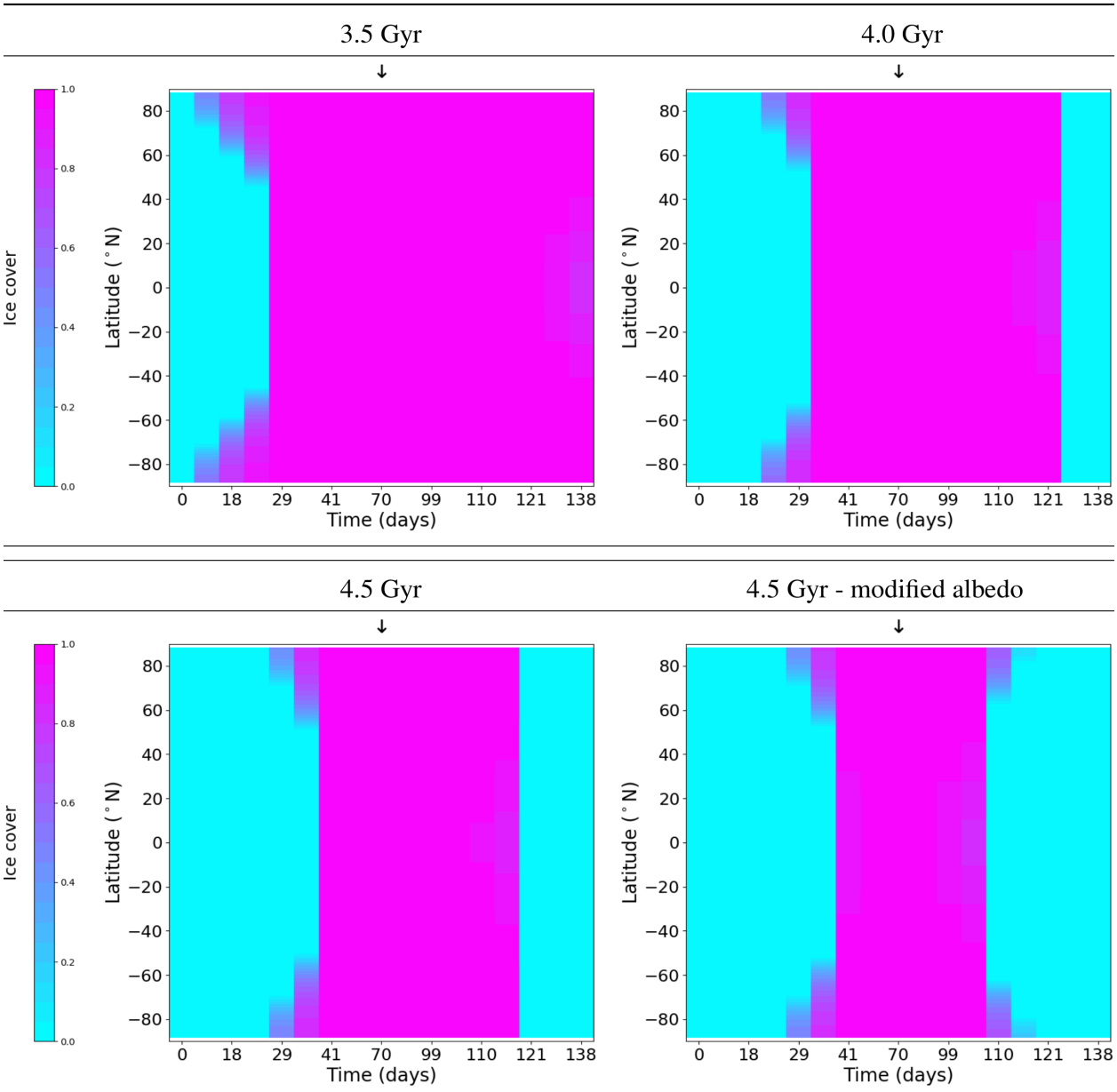

Figure 7.9: Temporal and latitudinal ice fraction maps of the *system 2* at the three considered epochs, and at the 4.5 Gyr case with the decreased ice albedo (to account for the different instellation SED). The arrows indicate the minimum instellation time. Credit: Maria Di Paolo.

Eon of Earth history, which spans the time from the end of the Hadean (informally set at 4.0 Gyr ago) to the beginning of Proterozoic (2.5 Gyr ago). It comprises a third of Earth total history and probably encompasses the emergence of life. Studying this Eon is fundamental in defining the concept of planetary habitability and relevant in the search for biosignatures, since we can expect that a significant fraction of the habitable exoplanets that may exist would resemble the Archean, rather than the Phanerozoic (or "modern"), Earth[4]. The study of mildy reducing N_2-CO_2 atmospheres like the one Earth had during the Archean (details in the next Section) is thus at least as important as the study of oxigenated, modern ones and chemical disequilibriums in absence of O_2 might be the first tentative biosignatures that will be detected (Thompson et al., 2022)

A well-known and discussed topic of paleoclimatology is the so-called *Faint Young Sun paradox* (see e.g. Feulner, 2012). As mentioned also in the previous Section, Sun-like stars increase their power output during time as an effect of the evolution of the stellar core, which implies that the Sun emitted ∼25-30% less flux at Earth's formation than now (Gough, 1981; Bahcall et al., 2001). This fact is difficult to reconcile with observational data indicating temperate conditions during most of the first few Gyr of our planet lifetime. Apart from the indirect evidence of the Earth habitability related to the birth and evolution of life (dating back to at least 3.5 Gyr ago[5]), several different proxies have confirmed the presence of temperate conditions on the surface of Earth nearly since its inception. Traces of the presence of liquid water has been found on 4.4 Gyr old zircons in Western Australia (Wilde et al., 2001). Robust estimates based on the formation conditions of, and the isotopic ratios in, gypsums (Walker, 1982), cherts (Hren et al., 2009) and phosphates (Blake et al., 2010) dated between 3.6 and 3.4 Gyr ago all point to warm climate conditions with temperatures well above freezing (20-40 °C) and possibly as high as 75 °C (Knauth & Lowe, 2003). While both the geothermal and the tidal heat fluxes were a factor of ∼3 higher than today (see respectively Taylor & McLennan, 2009; Feulner, 2012), they were still 3 and 4 orders of magnitude smaller than the Solar flux, thus completely unable to warm up the planet. This indicates that the solution to the Faint Young Sun paradox should be searched in the RT properties of the early Earth atmosphere.

Both of the planet-related terms in the energy balance equation have been investigated in this sense. Concerning the TOA albedo, Rosing et al. (2010) hypothesized that a combination of a smaller land-to-ocean surface ratio and a reduced cloud coverage due to the absence of biogenic cloud condensation nuclei would have decreased the planetary albedo enough to keep Earth unfrozen. Their results have been criticized by Goldblatt & Zahnle (2011).

The most straightforward solution to the Faint Young Sun paradox, however, is a stronger greenhouse effect. Many GHGs, once in a sufficiently higher concentration, can do the trick. Examples of proposed solutions include NH_3 (Sagan & Mullen, 1972), CH_4 (Hart, 1978) and/or higher concentrations of CO_2 (Owen et al., 1979). A considerably higher N_2 partial pressure enhancing CO_2 absorption via foreign broadening (Goldblatt et al., 2009) and the role the OLR cloud forcing (Rondanelli & Lindzen, 2010) have also been explored. All the explanations must, however, take into consideration known estimations on the chemical makeup

[4]At least under the hypothesis that habitable planets would evolve similarly to Earth. The Phanerozoic Eon begun 539 Myr ago and continues today.

[5]This value refer to the oldest direct evidence of life in the form of microfossils (Schopf, 1993). Indirect and less robust evidences in the form of biogenic disproportionation of carbon isotopes have been found in 3.8 (Rosing, 1999; Ohtomo et al., 2014) and possibly 4.3 Gyr old hydrothermal precipitates (Dodd et al., 2017). Molecular clock models date the Last Universal Common Ancestor to >3.9 Gyr (Betts et al., 2018).

Name	Short description	CO_2:N_2 ratio	p_s [bar]	N_2 [bar]	CO_2 [bar]	CH_4 [ppmv]
P100L0	low CO_2, no CH_4	1:99	1.0	0.99	0.01	0
P100LM	low CO_2, med CH_4	1:99	1.0	0.99	0.01	100
P100LH	low CO_2, high CH_4	1:99	1.0	0.99	0.01	1000
P100M0	med CO_2, no CH_4	1:24	1.0	0.96	0.04	0
P100MM	med CO_2, med CH_4	1:24	1.0	0.96	0.04	100
P100MH	med CO_2, high CH_4	1:24	1.0	0.96	0.04	1000
P100H0	high CO_2, no CH_4	1:9	1.0	0.90	0.10	0
P100HM	high CO_2, med CH_4	1:9	1.0	0.90	0.10	100
P100HH	high CO_2, high CH_4	1:9	1.0	0.90	0.10	1000
P40H0	low p_s, high CO_2	1:3	0.4	0.30	0.10	0
P40V0	low p_s, very high CO_2	1:1	0.4	0.20	0.20	0

Table 7.2: Summary of the atmospheric models tested here.

of the ancient Earth atmosphere and the modeled sources and sinks. For instance, NH_3 is not considered a good GHG candidate because it is easily photolyzed by UV radiation, easily dissolved in water oceans and there are not large enough plausible sources (Kasting, 1982) to sustain its concentration to non-negligible levels.

A thorough study of Archean Earth habitability is another perfect topic for the coupled EOS-ESTM model. In this case, the ability to conduct a rapid exploration of the vast parameter space is paramount. As said, the Archean Eon spans 1.5 Gyr during which several features of Earth changed, such as the rotation rate and the fraction of landmass. On the other hand, the insolation increased by ∼10%, from 0.74 to 0.82 $S_\odot$. As such, in order to draw a general picture of the Archean Earth, more than one epoch in that Eon must be probed, and for each epoch several different atmospheric compositions must be considered. This type of multiparametric investigation constituted the core of the Riccardo Bevilacqua's Master Degree Thesis, in which I have been involved both in the identification of a suitable set of test cases and by performing the RT calculations with EOS. Below I provide a brief description of this work.

7.2.1 The Archean Earth atmosphere composition

The first step in the Bevilacqua's study of Archean Earth was to select an appropriate set of atmospheric chemical compositions for producing the RT lookup tables. Geological records allowed us to derive several independent upper limits and estimations for both the total pressure and the concentrations of N_2, CO_2 and CH_4, establishing that:

(i) The total surface pressure at 2.7 Gyr from present was not significantly higher than now, and possibly lower than a quarter of bar. Som et al. (2012) investigated the raindrop imprints prserved in tuffs deriving an upper pressure limit of 2.1 bar in the case of a 70%-30% N_2-CO_2 dry atmosphere, and a fiducial [0.51; 1.1] bar range in the case of a pure N_2 atmosphere. Using the size distribution of preserved gas bubbles in lava flows from the same period, Som et al. (2016) calculated a pressure of 0.26 ± 0.26 bar.

(ii) The N_2 partial pressure p_{N2} was lower than 1.1 bar and possibly ∼0.5 bar (Marty et al., 2013). This value has been derived by isotopic analysis of N and Ar trapped in several

hydrothermal quartz inclusions formed between 3.5 and 3.0 Gyr ago.

(iii) The CO_2 partial pressure p_{CO2} was surely higher than today but uncertain. By studying the effects of CO_2 on the siderite-greenalite[6] chemical equilibrium in 2.8 Gyr old paleosols, Rye et al. (1995) derived an upper limit for p_{CO2} of 0.03 bars. Sheldon (2006) obtained a smaller value (0.003-0.02 bar) via mass balance relations in slightly more recent (2.2 Gyr old) paleosols, and Driese et al. (2011) confirmed this value on 2.7 Gyr old paleosols. Kanzaki & Murakami (2015) analyzed water inclusions in paleosols instead, calculating an upper limit of 0.2 bar at 2.8 and 2.5 Gyr. An even higher upper limit of 0.9 bar has been found in a 2.75 Gyr sample. Finally, Lehmer et al. (2020) obtained an estimate of the CO_2 volume concentration by applying an oxidative model to micrometeorites dated to 2.7 Gyr ago, finding that an atmosphere composed by at least 70% of CO_2 is required to explain observations. Their method, however, does not constrain p_{CO2}.

(iv) The CH_4 partial pressure p_{CH4} was almost surely higher than today due to the lack of molecular oxygen, making this gas the preferred choice for solving the Faint Young Sun paradox. By extrapolating its activity back in time, volcanism has been deemed able to support $\sim$3 ppmv (or μbar) of CH_4 (Tian et al., 2011). Estimations based on ecosystem models of ancient methanogens point to higher concentrations, up to 0.03 bar (or 30000 ppmv, Kharecha et al., 2005). A more direct estimate based on the modeling of hydrogen escape and its impact on Xe isotopic fractionation found a lower limit of 0.005 (5000 ppmv) bars at 3.5 Gyr in the past (Zahnle et al., 2019). Another directly derived lower limit, based on the ability to form atmospheric sulfur particulates observed as inclusions in Archean rocks is 20 ppmv (Zahnle et al., 2006). A last, less robust constraint is related to the formation of organic hazes in the upper atmosphere when in presence of high ($\gtrsim$0.1) CH_4/CO_2 ratios (Trainer et al., 2006). These hazes would have a net cooling effect, thus negating the advantge of high p_{CH4}. This would limit the p_{CH4} to $\lesssim$0.1 bars in the highest p_{CO2} scenario presented at (iii). However, a recent study on the topic (Arney et al., 2017) showed that a somewhat hazy atmosphere would have not prevented habitability.

Based on these considerations, it was decided to investigate 11 different atmospheric compositions, reported in Table 7.2. Nine of these cases are produced by the combination of three CO_2-to-N_2 ratios (1:9, 1:24 and 1:99) and three possible CH_4 concentrations (0, 100 and 1000 ppmv) for a total dry surface pressure of 1 bar. The other two cases consider a lower total pressure (0.4 bar) and higher CO_2-to-N_2 ratios (1:3 and 1:1) to compensate for the loss of pressure-induced opacity but do not include CH_4.

Compared with the values decribed above, it is clear that this work explored mainly the lower limit in GHGs concentrations, especially for CH_4. This choice was made for three reasons. First, it is at low concentrations that habitability problems for the Archean Earth may arise, making this end of the compositional interval more interesting to consider. Second, we decided to value more the estimations derived by paleosols, which are also largely concordant with each other. Finally, we wanted to avoid scenarios with high CH_4 concentrations that cause the formation of hazes, since at this point we are unable to treat them in the EOS-ESTM. Concerning N_2, we tested two possibilities. For the first nine models we chose

[6]Siderite and greenalite are, respectively, an iron carbonate and an iron silicate. Their equilibrium concentrations can be associated to atmospheric CO_2 concentrations.

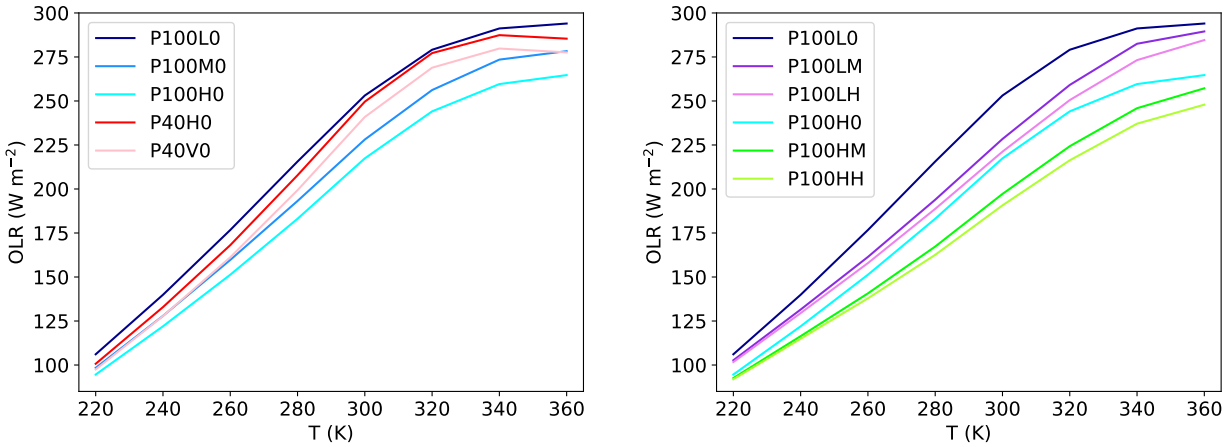

Figure 7.10: The dependence of OLR on surface temperature. Right panel shows the effect of changing the CO_2-to-N_2 ratio and the total dry surface pressure p_s. Dark, medium and light blue lines refer respectively to models with low, medium and high CO_2 , no CH_4 and with $p_s = 1.0$ bar. Red and pink lines refer to models with high and very high CO_2, no methane and with $p_s = 0.4$ bar. Left panel shows the effect of increasing the CH_4 concentrations (no, medium and high) in the low (dark blue, violet and purple) and high (light blue, light green and yellow-green) CO_2 cases.

a $p_{N2} \in [0.9; 0.99]$ bar, which is in the upper limit region of estimates. This choice brings the total dry surface pressure to 1.0 bar, as it is usually adopted in most of other studies in the field of Archean climate modeling. For the last two models p_{N2} was set to 0.3 and 0.2 bar to explore the Som et al. (2016) findings of a possible low-pressure Archean Earth. For convenience, throughout the rest of this Section we will sometimes refer to the CO_2 and CH_4 concentrations by using "low", "medium" and "high" adjectives. Please refer to the 2^{nd} column of Table 7.2 for their meaning in this context.

7.2.2 The RT model

As mentioned above, the model atmospheres have a surface total dry pressure of either 1 bar or 0.4 and are composed by variable amounts of N_2, CO_2, CH_4 and H_2O with a fixed relative humidity of 60%. The tropospheric pressure-temperture profile have been calculated following the method delineated in Section 2.2.6. The tropopause was fixed at 160 K and was overlain by an isothermal stratosphere. This tropopause temperature is lower than the current Earth one and it is justified by the absence of stratospheric O_3 that, by absorbing the UV radiation, heats up the stratosphere. The pressure grid adopted for RT calculations consisted in 60 layers (∼10 per order of magnitude) from the surface to the uppermost layer at 1μbar.

The absorption lines of N_2, CH_4 and H_2O were calculated using a Voigt profile truncated at 25 cm^{-1}. CO_2 lines are again calculated using a Voigt profile but truncated at 500 cm^{-1} and with sub-Lorentzian far wings in accordance with the Perrin & Hartmann (1989) model. H_2O continuum has been included via the MT_CKD 3.4 model and the CO_2 CIA are those described in Section 3.6.1 and labeled as "GBB". The TOA albedo has been calculated illuminating the atmosphere with a 5780 K blackbody consistent with the Sun SED at present time.

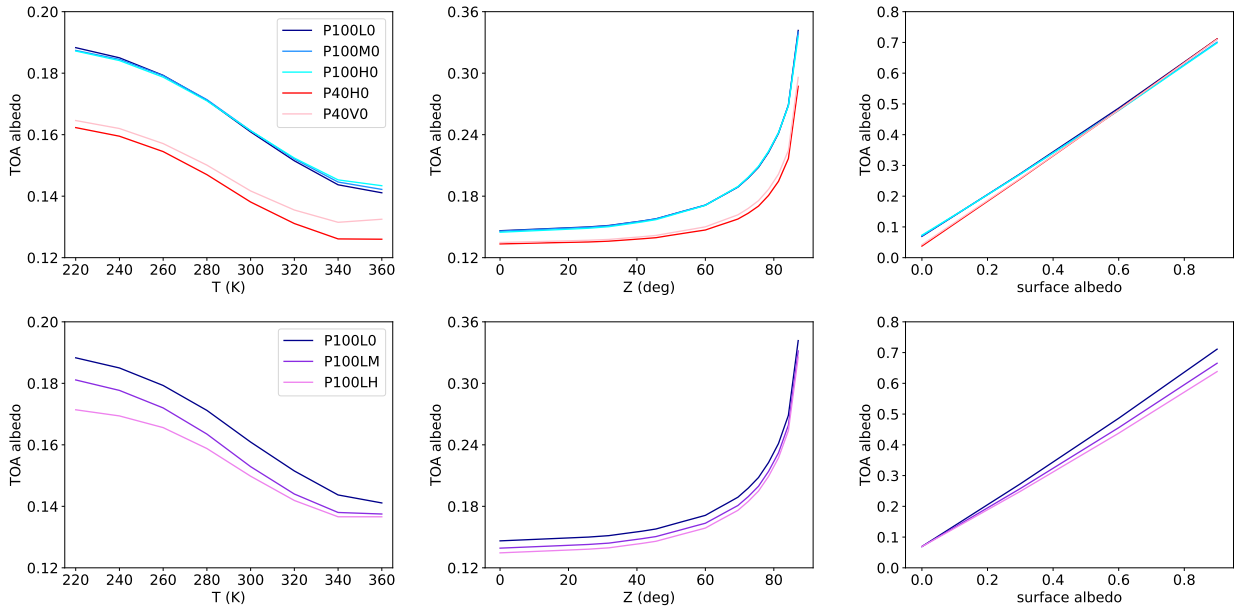

Figure 7.11: The dependence of TOA albedo on the surface temperature (left), the solar zenith angle (center) and the surface albedo (right). In the left panels $z = 60°$ and $a_{\rm srf} = 0.15$. In the central panels $T_s = 280$ K and $a_{\rm srf} = 0.15$. In the right panels $T_s = 280$ K and $z = 60°$. The first row show the effect of changing the CO_2-to-N_2 ratio (dark, medium and light blue respectively for low, medium and high values) and the total dry surface pressure p_s (blue and red shades respectively for 1.0 and 0.4 bar). The second row show the effect of changing the CH_4 concentration (dark blue, violet and purple respectively for no, medium and high values) in the low CO_2 case.

The OLR

Concerning the OLR, its dependence on T_s is presented for most of our 11 models in Fig. 7.10. Two things can be noted here. First, as it is possible to see in the left panel, the adoption of higher CO_2-to-N_2 ratios in the low pressure cases (P40H0 and P40V0) are just enough to lower the OLR below the levels of the low CO_2case (P100L0). In particular, the relative OLR difference between the P100L0 case and the P40H0 case is $\lesssim$9%, despite the fact that there is one order of magnitude of difference in the CO_2 concentration. This showcases again both the well-known non-linear relation between GHGs concentrations and forcing and the role of the vertical thermal structure of hte atmosphere in the final OLR. The latter concept is particularly evident observing the behaviour of the P40H0 and the P40V0 models at 360 K: the OLR derivative over T_s becomes negative: at that temperature the water vapor pressure at 60% RH is $\sim$0.37 bar, which means that the total (dry+vapor) surface pressure is nearly doubled with respect to that found e.g. at 280 K. The second thing that can be noted observing the right panel of Fig. 7.10 is that adding 100 ppm (0.1 mbar) of CH_4 has nearly the same effect of quadrupling the CO_2 concentration, from 0.01 to 0.04 bar (corresponding to 10000 and 40000 ppmv, respectively). Again, this is not new and it is related to the strongly sub-linear dependence between forcing and concentrations. However, this fact is relevant here because demonstrates that there is a certain degree of degeneracy between the resultant OLR calculated using substantially different CO_2 and CH_4 concentrations (see e.g. cases P100LH and P100H0).

The TOA albedo

Concerning the TOA albedo, its dependence on T_s, z and α_{srf} is show in Fig. 7.11 for 7 of the 11 tested models. Two more things can be noted here. The first one is the fact that changing the CO_2-to-N_2 ratios while keeping the dry p_s constant have only marginal effect on the TOA albedo, especially when compared to the far stronger effect on the OLR (first row of plots). In fact, the TOA albedo difference between the P100L0 and the P100H0 is at most 1.6% (at $\gtrsim$340 K). At lower temperatures, the model with the most CO_2 (P100H0) has slightly more TOA albedo than that with the least CO_2 (P100L0), while the opposite is true at higher temperatures. This is driven by the interplay between the Rayleigh scattering efficiency of CO_2, which is higher than that of N_2 (see Section 3.4) and the absorption in the near IR, where some of the incoming solar photons are still scattered. For higher CO_2 concentrations in lower overall pressures (P40H0 and P40V0 cases) increasing the CO_2 concentration further leads to a larger scattering increase with respect to the opacity increase, leading to an higher TOA albedo (red and pink lines in the upper left panel). The second thing is the fact that increased CH_4 concentrations markedly reduce the TOA albedo (second row of plots in Fig. 7.11. The relative difference between the P100L0 and the P100LH cases is as high as $\sim$10% at 220 K. This is due to the fact that methane have considerable absorption in the 1.66, the 3.3 and the 7.7 μm regions, and subtracts a non-negligible fraction of solar photons to the scattering, especially in the first two regions.

7.2.3 Planetary parameters adopted

The work presented here has been done by using ESTM2 (see Section 5.1). However, since the calibration process of the climate model was still underway, some minor differences in the parameters used are present. Moreover, simulating the Archean Earth required the adoption of an alternative set of inputs for some of the quantities (fraction of lands, the rotation rate and insolation).

Differences in ESTM parameterizations

The differences in the climate model general parameterizations are listed below.

- Concerning the parameterized dependence of the ice fraction coverage over lands on the annual temperature, the model employed for the study of the Archean Earth adopts a slightly different set of values fo the growth rate and the shape parameter of the logistic curve (see Eq. 5.2), in particular: $\theta_{lnd} = 0.7$ and $\xi_{lnd} = 6.0$. For comparison, the final version of ESTM2 adopts $\theta_{lnd} = 1.2$ and $\xi_{lnd} = 8.0$. This difference produces a slightly higher mean annual zonal ice coverage over lands for mean annual temperatures above 0°C, since the curve is less steep in that region. As a consequence, ice caps would grow slightly more.

- Concerning the parameterized dependence of the cloud OLR forcing on the instantaneous temperature, the coefficients in Eq. 5.11 are again slightly different. In ESTM2 the minimum forcing at very low temperatures is 20%, instead of 10%, of $CRE_\circ$. The midpoint temperature in the hyperbolic tangent is 258.15 K instead of 263.15 K. This means that the positive feedback between the cloud forcing and the temperature is somewhat stronger but happens at lower temperatures, making it slightly harder for the planet both to fall in a Snowball state and to exit said state once achieved.

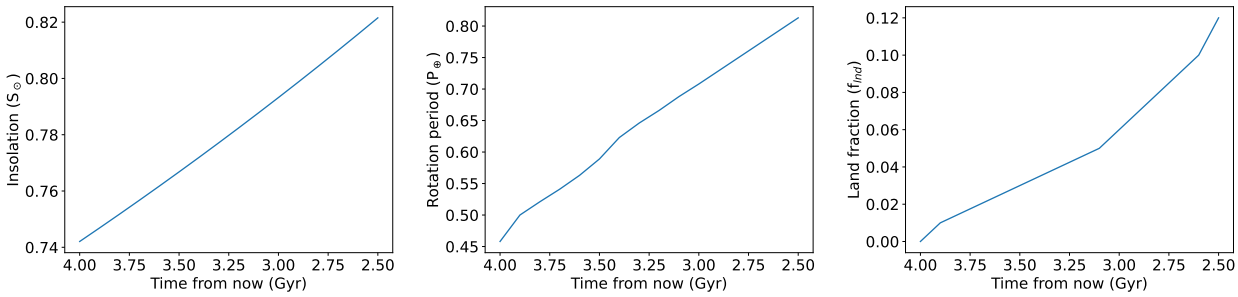

Figure 7.12: The temporal evolution of three climate model inputs during the Archean Eon as considered in this study. Left panel: the insolation. Central panel: the rotation period. Right panel: the land fraction. Credit: Riccardo Bevilaqua.

- The land α_{lnd} and land ice $\alpha_{\mathrm{i,lnd}}$ albedos are slightly different. In particular $\alpha_{\mathrm{lnd}} = 0.18$ (instead of 0.20) and $\alpha_{\mathrm{i,lnd}} = 0.75$ (instead of 0.70). As for the previous point, also these changes should make a bit harder for the planet to both enter and exit the Snowball state.

- The fractions of clouds over oceans ($f_{\mathrm{c,ocn}}$) and lands ($f_{\mathrm{c,lnd}}$) are equal, respectively, to 0.74 and 0.56. In the final version of ESTM2 these values are equal to 0.72 and 0.55, as per King et al. (2013).

Archean Earth modeling

The specific set of inputs adopted to simulate the Archean Earth concern instead:

- the insolation;

- the rotation period;

- the land fraction.

Concerning the insolation, we adopted the approximate formulation of Gough (1981) in order to follow its changes thorughout the Eon:

$$S(t) = \left(1 + \frac{2}{5}\left(1 - \frac{t}{t_\circ}\right)\right)^{-1} \tag{7.1}$$

where $t_\circ$ is equal to the Sun age at present time (4.603 Gyr) and t is the timme elapsed from the Sun's birth. Insolation evolution is shown in Fig. 7.12, left panel.

The rotation period of Earth has changed considerably during its history due to the tidal braking of the Moon. Direct geological evidences exist, although the most robust ones are limited to the Neoproterozioic age (∼670 Myr, Williams, 2000). In order to reconstruct the rotation period during the Archean Eon, tidal dissipation models are necessary. As briefly mentioned at the beginning of Section 7.1 though, these models are burdened by strong uncertainties. For example, by adopting the modern tidal dissipation rate and projecting the day length into the past it is not even possible to reconnect with Neoproterozoic data. Purely dissipative models tend to predict very short day lengths during the Archean ($\lesssim$6 h), that should have been accompained by tides so strong to leave traces in rocks (Spalding

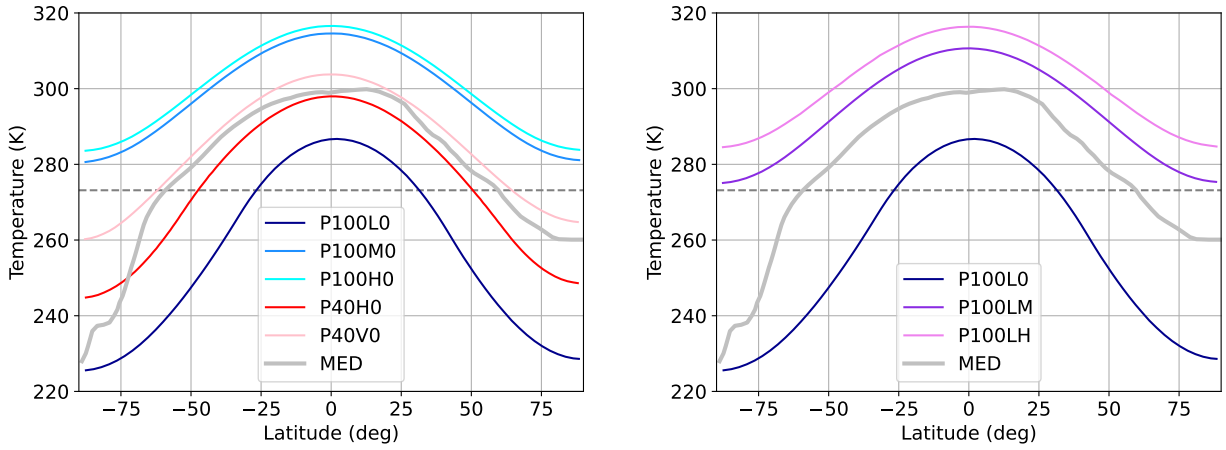

Figure 7.13: The mean annual latitudial profiles of Archean Earth at the 3.0 Gyr epoch, with respect to modern Earth data (MED, gray solid line) and the freezing temperature of water (gray dashed line). Left panel: profiles for different values of the CO_2-to-N_2 ratio at a surface pressure of 1 bar (blue shades) and 0.4 bar (red and pink lines). Right panel: profiles for different values of the CH_4 concentration. Model labels are reported in the legend. Credit: Riccardo Bevilaqua.

& Fischer, 2019)[7]. A solution of this dilemma is the so-called *21-h resonance model*. This model, proposed by Zahnle & Walker (1987), states that for a ∼1.3 Gyr period during the Proterozoic Eon the length of day on Earth remained constant at 21 h due to the resonance with the strong thermally driven semi-diurnal atmospheric tide. This long hiatus in the Earth despinning process allows for longer day lengths during the Archean and a better agreement with observations. In this work, we adopted the results from this model as calculated by Bartlett & Stevenson (2016) for their lowest *base torque* value. Rotatinal period evolution is shown in Fig. 7.12, central panel.

Finally, we also considered the evolution over time of the land fraction $t_{\rm lnd}$. The continuous formation of continental crust is a well-known feature of geology. Thus, the continents were less extended in the past with respect to the present. While there is only indirect observational evidence for it, modeling of the mantle-crust interaction predicts that the Earth became a waterworld when the magma ocean solidified and the atmospheric water vapor condensed (see e.g. Rollinson, 2007). The land fraction then began to rise either shortly afterwards, during the Hadean (Dhuime et al., 2012) or at the beginning of the Archean (Collerson & Kamber, 1999; Condie, 2000). We chose to follow the results of Collerson & Kamber (1999), starting at the beginning of the Archean with a $f_{\rm lnd} = 0.0$ and evolving it up to $f_{\rm lnd} = 0.12$ at the end of the Eon. The curve representing this model is shown in Fig. 7.12, right panel. As a final remark, several distributions of the landmasses were tested, but here I show the results only for the case in which $f_{\rm lnd}$ is constant in all the latitudinal bands.

7.2.4 Results

As previously stated, the Archean Eon encompasses a significant fraction of the Earth history, during which several changes occured. In order to conduct a thorough investigation of the

[7]The semi-major axis of the Moon can be linked to the Earth rotation period (see e.g. Bills & Ray, 1999). Shorter day lengths means lower lunar semi-major axis values, that in turn means stronger tides.

period a few epochs were sampled, making use of the evolutionary models shown in Fig. 7.12. this allowed us to follow the evolution of the planet under our hypotheses.

Since we tested several different atmospheric models (see Table 7.2), we needed first to disentagle the effects of atmospheric chemical composition changes from those caused by planetary parameter changes. As such, we conducted three set of tests. In the first one, we kept planetary parameters constant and changed the chemical makeup of the atmosphere. In the second, we changed one by one the planetary parameters by leaving the atmomspheric composition constant. Finally, in the third set of tests, we combined the previous two to follow the evolution of Earth through the Eon. The results are presented below.

Influence of chemical composition changes

First of all, we studied the effect on the Archean Earth climate of different CO_2-to-N_2ratios and in absence of CH_4. We initialized the ESTM2 with an insolation of 0.793 S_Sun, a rotation period of 17 h and a land fraction of 0.06. These values describe the possible state of our planet 3.0 Gyr ago. We then tested three model atmospheres, labeled as P100L0, P100M0 and P100H0. The average latitudinal profiles are shown in Fig. 7.13, left panel (blue shades), while the seasonal-latitudinal temperature maps for the two extreme cases (P100L0 and P100H0) are shown in Fig. 7.14, upper panels. As it is possible to see, for all the models we obtain a planet that is at least partially deglaciated. In the low CO_2 case (P100L0), the average global temperature is 266.5 K and just below 50% of the surface is free of ice. In the other two cases the CO_2 concentration is sufficiently high to thaw completely the ice caps. In the high CO_2 case in particular, the polar waters are ice-free year-round. The average global temperatures in the P100M0 and the P100H0 cases are 304.0 and 306.3 K respectively, in part thanks to the positive ice-albedo feedback (see Section 2.4.2). The difference between the medium and high CO_2 scenarios is small, and this is due to the previously discussed saturation effect on the CO_2 lines on on hand, and the absence of strong feedbacks at that temperature on the other.

Then we tested the effect of adopting different concentration levels of CH_4 while keeping constant the CO_2. We chose again the parameters describing the Earth 3.0 Gyr ago and considered the models labeled as P100L0, P100LM and P100LH. The latitudinal profile is shown in Fig. 7.13, right panel, while the seasonal-latitudinal map for the P100LH cases is shown in Fig. 7.14, lower left panel. As it possible to see, 100 ppm of CH_4 (P100LM) are already sufficient to deglaciate the poles. Some transient ice forms during polar winters in this scenario, but their fractional extent amount to few % points of the surface at worst. The average global temperature is 299.5 K. Under the high CH_4 scenario (P100LH), the average temperature is instead equal to 306.4 K and the temperature map is indistingushable to that obtained in the high CO_2, no CH_4 case (P100H0). This underlines again the degeneracy between different chemical compositions.

Finally we studied the low surface pressure (P40H0 and P40V0) scenarios applied to the 3.0 Gyr-old Earth case. The results are shown in Fig. 7.13, left panel as a red (P40H0) and pink (P40V0) curves. The seasonal-latitudinal map for the P40H0 case is shown in Fig. 7.14, lower right panel. As expected, despite having the same CO_2 partial pressure (and nearly the same CO_2 columnar mass) of the P100H0 case, the P40H0 model is considerably colder, with a average global temperature of 282.7 K. The P40V0 case is warmer and reaches 291.0 K. Despite having less than half of the atmospheric pressure than the P100L0 case, both the P40H0 an the P40V0 have a lower pole-equator temperature gradient (respectively 41.1

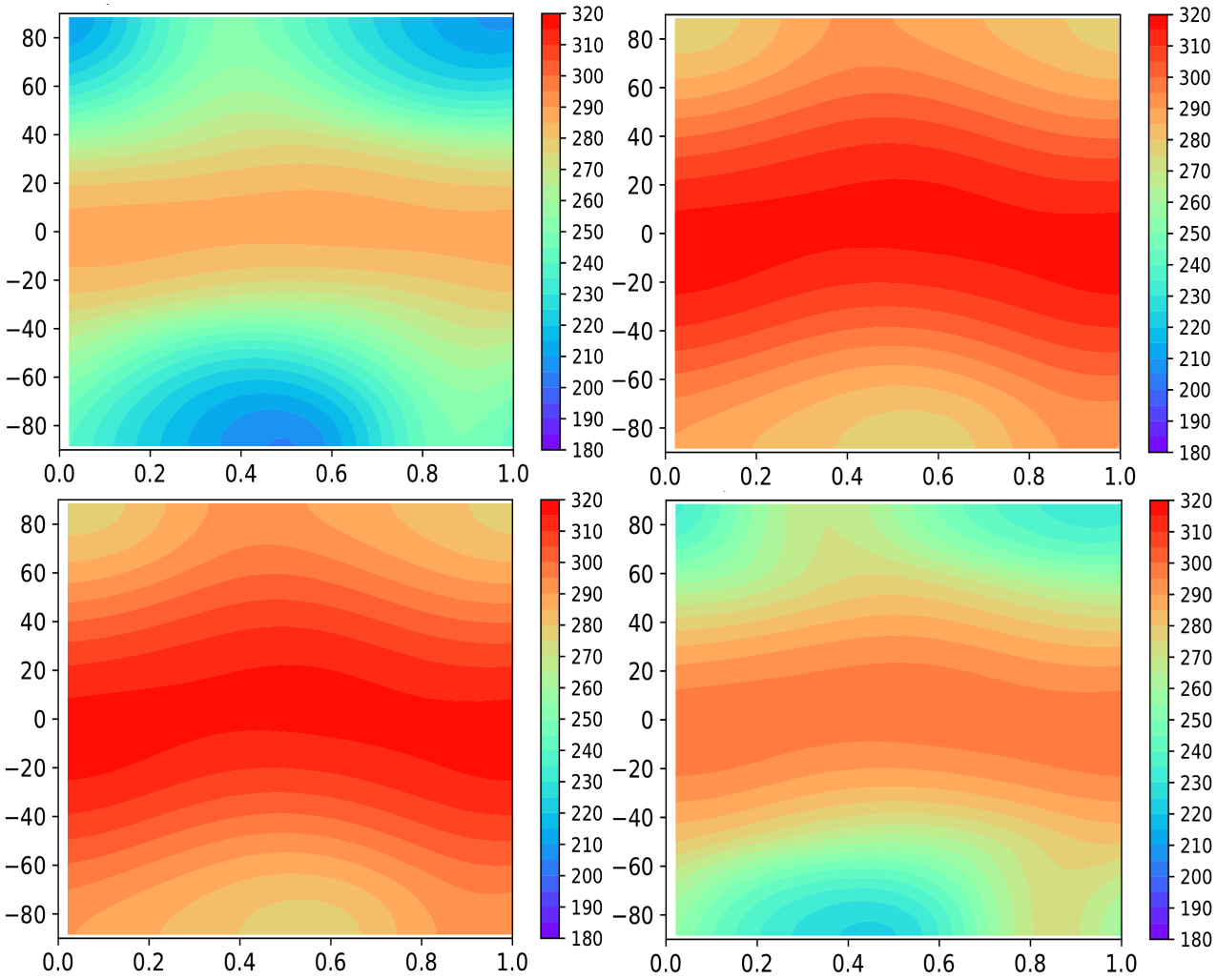

Figure 7.14: The seasonal-latitudinal temperature maps fof the Archean Earth at the 3.0 Gyr epoch for four different atmospheric models. Upper left: P100L0, Upper right: P100H0. Lower left: P100LH. Lower right: P40H0. Credit: Riccardo Bevilaqua.

and 50.8 K vs 58 K). This underlines the importance of factors like the presence of ice caps over the pressure-dependent meridional diffusion coefficient in determining the final planetary temperature gradient value. In both cases, permanent ices cover a small but non-negligible fraction of the globe (24% in the P40H0 case and 10% in the P40V0 case).

Influence of rotation rate and continental fraction

The first planetary parameter that we tested separately is the rotation rate. For this test, we set the insolation to 0.756 $S_{\odot}$ and the landmass fration to 0.98. These choices represent the state of Earth at 3.7 Gyr in the past. Concerning the atmosphere, we adopted the P100LM case. Three different rotation periods (11, 15 and 19 h) have been tested while keeping constant the other parameters. The two extreme cases represent the hypothetical rotation rate at the beginning (4.0 Gyr) and near the end (2.6 Gyr) of the Archean, just before entering the 21 h resonance described in the previous Section. The seasonal-latitudinal maps for them are shown in Fig. 7.15. As expected, the rotation rate have a substantial influence on the meridional diffusion coefficient. The pole-equator thermal gradient is equal to 53.9, 43.1 and

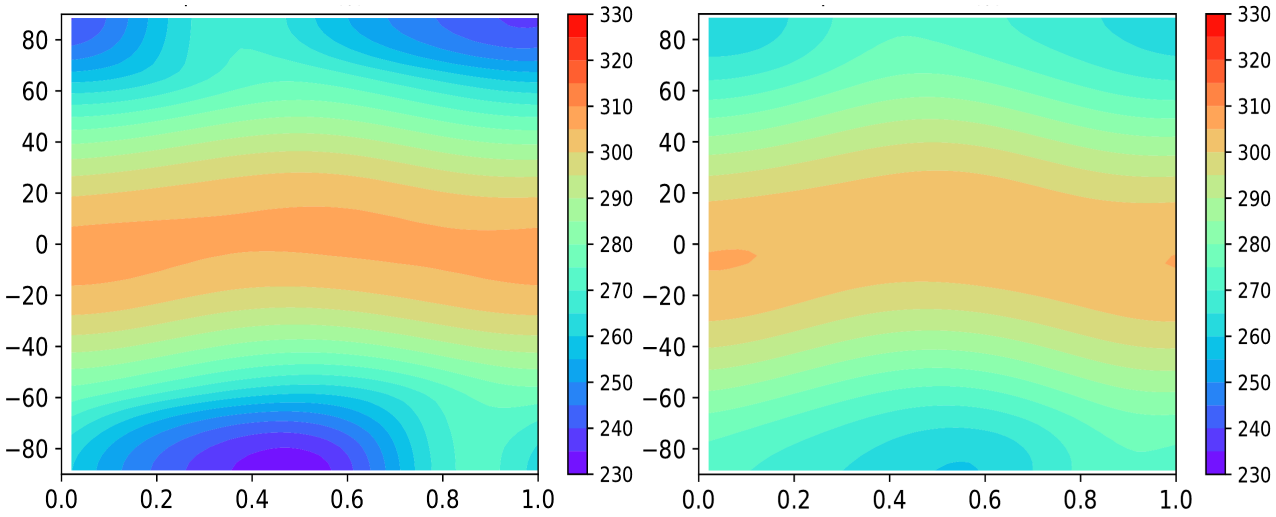

Figure 7.15: The seasonal-latitudinal temperature maps for the Archean Earth at the 3.7 Gyr epoch for different rotation periods. Left panel: 11 hours. Right panel: 19 hours. Credit: Riccardo Bevilaqua.

36.6 K respectively for the 11, 15 and 19 h period. An enhanced heat diffusion also favors the planetary habitability[8] by reducing the extent of the ice caps, that decrease from 11% to 2% of the planetary surface.

The second planetary parameter tested separately is the fraction of lands. Lands influence the model outcome mainly by changing the surface albedo. Land albedo is higher than ocean albedo apart for very high incident zenith angles ($\gtrsim 85^\circ$). Also, ice has an easier time forming over lands (at least in our model, but see how it compares to Earth observational data in Section 5.1.2) and has an higher albedo once formed. An higher fraction of lands should also increase the inter-seasonal temperature shifts due to the very low thermal capacity with respect to oceans. In practice, however, this effect is negligible for low ($\lesssim 50\%$) land fractions. For this test, we tried three different landmass fractions (0.0, 0.94 and 0.88). The two extreme cases represent the situation at the beginning and at the end of the Archean. As for the other parameters, we set the insolation to 0.756 $S_\odot$ and the rotation period to 13 h, which corresponds to the state of Earth at 3.7 Gyr in the past. The atmosphere employed is again the P100LM. The results for the two extreme cases are shown in Fig. 7.16. As it is possible to see, the difference is small. The global surface temperature is slightly higher (291.3 K vs 290.0) in the zero-continent case due to the lower overall albedo. The pole-equator thermal gradient is slightly smaller (48.8 vs 50.6) because of the marginally less extended polar caps (10% vs 8%).

Evolution over time

The final set of tests was aimed at studying the evolution of Earth habitability over time. We thus run ESTM2 for all the atmospheric models described in Table 7.2 at 7 different epochs during the Archean (4.0, 3.7, 3.4, 3.1, 2.8 and 2.5 Gyr in the past). At each epoch we selected the corresponding values for the insolation, the rotation period and the land fraction

[8]This is true at this level of insolation, at least. An enhanced heat diffusion can also cause a steeper transition between a completely deglaciated and a completely glaciated state, preventing the formation of a partially habitable equatorial waterbelt.

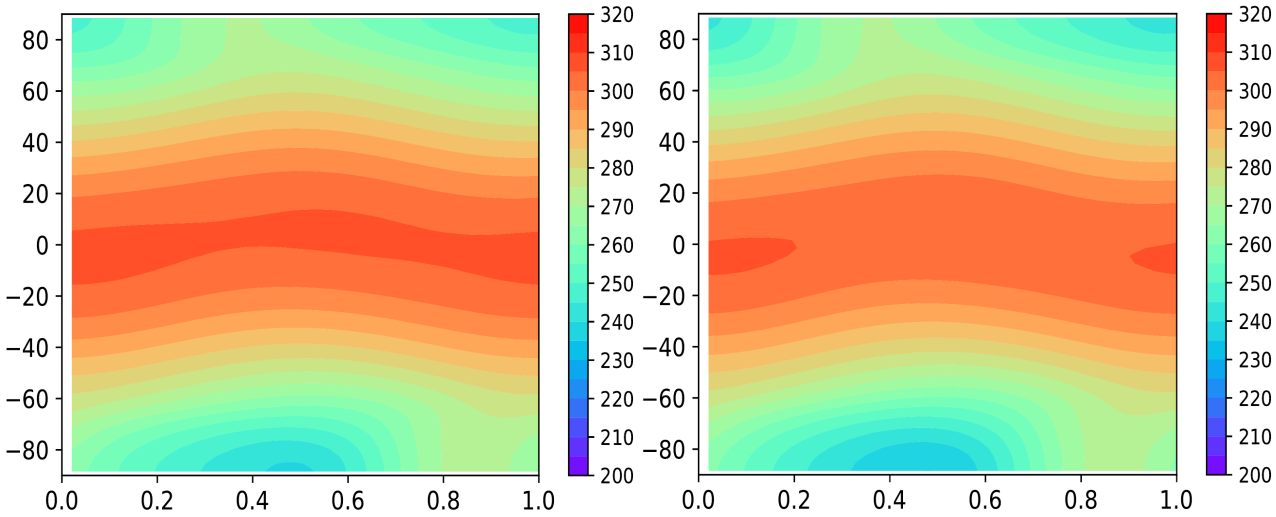

Figure 7.16: The seasonal-latitudinal temperature maps for the Archean Earth at the 3.7 Gyr epoch for different land fractions. Left panel: no land (i.e. waterworld). Right panel: 12% land. Credit: Riccardo Bevilaqua.

as described in Section 7.2.3. The result is shown in Fig. 7.17. Each curve represent the evolution of the average global temperature over time for a given atmospheric composition. The points represent available observational data on the surface temperature. Several things can be noted. First of all, the P100L0 model is the only one that is not able to guarantee Earth habitability over the entire Archean Eon. In fact, at the 4.0 and the 3.7 epochs it causes the planet to enter a Snowball state with very low (∼230 K) surface temperatures. At 3.4 and 3.1 Gyr it still produces extended ice caps, causing around half of the surface of to stay below 273 K for at least a part of the year. The P40H0 model also produces a relatively cold planet with extended ice caps in the early Archean, but it is able to keep the Earth out of a Snowball state. The other models are all considerable warmer. At the other end of the temperature spectrum, we found that the P100HH model causes the planet to enter a Moist Greenhouse state (identified in our models as an average global temperature in excess of 330 K) at all epochs. The P100HM and the P1000MH models allow for a warm, stable state in the early Archean but causes the planet to exceed 330 K at later times (between 3.7 and 3.4 Gyr in the first case, and between 3.4 and 3.1 Gyr in the second case). Second, taking into consideration the (sparse) observational data, we can identify the P100M0 model as the most suitable to describe the mid-Archean (at ∼3.4 Gyr) atmosphere, since it is well in agreement with Hren et al. (2009) and Blake et al. (2010) data, and it is just fraction of K above the upper limit given by Krissansen-Totton et al. (2018). The latter set of datapoints have been derived by considering the existence of glacial deposits at that age (de Wit & Furnes, 2016) and then using a climate simulation to find the upper temperature limit that allows for the formation of permanent ice caps. For P100M0, our model predicts an average zonal temperature at very high latitudes (>85°) equal to ∼273 K, thus allowing the protracted existence of ice oveer lands. If the Krissansen-Totton et al. (2018) upper limits are not considered, also the P100H0 and the P100LH (which are nearly superimposed) are good candidates. The low pressure models (P40H0 and P40V0) are too cold to describe the early and mid Archean climate, but show a better agreement with data at later epochs (2.9 to 2.5 Gyr). Since the Som et al. (2016) findings regarding the low surface pressure are also referred to the late Archean (2.7 Gyr ago), these models are viable candidates for describing the Earth atmosphere in that

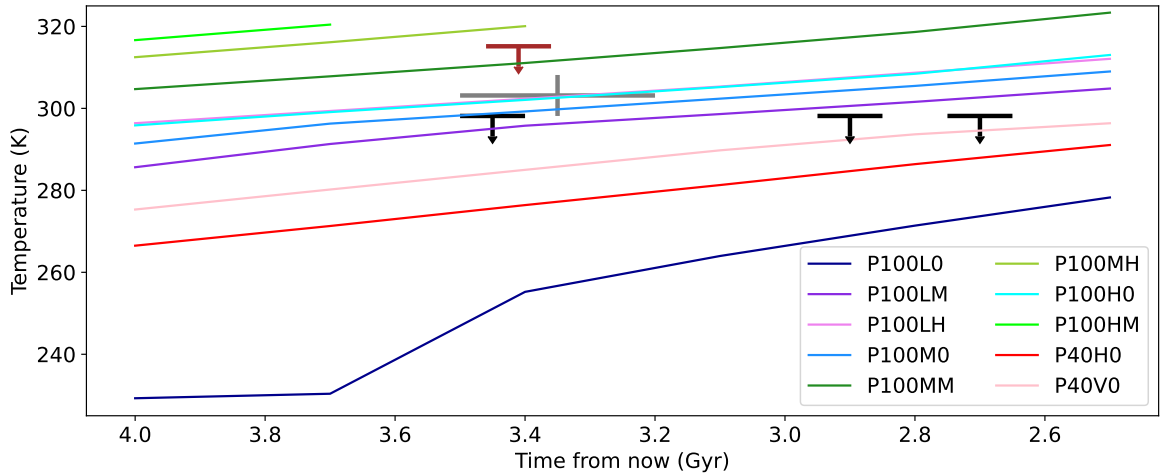

Figure 7.17: The global temperature evolution over the Archean Eon for the models reported in Table 7.2. The color code employed for the lines is described in the legend. Observational data points are taken from Hren et al. (2009, brown), Blake et al. (2010, gray) and Krissansen-Totton et al. (2018, black). The curves interrupt when the average temperature increases over 330 K, signaling the beginning of a Moist Greenhouse state (see Section 2.4.1). The P100HH model is not shown because it exceeds this limit at all epochs. Credit: Riccardo Bevilaqua.

age. Finally, we can link our results to the compositional limits expounded in Section 7.2.1. Concerning the CO_2, Driese et al. (2011) found a partial pressure value of ∼0.01 bar at 2.7 Gyr, while another analysis from Rye et al. (1995) found an upper limit of 0.03 bar at 2.8 Gyr. Based on these data, the correct atmosphere for that age would be the one described by the P100L0, P100LM and P100LH models. These in turn give an average surface temperature respectively equal to 271.4, 301.6 and 308.7 K. Only the first model (P100L0) is below the upper limit given by the presence of glacial deposits, while the second (P100LM) is just ∼3 K above. On the other hand, Kanzaki & Murakami (2015) provided considerably higher estimates, with fiducial p_{CO2} values of ∼0.1 bar at the same age. Based on their findings, the right cases would be the P100H0, P100HM and the P100HH. Only the first one produces an habitable Earth with an average temperature of 308.4 K. This model, however, is more than 10 K over the Krissansen-Totton et al. (2018) temperature upper limit. Concerning the CH_4 concentration, if we consider the lower limit of Zahnle et al. (2006) as robust, we cannot select the models labeled as P100L0, P100M0, P100H0, P40H0 and P40V0 as good representations of the Archean atmosphere. The best methane-bearing cases with respect to temperature data would be the P100LM and the P100LH. The latter reproduces very well the Blake et al. (2010) mid-Archean observational value, while the former agrees better with the glacial deposits upper limits in the late Archean.

By putting together our considerations on both the temperature and the chemical limits, we can identify the P1000LM as our best model. Despite its shortcomings, it is generally in agreement with the lower end of the CO_2 and CH_4 compositional limits on one hand, and it reproduces somewhat the temperature limits of both the mid and the late Archean. However, a variable atmospheric composition is much more likely. By lowering progressively both the concentrations of both CO_2 and CH_4 it is easy to maintain a constant (or a decreasing) temperature trend. The same would be true if the N_2 pressure decreases during the Eon. More data on both the paleotemperatures and the paleoatmosphere composition are required

to resolve the degeneracies and to give a better picture of the Archean Earth climate state.

7.3 Future applications: synthetic spectra of planetary atmospheres

The retrieval of spectra from exoplanetary atmospheres is the only practical way to extend our knowledge of these worlds' surfaces (for the Earth-like ones) or gaseous interiors (for the Neptune- and Jupiter-like ones). Concerning specifically the topic of astrobiology, information inferred from atmospheric spectra is fundamental in the search for biosignatures outside the Solar System. Since spectra are necessary to characterize exoplanets, a growing share of the astrophysical community effort is directed towards the spectroscopic observations of these bodies. This is either the main goal or among the most relevant scientific objectives of a variety of both ground- and space-based astronomical facilities that will come online in this decade. A brief overview of these endeavours is presented at the end of Section 1.1. Here I provide some more details of the observational methods for atmospheric spectra and briefly discuss the contribution that EOS can provide in this context.

While all similar in nature, three different type of atmospheric spectra that can be retrieved from exoplanets. These are transit spectra, emission spectra and reflectance spectra. Tinetti et al. (2013) offer a review on exoplanetary spectroscopy from which part of the description below is taken.

Transit spectra are obtained during the primary transit of a planet in front of its star (see Section 1.3.3). During the primary transit, part of the light from the star is blocked by a planet. However the depth of transit varies as a function of the wavelength considered due to the presence of absorbers and emitters in the otherwise transparent atmosphere. By compiling a list of transit depths for many different spectral bands it is possible to produce a spectrum of the upper atmosphere of the planet. By means of this technique, the first successful detection of a spectroscopic signature in an exoplanetary atmosphere was achieved (specifically, Na in the HD209468b atmosphere Charbonneau et al., 2002). There are, however, some limitations. First of all, only transiting planets can be studied in this way. Also, transits lasts for a small fraction of the orbital period and this could hamper the analysis of long-period objects. Second, only the upper part of the atmosphere can be effectively probed, because of the presence of continuously absorbing clouds or in any case due to atmospheric refraction. Third, low scale height atmospheres, such as those of terrestrial-type planets, are considerably harder to study since they cause only small variations of the transit depth, which may be already small overall if the considered planet has a small radius with respect to the host star.

Emission spectra are instead obtained directly by the planet. As such, they do not require a transit and can be collected at any moment during the orbit of the body[9], expanding substantially the sample of possible candidates. Emission spectra are primarily composed by the thermal emission of the planet, and as such are strongly dependent on the exact vertical structure of the atmosphere. Spectral features can appear in emission or in absorption depending whether they form above or below the tropopause, thus potentially allowing to recontruct also the compositional profile. Out-of-thermal equilibrium emission mechanisms can produce other bright emission lines (Swain et al., 2010; Waldmann et al., 2012). High

[9]Apart for the brief secondary transit if the geometrical configuration is appropriate.

resolution planetary emission spectra allow also to determine directly their orbital velocity curve, thus allowing to directly calculate the inclination with the line of sight. Together with the data obtained from the radial velocity of the star, this allow to estimate exacly the mass of the body, rather than relying on the $m_p \sin(i)$ lower limit. An example of this can be seen in Brogi et al. (2012). The main problem concerning the emission spectroscopy of exoplanets is the very low planetary flux with respect to the stellar one, coupled with the inability to spatially resolve the planet. Thus, the light collected by the instrument is contributed both by the star and the planet, and the two contributions must be disentangled. If the observation has been taken from the Earth surface, the absorption features of our atmosphere must be carefully subtracted. For this reason, emission spectra available now are those of highly irradiated (and thus particularly bright planets with extended atmospheres such as) hot Jupiters and Neptunes.

Reflectance spectra are not separated from emission spectra, at least for exoplanets. The inability to resolve spatially the planet means that any retrieved data will be contributed also by stellar light reflected by the atmosphere via scattering processes and possibly the surface. The evolution of the reflected component (both bolometric and spectrally resolved) during the orbit, which is known as phase curve, is another important source of information. As an example, Heng et al. (2021) demostrated how the it can be used to derive a series of parameters such as the single scattering albedo and the asymmetry factor, which can then be linked to specific atmospheric properties (such as the presence of clouds) within a self-consistent and unified framework. Reflectance spectra and phase curves have very interesting applications in astrobiology, since they can in theory be used to detect both the glint produced by the direct reflection of light on flat, reflective surfaces such as liquid water oceans (Lustig-Yaeger et al., 2018), and spectral-dependent features that may be difficult to produce abiotically, like the so-called *Red Vegetation Edge*[10] (Sagan et al., 1993; Seager et al., 2005). Since reflectance and emission spectra are usually considered together, they share most of the same advantages and limitations. Among the former, they do not require a transiting planet, while among the latter they are hindered by the very high constrast between the stellar light and the reflected component. Phase curves require continuous observations to be reconstructed completely, thus necessitating the use of space-based facilities. Also, they are often difficult to disentangle from the instrument systematics, such as the detector response function. Finally, part of the information contained in the reflected component, like the ocean glint, can be retrieved realistically only by direct imaging of the planet (see again Lustig-Yaeger et al., 2018).

Since the features of the exoplanetary spectra are the product of the combination of a large number of factors (composition, thermal structure, presence of hazes and clouds, non-thermal mechanisms etc.), the retrieval process must necessarily rely on Bayesian inference methods. In practice, a large number of synthetic spectra are generated by a forward RT model. The observed spectrum is thus compared against these synthetic spectra and a likelihood function is derived. The set of parameters that produce the best-fitting synthetic spectra are taken as the result. Generally, these parameters are not univocal but instead associated with a probability distribution function. An example of this methodology, concerning specifically the data analysis segment of the proposed LIFE mission (Quanz et al., 2021), is presented in Konrad et al. (2021). The same retrieval model has then been tested by using other

[10]The Red Vegetation Edge is identified in the reflectance spectra of vegetation-covered surfaces by a low ($\sim$0.05) albedo in the red part of the visible spectrum (0.65-0.7 μm), followed by a rapid increase ($\sim$0.20) in the near-IR (0.9-1.0 μm). It is caused by the widespread presence of chlorophyll.

artificially-generated spectra, since the type of data expected from this proposed instrument are (clearly) not yet available (Alei et al., 2022). Due to the large amount of synthetic data and the large number of parameters that must be sifted through, machine learning techniques have also been proposed for this task (Soboczenski et al., 2018).

It is thus evident that synthetic spectra are needed both to interpret currently available data and to lay the groundwork for future observations. Thanks to the features of one of its central components (HELIOS), EOS can be part of this process by simulating the spectral emission/reflection from rocky exoplanets. In fact, while the contribution of EOS to the results presented in the previous Chapters of this Thesis was in the form of integrated quantities (the OLR and the TOA albedo), it must be considered that the final products of EOS calculations include the outgoing TOA spectral flux from the visible to the microwave. This type of data can be easily fed into the restrieval codes described above. Moreover, EOS has the extra advantage of being capable of linking observations to climate calculations thanks to the coupled EOS-ESTM procedure. In practice, we can follow the procedure delineated below:

(i) from a certain set of priors, we can generate emission/reflection spectra;

(ii) from these spectra, we can calculate the OLR and the TOA albedo;

(iii) the OLR and the TOA albedo can be used in climate calculations in ESTM;

(iv) the seasonal-latitudinal temperature profiles can be used to perform an area-weighted average of the spectra calculated at (i) in order to produce a disk-averaged planetary spectrum;

(v) the disk-averaged spectrum can be compared with future observational data or be used now in tests of the retrieval codes for future missions;

(vi) the seasonal-latitudinal temperature profiles calculated at (iii) can also be used to assess the habitability for a broad range of planetary parameters.

In this way, the gap between observations and climate simulations can be bridged. A possible topic that can be investigated is the impact of climate variables on the planetary spectra. The computational efficiency of both EOS and ESTM make them uniquely suited for the tasks enumerated above.

7.3.1 A few examples of EOS-generated synthetic spectra

Fig. 7.18 shows the near- and mid-IR parts of the EOS-generated, clear-sky synthetic spectrum for a modern Earth atmosphere for four different values of the surface temperature. The $\lambda/\Delta\lambda$ spectral resolution is 3000. The chemical composition includes N_2, O_2, 360 ppm of CO_2, 1.8 ppm of CH_4 and an amount of H_2O corresponding to a relative humidity of 100%. The tropospheric lapse rate has been computed using Eq. 2.24 and the stratospheric temperature has been set to 200 K. The surface pressure evolves from 1 bar at 240 K to 1.46 bar at 360 K because of the rising H_2O partial pressure. Similarly, the mean molecular weight of the atmosphere decreases from 29 to 24 g mol^{-1}. These calculations have been performed during the production of the OLR and TOA albedo tables used for the robustness assessment process described in Chapter 4. As it is possible to see, apart from the change in the overall brightness temperature, the increasing amount of water vapor in the atmosphere causes the spectrum to change substantially, becoming dominated by H_2O absorption features at 320 and 360 K.

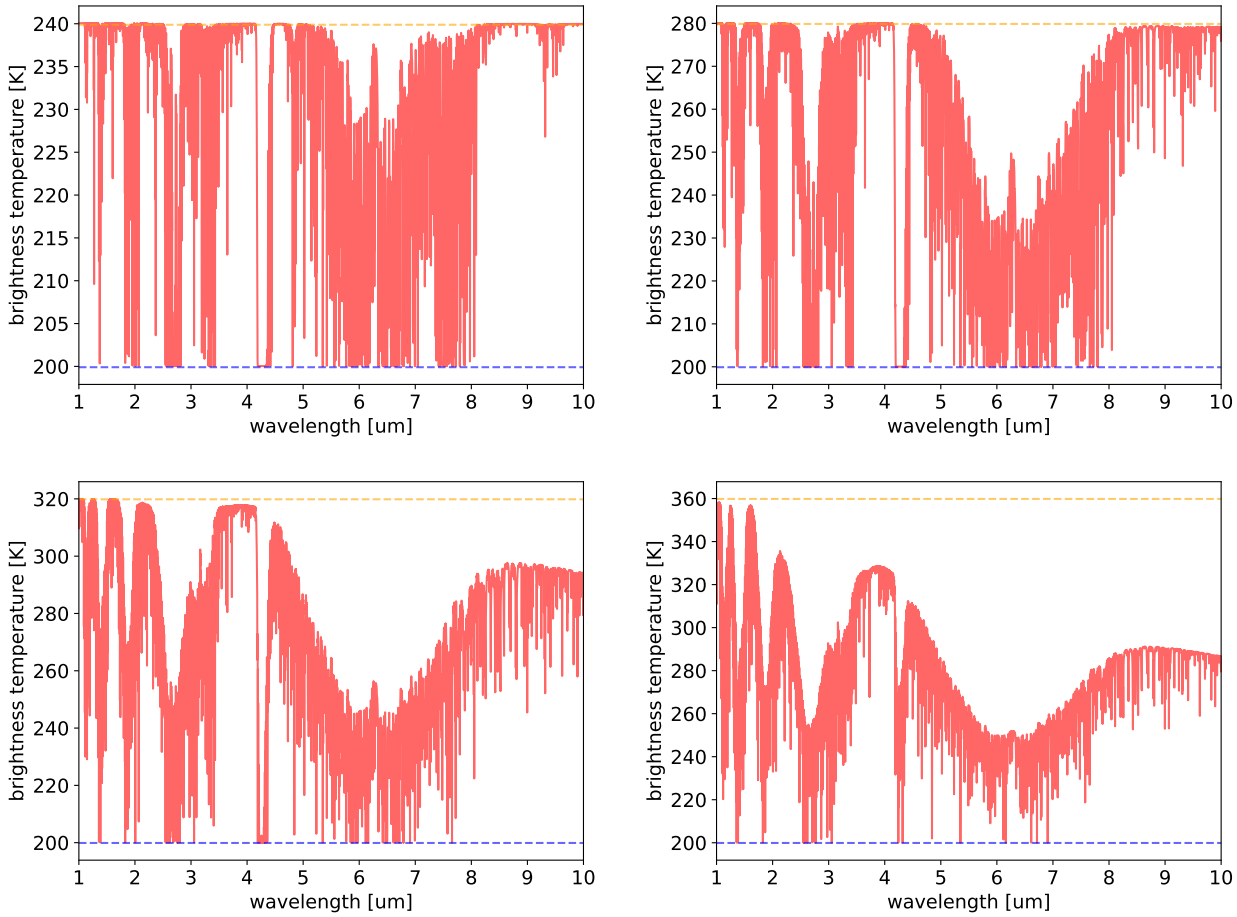

Figure 7.18: The clear-sky, single-column emission spectrum of the *Saturated Modern Earth* case described in Table 4.1 for four different surface temperatures in the near- and mid-IR. Upper left: 240 K. Upper right: 280 K. Lower left: 320 K. Lower right: 360 K. The orange and blue dashed lines represent respectively the emission blackbody of the surface and of the isothermal stratosphere.

Fig. 7.19 shows instead the clear-sky synthetic spectra of an anoxic Archean Earth-like atmosphere with 0.25 bar of CO_2, 0.75 bar of N_2 and a relative water humidity of 60%. The concentration of CH_4 is zero in the panel on the left and 100 ppm in the panel on the right. CO_2 absorption has been modeled using the Perrin & Hartmann (1989) sub-Lorentzian profile and includes the GBB collisional features. The surface temperature is 280 K for both the atmospheres and the thermal structure is calculated following Eq. 2.28. The stratosphere's temperature is set to 160 K.

The plots in Figs. 7.18 and 7.19 represent just a few examples of the potential of generating near- and mid-IR spectra with EOS. Depending on the needs of future applications, the spectral resolution and the parameters that define the vertical atmospheric structure can be easily changed. With the aid of the synthetic spectra it will be possibile to assess the detectability of atmospheric features for a given setup of instruments capable of collecting exoplanetary spectra. At the same time, for each type of atmosphere considered, the physical conditions at the planetary surface can be assessed by coupling the specific atmospheric RT properties calculated with EOS with a proper set of planetary parameters to be given

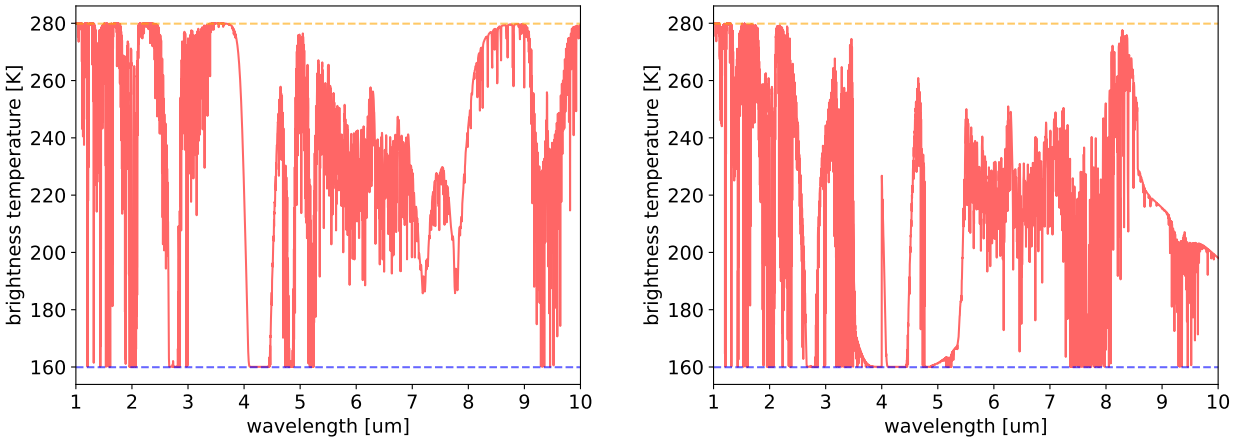

Figure 7.19: The clear-sky, single-column emission spectrum of two possible Archean Earth-like atmospheres with 0.25 bar of CO_2, 0.75 bar of N_2 and a relative humidity for H_2O of 60%. The panel on the left shows the case with 0 ppm of CH_4, the panel on the righe shows the case with 100 ppm of CH_4. The orange and blue dashed lines represent respectively the emission blackbody of the surface and of the isothermal stratosphere.

as an input to ESTM. Some of these parameters (e.g. mass, radius and time variation of the insolation) will be constrained by observational data. Other important parameters unconstrained by observations (e.g. rotation period, surface distribution of lands and oceans, average cloud properties, etc.) can be easily parametrised in ESTM. In summary, starting from the synthetic spectra calculated with EOS and the climate predictions obtained with ESTM for the same type of atmosphere, it will be possible to establish a link between the detectability of spectral features with a given instrumentation and the surface habitability of the planet under investigation.

7.3.2 The impact of clouds on planetary spectra

As underlined also in other Chapters, EOS-generated spectra are clear-sky, meaning that no clouds or other particulates are considered throughout the atmospheric column. In other words, the Mie scattering is not included in the model. This is an important approximation that warrants a brief discussion.

First of all, the reason behind this choice is practical and related to the original goal of EOS, which was to provide ESTM with an up-to-date and flexible radiative transfer model. In this framework, clouds are treated at the climate simulation level by simply subtracting a given amount of OLR and changing the zonal surface albedo of the planet (see Sections 5.2.1 and 5.1.5). This approach is adequate for the preliminary characterization of EOS and the calibration of the EOS-ESTM model on the modern Earth case, but limits its operational range and reduces its usefulness as a synthetic spectra generator. As such, adding the treatment of Mie scattering is now part of the future expansion prospects of our procedure.

Cloud particles can scatter the incoming visible light from the star (which cools the planet), and both scatter and absorb the infrared radiation from the surface (which heats the planet). All three these effects influence the planetary spectrum, both in emission/reflection and in transmission. Their impact depends on several variables such as the chemical composition, the particle size distribution, the horizontal distribution and the position in the atmospheric

column (in particular, with respect to the cold trap). The most studied case is that of H_2O clouds due to it relevance for both Earth climatology and Earth-like planet detection and characterization.

Water is present in clouds both in liquid and solid state. Their radiative transfer properties can be calculated using the Mie theory starting from the complex refractive index of condensed water and the features of the cloud particles (see e.g. Kitzmann et al., 2010). Liquid water droplets in clouds are spherical and have a log-normal distribution in sizes (Kokhanovsky, 2006). Mean radii are different in continental and maritime clouds, the former being smaller (4 vs 6 μm), while the standard deviation is similar (0.4 in both cases). Continental clouds are also denser (254 vs 91 cm^{-3}). The single scattering albedo ω_0 is unitary between 0.2 and 2 μm, oscillates in the infrared because of the presence of absorption bands and steadily decreases above 20 μm due to entering in the Rayleigh scattering limit. The asymmetry factor g_0 is $\sim$0.8 and nearly constant up to around 10 μm, while decreases at longer wavelengths. Both ω_0 and g_0 become negligible at around 200 μm. Since much of the visible light in scattered forward, sizeable path lenghts are necessary to produce reflective clouds. Absorption occurs in bands between 3 and 100 μm. Water ice crystals have instead a large variety of irregular and usually elongated shapes that can be adequately modeled as hexagonal prisms with an aspect ratio of 2 and distributed in size following a power law with index -3.23 (Heymsfield & Platt, 1984). The optical properties of these particles can then be efficiently calculated (i.e. without using ray-tracing techniques) in terms of *equivalent spheres* that mimic these hexagonal prisms (Neshyba et al., 2003). Ice particles can grow up to hundrends of μm, causing ω_0 to hover around 0.8 for wavelengths up to 1000 μm. The g_0 factor is nearly equal to that of water droplets up to 20 μm but then decreases more gently, producing an asymmetric scattering of light in the FIR. The absorption pattern is similar to that of liquid water.

Water clouds effects can be studied separately for low-, mid- and high-altitude clouds (see e.g. Tinetti et al., 2006a). On Earth, the most common cloud types for each of these categories are stratocumuli, altostrati and cirri, respectively (Manabe & Strickler, 1964). Stratocumuli are composed by liquid water and have a net cooling effect due to their high path length. Cirri on the other hand are formed by water ice and have a net greenhouse effect. Finally, altostrati are a mix of the two phases and are generally radiatively neutral.

The impact of clouds on the surface temperature amounts to tens of K. Using a 1D radiative-convective model, Kitzmann et al. (2010) found that changing the stratocumulus coverage from 0% to 100% causes T_s to decrease by $\sim$35 K by increasing the TOA albedo from 0.15 to 0.45. Changing instead the cirrus coverage from 0% to 100% causes instead T_s to increase by $\sim$15 K. The thermal structure of the atmosphere is also affected, with the same model predicting a shift from a radiative to a convective regime in the cirrus region when cirrus coverage increases above 50%. The climate effect of clouds is also dependent on the incoming stellar radiation spectrum. F-type stars are more affected by clouds than M-type stars, and especially by cirri, whose effect on T_s is nearly doubled.

The planetary emission and reflection spectra are also impacted, in turn influencing our ability to correctly retrieve the real surface temperature and chemical composition of the atmosphere. High levels of cloudiness decrease the OLR (since cloud tops are always cooler than the underlying surface), decreasing in turn the thermal contrast with the overlying atmosphere and thus reducing the amplitude of spectral features even for those formed above the cloud deck (Tinetti et al., 2006a). This effect is strongest for cirri, which for high coverage percentages can make the 9.6 μm O_3 absorption band undetectable in low resolution spectra

(Kitzmann et al., 2011a). The same work shows that in the case of a planet orbiting an F-type star, clouds can make also CO_2 and H_2O bands in the mid-IR undetectable, effectively preventing the retrieval of any molecular species in this part of the spectrum. Minor compounds with an inhomogeneous distribution throughout the atmosphere can be completely hidden by the cloud deck. Concerning reflection, clouds can also mimic the Red Vegetation Edge in the near-IR, making its identification more difficult (Tinetti et al., 2006b). On the other hand, the increased path legth due to multiple scattering in the visible light can instead amplify the spectral signatures of an Earth-like atmosphere illuminated by a Sun-like star (i.e. O_2, O_2 dimers, CH_4 and H_2O), especially if a low cirrus and high stratocumulus coverages are present simultaneously (Tinetti et al., 2006a; Rugheimer & Kaltenegger, 2018). Rugheimer & Kaltenegger (2018) also showed that O_2 is visible also at 10% PAL concentrations and possibly down to 1% PAL concentrations around F-type stars if sufficiently high resolution spectra are available. Simulating instead low resolution spectra, Kitzmann et al. (2011b) found that they will probably prevent the direct detection of O_2 and O_3 around late-type stars unless a very large amount of low-altitude clouds are present.

Conclusions and future prospects

This Thesis presents the ensemble of different fields on which I worked during my PhD studies. The main topic, which is identified in the title, is the development of EOS. The other two relevant and independent subjects treated here are the updating of ESTM climate model and the analysis of the binary systems habitability. On top of these, two application examples have been presented.

Going more into details, the main topic concerns the adaptation, validation and application of the opacity calculator HELIOS-K and the radiative transfer code HELIOS to the study of terrestrial-type atmospheres. This task required the creation of several ad-hoc routines to integrate the relevant physical recipes of this topic, in particular the collision-induced absorption (CIA) features for H_2O and CO_2, the sub-Lorentzian shapes of far wing line shapes of CO_2 and the vertical thermal profile generations under a variety of different assumptions. An infrastructure of wrappers and analysis tools complete the picture. The new multicomponent software that resulted was called EOS. Throughout this Thesis, it has been referred to as a (numerical) "procedure" to acknowledge precisely its modular nature, which is also part of the reason behind its efficiency. The scientific case behind this endeavour has been delineated in the Chapters 1 and 2: exoplanets are difficult to characterize and thus require a large amount of modeling. Concerning specifically astrobiology, climate simulations are needed to assess the habitability on rocky exoworlds surfaces. EOS satisfies both the need for energy balance calculations in climate simulations and the need for synthetic spectra to fit future observational data.

The two other topics of this Thesis concern the work on updating ESTM to ESTM2 and to study the habitability of the binary star systems in a systematic way. The first task has been carried on by developing a series of new parameterizations for the land albedo, the cloud OLR forcing and albedo, the ice fraction as a function of the type of surface and the temperature and the cloud fraction. These new prescriptions have been tested against observational Earth data both separately and concurrently and allow ESTM to better reproduce the current Earth state on one hand, and to better operate under exotic conditions (such as a Snowball state) on the other. The second task has instead been completed by generating a synthetic population of binary systems using up-to-date knowledge of the binary star parameters distributions (concerning occurrence rate, mass ratios, semi-major axis and eccentricity) and then calculating the circumstellar and circumbinary radiative habitable zones (HZs) and gratitational instability regions. This study allowed us to identify combinations of parameters that are most conductive to the existence of gravitationally stable HZs, thus offering a possible guideline for future time-consuming detection campaigns. We finally studied more in detail the known planet-harboring binary systems.

Finally, I have presented two application examples. The first one concerns a deeper investigation of a special habitability niche around low mass stars with higher mass companions in binary star systems. The habitability of planets with strong variations in both the total flux

and its spectral energy distribution require a large amount of atmospheric single-column calculations and at least a 2D seasonal-latitudinal climate model to assess the physical conditions on the planetary surface. The second one concerns instead a parameter space exploration of the conditions on the surface of Earth during the Archean Eon. The coupled EOS-ESTM pipeline fits perfectly the necessities of both these tasks, since it offers a fast, low-complexity model that is nonetheless capable of capturing the main climate feedbacks that may hamper habitability by precipitating the planet either in a completely glaciated Snowball state or in a Runaway Greenhouse state. The absence of limits on the compositional and thermal structure of the atmospheres that can be simulated in EOS and the computational efficiency of the procedure allow for the treatment of a large variety of cases.

The main topic of this Thesis concerns the development and testing of models rather than their application, thus here only few new scientific results are presented. However, the groundwork for future studies has been laid, as presented in Chapter 7, and shows the potential of our procedure. Moreover, several possible avenues not yet explored are described in the Future Prospects. On the other hand, the analysis work on the binary star habitability yielded already some clear conclusions. A brief and general summary of findings, both general and specific, is presented below.

(i) At first we tested the robustness of EOS with respect to variations of both model parameters and physical inputs, thus characterizing the uncertainties that are related to specific choices usually adopted in literature for the modeling of Earth-like atmospheres in the 220-360 K surface temperature range. Concerning the variations in the model parameters, we determined that increasing by 6 times the density of points in the pressure vertical grid (from 5 to 30 per order of magnitude) amount to $\sim$2.5% deviations in the OLR and $\sim$1% in the TOA albedo. This deviation peaks at the mid-point of the temperature range (i.e. at 300 K). The impact of choosing a different uppermost layer pressure is instead negligible.

(ii) Concerning the variations in the physical input, we determined the importance of choosing appropriately the stratospheric temperature when evaluating the OLR at low ($\lesssim$300 K) surface temperatures and the lapse rate when evaluating the OLR at high ($\gtrsim$300 K) surface temperatures. In the former case, the maximum deviation amounts to $\sim$5.5% when changing the stratospheric temperature from 190 to 220 K. In the latter case, the maximum deviation amounts to $\sim$5% when changing from a moist to a dry lapse rate while keeping the composition constant. The deviations in TOA albedo are respectively 0.75% and 5%.

(iii) Compared to other RT codes, EOS produces results that are in line with respect of the current understanding of the subject. Concerning a 100% moist modern Earth atmosphere, EOS produces an OLR which is between 4 and 11% higher than that calculated by CAM3, SMART, SBDART, LBLRTM, LMDG, *WK97* and *KOP13*, but 6% lower than that calculated by CCM3. The TOA albedo is instead lower by 3% to 20% with respect to the one calculated by all the other models. For both quantities the worst case occur at 360 K, where the prescriptions concerning the opacity of H_2O are amplified the most. Concerning CO_2-dominated dry and moist atmospheres, EOS results are inside the envelope of models tested by Halevy et al. (2009) and Kasting (1991), both in terms of OLR and, for the second, in terms of TOA albedo.

(iv) During the robustness testing of EOS we found that the fixed-pressure tropopause at

0.1 bar description proposed by Robinson & Catling (2014) seems unable to reproduce the change in the OLR slope expected at high surface temperatures for water-bearing planets. This behaviour is expected since it signals the approaching of the Komabayashi-Ingersoll limit and the onset of a Runaway Greenhouse state, which are robust findings of planetology studies. Thus, their conclusions may warrant a re-investigation.

(v) The study of the population of binary star systems show that circumbinary habitability is hampered by the gravitational instability in most cases. Instead, circumstellar habitability is unhindered in most cases. Concerning the former, only ∼3-5% of the binaries seem able to host an HZ. In order to do so, these systems must have small m_B/m_A ratios, very small ($\lesssim$0.3 AU) semi-major axes and near-zero ($\lesssim$0.1) eccentricities. On the other hand, concerning the latter, 78-94% systems are conductive to habitability. In this case, semi-major axes $\gtrsim$1.0 AU are strongly favored while there are not preferences for specific m_B/m_A ratio and eccentricity values. Different hypotheses on the binary occurrence rate for different type of primaries, on the stellar mass function, on stellar metallicity and on the mass ratio distributions do not affect the results, that are thus very robust.

(vi) Some peculiar set of stellar parameteres allow for the existence of widened HZs in binary systems with respect to the single star counterparts. Circumbinary HZs are up to 1.44 times wider than single star HZs around a single star of the same type of the primary, while circumstellar HZs can be up to ∼10 times wider. This last possibility, albeit rare, can in theory allow for non-tidally locked planets around M-type dwarfs in a small but non-negligible amount of cases (1-2%). This is relevant since ∼50% of the stars of our Galaxy are binaries.

(vii) Two of the cases identified at (vi) has been subjected to a thorough investigation via the coupled EOS-ESTM pipeline. While only preliminary, the study identified an important issue that would have gone unnoticed under a simpler analysis based solely on the general definition of HZ. This issue concerns the climate impact of the large excursion in instellation due to the change in the relative position of the circumsecondary planet with respect to the primary component of the system. Our calculations indicate that the planet may enter and exit from a Snowball state during which the collapse of the CO_2-dominated atmosphere can in theory occur, preventing the planet from recovering from the completely glaciated state. On the other hand, if the total instellation is sufficiently larger to prevent long-term and widespread glaciations, the planet can potentially enter a Runaway Greenhouse state during the flux maxima.

(viii) By applying the EOS-ESTM pipeline to the study of the Archean Earth we found that a single atmospheric composition cannot explain the (few) estimates regarding the chemical composition of the atmosphere and the surface temperature at that time. While this conclusion needs to be corroborated by testing a broader portion of the planetary parameter space, we nonetheless observed how the substantial changes in the insolation, the rotation period and the continental fraction during the 1.5 Gyr-long Archean Eon force us to identify different "best models" at different epochs. In general, surface temperature data require either the abundance of CO_2 or that of CH_4 to decrease in time. High CO_2 scenarios must be necessarily accompained by lower overall pressures produced by considering a reduced N_2 partial pressure. This last scenario would be in line with the findings of Som et al. (2016).

Future prospects

The work presented here can be expanded in along a multitude of different avenues. Each of the components of this Thesis can either be expanded in some way or applied to the study of specific topics. They also need to be kept updated with the newest available data on opacity and scattering cross sections. First of all, these tools can be enhanced in the following ways by:

- Updating both the opacity line lists and the formulations used to calculate the opacity continua. While I was writing the Thesis the HITRAN group formally released the new version of the database, namely HITRAN2020 (Gordon et al., 2022). EOS currently uses HITRAN2016 (Gordon et al., 2017). Concerning specifically H_2O, we plan to include the most recent data on self-broadening (Anisman et al., 2022a) and opacity continuum (Anisman et al., 2022b).

- Expanding the set of specific radiative transfer provisions to study more exotic atmospheric chemical makeups and to increase the precision of known mixtures by adding further (and not yet considered) prescriptions. Concerning the former, we plan to expand our treatment to include ozone, nitrogen and sulfur oxides and hydrogen sulfide. This would allow a deeper analysis of the Archean Earth conditions. Additional greenhouse gases are probably required to explain the presencce of liquid water on the surface of Mars during the same age. Concerning the latter, a primary expansion path would involve the integration of the N_2 continuum that may be useful to both increase the precision of OLR calculations in Earth-like atmospheres and to apply them to super-Earths (for which we can expect denser atmospheres).

- Expanding, testing and validating for terrestrial-type planets the treatment of the cloud Mie scattering and absorption routines in HELIOS, which will allow us to consider the effect of clouds self-consistently (at least from the radiative point of view) in our calculations.

- Making use of the *iterative*, rather than the *post-processing* mode in HELIOS. This will increase the precision of RT calculations under non Earth-like conditions by allowing us to ditch the older parameterizations that has been used throughout this thesis.

- Better integrating EOS with the other codes of the Exoclime Simulation Platform software suite, in particular VULCAN (Tsai et al., 2017) and THOR (Mendonça et al., 2016; Deitrick et al., 2020). The first would allow EOS to correctly take into consideration gases that may form under the initialized atmosphere but that now are not treated (such as HCN in N_2-CO_2-CH_4 Archean-like atmospheres). The second would complement ESTM as the end-point for the EOS radiative transfer calculations, allowing for a more specific analysis of the most interesting cases identified by the lower-complexity ESTM.

- Adapting ESTM2 to treat synchronously rotating planets by zoning the surface concentrically with respect to the substellar point, as done e.g. by Haqq-Misra & Hayworth (2022). This would allow to analyze the surface conditions (under a simplified model) of already known terrestrial-type planets such as those in the TRAPPIST-1 system.

As for the applications, some topics of interest can be:

- a reanalysis of the inner and outer edge of the HZ by using a 2D model such as ESTM rather than single-column calculations (Kopparapu et al., 2013a,b). This would allow to include the effects of important climate feedbacks that are usually ignored but fundamental to assess the actual habitability under edge conditions.

- the study of specific, newly discovered or better characterized non-tidally locked exoplanets near the edges of the habitable zone. An interesting example can be Gl 514 b (Damasso et al., 2022). The computational efficiency can play a role by providing a rapid assessment about the merit of successive, costly observational follow-ups for these bodies.

- the compilation of an open-access database of OLR and TOA albedo lookup tables to be used in a wide range of climate models. This will allow for a more consistent intercomparison between different codes by distinguishing the contribution to the final results produced by differences in climate parameters prescriptions and RT-dependent differences.

- by linking the OLR and TOA albedo database to a synthetic emission/reflectance spectra database it will be possible to bridge the gap between the capability of climate models to predict surface conditions and the detectability of specific signatures in exoplanetary atmospheres, as proposed in Section 7.3.

Acknowledgements

This work would be incomplete without acknowledging the people that made it possible. First of all my supervisor Giovanni Vladilo, whose kindness and patience are only comparable to his creativity and attention to details. These features make him the boss that everyone would like to have. But he was not the only mentor that I found at the Observatory of Trieste. I am equally grateful to Stavro Ivanovski and Laura Silva for their unflinching support and the countless teachings during these years. I also thank all the other exoplanets group members: Michele Maris, Giuseppe Murante, Sergio Monai and Erica Bisesi. They welcomed me among them and were always ready to help during this journey.

A special thanks goes to Francesca Matteucci. She guided me in my first steps in the scientific world during the Master studies and, despite not being one of her students anymore, continued to watch over me.

Finally, I want to acknowledge Giovanna Tinetti and Kevin Heng for having kindly accepted to read and review this Thesis.

Bibliography

Abbot, D. S. 2014, Journal of Climate, 27, 4391, doi: 10.1175/JCLI-D-13-00738.1

Airapetian, V. S., Glocer, A., Gronoff, G., Hébrard, E., & Danchi, W. 2016, Nature Geoscience, 9, 452, doi: 10.1038/ngeo2719

Aitta, A. 2012, Icarus, 218, 967, doi: 10.1016/j.icarus.2012.01.007

Alei, E., Konrad, B. S., Angerhausen, D., et al. 2022, arXiv e-prints, arXiv:2204.10041

Alves, F. O., Caselli, P., Girart, J. M., et al. 2019, Science, 366, 90, doi: 10.1126/science.aaw3491

Ambrose, D. 1956, Trans. Faraday Society, 52, 1536

Ananyeva, V. I., Ivanova, A. E., Venkstern, A. A., et al. 2020, Icarus, 346, 113773, doi: 10.1016/j.icarus.2020.113773

Anglada-Escudé, G., Amado, P. J., Barnes, J., et al. 2016, Nature, 536, 437, doi: 10.1038/nature19106

Anisman, L. O., Chubb, K. L., Elsey, J., et al. 2022a, JQSRT, 278, 108013, doi: 10.1016/j.jqsrt.2021.108013

Anisman, L. O., Chubb, K. L., Changeat, Q., et al. 2022b, JQSRT, 283, 108146, doi: 10.1016/j.jqsrt.2022.108146

Ansdell, M., Williams, J. P., van der Marel, N., et al. 2016, ApJ, 828, 46, doi: 10.3847/0004-637X/828/1/46

Armstrong, D., Martin, D. V., Brown, G., et al. 2013, MNRAS, 434, 3047, doi: 10.1093/mnras/stt1226

Arney, G. N., Meadows, V. S., Domagal-Goldman, S. D., et al. 2017, ApJ, 836, 49, doi: 10.3847/1538-4357/836/1/49

Artymowicz, P., & Lubow, S. H. 1994, ApJ, 421, 651, doi: 10.1086/173679

Asplund, M., Grevesse, N., Sauval, A. J., & Scott, P. 2009, Ann. Rev. Astron. Astrophys., 47, 481, doi: 10.1146/annurev.astro.46.060407.145222

Bahcall, J. N., Pinsonneault, M. H., & Basu, S. 2001, ApJ, 555, 990, doi: 10.1086/321493

Bakos, G. Á., Lázár, J., Papp, I., Sári, P., & Green, E. M. 2002, PASP, 114, 974, doi: 10.1086/342382

Ballard, S., Fabrycky, D., Fressin, F., et al. 2011, ApJ, 743, 200, doi: 10.1088/0004-637X/743/2/200

Baranov, Y. I. 2018, Journal of Molecular Spectroscopy, 345, 11, doi: 10.1016/j.jms.2017.11.005

Baranov, Y. I., Fraser, G. T., Lafferty, W. J., & Vigasin, A. A. 2003, in Weakly Interacting Molecular Pairs: Unconventional Absorbers of Radiation in the Atmosphere, ed. C. Camy-Peyret & A. A. Vigasin (Dordrecht: Springer Netherlands), 149–158

Baranov, Y. I., Lafferty, W. J., & Fraser, G. T. 2004, Journal of Molecular Spectroscopy, 228, 432, doi: 10.1016/j.jms.2004.04.010

Baranov, Y. I., & Vigasin, A. A. 1999, Journal of Molecular Spectroscopy, 193, 319, doi: 10.1006/jmsp.1998.7743

Barbosa, G. O., Winter, O. C., Amarante, A., et al. 2020, MNRAS, 494, 1045, doi: 10.1093/mnras/staa757

Barnes, J. R., Haswell, C. A., Staab, D., et al. 2020, Nature Astronomy, 4, 419, doi: 10.1038/s41550-019-0972-z

Barron, E. T., & Glorioso, R. M. 1973, in Conference Record of the 6th Annual Workshop on Microprogramming, MICRO 6 (New York, NY, USA: Association for Computing Machinery), 122–128, doi: 10.1145/800203.806247

Barry, L., Craig, G. C., & Thuburn, J. 2002, Nature, 415, 774, doi: 10.1038/415774a

Bartlett, B. C., & Stevenson, D. J. 2016, GeoRL, 43, 5716, doi: 10.1002/2016GL068912

Baudena, M., D'Andrea, F., & Provenzale, A. 2008, Water Resources Research, 44, W12429, doi: 10.1029/2008WR007172

Bazso, A., & Pilat-Lohinger, E. 2019, in EPSC-DPS Joint Meeting 2019, Vol. 2019, EPSC–DPS2019–1752

Beaulieu, J. P., Bennett, D. P., Fouqué, P., et al. 2006, Nature, 439, 437, doi: 10.1038/nature04441

Bergfors, C., Brandner, W., Janson, M., et al. 2010, A&A, 520, A54, doi: 10.1051/0004-6361/201014114

Betts, H. C., Puttick, M. N., Clark, J. W., et al. 2018, Nature Ecology and Evolution, 2, 1556, doi: 10.1038/s41559-018-0644-x

Beuermann, K., Hessman, F. V., Dreizler, S., et al. 2010, A&A, 521, L60, doi: 10.1051/0004-6361/201015472

Bezard, B., de Bergh, C., Crisp, D., & Maillard, J. P. 1990, Nature, 345, 508, doi: 10.1038/345508a0

Bills, B. G., & Ray, R. D. 1999, GeoRL, 26, 3045, doi: 10.1029/1999GL008348

Blake, R. E., Chang, S. J., & Lepland, A. 2010, Nature, 464, 1029, doi: 10.1038/nature08952

Blanksby, S. J., & Ellison, B. 2003, Acc. Chem. Res., 36, 255

Bond, I. A., Udalski, A., Jaroszyński, M., et al. 2004, ApJL, 606, L155, doi: 10.1086/420928

Borysow, A., & Frommhold, L. 1986, ApJ, 311, 1043, doi: 10.1086/164841

Bressan, A., Marigo, P., Girardi, L., et al. 2012, MNRAS, 427, 127, doi: 10.1111/j.1365-2966.2012.21948.x

Briegleb, B., & Ramanathan, V. 1982, Journal of Applied Meteorology, 21, 1160, doi: 10.1175/1520-0450(1982)021<1160:SADVIC>2.0.CO;2

Briegleb, B. P. 1992, JGRe, 97, 7603, doi: 10.1029/92JD00806

Briegleb, B. P., Minnis, P., Ramanathan, V., & Harrison, E. 1986, Journal of Applied Meteorology, 25, 214

Brogi, M., Snellen, I. A. G., de Kok, R. J., et al. 2012, Nature, 486, 502, doi: 10.1038/nature11161

Bromley, B. C., & Kenyon, S. J. 2015, ApJ, 806, 98, doi: 10.1088/0004-637X/806/1/98

Buchhave, L. A., Latham, D. W., Johansen, A., et al. 2012, Nature, 486, 375, doi: 10.1038/nature11121

Budyko, M. I. 1969, Tellus, 21, 611, doi: 10.3402/tellusa.v21i5.10109

Burch, D. E., Gryvnak, D. A., Patty, R. R., & Bartky, C. E. 1969, Journal of the Optical Society of America (1917-1983), 59, 267

Butler, R. P., & Marcy, G. W. 1996, ApJL, 464, L153, doi: 10.1086/310102

Butler, R. P., Marcy, G. W., Fischer, D. A., et al. 1999, ApJ, 526, 916, doi: 10.1086/308035

Butler, R. P., Wright, J. T., Marcy, G. W., et al. 2006, ApJ, 646, 505, doi: 10.1086/504701

Caldeira, K., & Kasting, J. F. 1992, Nature, 359, 226, doi: 10.1038/359226a0

Campbell, B., Walker, G. A. H., & Yang, S. 1988, ApJ, 331, 902, doi: 10.1086/166608

Catling, D. C., & Kasting, J. F. 2017, Atmospheric evolution of inhabited and lifeless worlds (Cambridge University Press)

Catling, D. C., & Zahnle, K. J. 2009, Scientific American, 36

—. 2020, Science Advances, 6, eaax1420, doi: 10.1126/sciadv.aax1420

Cess, R. D. 1976, Journal of Atmospheric Sciences, 33, 1831

Cess, R. D., Potter, G. L., Blanchet, J. P., et al. 1990, JGRe, 95, 16,601, doi: 10.1029/JD095iD10p16601

Chabrier, G. 2003, PASP, 115, 763, doi: 10.1086/376392

Chambers, J. E., Wetherill, G. W., & Boss, A. P. 1996, Icarus, 119, 261, doi: 10.1006/icar.1996.0019

Chandrasekar, S. 1960, Radiative Transfer (Cambridge University Press, Cambridge, UK)

Charbonneau, D., Brown, T. M., Burrows, A., & Laughlin, G. 2007, in Protostars and Planets V, ed. B. Reipurth, D. Jewitt, & K. Keil, 701

Charbonneau, D., Brown, T. M., Latham, D. W., & Mayor, M. 2000, ApJL, 529, L45, doi: 10.1086/312457

Charbonneau, D., Brown, T. M., Noyes, R. W., & Gilliland, R. L. 2002, ApJ, 568, 377, doi: 10.1086/338770

Charlson, R. J., Warren, S. G., Lovelock, J. E., & Andreae, M. O. 1987, Nature, 326, 655, doi: 10.1038/326655a0

Charney, J., Stone, P. H., & Quirk, W. J. 1975, Science, 187, 434, doi: 10.1126/science.187.4175.434

Chauvin, G., Lagrange, A. M., Dumas, C., et al. 2004, A&A, 425, L29, doi: 10.1051/0004-6361:200400056

Claire, M. W., Kasting, J. F., Domagal-Goldman, S. D., et al. 2014, Geochimica et Cosmochimica Acta, 141, 365, doi: 10.1016/j.gca.2014.06.032

Clanton, C., & Gaudi, B. S. 2016, ApJ, 819, 125, doi: 10.3847/0004-637X/819/2/125

Cleaves, H. J., Scott, A. M., Hill, F. C., et al. 2012, Chem. Soc. Rev., 41, 5502, doi: 10.1039/c2cs35112a8

Clough, S. A., Kneizys, F. X., & Davies, R. W. 1989, Atmospheric Research, 23, 229, doi: 10.1016/0169-8095(89)90020-3

Clough, S. A., Shephard, M. W., Mlawer, E. J., et al. 2005, JQSRT, 91, 233, doi: 10.1016/j.jqsrt.2004.05.058

Coakley, J. 2003, Encyclopedia of Atmospheric Sciences, doi: 10.1016/B0-12-227090-8/00069-5

Cochran, W. D., Hatzes, A. P., Endl, M., et al. 2002, in AAS/Division for Planetary Sciences Meeting Abstracts, Vol. 34, AAS/Division for Planetary Sciences Meeting Abstracts #34, 42.02

Collerson, K. D., & Kamber, B. S. 1999, Science, 283, 1519, doi: 10.1126/science.283.5407.1519

Collins, W. D., Hackney, J. K., & Edwards, D. P. 2002, Journal of Geophysical Research (Atmospheres), 107, 4664, doi: 10.1029/2001JD001365

Collins, W. D., Ramaswamy, V., Schwarzkopf, M. D., et al. 2006, Journal of Geophysical Research (Atmospheres), 111, D14317, doi: 10.1029/2005JD006713

Condie, K. C. 2000, Tectonophysics, 322, 153, doi: 10.1016/S0040-1951(00)00061-5

Correia, A. C. M., Udry, S., Mayor, M., et al. 2008, A&A, 479, 271, doi: 10.1051/0004-6361:20078908

Cresto Aleina, F., Baudena, M., D'Andrea, F., & Provenzale, A. 2013, Tellus Series B Chemical and Physical Meteorology B, 65, 17662, doi: 10.3402/tellusb.v65i0.17662

Cukier, W., Kopparapu, R. k., Kane, S. R., et al. 2019, PASP, 131, 124402, doi: 10.1088/1538-3873/ab50cb

Cumming, A., Butler, R. P., Marcy, G. W., et al. 2008, PASP, 120, 531, doi: 10.1086/588487

Cuntz, M. 2014, ApJ, 780, 14, doi: 10.1088/0004-637X/780/1/14

—. 2015, ApJ, 798, 101, doi: 10.1088/0004-637X/798/2/101

Curiel, S., Ortiz-León, G. N., Mioduszewski, A. J., & Torres, R. M. 2020, AJ, 160, 97, doi: 10.3847/1538-3881/ab9e6e

Czekala, I., Chiang, E., Andrews, S. M., et al. 2019, ApJ, 883, 22, doi: 10.3847/1538-4357/ab287b

Damasso, M., Perger, M., Almenara, J. M., et al. 2022, arXiv e-prints, arXiv:2204.06376

Dawson, R. I., & Murray-Clay, R. A. 2013, ApJL, 767, L24, doi: 10.1088/2041-8205/767/2/L24

de Vizia, M. D., Rohart, F., Castrillo, A., et al. 2011, Physical Review A, 83, 052506, doi: 10.1103/PhysRevA.83.052506

de Wit, M. J., & Furnes, H. 2016, Science Advances, 2, e1500368, doi: 10.1126/sciadv.1500368

Deitrick, R., Mendonça, J. M., Schroffenegger, U., et al. 2020, ApJS, 248, 30, doi: 10.3847/1538-4365/ab930e

Dessler, A. E., & Wong, S. 2009, Journal of Climate, 22, 6404, doi: 10.1175/2009JCLI3052.1

DeWitt, H. L., Trainer, M. G., Pavlov, A. A., et al. 2009, Astrobiology, 9, 447, doi: 10.1089/ast.2008.0289

Dhuime, B., Hawkesworth, C. J., Cawood, P. A., & Storey, C. D. 2012, Science, 335, 1334, doi: 10.1126/science.1216066

Dodd, M. S., Papineau, D., Grenne, T., et al. 2017, Nature, 543, 60, doi: 10.1038/nature21377

Doolin, S., & Blundell, K. M. 2011, MNRAS, 418, 2656, doi: 10.1111/j.1365-2966.2011.19657.x

Doyle, L. R., Carter, J. A., Fabrycky, D. C., et al. 2011, Science, 333, 1602, doi: 10.1126/science.1210923

Driese, S. G., Jirsa, M. A., Ren, M., et al. 2011, Precambrian Research, 189, 1, doi: 10.1016/j.precamres.2011.04.003

Duchêne, G., & Kraus, A. 2013, Ann. Rev. Astron. Astrophys., 51, 269, doi: 10.1146/annurev-astro-081710-102602

Dupuy, T. J., Liu, M. C., Allers, K. N., et al. 2018, AJ, 156, 57, doi: 10.3847/1538-3881/aacbc2

Duquennoy, A., & Mayor, M. 1991, A&A, 248, 485

Dvorak, R., Froeschle, C., & Froeschle, C. 1989, A&A, 226, 335

Dvorak, R., & Henrard, J. 1988, Celestial Mechanics, 43

Eggl, S., Pilat-Lohinger, E., Georgakarakos, N., Gyergyovits, M., & Funk, B. 2012, ApJ, 752, 74, doi: 10.1088/0004-637X/752/1/74

Ellis, J. S., & Haar, T. H. V. 1976, Zonal average earth radiation budget measurements from satellites for climate studies. https://mountainscholar.org/bitstream/handle/10217/87/0240_Bluebook.pdf?sequence=1

Enomoto, T. 2007, JAMSTEC Report of Research and Development, 6, doi: 10.5918/jamstecr.6.21

Etminan, M., Myhre, G., Highwood, E. J., & Shine, K. P. 2016, GeoRL, 43, 12,614, doi: 10.1002/2016GL071930

Evans, D. A., Beukes, N. J., & Kirschvink, J. L. 1997, Nature, 386, 262, doi: 10.1038/386262a0

Fairchild, I. J., & Kennedy, M. J. 2007, Journal of the Geological Society, 164, 895, doi: 10.1144/0016-76492006-191

Fels, S. B. 1979, Applied Optics, 18, 2634, doi: 10.1364/AO.18.002634

Feulner, G. 2012, Reviews of Geophysics, 50, RG2006, doi: 10.1029/2011RG000375

Fischer, D. A., & Marcy, G. W. 1992, ApJ, 396, 178, doi: 10.1086/171708

Fischer, D. A., & Valenti, J. 2005, ApJ, 622, 1102, doi: 10.1086/428383

Fleming, D. P., Barnes, R., Graham, D. E., Luger, R., & Quinn, T. R. 2018, ApJ, 858, 86, doi: 10.3847/1538-4357/aabd38

Forget, F., & Pierrehumbert, R. T. 1997, Science, 278, 1273, doi: 10.1126/science.278.5341.1273

Frierson, D. M. W., Held, I. M., & Zurita-Gotor, P. 2007, Journal of Atmospheric Sciences, 64, 1680, doi: 10.1175/JAS3913.1

Fulton, B. J., Petigura, E. A., Howard, A. W., et al. 2017, AJ, 154, 109, doi: 10.3847/1538-3881/aa80eb

Galatry, L. 1961, Physical Review, 122, 1218

Georgakarakos, N. 2006, MNRAS, 366, 566, doi: 10.1111/j.1365-2966.2005.09888.x

Georgakarakos, N., & Eggl, S. 2015, ApJ, 802, 94, doi: 10.1088/0004-637X/802/2/94

Gilliland, R. L., Chaplin, W. J., Dunham, E. W., et al. 2011, ApJS, 197, 6, doi: 10.1088/0067-0049/197/1/6

Gillon, M., Triaud, A. H. M. J., Demory, B.-O., et al. 2017, Nature, 542, 456, doi: 10.1038/nature21360

Ginzburg, S., Schlichting, H. E., & Sari, R. 2018, MNRAS, 476, 759, doi: 10.1093/mnras/sty290

Goldblatt, C., Claire, M. W., Lenton, T. M., et al. 2009, Nature Geoscience, 2, 891, doi: 10.1038/ngeo692

Goldblatt, C., Robinson, T. D., Zahnle, K. J., & Crisp, D. 2013, Nature Geoscience, 6, 661, doi: 10.1038/ngeo1892

Goldblatt, C., & Zahnle, K. J. 2011, Nature, 474, E1, doi: 10.1038/nature09961

Goldman, A., & Kyle, T. G. 1968, ApOpt, 7, 1167, doi: 10.1364/AO.7.001167

Goldreich, P., & Soter, S. 1966, Icarus, 5, 375, doi: 10.1016/0019-1035(66)90051-0

Goldschmidt, V. 1937, Journal of the Chemical Society, 655, doi: 10.1039/JR9370000655

Gómez-Leal, I., Kaltenegger, L., Lucarini, V., & Lunkeit, F. 2018, ApJ, 869, 129, doi: 10.3847/1538-4357/aaea5f

Goody, R., West, R., Chen, L., & Crisp, D. 1989, JQRST, 42, 539, doi: 10.1016/0022-4073(89)90044-7

Goody, R. M. 1964, Atmospheric Radiation (Oxford University Press, London)

Gordon, I. E., Rothman, L. S., Hill, C., et al. 2017, JQSRT, 203, 3, doi: 10.1016/j.jqsrt.2017.06.038

Gordon, I. E., Rothman, L. S., Hargreaves, R. J., et al. 2022, JQSRT, 277, 107949, doi: 10.1016/j.jqsrt.2021.107949

Gough, D. O. 1981, Solar Physics, 74, 21, doi: 10.1007/BF00151270

Greene, T. P., Line, M. R., Montero, C., et al. 2016, ApJ, 817, 17, doi: 10.3847/0004-637X/817/1/17

Grimm, S. L., & Heng, K. 2015, ApJ, 808, 182, doi: 10.1088/0004-637X/808/2/182

Grimm, S. L., Malik, M., Kitzmann, D., et al. 2021, ApJS, 253, 30, doi: 10.3847/1538-4365/abd773

Gruszka, M., & Borysow, A. 1997, Icarus, 129, 172, doi: 10.1006/icar.1997.5773

—. 1998, Molecular Physics, 93, 1007

Haghighipour, N., & Kaltenegger, L. 2013, ApJ, 777, 166, doi: 10.1088/0004-637X/777/2/166

Halevy, I., Pierrehumbert, R. T., & Schrag, D. P. 2009, Journal of Geophysical Research (Atmospheres), 114, D18112, doi: 10.1029/2009JD011915

Halliday, A. N., Wänke, H., Birck, J. L., & Clayton, R. N. 2001, Space Science Reviews, 96, 197, doi: 10.1023/A:1011997206080

Halliday, D., Resnick, R., & Walker, J. 2009, Fondamenti di Fisica (Zanichelli)

Hannula, H.-R., & Pulliainen, J. 2019, Journal of Glaciology, 65, 926

Haqq-Misra, J., & Hayworth, B. P. C. 2022, PSJ, 3, 32, doi: 10.3847/PSJ/ac49eb

Haqq-Misra, J., Wolf, E. T., Welsh, W. F., et al. 2019, Journal of Geophysical Research (Planets), 124, 3231, doi: 10.1029/2019JE006222

Haqq-Misra, J. D., Domagal-Goldman, S. D., Kasting, P. J., & Kasting, J. F. 2008, Astrobiology, 8, 1127, doi: 10.1089/ast.2007.0197

Harding, S. P. 1999, Tellus Series B Chemical and Physical Meteorology B, 51, 815, doi: 10.3402/tellusb.v51i4.16489

Harrington, R. S. 1977, AJ, 82, 753, doi: 10.1086/112121

Hart, M. H. 1978, Icarus, 33, 23, doi: 10.1016/0019-1035(78)90021-0

Hartman, Z. D., & Lépine, S. 2020, ApJS, 247, 66, doi: 10.3847/1538-4365/ab79a6

Hartmann, D. L. 2016, Global Physical Climatology (Second Edition) (Boston: Elsevier), doi: https://doi.org/10.1016/B978-0-12-328531-7.00021-9

Hartmann, D. L., Ockert-Bell, M. E., & Michelsen, M. L. 1992, Journal of Climate, 5, 1281

Haswell, C. A. 2010, Transiting Exoplanets

Hatzes, A. P. 2016, SSRev, 205, 267, doi: 10.1007/s11214-016-0246-3

Hatzes, A. P., Cochran, W. D., Endl, M., et al. 2003, ApJ, 599, 1383, doi: 10.1086/379281

Haus, R., & Arnold, G. 2010, Planetary and Space Science, 58, 1578

Haynes, H. 2017, CRC Handbook of Chemistry and Physics (CRC Press)

He, M. Y., Ford, E. B., Ragozzine, D., & Carrera, D. 2020, AJ, 160, 276

Helling, C. 2019, Annual Review of Earth and Planetary Sciences, 47, 583

Heng, K., Malik, M., & Kitzmann, D. 2018, ApJS, 237, 29, doi: 10.3847/1538-4365/aad199

Heng, K., Mendonça, J. M., & Lee, J.-M. 2014, ApJS, 215, 4, doi: 10.1088/0067-0049/215/1/4

Heng, K., Morris, B. M., & Kitzmann, D. 2021, Nature Astronomy, 5, 1001, doi: 10.1038/s41550-021-01444-7

Henry, G. W., Marcy, G. W., Butler, R. P., & Vogt, S. S. 2000, ApJL, 529, L41

Hershey, J. L. 1973, AJ, 78, 421

Heymsfield, A. J., & Platt, C. M. R. 1984, Journal of Atmospheric Sciences, 41, 846, doi: 10.1175/1520-0469(1984)041<0846:APOTPS>2.0.CO;2

Hill, C., Yurchenko, S. N., & Tennyson, J. 2013, Icarus, 226, 1673

Ho, W., Birnbaum, G., & Rosenberg, A. 1971, Journal of Chemical Physics, 55, 1028, doi: 10.1063/1.1676181

Holland, H. D. 2002, Geochim. Cosmochim. Acta, 66, 3811

Hollister, C., & Sinanoglu, O. 1966, J. Am. Chem. Soc., 153, 13

Holman, M. J., & Wiegert, P. A. 1999, AJ, 117, 621, doi: 10.1086/300695

Homann, M., Sansjofre, P., Van Zuilen, M., et al. 2018, Nature Geoscience, 11, 665, doi: 10.1038/s41561-018-0190-9

Hourdin, F., Musat, I., Bony, S., et al. 2006, Climate Dynamics, 27, 787

Hren, M. T., Tice, M. M., & Chamberlain, C. P. 2009, Nature, 462, 205, doi: 10.1038/nature08518

Hu, R., Seager, S., & Yung, Y. L. 2015, ApJ, 807, 8

Hu, Y., Yang, J., Ding, F., & Peltier, W. R. 2011, Climate of the Past, 7, 17, doi: 10.5194/cp-7-17-2011

Huang, C. J., Qiao, F. andChen, S., Xue, Y., & Guo, J. 2019, Journal of Geophysical Research: Oceans, 124, 4480–4491

Ikeda, T., & Tajika, E. 1999, GeoRL, 26, 349

Ingersoll, A. P. 1969, Journal of Atmospheric Sciences, 26, 1191

Jacob, W. S. 1855, MNRAS, 15, 228

Jang-Condell, H. 2015, ApJ, 799, 147, doi: 10.1088/0004-637X/799/2/147

Johnson, B., & Goldblatt, C. 2015, Earth Science Reviews, 148, 150, doi: 10.1016/j.earscirev.2015.05.006

Johnson, J. A., Aller, K. M., Howard, A. W., & Crepp, J. R. 2010, PASP, 122, 905

Joshi, M. M., & Haberle, R. M. 2012, Astrobiology, 12, 3, doi: 10.1089/ast.2011.0668

Jurić, M., & Tremaine, S. 2008, ApJ, 686, 603

Kaltenegger, L., & Haghighipour, N. 2013, ApJ, 777, 165, doi: 10.1088/0004-637X/777/2/165

Kane, S. R., & Hinkel, N. R. 2013, ApJ, 762, 7, doi: 10.1088/0004-637X/762/1/7

Kanzaki, Y., & Murakami, T. 2015, Geochimica et Cosmochimica Acta, 159, 190, doi: 10.1016/j.gca.2015.03.011

Karman, T., Koenis, M. A. J., Banerjee, A., et al. 2018, Nature Chemistry, 10, 549, doi: 10.1038/s41557-018-0015-x

Karman, T., Gordon, I. E., van der Avoird, A., et al. 2019, Icarus, 328, 160, doi: 10.1016/j.icarus.2019.02.034

Kasting, J. F. 1982, JGRe, 87, 3091, doi: 10.1029/JC087iC04p03091

—. 1988, Icarus, 74, 472

—. 1991, Icarus, 94, 1

Kasting, J. F., Eggler, D. H., & Raeburn, S. P. 1993a, Journal of Geology, 101, 245, doi: 10.1086/648219

Kasting, J. F., Pollack, J. B., & Ackerman, T. P. 1984a, Icarus, 57, 335, doi: 10.1016/0019-1035(84)90122-2

Kasting, J. F., Pollack, J. B., & Crisp, D. 1984b, Journal of Atmospheric Chemistry, 1, 403

Kasting, J. F., Whitmire, D. P., & Reynolds, R. T. 1993b, Icarus, 101, 108

Kasting, J. F., Zahnle, K. J., Pinto, J. P., & Young, A. T. 1989, Origins of Life and Evolution of the Biosphere, 19, 95, doi: 10.1007/BF01808144

Keles, E., Grenfell, J. L., Godolt, M., Stracke, B., & Rauer, H. 2018, Astrobiology, 18, 116, doi: 10.1089/ast.2016.1632

Kharecha, P., Kasting, J., & Siefert, J. 2005, Geobiology, 3, 53, doi: https://doi.org/10.1111/j.1472-4669.2005.00049.x

Kiehl, J. T., Hack, J. J., Bonan, G. B., et al. 1998, Journal of Climate, 11, 1131

King, L. V. 1923, Proceedings of the Royal Society of London Series A, 104, 333, doi: 10.1098/rspa.1923.0113

King, M. D., Platnick, S., Menzel, W. P., Ackerman, S. A., & Hubanks, P. A. 2013, IEEE Transactions on Geoscience and Remote Sensing, 51, 3826, doi: 10.1109/TGRS.2012.2227333

Kipping, D. M. 2013, MNRAS, 434, L51

Kirchner, J. W. 2002, Climate Change, 52, 391

Kirk, B., Conroy, K., Prša, A., et al. 2016, AJ, 151, 68, doi: 10.3847/0004-6256/151/3/68

Kirschvink, J. R. 1992, in The Proterozoic Biosphere: a Multidisciplinary Study, ed. J. W. Schopf & C. Klein (Cambridge University Press), 51–52

Kislyakova, K. G., Holmström, M., Lammer, H., Odert, P., & Khodachenko, M. L. 2014, Science, 346, 981

Kitzmann, D. 2016, ApJL, 817, L18, doi: 10.3847/2041-8205/817/2/L18

—. 2017, A&A, 600, A111, doi: 10.1051/0004-6361/201630029

Kitzmann, D., Patzer, A. B. C., von Paris, P., Godolt, M., & Rauer, H. 2011a, A&A, 531, A62, doi: 10.1051/0004-6361/201014343

Kitzmann, D., Patzer, A. B. C., von Paris, P., Godolt, M., & Rauer, H. 2011b, A&A, 534, A63, doi: 10.1051/0004-6361/201117375

Kitzmann, D., Patzer, A. B. C., & Rauer, H. 2013, A&A, 557, A6, doi: 10.1051/0004-6361/201220025

Kitzmann, D., Patzer, A. B. C., von Paris, P., et al. 2010, A&A, 511, A66, doi: 10.1051/0004-6361/200913491

Knauth, L. P., & Lowe, D. R. 2003, Geological Society of America Bulletin, 115, 566

Kochanov, R. V., Gordon, I. E., Rothman, L. S., et al. 2016, JQSRT, 177, 15, doi: 10.1016/j.jqsrt.2016.03.005

Kokaly, R. F., Clark, R. N., Swayze, G. A., et al. 2017, USGS Spectral Library Version 7, Tech. Rep. US Geological Survey Data Series 1035, United States Department of the Interior, Reston, Virginia (USA)

Kokhanovsky, A. A. 2006, Cloud Optics (Dordrecht: Springer)

Koll, D. D. B., & Cronin, T. W. 2018, Proceedings of the National Academy of Science, 115, 10293, doi: 10.1073/pnas.1809868115

Komabayashi, M. 1967, Journal of the Meteorological Society of Japan, 45, 137

Konacki, M., & Wolszczan, A. 2003, ApJL, 591, L147

Konrad, B. S., Alei, E., Angerhausen, D., et al. 2021, arXiv e-prints, arXiv:2112.02054

Kopparapu, R. K., Ramirez, R., Kasting, J. F., et al. 2013a, ApJ, 765, 131

—. 2013b, ApJ, 770, 82

Kostov, V. B., McCullough, P. R., Carter, J. A., et al. 2014a, ApJ, 784, 14, doi: 10.1088/0004-637X/784/1/14

—. 2014b, ApJ, 787, 93, doi: 10.1088/0004-637X/787/1/93

Kostov, V. B., Orosz, J. A., Welsh, W. F., et al. 2016, ApJ, 827, 86, doi: 10.3847/0004-637X/827/1/86

Kostov, V. B., Orosz, J. A., Feinstein, A. D., et al. 2020, AJ, 159, 253, doi: 10.3847/1538-3881/ab8a48

Kouwenhoven, M. B. N., Brown, A. G. A., Portegies Zwart, S. F., & Kaper, L. 2007, A&A, 474, 77, doi: 10.1051/0004-6361:20077719

Kramida, A., Yu. Ralchenko, Reader, J., & and NIST ASD Team. 2019, NIST Atomic Spectra Database (ver. 5.7.1), [Online]. Available: https://physics.nist.gov/asd [2020, July 22]. National Institute of Standards and Technology, Gaithersburg, MD.

Kraus, A. L., Ireland, M. J., Huber, D., Mann, A. W., & Dupuy, T. J. 2016, AJ, 152, 8

Krissansen-Totton, J., Arney, G. N., & Catling, D. C. 2018, Proceedings of the National Academy of Science, 115, 4105, doi: 10.1073/pnas.1721296115

Kuell, V., Offermann, D., Jarisch, M., et al. 2005, JGRe, 110, D16104

Kunii, M., Shoji, Y., Ueno, M., & Saito, K. 2010, Journal of the Meteorological Society of Japan, 88, 455

Kunimoto, M., & Matthews, J. M. 2020, AJ, 159, 248

Kurokawa, H., & Nakamoto, T. 2014, ApJ, 783, 54

Kurucz, R. L., & Bell, B. 1995, Kurucz CD-ROM No. 23. Available online: https://lweb.cfa.harvard.edu/amp/ampdata/kurucz23/sekur.html [2022, Aug 06]. Smithsonian Astrophysical Observatory, Cambridge, Mass.

Lacis, A. A., & Oinas, V. 1991, JGRe, 96, 9027

Lahav, N., White, D., & Chang, S. 1978, Science, 201, 67, doi: 10.1126/science.663639

Le Doucen, R., Cousin, C., Boulet, C., & Henry, A. 1985, ApOpt, 24, 897, doi: 10.1364/AO.24.000897

Le Hir, G., Donnadieu, Y., Krinner, G., & Ramstein, G. 2010, Climate Dynamics, 35, 285, doi: 10.1007/s00382-010-0748-8

Leconte, J., Forget, F., Charnay, B., et al. 2013, A&A, 554, A69

Léger, A., Grasset, O., Fegley, B., et al. 2011, Icarus, 213, 1

Lehmer, O. R., Catling, D. C., Buick, R., Brownlee, D. E., & Newport, S. 2020, Science Advances, 6, eaay4644, doi: 10.1126/sciadv.aay4644

Lenton, T. M., & Lovelock, J. E. 2001, Tellus Series B Chemical and Physical Meteorology B, 53, 288

Limbach, M. A., & Turner, E. L. 2015, Proceedings of the National Academy of Science, 112, 20

Lin, S.-J., & Rood, R. B. 1996, Monthly Weather Review, 124, 2046

Lindegren, L., Hernández, J., Bombrun, A., et al. 2018, A&A, 616, A2, doi: 10.1051/0004-6361/201832727

Line, M. R., Wolf, A. S., Zhang, X., et al. 2013, ApJ, 775, 137, doi: 10.1088/0004-637X/775/2/137

Lippincott, S. L. 1960, AJ, 65, 445

Loeb, N. G., Doelling, D. R., Wang, H., et al. 2018, Journal of Climate, 31, 895, doi: 10.1175/JCLI-D-17-0208.1

Love, A. E. H. 1909, Proceedings of the Royal Society of London Series A, 82, 73, doi: 10.1098/rspa.1909.0008

Lovelock, J. E., & Margulis, L. 1974a, Origins of Life, 5, 93, doi: 10.1007/BF00927016

—. 1974b, Tellus, 26, 2, doi: 10.3402/tellusa.v26i1-2.9731

Lubin, P. 2016, Journal of the British Interplanetary Society, 69, 40

Lustig-Yaeger, J., Meadows, V. S., Tovar Mendoza, G., et al. 2018, AJ, 156, 301, doi: 10.3847/1538-3881/aaed3a

Lyons, T. W., Reinhard, C. T., & Planavsky, N. J. 2014, Nature, 506, 307

Ma, Q., Tipping, R. H., Boulet, C., & Bouanich, J.-P. 1999, Applied Optics, 38, 599

MacDonald, G. J. F. 1964, Reviews of Geophysics and Space Physics, 2, 467, doi: 10.1029/RG002i003p00467

Madhusudhan, N., Harrington, J., Stevenson, K. B., et al. 2011, Nature, 469, 64, doi: 10.1038/nature09602

Makarov, V. V., Beichman, C. A., Catanzarite, J. H., et al. 2009, ApJL, 707, L73

Malik, M., Kitzmann, D., Mendonça, J. M., et al. 2019a, AJ, 157, 170

Malik, M., Kempton, E. M. R., Koll, D. D. B., et al. 2019b, ApJ, 886, 142, doi: 10.3847/1538-4357/ab4a05

Malik, M., Grosheintz, L., Mendonça, J. M., et al. 2017, AJ, 153, 56

Manabe, S., & Möller, F. 1961, Monthly Weather Review, 89, 503

Manabe, S., & Strickler, R. F. 1964, Journal of Atmospheric Sciences, 21, 361, doi: 10.1175/1520-0469(1964)021<0361:TEOTAW>2.0.CO;2

Mandushev, G., O'Donovan, F. T., Charbonneau, D., et al. 2007, ApJL, 667, L195

Marcy, G., Butler, R. P., Fischer, D., et al. 2005, Progress of Theoretical Physics Supplement, 158, 24

Marois, C., Macintosh, B., Barman, T., et al. 2008, Science, 322, 1348

Martin, D. V. 2018, in Handbook of Exoplanets, ed. H. J. Deeg & J. A. Belmonte, 156, doi: 10.1007/978-3-319-55333-7_156

—. 2020, Contributions of the Astronomical Observatory Skalnate Pleso, 50, 463, doi: 10.31577/caosp.2020.50.2.463

Martin, D. V., Mazeh, T., & Fabrycky, D. C. 2015, MNRAS, 453, 3554, doi: 10.1093/mnras/stv1870

Marty, B., Zimmermann, L., Pujol, M., Burgess, R., & Philippot, P. 2013, Science, 342, 101, doi: 10.1126/science.1240971

Mason, P. A., Zuluaga, J. I., Clark, J. M., & Cuartas-Restrepo, P. A. 2013, ApJL, 774, L26, doi: 10.1088/2041-8205/774/2/L26

Mason, P. A., Zuluaga, J. I., Cuartas-Restrepo, P. A., & Clark, J. M. 2015, International Journal of Astrobiology, 14, 391, doi: 10.1017/S1473550414000342

Masson-Delmotte, V., Zhai, P., Pirani, A., et al. 2021, Climate Change 2021: The Physical Science Basis. Contribution to Working Group I of the Sixth Assessment Report of the Intergovernmental Panel of Climate Change (Cambridge, UK: Cambridge University Press)

Matteucci, F. 2012, Chemical Evolution of Galaxies (Springer Berlin, Heidelberg), doi: 10.1007/978-3-642-22491-1

May, E. M., & Rauscher, E. 2016, ApJ, 826, 225, doi: 10.3847/0004-637X/826/2/225

Mayor, M., & Queloz, D. 1995, Nature, 378, 355

Mayor, M., Pepe, F., Queloz, D., et al. 2003, The Messenger, 114, 20

Mazeh, T., Holczer, T., & Faigler, S. 2016, A&A, 589, A75

McClatchey, R. A., Fenn, R. W., Selby, J. E. A., Volz, E., & Garing, J. S. 1971, Optical properties of the atmosphere, Tech. Rep. AFCRL-71-0279, Air Force Geophysical Laboratory, Bedford, MA

Meadows, V. S., & Crisp, D. 1996, JGRe, 101, 4595, doi: 10.1029/95JE03567

Mendonça, J. M., Grimm, S. L., Grosheintz, L., & Heng, K. 2016, ApJ, 829, 115

Mihalas, D. 1970, Stellar atmospheres (Freeman, San Francisco)

Mlawer, E. J., Payne, V. H., Moncet, J. L., et al. 2012, Philosophical Transactions of the Royal Society of London Series A, 370, 2520

Moe, M., & Di Stefano, R. 2017, ApJS, 230, 15, doi: 10.3847/1538-4365/aa6fb6

Moe, M., & Kratter, K. M. 2019, arXiv e-prints, arXiv:1912.01699. https://arxiv.org/abs/1912.01699

Moncet, J. L., & Clough, S. A. 1997, JGRe, 102, 21,853, doi: 10.1029/97JD01551

Moore, J. F. 1971, Infrared absorption of Carbon Dioxide at High Densities with Application to the Atmosphere of Venus, Tech. Rep. Technical Report X-630-72-48, NASA Goddard Space Flight Center, Greenbelt, MD

Mordasini, C. 2018, Planetary Population Synthesis, ed. H. J. Deeg & J. A. Belmonte, 143

Morgan, J. W., & Anders, E. 1980, Proceedings of the National Academy of Science, 77, 6973, doi: 10.1073/pnas.77.12.6973

Mróz, P., Poleski, R., Gould, A., et al. 2020, ApJL, 903, L11

Mugrauer, M., & Neuhäuser, R. 2009, A&A, 494, 373, doi: 10.1051/0004-6361:200810639

Mulders, G. D., Pascucci, I., & Apai, D. 2015, ApJ, 814, 130

Murante, G., Provenzale, A., Vladilo, G., et al. 2020, MNRAS, 492, 2638

Murphy, W. F. 1977, Journal of Chemical Physics, 67, 5877, doi: 10.1063/1.434794

Murray, C. D., & Dermott, S. F. 1999, Solar System Dynamics (Cambridge, UK: Cambridge University Press)

Muterspaugh, M. W., Lane, B. F., Kulkarni, S. R., et al. 2010, AJ, 140, 1657

Myhre, G., Highwood, E. J., Shine, K. P., & Stordal, F. 1998, GeoRL, 25, 2715, doi: 10.1029/98GL01908

Nakajima, S., Hayashi, Y.-Y., & Abe, Y. 1992, Journal of Atmospheric Sciences, 49, 2256

Navarro-González, R., McKay, C. P., & Mvondo, D. N. 2001, Nature, 412, 61

Neshyba, S. P., Grenfell, T. C., & Warren, S. G. 2003, JGRe, 108, 4448, doi: 10.1029/2002JD003302

Ngo, N. H., Lisak, D., Tran, H., & Hartmann, J. M. 2013, JQSRT, 129, 89

North, G. R., & Coakley, James A., J. 1979, Journal of Atmospheric Sciences, 36, 1189

North, G. R., Short, D. A., & Mengel, J. G. 1983, JGRe, 88, 6576

Ohtomo, Y., Kakegawa, T., Ishida, A., Nagase, T., & Rosing, M. T. 2014, Nature Geoscience, 7, 25, doi: 10.1038/ngeo2025

O'Neill, C., & Lenardic, A. 2007, GeoRL, 34, L19204, doi: 10.1029/2007GL030598

Orosz, J. A., Welsh, W. F., Carter, J. A., et al. 2012a, Science, 337, 1511, doi: 10.1126/science.1228380

—. 2012b, ApJ, 758, 87, doi: 10.1088/0004-637X/758/2/87

Otegi, J. F., Bouchy, F., & Helled, R. 2020, A&A, 634, A43

Owen, J. E., & Lai, D. 2018, MNRAS, 479, 5012

Owen, J. E., & Murray-Clay, R. 2018, MNRAS, 480, 2206

Owen, T., Cess, R. D., & Ramanathan, V. 1979, Nature, 277, 640, doi: 10.1038/277640a0

Park, K.-T., Yoon, Y. J., Lee, K., et al. 2021, Global Biogeochemical Cycles, 35, e06969

Paynter, D. J., & Ramaswamy, V. 2011, Journal of Geophysical Research (Atmospheres), 116, D20302

Peña Ramírez, K., Béjar, V. J. S., Zapatero Osorio, M. R., Petr-Gotzens, M. G., & Martín, E. L. 2012, ApJ, 754, 30

Perrin, M. Y., & Hartmann, J. M. 1989, JQSRT, 42, 311

Pierrehumbert, R. T. 2005, Journal of Geophysical Research (Atmospheres), 110, D01111

—. 2010, Principles of Planetary Climate (Dover)

Pierrehumbert, R. T., Brogniez, H., & Roca, R. 2007, in The Global Circulation of the Atmosphere, ed. T. Schneider & A. H. Sobel (Princeton University Press, Princeton (NJ)), 143–185

Pilat-Lohinger, E., Eggl, S., & Bazsó, Á. 2019, Planetary Habitability in Binary Systems, doi: 10.1142/11125

Pirazzini, R., Vihma, T., Granskog, M. A., & Cheng, B. 2006, Annals of Glaciology, 44, 7, doi: 10.3189/172756406781811565

Pollacco, D. L., Skillen, I., Collier Cameron, A., et al. 2006, PASP, 118, 1407

Pollack, J. B., Toon, O. B., & Boese, R. 1980, JGRe, 85, 8223

Pollack, J. B., Dalton, J. B., Grinspoon, D., et al. 1993, Icarus, 103, 1

Popp, M., & Eggl, S. 2017, Nature Communications, 8, 14957, doi: 10.1038/ncomms14957

Ptashnik, I. V., Shine, K. P., & Vigasin, A. A. 2011, JQSRT, 112, 1286

Quanz, S. P., Ottiger, M., Fontanet, E., et al. 2021, arXiv e-prints, arXiv:2101.07500

Quarles, B., Li, G., Kostov, V., & Haghighipour, N. 2020, AJ, 159, 80, doi: 10.3847/1538-3881/ab64fa

Quarles, B., Li, G., & Lissauer, J. J. 2019, ApJ, 886, 56, doi: 10.3847/1538-4357/ab46b5

Quarles, B., Satyal, S., Kostov, V., Kaib, N., & Haghighipour, N. 2018, ApJ, 856, 150, doi: 10.3847/1538-4357/aab264

Queloz, D., Mayor, M., Weber, L., et al. 2000, A&A, 354, 99

Quintana, E. V., Adams, F. C., Lissauer, J. J., & Chambers, J. E. 2007, ApJ, 660, 807, doi: 10.1086/512542

Quintana, E. V., & Lissauer, J. J. 2006, Icarus, 185, 1, doi: 10.1016/j.icarus.2006.06.016

Quintana, E. V., Barclay, T., Raymond, S. N., et al. 2014, Science, 344, 277

Rabl, G., & Dvorak, R. 1988, A&A, 191, 385

Rafikov, R. R., & Silsbee, K. 2015a, ApJ, 798, 70, doi: 10.1088/0004-637X/798/2/70

—. 2015b, ApJ, 798, 69, doi: 10.1088/0004-637X/798/2/69

Raghavan, D., Henry, T. J., Mason, B. D., et al. 2006, ApJ, 646, 523, doi: 10.1086/504823

Raghavan, D., McAlister, H. A., Henry, T. J., et al. 2010, ApJS, 190, 1, doi: 10.1088/0067-0049/190/1/1

Ramirez, R. M., & Kaltenegger, L. 2017, ApJL, 837, L4, doi: 10.3847/2041-8213/aa60c8

—. 2018, ApJ, 858, 72, doi: 10.3847/1538-4357/aab8fa

Rap, A., Scott, C. E., Spracklen, D. V., et al. 2013, GeoRL, 40, 3297

Rautian, S. G., & Sobel'man, I. I. 1967, Soviet Physics Uspekhi, 9, 701

Reid, I. N., & Gizis, J. E. 1997, AJ, 114, 1992, doi: 10.1086/118620

Rhines, P. B. 1979, Annual Review of Fluid Mechanics, 11, 401

Richard, F. J. 1959, Journ. of Experimental Botany, 10, 290

Richardson, L. J., Deming, D., Horning, K., Seager, S., & Harrington, J. 2007, Nature, 445, 892

Robinson, T. D., & Catling, D. C. 2014, Nature Geoscience, 7, 12

Rodgers, C. D., & Walshaw, C. D. 1966, Quarterly Journal of the Royal Meteorological Society, 92, 67, doi: 10.1002/qj.49709239107

Roell, T., Neuhäuser, R., Seifahrt, A., & Mugrauer, M. 2012, A&A, 542, A92, doi: 10.1051/0004-6361/201118051

Rollinson, H. R. 2007, Early Earth Systems: A Geochemical Approach (Wiley-Blackwell)

Rondanelli, R., & Lindzen, R. S. 2010, JGRe, 115, D02108, doi: 10.1029/2009JD012050

Rosing, M. T. 1999, Science, 283, 674, doi: 10.1126/science.283.5402.674

Rosing, M. T., Bird, D. K., Sleep, N. H., & Bjerrum, C. J. 2010, Nature, 464, 744, doi: 10.1038/nature08955

Rothman, L. S., Jacquemart, D., Barbe, A., et al. 2005, JQSRT, 96, 139

Rothman, L. S., Gordon, I. E., Barbe, A., et al. 2009, JQSRT, 110, 533

Rothman, L. S., Gordon, I. E., Barber, R. J., et al. 2010, JQSRT, 111, 2139

Rugheimer, S., & Kaltenegger, L. 2018, ApJ, 854, 19, doi: 10.3847/1538-4357/aaa47a

Russell, C. T., Raymond, C. A., Coradini, A., et al. 2012, Science, 336, 684, doi: 10.1126/science.1219381

Ryabchikova, T., Piskunov, N., Kurucz, R. L., et al. 2015, Physica Scripta, 90, 054005, doi: 10.1088/0031-8949/90/5/054005

Rye, R., Kuo, P. H., & Holland, H. D. 1995, Nature, 378, 603, doi: 10.1038/378603a0

Sagan, C., & Mullen, G. 1972, Science, 177, 52, doi: 10.1126/science.177.4043.52

Sagan, C., Thompson, W. R., Carlson, R., Gurnett, D., & Hord, C. 1993, Nature, 365, 715, doi: 10.1038/365715a0

Sahlmann, J., Ségransan, D., Queloz, D., & Udry, S. 2011, in The Astrophysics of Planetary Systems: Formation, Structure, and Dynamical Evolution, ed. A. Sozzetti, M. G. Lattanzi, & A. P. Boss, Vol. 276, 117–120

Salpeter, E. E. 1955, ApJ, 121, 161, doi: 10.1086/145971

Sanders, J., & Kandrot, E. 2010, CUDA by Example: An Introduction to General-Purpose GPU Programming (Addison-Wesley, Indianapolis (IN))

Sanromá, E., & Pallé, E. 2012, ApJ, 744, 188

Santerne, A., Hébrard, G., Deleuil, M., et al. 2014, A&A, 571, A37, doi: 10.1051/0004-6361/201424158

Schiebener, P., Straub, J., Levelt Sengers, J. M. H., & Gallagher, J. S. 1990, Journal of Physical and Chemical Reference Data, 19, 677, doi: 10.1063/1.555859

Schneider, J., Dedieu, C., Le Sidaner, P., Savalle, R., & Zolotukhin, I. 2011, A&A, 532, A79

Schopf, J. W. 1993, Science, 260, 640, doi: 10.1126/science.260.5108.640

Schwarz, R., Bazsó, Á., Érdi, B., & Funk, B. 2012, MNRAS, 427, 397, doi: 10.1111/j.1365-2966.2012.21986.x

Schwarz, R., Funk, B., Zechner, R., & Bazsó, Á. 2016, MNRAS, 460, 3598, doi: 10.1093/mnras/stw1218

Seager, S., Turner, E. L., Schafer, J., & Ford, E. B. 2005, Astrobiology, 5, 372, doi: 10.1089/ast.2005.5.372

See, T. J. J. 1896, AJ, 16, 17

Seidel, D. J., Ross, R. J., Angell, J. K., & Reid, G. C. 2001, JGRe, 106, 7857

Sellers, W. D. 1969, Journal of Applied Meteorology, 8, 392

Selsis, F., Kasting, J. F., Levrard, B., et al. 2007, A&A, 476, 1373, doi: 10.1051/0004-6361:20078091

Serov, E. A., Koshelev, M. A., Odintsova, T. A., Parshin, V. V., & Tretyakov, M. Y. 2014, Physical Chemistry Chemical Physics (Incorporating Faraday Transactions), 16, 26221, doi: 10.1039/C4CP03252G

Shah, O., Helled, R., Alibert, Y., & Mezger, K. 2022, ApJ, 926, 217, doi: 10.3847/1538-4357/ac410d

Sheldon, N. D. 2006, Precambrian Research, 147, 148, doi: 10.1016/j.precamres.2006.02.004

Shen, Y., & Turner, E. L. 2008, ApJ, 685, 553

Shevchenko, I. I. 2017, AJ, 153, 273, doi: 10.3847/1538-3881/aa71b2

Shields, A. L., Bitz, C. M., Meadows, V. S., Joshi, M. M., & Robinson, T. D. 2014, ApJL, 785, L9

Shields, A. L., Meadows, V. S., Bitz, C. M., et al. 2013, Astrobiology, 13, 715

Shine, K. P., Campargue, A., Mondelain, D., et al. 2016, Journal of Molecular Spectroscopy, 327, 193

Shukla, P. R., Skea, J., Slade, R., et al. 2019, Climate Change and Land: an IPCC special report on climate change, desertification, land degradation, sustainable land management, food security, and greenhouse gas fluxes in terrestrial ecosystems, Tech. Rep. IPCC-AR6, Intergovernmental Panel on Climate Change, Geneva, CH

Sillen, L. G. 1966, Tellus, 18, 198, doi: 10.3402/tellusa.v18i2-3.9681

Silsbee, K., & Rafikov, R. R. 2015, ApJ, 798, 71, doi: 10.1088/0004-637X/798/2/71

Silva, L., Vladilo, G., Murante, G., & Provenzale, A. 2017, MNRAS, 470, 2270

Silvotti, R., Schuh, S., Janulis, R., et al. 2007, Nature, 449, 189

Simonetti, P., Vladilo, G., Silva, L., & Sozzetti, A. 2020, ApJ, 903, 141

Simpson, G. C. 1927, Quarterly Journal of the Royal Meteorological Society, 53, 213

Sneep, M., & Ubachs, W. 2005, JQSRT, 92, 293, doi: 10.1016/j.jqsrt.2004.07.025

Snellen, I. A. G., de Kok, R. J., de Mooij, E. J. W., & Albrecht, S. 2010, Nature, 465, 1049

Soboczenski, F., Himes, M. D., O'Beirne, M. D., et al. 2018, arXiv e-prints, arXiv:1811.03390

Socia, Q. J., Welsh, W. F., Orosz, J. A., et al. 2020, AJ, 159, 94, doi: 10.3847/1538-3881/ab665b

Soden, B. J., & Held, I. M. 2006, Journal of Climate, 19, 3354

Som, S. M., Buick, R., Hagadorn, J. W., et al. 2016, Nature Geoscience, 9, 448, doi: 10.1038/ngeo2713

Som, S. M., Catling, D. C., Harnmeijer, J. P., Polivka, P. M., & Buick, R. 2012, Nature, 484, 359, doi: 10.1038/nature10890

Spalding, C., & Fischer, W. W. 2019, Earth and Planetary Science Letters, 514, 28, doi: 10.1016/j.epsl.2019.02.032

Span, R., & Wagner, W. 1996, Journal of Physical and Chemical Reference Data, 25, 1509

Spencer, H. 1844, London Edinburgh Dublin Phil. Magazine and J. Science, 24, 90

Spiegel, D. S., Burrows, A., & Milsom, J. A. 2011, ApJ, 727, 57

Stamnes, K., Tsay, S. C., Jayaweera, K., & Wiscombe, W. 1988, ApOpt, 27, 2502, doi: 10.1364/AO.27.002502

Stephens, G. L., Li, J., Wild, M., et al. 2012, Nature Geoscience, 5, 691

Stepinski, T. F., & Black, D. C. 2001, A&A, 371, 250, doi: 10.1051/0004-6361:20010357

Stevenson, D. J. 1999, Nature, 400, 32

Strand, K. A. 1957, AJ, 62, 35

Stringer, W., & Groves, J. 1991, ARCTIC, 44, doi: 10.14430/arctic1583

Stubenrauch, C. J., Rossow, W. B., Kinne, S., et al. 2013, Bulletin of the American Meteorological Society, 94, 1031

Suissa, G., Wolf, E. T., Kopparapu, R. k., et al. 2020, AJ, 160, 118

Swain, M. R., Deroo, P., Griffith, C. A., et al. 2010, Nature, 463, 637, doi: 10.1038/nature08775

Szabó, G. M., & Kiss, L. L. 2011, ApJL, 727, L44

Taylor, S. R., & McLennan, S. 2009, Planetary Crusts: Their Composition, Origin and Evolution, doi: 10.1017/CBO9780511575358

Teitler, Y., Le Hir, G., Fluteau, F., Philippot, P., & Donnadieu, Y. 2014, Earth and Planetary Science Letters, 395, 71

Telegadas, K., & London, J. 1954, A physical model for Northern Hemisphere troposphere for winter and summer, Tech. Rep. AF19(122)-165, College of Engineering, New York University, New York, NY

Tennyson, J., Yurchenko, S. N., Al-Refaie, A. F., et al. 2020, JQSRT, 255, 107228, doi: 10.1016/j.jqsrt.2020.107228

Thalman, R., Zarzana, K. J., Tolbert, M. A., & Volkamer, R. 2014, JQSRT, 147, 171, doi: 10.1016/j.jqsrt.2014.05.030

Thebault, P., & Haghighipour, N. 2015, in Planetary Exploration and Science: Recent Results and Advances, 309–340, doi: 10.1007/978-3-662-45052-9_13

Thompson, M. A., Krissansen-Totton, J., Wogan, N., Telus, M., & Fortney, J. J. 2022, PNAS, 119, 10, doi: 10.1073/pnas.2117933119

Thompson, S. L., & Barron, E. J. 1981, Journal of Geology, 89, 143

Tian, F., Kasting, J. F., & Zahnle, K. 2011, Earth and Planetary Science Letters, 308, 417, doi: 10.1016/j.epsl.2011.06.011

Tinetti, G., Encrenaz, T., & Coustenis, A. 2013, A&A Review, 21, 63, doi: 10.1007/s00159-013-0063-6

Tinetti, G., Meadows, V. S., Crisp, D., et al. 2006a, Astrobiology, 6, 34, doi: 10.1089/ast.2006.6.34

Tinetti, G., Meadows, V. S., Crisp, D., et al. 2006b, Astrobiology, 6, 881, doi: 10.1089/ast.2006.6.881

Tinetti, G., Liang, M.-C., Vidal-Madjar, A., et al. 2007, ApJL, 654, L99

Tokovinin, A. 2014, AJ, 147, 87, doi: 10.1088/0004-6256/147/4/87

Tonkov, M. V., Filippov, N. N., Bertsev, V. V., et al. 1996, Applied Optics, 35, 4863

Toon, O. B., McKay, C. P., Ackerman, T. P., & Santhanam, K. 1989, JGRe, 94, 16287

Trail, D., Watson, E. B., & Tailby, N. D. 2011, Nature, 480, 79, doi: 10.1038/nature10655

Trainer, M. G., Pavlov, A. A., Dewitt, H. L., et al. 2006, Proceedings of the National Academy of Science, 103, 18035, doi: 10.1073/pnas.0608561103

Tran, H., Auwera, J. V., Bertin, T., et al. 2022, Icarus, 384, 115093, doi: 10.1016/j.icarus.2022.115093

Tremaine, S., & Dong, S. 2012, AJ, 143, 94

Trenberth, K. E., & Caron, J. M. 2001, Journal of Climate, 14, 3433

Tretyakov, M. Y., Serov, E. A., Koshelev, M. A., Parshin, V. V., & Krupnov, A. F. 2013, Physical Review Letters, 110, 093001

Trilling, D. E., Stansberry, J. A., Stapelfeldt, K. R., et al. 2007, ApJ, 658, 1289, doi: 10.1086/511668

Tsai, S.-M., Lyons, J. R., Grosheintz, L., et al. 2017, ApJS, 228, 20, doi: 10.3847/1538-4365/228/2/20

Turbet, M., Bolmont, E., Chaverot, G., et al. 2021, Nature, 598, 276, doi: 10.1038/s41586-021-03873-w

Turbet, M., Boulet, C., & Karman, T. 2020, Icarus, 346, 113762, doi: 10.1016/j.icarus.2020.113762

Turbet, M., Tran, H., Pirali, O., et al. 2019, Icarus, 321, 189, doi: 10.1016/j.icarus.2018.11.021

Udry, S., Mayor, M., & Santos, N. C. 2003, A&A, 407, 369

Valencia, D., O'Connell, R. J., & Sasselov, D. D. 2007, ApJL, 670, L45, doi: 10.1086/524012

van de Kamp, P. 1963, AJ, 68, 515

—. 1969, AJ, 74, 238

Van Eylen, V., Agentoft, C., Lundkvist, M. S., et al. 2018, MNRAS, 479, 4786

Van Eylen, V., & Albrecht, S. 2015, ApJ, 808, 126

van Vleck, J. H., & Weisskopf, V. F. 1945, Reviews of Modern Physics, 17, 227, doi: 10.1103/RevModPhys.17.227

Vigasin, A. A. 2014, JQSRT, 148, 58

Vladilo, G., Murante, G., Silva, L., et al. 2013, ApJ, 767, 65

Vladilo, G., Silva, L., Murante, G., Filippi, L., & Provenzale, A. 2015, ApJ, 804, 50

Vukalovich, M., & Altunin, V. 1968, Thermophysical properties of Carbon Dioxide (Collet's Publ. Ltd, London)

Wagner, W., & Kretzschmar, H.-J. 2008, International Steam Tables - Properties of Water and Steam based on the Industrial Formulation IAPWS-IF97 (Springer Verlag Berlin Heidelberg)

Wahl, S. M., Wilson, H. F., & Militzer, B. 2013, ApJ, 773, 95

Waldmann, I. P., Tinetti, G., Drossart, P., et al. 2012, ApJ, 744, 35, doi: 10.1088/0004-637X/744/1/35

Walker, J. C. G. 1982, Palaeogeography Palaeoclimatology Palaeoecology, 40, 1, doi: 10.1016/0031-0182(82)90082-7

Wang, Z., & Cuntz, M. 2017, AJ, 154, 157, doi: 10.3847/1538-3881/aa8621

Warwick, N., Griffiths, P., Keeble, J., et al. 2022, Atmospheric implications of increased Hydrogen use, Tech. Rep. 00, United Kingdom Department of Business, Energy and Industrial Strategy, London, UK

Watson, A. J., & Lovelock, J. E. 1983, Tellus Series B Chemical and Physical Meteorology B, 35, 284

Welsh, W. F., Orosz, J. A., Carter, J. A., et al. 2012, Nature, 481, 475, doi: 10.1038/nature10768

Welsh, W. F., Orosz, J. A., Short, D. R., et al. 2015, ApJ, 809, 26, doi: 10.1088/0004-637X/809/1/26

West, R. G., Gillen, E., Bayliss, D., et al. 2019, MNRAS, 486, 5094

Wilde, S. A., Valley, J. W., Peck, W. H., & Graham, C. M. 2001, Nature, 409, 175

Williams, D. M., & Kasting, J. F. 1997, Icarus, 129, 254

Williams, D. M., & Pollard, D. 2002, International Journal of Astrobiology, 1, 61, doi: 10.1017/S1473550402001064

Williams, G. E. 2000, Reviews of Geophysics, 38, 37, doi: 10.1029/1999RG900016

Wilson, H. F., & Militzer, B. 2012, Phys. Rev. Lett., 108, 111101

Winn, J. N., & Fabrycky, D. C. 2015, Ann. Rev. Astron. Astrophys., 53, 409

Winters, B. 1964, JQSRT, 4, 527

Winton, M. 2006, Journal of Climate, 19, 359

Wittenmyer, R. A., O'Toole, S. J., Jones, H. R. A., et al. 2010, ApJ, 722, 1854

Wolf, E. T., & Toon, O. B. 2015, Journal of Geophysical Research (Atmospheres), 120, 5775

Wolszczan, A. 1999, Nature, 400, 812

Wolszczan, A., & Frail, D. A. 1992, Nature, 355, 145

Wordsworth, R. 2015, ApJ, 806, 180, doi: 10.1088/0004-637X/806/2/180

Wordsworth, R., Kalugina, Y., Lokshtanov, S., et al. 2017, GeoRL, 44, 665, doi: 10.1002/2016GL071766

Wordsworth, R. D., Forget, F., Selsis, F., et al. 2010a, A&A, 522, A22, doi: 10.1051/0004-6361/201015053

Wordsworth, R. D., Forget, F., & Eymet, V. 2010b, Icarus, 210, 992, doi: 10.1016/j.icarus.2010.06.010

Wordsworth, R. D., & Pierrehumbert, R. T. 2013, ApJ, 778, 154, doi: 10.1088/0004-637X/778/2/154

Wordsworth, R. D., Schaefer, L. K., & Fischer, R. A. 2018, AJ, 155, 195, doi: 10.3847/1538-3881/aab608

Wright, J. T., Upadhyay, S., Marcy, G. W., et al. 2009, ApJ, 693, 1084

Xie, J.-W., Dong, S., Zhu, Z., et al. 2016, Proceedings of the National Academy of Science, 113, 11431

Yadavalli, S. K., Quarles, B., Li, G., & Haghighipour, N. 2020, MNRAS, 499, 1506, doi: 10.1093/mnras/staa2980

Yang, J., Leconte, J., Wolf, E. T., et al. 2016, ApJ, 826, 222

Yang, J.-Y., Xie, J.-W., & Zhou, J.-L. 2020, AJ, 159, 164

Yang, S., Ricchiazzi, P., & Gautier, C. 2000, JQSRT, 64, 585, doi: 10.1016/S0022-4073(99)00140-5

Yoshizaki, T., & McDonough, W. F. 2021, Chemie der Erde / Geochemistry, 81, 125746, doi: 10.1016/j.chemer.2021.125746

Zahnle, K., Claire, M., & Catling, D. 2006, Geobiology, 4, 271, doi: https://doi.org/10.1111/j.1472-4669.2006.00085.x

Zahnle, K., & Walker, J. C. G. 1987, Precambrian Research, 37, 95, doi: 10.1016/0301-9268(87)90073-8

Zahnle, K. J., Gacesa, M., & Catling, D. C. 2019, Geochimica et Cosmochimica Acta, 244, 56, doi: 10.1016/j.gca.2018.09.017

Zhu, W. 2019, ApJ, 873, 8

Zhu, W., & Dong, S. 2021, arXiv e-prints, arXiv:2103.02127. https://arxiv.org/abs/2103.02127

Ziegler, C., Law, N. M., Morton, T., et al. 2017, AJ, 153, 66, doi: 10.3847/1538-3881/153/2/66

Zucker, S., Mazeh, T., Santos, N. C., Udry, S., & Mayor, M. 2004, A&A, 426, 695, doi: 10.1051/0004-6361:20040384

Zuluaga, J. I., Mason, P. A., & Cuartas-Restrepo, P. A. 2016, ApJ, 818, 160, doi: 10.3847/0004-637X/818/2/160